MAGNETIC RESONANCE IMAGING OF THE CEREBRAL BLOOD VOLUME FOR THE CHARACTERIZATION OF EXPERIMENTAL BRAIN TUMOR NEOVASCULARIZATION

Teodora-Adriana Perles-Barbacaru

Faculty of Medicine - Joseph Fourier University - Grenoble - France
Ecole Doctorale Ingénierie pour la Santé, la Cognition et l'Environnement
Grenoble Institut des Neurosciences UMR-S INSERM / UJF / CEA 836

---

presented by

Adriana T. Perles-Barbacaru

Dissertation for the Degree of Doctor of Philosophy (PhD) in Physics
Signals and Imaging in Medicine and Biomedicine

English title:

Magnetic resonance imaging of the cerebral blood volume for the characterization of experimental brain tumor neovascularization

French title:

Imagerie par résonance magnétique du volume sanguin pour la caractérisation de la néovascularisation dans les tumeurs cérébrales expérimentales

presented at the Joseph Fourier University December 20, 2007

jury:
Anne Marguerite Leroy-Willig (reporter)
Robert Nicolas Henry Muller (reporter)
Isabelle Berry (examiner)
Jean François Le Bas (examiner)
Christoph Segebarth (co-supervisor)
Hana Lahrech (supervisor)

Acknowledgements

The present work was carried out in the Department of Functional and Metabolic Neuroimaging, French National Institute of Health and Medical Research (INSERM), University Joseph-Fourier, Grenoble, France from 2004 to 2007.

This work would not exist without the encouragement of Professor Jean-François Le Bas from the Department of Neuroimaging of the University Hospital in Grenoble. I am grateful for his confidence and letters of recommendation, which certainly played a considerable role in finding research funding.

I would like to thank my principal supervisor, Hana Lahrech, PhD, and my co-supervisor and director of the laboratory, Christoph Segebarth, PhD, for the support and advice they have provided throughout the duration of my Ph.D, Professor Robert Muller and Professor Anne Ieroy-Willig for acceptance to review this work and Professor Isabelle Berry for agreeing to be part of the jury.

I would also like to thank all the people with whom I have worked over the past three years, without whom this work would have been much more difficult, and particularly

- Régine Farion for the cryosections, the histological staining and for teaching me some surgical procedures and the art of handling rats and biological material like tumor cells, histochemicals etc,
- Boudewijn van der Sanden, PhD, for explaining me the use of microscopic image acquisition and processing software and for helpful comments,
- Taoufik Fadlallah, MSc, for his preliminary work on stereological methods,
- Marion Gandit for a first version of an ImageJ macro for the analysis of immunofluorescent histological images of the microvasculature,
- Lionel Chièze, who was a Master degree student, for his participation in studying the relaxation properties of the Gd-BCX compound and for working late during our experiments,
- Nils Kickler, PhD, for his IT skills and his friendship,
- the engineers Olivier Montigon and Hervé Mathieu, PhD, for frequent technical assistance during the MRI experiments,
- Marine Beaumont, Irène Troprès and Emanuel Barbier for the introduction to the practical aspects of CBVf measurements using the ΔR_2*-method, and for the discussion about brain tumor models and their permeability to Sinerem,
- Jean-Claude Vial, PhD, from the "SPECTRO Laboratory" for the Turbo Pascal code for the creation of a "virtual phantom"
- Jean-Claude Debouzy, MD, from the "Laboratoire de Biophysique" of the French Research Center of the Army Health Services (CRSSA) and Pascal Fries, PhD, and Andrée Gadelle, PhD, from the "Laboratoire de Reconnaissance Ionique/Service de Chimie Inorganique et Biologique", of the French Atomic Energy Commission (CEA) for fruitful discussions and for teaching me some basic chemistry techniques, as well as
- Laurent Lamalle, PhD, for the image reconstruction of Projection Reconstruction acquisitions.

The project described in this manuscript is based on the theoretical and experimental work carried out by Hana Lahrech and her PhD student Emanuel Fonchy a couple of years before my arrival to the laboratory. I have relied on some of their results, and I would like to acknowledge this contribution.

Guerbet Laboratories provided most of the contrast agents employed in this study and I thank particularly Philippe Robert for his interest in and support of our experiments.

In a more personal context, I want to acknowledge the collegial friendship of Mathilde Pachot-Clouard and Hana Lahrech, who not only shared their office with me, but also helped me out in private issues.

I am deeply grateful to my parents for laying the foundations of scientific approaches during my childhood.

The most precious support came from my husband who took care of our daughter in the evenings waiting for me to finish the experiments: “Merci infiniment, Michel!” for lovingly supporting me and for your willingness to adapt your professional plans to my career.

Finally I would like to thank the Association for Anti-Cancer Research (Association pour la Recherche contre le Cancer, ARC) for their 3- years funding of my PhD and the early recognition of my work by a prize, but I also want to acknowledge the German Academic Exchange Service (Deutscher Akademischer Austauschdienst, DAAD) and the French National Academy of Medicine (Académie Nationale de Médecine, ANM) for offering each of them a one year funding.

Fig. 0: Some of my colleagues in the Department of Functional and Metabolic Neuroimaging

English abstract

Cerebral blood volume fraction (CBVf) mapping by magnetic resonance imaging (MRI) can provide information about the progression of tumor angiogenesis without harmful side-effects. In this work, a novel MRI method for in vivo CBVf mapping is developed: the Rapid Steady State T_1 ($RSST_1$) method.

The method is based on a two-compartment model, intra- and extravascular, without water exchange, and on the longitudinal relaxivity of intravascular MRI contrast agents (CAs). This method has been validated on healthy Wistar rats at 2.35 T (CBVf: 2 to 3%) and its sensitivity has been evaluated in a hypercapnia experiment (CBVf increase of 1%/mmHg CO_2).

In order to apply this method for monitoring disease evolution or treatment efficacy, CAs are evaluated that do not leak across the blood brain barrier during the measuring time. Two experimental CA, Gd-ACX and SINEREM were used on two rat glioma models C6 and RG2. The CBVf measures in tumor tissue obtained with Gd-ACX are confirmed by a histologic vascular morphometric analysis. CBVf mapping with SINEREM necessitates acquisitions with short echo time. The measures were compared with those obtained by a ΔR_2^*-based steady state method using the same SINEREM injection.

In case of CA extravasation, such as occurs in tumor tissue with CAs approved for clinical use, the CBVf along with the transfer coefficient κ (a measure related to the endothelial permeability) were obtained by pharmacokinetic two-compartment analysis of dynamic $RSST_1$ acquisitions.

In conclusion, the $RSST_1$ method in conjunction with appropriate CAs can be used for longitudinal angiogenesis studies to quantify the CBVf and the vascular permeability.

Keywords
Angiogenesis
Cerebral blood volume
Magnetic resonance imaging
Paramagnetic contrast agent

Résumé français

La mesure du volume sanguin cérébral (VSC) par Imagerie par Résonance Magnétique (IRM) permet d'étudier l'angiogénèse tumorale. Dans cette thèse, une méthode IRM, dite méthode T_1 stationnaire rapide ($RSST_1$) pour quantifier le VSC est proposée.

Le principe repose sur les propriétés de la relaxation longitudinale avec des agents de contraste (AC) paramagnétiques intravasculaires et sur un modèle du cerveau bi-compartimental extra/intravasculaire sans échange d'eau. La méthode a été validée sur des rats sains à 2.35T (VSC: 2 à 3%) et la sensibilité évaluée sous hypercapnie (augmentation du VSC de 1%/mmHg CO_2).

Pour évaluer l'efficacité d'un traitement antitumoral, des AC ne s'extravasant pas durant la mesure à travers une barrière hématoencéphalique (BHE) lésée sont nécessaires. Deux AC expérimentaux, le Gd-ACX et le SINEREM, ont été étudiés sur deux modèles de rat gliome C6 et RG2. Avec le Gd-ACX, les mesures ont été confrontées à une analyse morphométrique de la microvascularisation sur des coupes immuno-histologiques. Les mesures avec le SINEREM ont nécessité le développement d'acquisitions à temps d'écho court et ont été comparées à ceux obtenus par la méthode ΔR_2^* utilisant le même AC.

Pour des AC qui s'extravasent (Gd-DOTA admis en clinique), utilisant une analyse pharmacocinétique à deux compartiments, les acquisitions de la méthode $RSST_1$ conduisent à la mesure du VSC et au coefficient de transfert κ lié à la perméabilité de la BHE.

En conclusion, la méthode $RSST_1$, méthode quantitative de mesure de VSC, permet avec des AC appropriés, de réaliser des études longitudinales de l'angiogénèse tumorale et d'accéder à la perméabilité vasculaire.

Mots-clés
Angiogenèse
Volume sanguine cérébral
Imagerie par resonance magnétique
Agent de contraste paramagnétique

Lists of abbreviations and symbols

List of abbreviations

2DFT	two dimensional Fourier transform
AC	agent de contraste
ACD	natural alpha-cyclodextrin
ACX	modified alpha-cyclodextrin
AIF	arterial input function
ANN	averaged nearest neighbor gridding algorithm
ASL	arterial spin labeling
AV	vascular area density
BBB	blood brain barrier
BCX	modified beta-cyclodextrin
BHE	barrière hématoencéphalique
BOLD	blood oxygenation level dependent
CA	contrast agent
CAs	contrast agents
CBF	cerebral blood flow
CBV	cerebral blood volume
CBVf	cerebral blood volume fraction
CEA	Commission d'Energie Atomique, French Atomic Energy Commission
CGS	centimetre-gram-second unit
CNR	contrast to noise ratio
CNS	central nervous system
CT	computed tomography
DCE	dynamic contrast enhanced
DFT	discrete Fourier transform
DNA	deoxy-ribonucleic acid
DOTA	tetraazocyclododecane tetraacetic acid
DSC	dynamic susceptibility contrast
DTPA	diethylene triamine pentaacetic acid
EPI	echo planar imaging
eve	extravascular extracellular
evi	extravascular intracellular
FDA	food and drug administration
FGF	fibroblast growth factor
FID	free induction decay
FLASH	fast low angle shot
FOV	field of view
GM	gray brain matter
HE	Hematoxylin Erythosine
INSERM	institut national de la santé et de la recherche médicale
IR	inversion recovery
IRM	imagerie par résonance magnétique
ivi	intravascular intracellular
l	leakage
LD_{50}	median lethal dose

MR	magnetic resonance
MRA	magnetic resonance angiography
MRI	magnetic resonance imaging
MRS	magnetic resonance spectroscopy
MTT	mean transit time
MV	macroscopic vessels
NMR	nuclear magnetic resonance
NMRD	nuclear magnetic resonance dispersion
NN	nearest neighbor gridding algorithm
p	plasma
$PaCO_2$	partial arterial carbon dioxide tension
PaO_2	partial arterial oxygen tension
PBS	phosphate-buffered saline
PDGF	platelet derived growth factor
PET	positron emission tomography
PGSE	pulsed gradient spin echo
PR	projection reconstruction
PR3D	three dimensional projection reconstruction acquisition mode
RF	radio frequency
ROI	region of interest
rpm	rounds per minute
$RSST_1$	rapid steady state T_1
SENSE	sensitivity encoding
SNR	signal to noise ratio
SPECT	single photon emission computed tomography
SPIO	superparamagnetic iron oxide
SS	steady state
TE	echo time
T_{inv}	inversion time
TNF	tumor necrosis factor
TR	repetition time
USPIO	ultrasmall superparamagnetic iron oxide
VASO	vascular space occupancy
VPF/VEGF	vascular permeability factor/vascular endothelial growth factor
VSC	volume sanguin cérébral
VSI	vessel size index
VSOP	very small superparamagnetic iron oxide particles
WM	white brain matter

List of symbols

a	major axis of ellipse
$\Re(t)$	residue function
A_V	vascular area density
b	minor axis of ellipse
B_0	main magnetic field
$B_1(t)$	oscillating magnetic field perpendicular to B_0
C_a	arterial concentration (of the CA)
CBF × $\Re(t)$	impulse response function

C_e	extravascular concentration (of the CA)
C_{iv}	intravascular concentration (of the CA)
C_l	CA concentration in the leakage compartment
C_p	plasma concentration (of the CA)
C_{tissue}	tissue concentration (of the CA)
C_v	venous concentration (of the CA)
D	water diffusion coefficient
đ	mean vessel diameter
d	mean diffusion length
E	extraction fraction
E(t)	signal enhancement
F	blood flow
f_D	transverse relaxation decay term
F_{pl}	trans endothelial CA flow between plasma and leakage compartment
G	G_x,G_y,G_z magnetic field gradient
ħ	reduced Planck's constant
Hct	hematocrit
inv	inversion factor
K	exchange regime
k	k_x,k_y,k_z spatial frequencies
k_B	Boltzmann's constant
k_{ei}	extracellular-intracellular exchange rate
k_{ep}	extravascular-plasma exchange rate constant
$k_{ev\text{-}iv}$	extravascular-intravascular exchange rate
k_{ie}	intracellular-extracellular exchange rate
$k_{iv\text{-}ev}$	intravascular-extravascular exchange rate
K^{trans}	endothelial permeability coefficient
L_V	vascular length density
m	characteristic time of the compartments participating in the water exchange, inverse of the shutter speed
M	magnetization
M_0	longitudinal magnetization at thermal equilibrium
M_{0ev}	extravascular longitudinal magnetization at thermal equilibrium
M_{0iv}	intravascular longitudinal magnetization at thermal equilibrium
M_{xy}	transverse magnetization
M_z	longitudinal magnetization
M_{zev}	longitudinal magnetization of the extravascular compartment
M_{ziv}	longitudinal magnetization of the intravascular compartment
N	number of acquisitions
n_{ev}	number of extravascular water protons or spins
n_{Ex}	number of experiments
n_{iv}	number of intravascular water protons or spins
Nk	number of α-pulses
n_{Ph}	number of phase encode steps
n_{ps}	number of water protons or spins in the system
n_S	number of samples

n_{total}	total number of water protons or spins $n_{iv} + n_{ev}$
N_v	vascular density
P	endothelial diffusional permeability coefficient
P_m	mole fraction of bound water protons
R	vessel radius
r	x,y,z position
r	distance
R_1	longitudinal relaxation rate
r_1	longitudinal relaxivity
R_{10}	intrinsic longitudinal relaxation rate
R_2	transverse relaxation rate
r_2	transverse relaxivity
R_2^*	apparent transverse relaxation rate
R_2^*	effective transverse relaxation rate
R_{20}	intrinsic transverse relaxation rate
S	signal intensity
S(**k**)	spatial frequency spectrum
S*(**k**)	complex conjugate to the spatial frequency spectrum
S_0	signal intensity corresponding to magnetization at thermal equilibrium
S_{0ev}	signal intensity corresponding to extravascular magnetization at thermal equilibrium
S_{0iv}	signal intensity corresponding to intravascular magnetization at thermal equilibrium
S_{ev}	extravascular signal intensity
S_{iv}	intravascular signal intensity
S^{norm}, S_{post}^{norm}	normalized signal intensity
S_{post}	signal acquired after contrast agent injection
S_{pre}	signal acquired prior to contrast agent injection
S_V	vascular surface
T	absolute temperature
t	time
T_1	longitudinal relaxation time constant
T_1^{app}	apparent longitudinal relaxation time
T_{1e}, T_{2e}	longitudinal and transverse electronic relaxation rates
T_{1ev}	extravascular longitudinal relaxation time constant
T_{1iv}	intravascular longitudinal relaxation time constant
T_2	transverse relaxation time constant
T_2^*	effective transverse relaxation time, experimentally observed decay time constant of an FID signal
T_{2ev}	extravascular transverse relaxation time constant
T_{2iv}	intravascular transverse relaxation time constant
τ_a	water residence or life time in compartment a
T_{acq}	total acquisiton time of a MR scan
τ_C	correlation time
τ_{ep}	time constant for transendothelial contrast agent flow k_{ep}^{-1}
τ_{ev}	extravascular water residence or life time
τ_{exch}	exchange time
τ_{exch}^{-1}	exchange rate
τ_{iv}	intravascular water residence or life time

τ_m	residence time of coordinated water molecule
τ_R	rotational correlation time
V	volume
v	volume fraction
v_d	distribution volume fraction
V_e	extravascular volume accessible to the contrast agent
v_e	fractional volume of the extravascular compartment accessible to the contrast agent
V_{ev}	extravascular volume
V_{eve}	extravascular extracellular volume inaccessible to the CA
V_{evi}	extravascular intracellular volume
V_{iv}	intravascular volume
v_{iv}	intravascular volume fraction
V_{ivi}	intravascular intracellular volume
V_l	volume of the leakage compartment
v_l	volume fraction of the leakage compartment
v_p	fractional volume of the plasma compartment
V_p	plasma volume
V_{total}	total tissue volume $V_{iv} + V_{ev}$
V_V	vascular volume density
w_{blood}	blood water content
w_{tissue}	tissue water content
α	flip angle
γ	proton gyromagnetic ratio: 42.58 MHz/T
Θ	polar angle
κ	signal enhancement rate
κ_{ev}	enhancement rate of the extravascular compartment
κ_{iv}	enhancement rate of the intravascular compartment
λ	brain - blood partition coefficient for water
π	180° pulse
ρ(**r**)	proton/spin density function
ρ_{blood}	blood water density
ρ_{tissue}	tissue water density
σ_S	standard deviation of the averaged signal
Φ	azimuthal angle
X	susceptibility
ω	Larmor pecession frequency

General introduction

Research environment

This work was carried out in the laboratory for Functional and Metabolic Neuroimaging, affiliated to the French National Institute for Health and Medical Research (INSERM), the Joseph Fourier University of Grenoble and the Federal Institute of Research “NMR: from cell to man”. It is an officially recognized research laboratory of the Atomic Energy Commission (CEA) and has recently become part of the Grenoble Institute of Neuroscience. This interdisciplinary laboratory develops in vivo magnetic resonance imaging (MRI) techniques that are tested on glioma, trauma and ischemia models in rodent brains, before they are transferred to the clinical applications. During the research project that is subject of this dissertation, the laboratory was equipped with two horizontal animal MR scanners (7T and 2.35T), a 4.7T vertical MR scanner, and two human full body MR scanners (1.5T and a 3T). It has fluorescent and confocal microscopes, and access to a two photon microscope for in vivo imaging.

Objectives

Although the human brain makes up only about 2% of the total body weight, it receives up to 20% of the heart's output. A constant and efficient blood supply of the brain is vital. The vasculature of brain tissue is a complex entity having multiple functions and regulatory mechanisms. Most adjustments occur at the microscopic level. Tissues with a high metabolic turnover are generally equipped with a more extensive network of microvessels. Cerebral blood volume (CBV) is defined as the volume occupied by blood per tissue mass (ml/g) or alternatively per volume of brain tissue (%), in which case we call it the cerebral blood volume fraction (CBVf). It can be used to quantify the extent of tissue vasculature. Highly vascularised areas of the brain such as the basal ganglia or the cortical gray matter have a higher CBVf than the less vascularised cerebral white matter. As a functional parameter, the CBVf is altered in the context of vascular auto-regulation. Some diseases affect morphological parameters, such as the vessel density and their size, or hemodynamic parameters, such as the perfusion, which in turn can be detected by an alteration of the CBV. A major research area in which absolute CBV measurements play an important role, are the study of the formation of new microvessels (angiogenesis) for example for the growth and metastasis of malignant brain tumors.

As MRI is a noninvasive technique that does not use ionizing radiation, it is excellent for in vivo experiments especially when repeated studies are required such as in a clinical context. In addition to anatomical and structural information, MRI can also provide quantitative information of physiologic parameters (e.g. membrane permeability, blood oxygenation) and dynamic events (e.g. diffusion and convection of water, concentration time course of magnetic tracers).

The aim of this work is to establish a new MRI method for CBVf quantification and mapping in healthy and diseased brain tissue. It is called the Rapid Steady State T_1 ($RSST_1$) method because it exploits T_1 relaxation effects and a dynamic steady state of the magnetization created by fast MRI. It is based on a two compartment model of the brain tissue and requires the injection of exogenous paramagnetic contrast agents (CAs) that modify the longitudinal relaxation of the intravascular water to distinguish it from the water of the extravascular compartment.

Given the recent developments of antiangiogenic drugs in the treatment of cancer, the proposed $RSST_1$ method is aimed at CBVf-quantification in malignant brain lesions. Several commercial and experimental CAs are therefore studied for their blood pool properties in malignant brain tumor models in rats.

The following introductory chapter is a literature review of MRI methods providing functional vascular parameters for the evaluation of cancer. Owing to the interdisciplinary character of this work, it is composed of three major parts. The first part provides an overview of the morphological and functional parameters of the microvasculature, describes the process of angiogenesis and the factors involved and reviews the clinical classification of brain tumors and the available animal models of malignant brain tumor. The second part deals with the relaxation properties of CAs and in particular their compartmentalization in the tissue. Finally, the methodological background of medical imaging techniques and in particular of MRI techniques used for CBV quantification is introduced in the last part.

The experimental part of the manuscript is organized into six chapters, corresponding to six studies having different purposes. The first two chapters deal with the methodological development of the $RSST_1$ method and its application to healthy rat brain. The remaining chapters investigate the utility of different CAs for CBVf quantification in two malignant brain tumor models, RG2 and C6. The CBVf measures are validated using another steady state MRI

method for CBVf mapping based on the transverse relaxation (T_2*) effect and using histological vascular morphometric analysis.

In chapter I, the theoretical background is exposed and the assumptions and experimental conditions are verified by signal modeling and in vitro experiments. Gd-DOTA, a clinically approved small molecular CA, and P760, an experimental intermediate size CA characterized by a higher longitudinal relaxivity, both from Guerbet Laboratories, are used. The sensitivity of the $RSST_1$ method to physiologically occurring CBVf changes is studied. Factors that influence the accuracy of the CBVf measure are evaluated and the advantages and limits of the method are investigated.

Chapter II concerns further methodological developments necessary for the use of SINEREM, a clinically approved superparamagnetic CA from Guerbet laboratories characterized by a high transverse relaxivity. These developments consist in the implementation of a three dimensional projection reconstruction acquisition mode to image the entire brain volume and to allow a short echo time. In this context the studied method is compared to the T_2* based steady state method for CBVf mapping using the same CA.

The study in chapter III is designed to evaluate SINEREM for its intravascular confinement in an RG2 brain tumor model using the $RSST_1$ method and the T_2* based steady state method.

Chapter IV deals with the physicochemical characterization, biocompatibility and biodistribution of Gd-ACX, an experimental CA from the CEA. Its potential for CBVf mapping in a C6 tumor model is evaluated and compared with Gd-DOTA.

In chapter V, a study is described, in which the CBVf measure obtained with Gd-ACX is validated using histological vascular morphometric analysis combined with a stereological technique for CBVf estimation.

Finally, chapter VI deals with the ability to estimate the CBVf in case of CA leakage out of the vasculature. The proposed $RSST_1$ method is investigated for its potential to dynamically monitor the leakage profile of Gd-DOTA and P760 in a RG2 tumor model. A pharmacokinetic model is applied to the leakage profile allowing the simultaneous estimation of the CBVf, the transfer

constant (related to the permeability of the endothelium to the CA) and the distribution volume of the CA.

Introduction générale

Environnement de recherche

Ce travail a été réalisé dans le laboratoire de Neuroimagerie Fonctionnelle et Métabolique dirigé par Christoph Segebarth. Ce laboratoire est affilié à l'Institut National de Santé et de Recherche Médicale (INSERM), à l'Université Joseph Fourier (UJF) et l'Institut Fédéral de Recherche (IFR) « RMN : de la cellule à l'Homme ». Il est également associé au Commissariat d'Energie Atomique (CEA). Récemment et depuis janvier 2007, ce laboratoire est intégré dans l'Institut de Neuroscience de Grenoble dirigé par Claude Feuerstein. Les travaux de recherche sont centrés autour de développements de méthodes en IRM et leur utilisation pour l'exploration in vivo du système nerveux central. Le laboratoire dispose de deux plate-formes, une plate-forme petit animal et une plate-forme pour la recherche clinique chez l'Homme. L'expérimentation animale est menée sur plusieurs modèles chez le rat ou la souris (tumeur, ischémie, traumatisme crânien, modèle d'épilepsie). Ce volet préclinique concerne le développement méthodologique et leur validation dans un modèle animal, l'évaluation de méthodes IRM pour l'étude et la caractérisation du modèle ou encore l'évaluation de l'effet de nouvelles drogues. Très souvent, les résultas IRM sont confrontés aux résultats obtenus par analyse histologique par microscopie optique. Pendant la durée de mon travail de thèse, le laboratoire était équipé de deux aimants horizontaux 7T (20 cm) et 2.35T (40 cm), et d'un aimant vertical de 4.7T (11 cm). La plate-forme pour la recherche chez l'Homme est composée de deux aimants (1.5T et 3T). Par ailleurs, le laboratoire est également équipée de microscopes à fluorescence et confocaux et d' un microscope biphoton pour l'imagerie in vivo.

Objectifs

Le cerveau humain ne pèse que 2% du poids total et malgré cela, il reçoit jusqu'à 20% du sang distribué par le cœur. Pour le cerveau, il est vitale et essentiel que la quantité de sang soit constante. La vascularisation cérébrale est complexe avec des fonctions et des mécanismes régulateurs multiples, qui sont contrôlés au niveau microscopique. Les tissus avec un métabolisme élevé sont généralement dotés d'un réseau de microvaisseaux plus important. Le volume sanguin cérébral (VSC) est défini comme le volume occupé par le sang par masse tissulaire (ml/g) ou alternativement par volume cérébral (%), dans quel cas on parle de la fraction volumique sanguine cérébrale (fVSC). Le VSC est un paramètre qui permet de

quantifier la vascularisation. Les régions du cerveau hautement vascularisées, comme les ganglions de la base ou le cortex cérébral ont un VSC plus élevé que la matière blanche moins vascularisée. Puisque c'est un paramètre fonctionnel, le VSC est altéré/modifié dans l'auto-régulation vasculaire cérébrale. Dans le cas de pathologies, des paramètres morphologiques tels que la densité vasculaire, la taille des vaisseaux, ou encore les paramètres hémodynamiques (VSC, débit..) peuvent être affectés. Dans le cas de tumeurs cérébrales, une altération du VSC peut être observée. Un des sujets de recherche dans lequel la mesure du VSC absolu joue un rôle important, est l'étude de la formation des nouveaux microvaisseaux (angiogenèse) qui accompagne par exemple la croissance des tumeurs cérébrales malignes.

En Neurosciences, l'IRM est une technique incontournable et permet d'avoir des informations très précieuses aussi bien pour détecter des pathologies ou encore pour étudier les fonctions cérébrales. L'IRM est une technique non invasive qui n'utilise pas de rayonnement ionisant, elle est excellente pour les expériences in vivo, particulièrement quand des études répétées sont nécessaires, comme en clinique. Hormis l'information anatomique des structures cérébrales qui est l'origine du succès de l'IRM, l'IRM fournit également des informations quantitatives sur des paramètres physiologiques (p. ex. la perméabilité membranaire, l'oxygénation sanguine) ou encore des paramètres dynamiques (p. ex. la diffusion et la convection de l'eau, la concentration des traceurs magnétiques au cours du temps).

Le but de ce travail est de développer une nouvelle méthode IRM pour la quantification et la cartographie de la fVSC dans le tissu cérébral sain et pathologique. La méthode proposée - Rapid Steady State T_1 ($RSST_1$), méthode T_1 stationnaire rapide, est une méthode IRM rapide qui exploite les effets de relaxation longitudinale T_1 en présence d'un agent de contraste (AC) paramagnétique et conduit à créer un état stationnaire dynamique rapide du signal. La méthode $RSST_1$ est basée sur un modèle à deux compartiments du tissu cérébral (extra- et intravasculaire). Le compartiment extravasculaire est caractérisé par des temps de relaxation T_1 longs et le milieu intravasculaire est caractérisé par des temps de relaxation T_1 courts car, dans ce compartiment les molécules d'eau sont en contact avec l'AC supposé purement vasculaire.

Avec les développements récents dans le traitement du cancer par des médicaments antiangiogéniques, il est fort utile de pouvoir quantifier l'effet de ces médicaments en mesurant le VSC qui est directement lié à la densité vasculaire. Pour que la méthode $RSST_1$ proposée puisse être adaptée pour la quantification du VSC dans des tumeurs cérébrales malignes,

souvent accompagnées par des lésions de la BHE, il est important que le modèle à deux compartiments puisse être valable. Les AC autorisés en clinique sont connus pour s'extravaser dans la plupart des tumeurs et quittent le système vasculaire. Des mesures de la fVSC réalisées dans ce cas seront erronées. Une partie de ce travail de thèse a été orientée pour évaluer les conditions de leur utilisation pour des mesures précises du VSC dans des modèles de tumeur maligne chez le rat.

Le chapitre suivant est un chapitre de revue bibliographique des méthodes IRM qui permettent de mesurer des paramètres vasculaires fonctionnelles pour l'évaluation du cancer. Comme ce travail est interdisciplinaire, il est composé de trois grandes parties.
La première partie est une vue d'ensemble sur les paramètres morphologiques et fonctionnels de la microvascularisation et décrit l'angiogenèse et les facteurs impliqués dans ce processus. On définit également la classification des tumeurs cérébrales et on présente les différents modèles animaux des tumeurs cérébrales malignes.
La deuxième partie concerne les propriétés de relaxation des AC et en particulier leur compartimentation dans le tissu. Finalement, dans la dernière partie, les bases méthodologiques des techniques d'imagerie médicale sont introduites et en particulier des techniques IRM utilisés pour quantifier le VSC.

La partie expérimentale de ce manuscrit est divisée en six chapitres correspondant à six études avec des buts différents. Les deux premiers chapitres concernent le développement méthodologique de la méthode $RSST_1$ et ses applications au cerveau de rat sain. Les autres chapitres étudient les conditions d'utilisation de différent AC expérimentaux pour la quantification de la fraction volumique sanguine cérébrale (fVSC) dans deux modèles de tumeur chez le rat RG2 et C6. Les mesures de la fVSC sont comparées puis validées en utilisant des méthodes alternatives. Dans un cas on utilise la méthode IRM stationnaire basée sur les effets de la relaxation transverse T_2* et dans un autre cas on utilise une analyse histologique de la morphologie vasculaire.

Dans le chapitre I, la théorie de la méthode est détaillée et les hypothèses et les conditions expérimentales sont vérifiées par des modélisations du signal et par des expériences in vitro. Le Gd-DOTA, un AC de petite taille moléculaire admis en clinique, et le P760, un AC expérimental de taille moléculaire intermédiaire caractérisé par une relaxivité longitudinale plus élevée, tous les deux des Laboratoires Guerbet, sont utilisés. La sensibilité de la méthode $RSST_1$ aux

changements physiologiques du VSC est étudiée. Les facteurs qui influencent la précision de la mesure de la fVSC sont évalués et les avantages et les limites de la méthode sont étudiés.

Le chapitre II concerne d'autres développements nécessaires pour l'utilisation de la méthode $RSST_1$ avec le SINEREM, un AC superparamagnétique admis en clinique des Laboratoires Guerbet, et caractérisé par une relaxivité transversale élevée. Les développements consistent en l'implémentation d'une méthode d'acquisition de projection rétroprojection en trois dimensions, pour cartographier la fVSC du cerveau entier et pour permettre un temps d'écho court. La fVSC est comparée à celle obtenue par la méthode stationnaire basée sur les effets T_2* en utilisant le même AC.

L'étude décrite dans le chapitre III a été menée pour évaluer en utilisant la méthode $RSST_1$ et la méthode stationnaire basée sur les effets T_2* si le SINEREM reste intravasculaire dans un modèle de tumeur RG2.

Le chapitre IV concerne la caractérisation physicochimique, la biocompatibilité et la biodistribution de Gd-ACX, un AC expérimental du CEA. Son potentiel pour la cartographie de la fVSC dans un modèle de tumeur C6 est évalué et comparé avec le Gd-DOTA.

Dans le chaptire V, une étude est décrite, qui valide la mesure de la fVSC dans les tumeurs C6 obtenu par IRM avec le Gd-ACX comme AC, en utilisant une analyse histologique de la morphométrie vasculaire combinée avec une méthode stéréologique pour l'estimation de la fVSC.

Finalement, le chapitre VI concerne la possibilité d'estimer la fVSC quand l'AC s'extravase. Le potentiel de la méthode $RSST_1$ proposée pour suivre dynamiquement le profil d'extravasation de Gd-DOTA et P760 dans un modèle de tumeur RG2 est étudié. Un modèle pharmacocinétique est appliqué au profil d'extravasation permettant simultanément l'estimation de la fVSC, d'un paramètre lié à la perméabilité de l'endothelium pour l'AC et du volume de distribution extravasculaire de l'AC.

Literature review

1. Purpose of the literature review

The purpose of this work is to validate a fast T_1-based MRI method for CBV quantification in malignant tumor tissue.

Before describing the theoretical framework of this method and the validation studies in chapter I to VI, this introductory chapter presents a literature review of existing MRI methods for CBVf mapping. Furthermore, the purpose of this chapter is:

to define the physiological parameter called CBV or CBVf,
to show how it is altered in the case of brain pathologies,
to demonstrate its importance in the clinical assessment of brain tumors,
to explain why a quantitative measurement, i.e. absolute CBV, is preferred,
to explain why an imaging technique is necessary,
to show the benefit of MRI techniques with respect to other medical imaging techniques,
to describe fast MRI techniques,
to compare T_1- T_2- and T_2*-based MRI methods for CBVf mapping, and to explain why a T_1-based technique has been chosen,
to review the classes of CA that are used to assign different relaxation properties to the vascular compartment.

To begin with, the morphology and physiology of microvasculature is first described in order to correctly define the CBVf and to determine the accuracy with which this parameter is measured with different techniques. Then the relevance of CBVf quantification in cancer research and in the management of cancer patients is pointed out. Medical imaging and in particular MRI techniques used in oncology are reviewed.

2. Brain microvasculature

In the direction of blood flow, the brain vasculature is composed of large arteries (e. g. anterior cerebral artery, pial arteries) branching into smaller arteries followed by arterioles (diameters ≈ 100 µm). With decreasing radii, the total amount of vessels and vascular surface S_v (cm^2/cm^3 or cm^2/g) increases considerably (Fig. 0-2a), facilitating the homogeneous irrigation of the tissue and the transport of molecules to or from the interstitium, respectively. This exchange takes place in the capillary network. The blood pressure and velocity decrease to facilitate the exchange. The blood flow into the capillary network is regulated by nerve-controlled sphincters that exist at the arteriolar level. The blood is then drained from the tissue by small venules and veins increasing in size into high-volume, low-pressure venous systems known as venous or dural sinuses.

Moving in an outward direction across the blood vessel wall, arterial vessels are formed by layers called intima (made up of endothelial cells), the basal lamina (also called basement membrane, a 40 nm thick membrane composed of type IV collagen and other substances), the elastic lamina, media (comprised of smooth muscle cells) and adventitia (comprised of fibroblasts producing collagen fibers). The veins have thinner walls, and most lack the smooth muscle cell layer.

2.1. The blood brain barrier

The radii of capillaries average 4 µm (Guyton and Hall 1997; Ross 1991). They are composed of a unique layer of endothelial cells, the endothelium, which is of continuous type in the brain (Fig. 0-2b). The adjacent endothelial cell membranes at the luminal end fuse and are connected by structures called the tight junctions, composed of transmembrane proteins called occludin and claudin. Other transmembrane proteins such as zonula occludens proteins and cadherins provide additional adhesion towards the abluminal (brain) side. A molecular model of this cellular adhesions is proposed by Huber et al (Huber et al. 2001). In addition, pericytes and foot like processes of astrocytes surround the basal lamina. This forms an entity called the blood brain barrier (BBB), which is a regulatory interface between the blood and the cerebral parenchyma. It is permeable to oxygen, carbon dioxide, hormones, carbohydrates, amino acids, fat, ammonia, lactate etc, but impermeable to many water soluble macromolecules, such as drugs (penicillin) and albumin. Since the paracellular transport of molecules is greatly reduced by the

interendothelial tight junctions, they have to cross the endothelial cells (transendothelial transport), with the consequence that intra-/extravascular exchange is controlled by the cell. The paucity of cytoplasmatic vesicles shows that substances are rarely carried across the endothelial cell by vesicular transport as it happens in most extracerebral tissues (Coomber and Stewart 1985). Differences in the activity of various hydrolytic enzymes at the luminal and abluminal cell membrane indicate the polarity of endothelial function in the control of the blood brain interface (Betz and Goldstein 1978; Brownson et al. 1994; Farrell and Pardridge 1991; Minn et al. 1991). The passage of a substance across the BBB may depend upon its lipid solubility, electrical charge, molecular size, dissociation constant, affinity for a carrier molecule or the capacity of the BBB for active transport of this substance.

Fig 0-2: the vascular system in vertebrates

a: Changes in blood pressure, velocity, and the surface area of the arteries, capillaries, and veins of the circulatory system. Image source (Purves et al. 1995)

b: Continuous capillary endothelium in brain (left) and discontinuous capillary endothelium in liver (right) with distinct intercellular gaps and broken basal lamina. 1. capillary lumen, 2. endothelial cell, 3. basal lamina, 4 Astrocyte process. Image source (Kahle 1991)

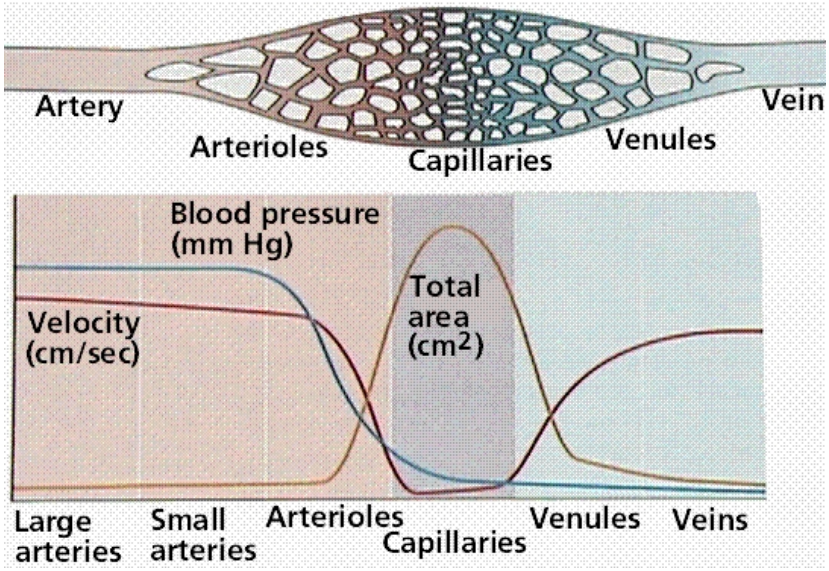

a

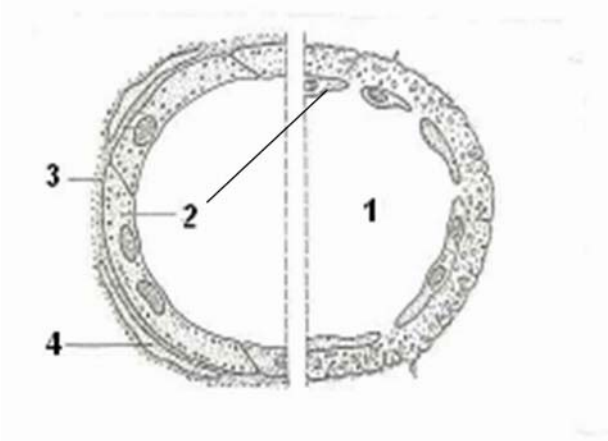

b

2.2. The morphology of vasculature

The morphology and quantity of the vasculature is organ specific (Chang et al. 1982). Both can change considerably during a disease process (Seitz et al. 1988) either because of adaptation to new metabolic demands of the affected tissue or because the cells forming the vessels are affected themselves by the pathology. In adaptation to temporally varying metabolic demands, the vasculature undergoes dynamic changes even under physiologic conditions. For example, the vessels are known to dilate or to open vascular shunts (alternative circulatory pathways) when the partial arterial carbon dioxide tension ($PaCO_2$), the arterial pH or the core temperature increases or the partial arterial oxygen tension (PaO_2) decreases. In some pathologies, such as in malignant tumors, the ability of the microvasculature to respond to such physiologic stimuli can be reduced, and can be used to characterize the disease (Julien et al. 2004; Mazurchuk et al. 1999).

Several parameters are used to describe and quantify the vascular network at a microscopic level. Microvascular density, N_v (cm^{-2}), simply reports the number of vessels regardless of their shape, orientation or size. The microvascular surface S_v is important for the exchange processes. The total surface area of the brain microvasculature, available for exchange processes between blood and interstitium is approximately 100 cm^2g^{-1} tissue (Pardridge et al. 1990). Another such parameter is the length density L_v (cm/cm^3), which is the total length of microvessels existing per unit volume or tissue mass. The vessel radii are important for rheological considerations because they define the cross sectional area that in turn is one of the

parameters that determines the blood flow rate. The mean intervascular distance is an index of the access of an interstitial cell to the exchange processes at the vascular boundary, since in the interstitium transport is mainly governed by diffusion. The mean intercapillary distance in the human brain is about 40 µm (Duvernoy et al. 1983). Other morphological parameters that change under physiologic and pathologic conditions exist, e. g. the tortuosity.

2.3. Hemodynamic parameters

From this point of view, medical imaging techniques, such as computed tomography (CT), positron emission tomography (PET) and MRI are rather macroscopic techniques. Vascular parameters accessible by these imaging techniques are the regional blood volume, which is the quantity of blood that participates in the supply of oxygen and nutrients and in the discharge of toxic metabolites. In addition, techniques exist, that allow the measurement of the amount of blood arriving and leaving the tissue of interest in a time interval. This is called the regional perfusion or blood flow. The average cerebral blood flow (CBF) in humans is approximately 50 ml/min per 100g of brain tissue, but may be higher (above 150 ml/min per 100g) in small animals (Calamante et al. 1999; Ginsberg et al. 1985; Rudin and Sauter 1991). Another often reported quantity related to the regional blood volume and flow is the mean transit time (MTT), the average time required for blood to pass through the tissue volume of interest. The permeability of the microvasculature to a substance is often reported as the product of the diffusional permeability coefficient P (cm min^{-1}) and the surface area S_v. PS_v has the unit of a volume flow per tissue mass (ml min^{-1} g^{-1}). Only values averaged over the volume of the voxel can be obtained and information about the morphology of the vasculature is lost. However, one MRI technique is sensitive to vessel radii, and the parameter obtained is called the vessel size index (VSI). It will be briefly described in a different paragraph.

Just like and in addition to morphologic analysis of the vasculature, the quantification of such hemodynamic parameters can be useful to study the tissue function and viability in the case of pathologic transformation (Aksoy and Lev 2000). Although the macrovasculature can be involved (Bullitt et al. 2005), most cerebrovascular diseases begin at the microvascular or capillary level. Detection of pathology at the microvascular level is consequently favorable because treatment could be started at an earlier stage of the disease, possibly even before irreversible clinical symptoms develop. The CBV and perfusion are tightly related since only perfused vessels will contribute to the signal change when CAs are used for the measurement.

Therefore, even in brain pathologies that mostly affect tissue perfusion, such as acute cerebral ischemia, the CBVf measure can be of use. Brain pathologies that are accompanied by vascular changes reflected by altered CBV, CBF, BBB permeability or combinations thereof, are brain infarction (ischemia) (Maeda et al. 1997; Rosen 1992; Rother et al. 1996), multiple sclerosis (Broom et al. 2005; Sibson et al. 2002), some forms of dementia such as Alzheimer's disease (Harris et al. 1996; Harris et al. 1998; Maas et al. 1997), Aquired Immune Deficiency Syndrome associated brain diseases (Ernst et al. 1998; Tracey et al. 1998), and traumatic brain injury (Garnett et al. 2001). The main objects of this work are the vascular changes occurring in the development of brain tumors, which require particular methodologic developments, because the BBB becomes permeable to most CAs.

3. Brain tumors

3.1. Epidemiology

In many countries, cancer is one of the three leading causes of death, only outnumbered by cardiovascular diseases (heart diseases, stroke etc). Despite some medical advances reflected in prolonged survival times, no curative treatment has been developed for the majority of tumors. In a report from the American Cancer Society in 2007 (American-Cancer-Society 2007), the annual incidence and mortality of brain and other central nervous system (CNS) tumors in the United States are 20 500 (1.4% of all new cancer cases) and 12 740 (2.3% of all cancer related deaths), respectively. Worldwide, approximately 176,000 new cases of brain and other CNS tumors were diagnosed in the year 2000, with an estimated mortality of 128,000 (Parkin et al. 2001).

3.2. Primary brain tumors

Brain tumors account for over 4/5 of all primary central nervous system tumors (Levin et al. 2001). Primary brain tumors (Fig. 0-3) arise from brain cells, rather than metastasizing to the brain from elsewhere in the body. Meningiomas and other mesenchymal tumors account for approximately 27% of primary brain tumors (Levin et al. 2001). Gliomas are the most common (about 50%) primary neoplasms of the brain (Russell and Rubinstein 1989). There are three

main types of glioma: astrocytoma, ependymoma and oligodendroglioma. About 5% of brain tumors are ependymomas. These develop from so-called ependymal cells, which line the ventricles and spinal cord. Oligodendrogliomas develop from cells called oligodendrocytes that produce the myelin. This glioma type can contain calcium and bleeds easily. Astrocytoma is the commonest type of glioma. Therefore, the terms "astrocytoma" and "glioma" are often employed interchangeably. They vary histologically and are graded into four categories by the World Health Organization (Kleihues et al. 1993).

3.3. Grading

Criteria for grading are the mitotic index (growth rate), vascularity, presence of necrotic areas, invasive potential and the cell differentiation. Grade I gliomas are pilocytic astrocytomas. They grow slowly and rarely spread into adjacent tissue. Grade II gliomas are diffuse astrocytomas, which can invade adjacent tissues and progress to a higher grade. Grade III anaplastic astrocytomas are classified as malignant. The most aggressive grade IV astrocytoma is also called glioblastoma multiforme. Anaplastic astrocytoma and glioblastoma account for approximately 38% of primary brain tumors (Levin et al. 2001).

Mixed gliomas or anaplastic oligodendrogliomas (e.g. oligoastrocytoma = grade II and anaplastic oligoastrocytoma = grade III) contain more than one type of glial cell, usually astrocytes and other glial cell types like oligodendrocytes. The gliosarcoma variant of glioblastoma contains both neuro-ectodermal and mesenchymal elements (fibrous, muscle, bone, cartilage tissue). The prognosis is affected by the cell type with the highest grade present in the tumor. Treatment also focuses on the most malignant cell type found within the tumor.

Other less common primary brain tumors include for example pituitary tumors, schwannomas, CNS lymphomas, and medulloblastomas, the latter mainly occurring in children. The frequency of brain metastases is at least 10 fold higher than primary neoplasms. Brain metastasis occurs in 20% to 40% of cancer patients (Patchell 2003). The exact incidence is unknown, because no national cancer registry documents brain metastases, but it has been estimated that 98,000 to 170,000 new cases are diagnosed in the United States each year (Hutter et al. 2003; Levin et al. 2001). This number may be increasing because of the capacity and increasing sensitivity of imaging modalities such as MRI to detect small metastases and because of prolonged survival resulting from improved systemic therapy (Levin et al. 2001; Patchell 2003). The most common

primary cancers metastasizing to the brain are lung cancer (50%), breast cancer (15%–20%), melanoma (10%), and colon cancer (5%) (Patchell 2003).

Fig. 0-3: Primary CNS tumors, major histopathologic types and their distribution. Source Central Brain Tumor Registry of the United States 1998 - 2002 (http://www.cbtrus.org/2005-2006/tables/2006.table8.pdf)

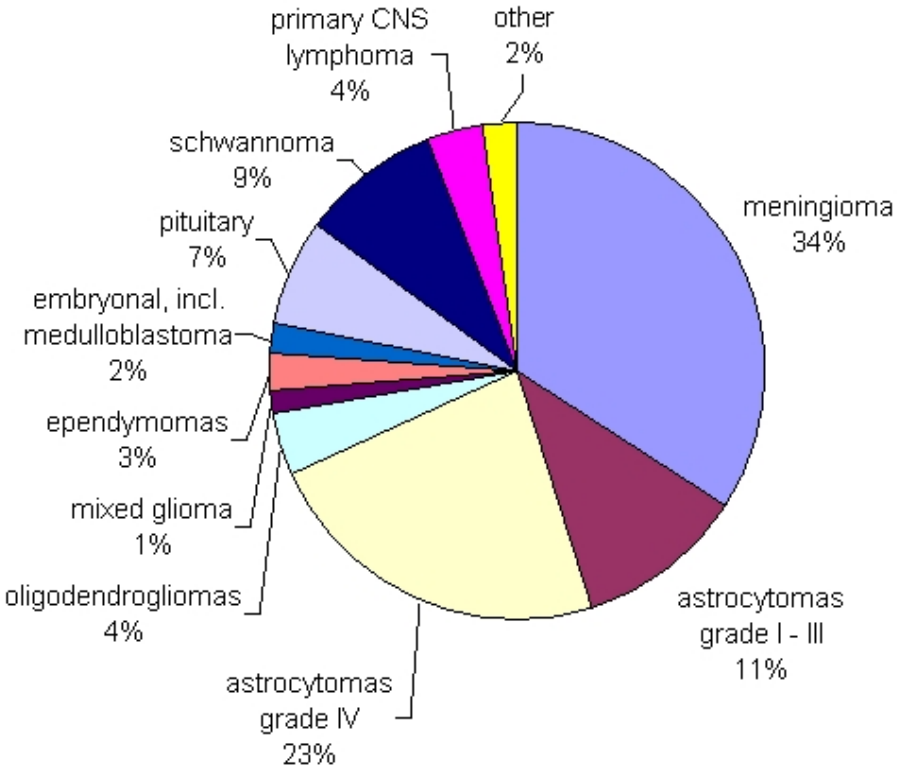

3.4. Orthotopic rat brain tumor models

Fundamental research necessitating invasive procedures is carried out on animal models of diseases. Although no animal brain tumor model exactly simulates human high grade brain tumors, many of their biological and biochemical properties, including invasive growth pattern, neovascularization and alteration of the BBB, are similar enough to clinically encountered neoplasms. They provide a means to study many issues, from fundamental aspects of

oncogenesis, angiogenesis and invasion to the in vivo response to anticancer therapies. Orthotopic brain tumor models grow in their natural environment, the brain, and additionally provide information about their effect on the adjacent nervous tissue. Syngeneic tumor models can be used in immunocompetent animals without induction of alloimmunogenic responses. Table 0-1 sums up the main orthotopic rat glioma models used in preclinical research and is focused on those obtained by stereotactical intracerebral implantation as concentrated cell suspensions, exhibiting the highest reproducibility. Except the U87 MG cell line, which is a human glioma xenograft, all tumor types have originally been induced in rat brain by a carcinogenic procedure (chemical substance, avian sarcoma virus or radiation) (Barth 1998).

Table 0-1: main orthotopic rat glioma models

tumor model	reference	histopathologic classification	grade	rat strain
9L, TL	(Benda et al. 1971; Schmidek et al. 1971)	gliosarcoma	IV	Fischer
C6		astrocytoma	III	Wistar
F98	(Ko et al. 1980)	anaplastic glioma	III - IV	Fischer
RG2, D74	(Aas et al. 1995)	anaplastic glioma	IV	Fischer
RT 2	(Copeland et al. 1975)	anaplastic astrocytoma	III	Fischer
U87 MG	(Tamargo et al. 1988)	human glioblastoma	IV	nude athymic rats or other species

3.5. Angiogenesis

The more aggressive tumor types grow rapidly and have a high metabolism. Growth of solid tumors beyond a diameter of 1 – 2 mm requires the proliferation and formation of new blood vessels by sprouting from existent vessels for the supply of nutriments and oxygen (Folkman 1996; Zama et al. 1991). This process is called neo-angiogenesis. Metastasis occurs via the new tumor microvasculature, too. Failure to induce appropriate angiogenesis leads to necrosis and apoptosis of the cells in the central parts of the tumor that suffer for example of hypoxia.

Blood vessel proliferation is a dynamic balance of stimulators and inhibitors. Tumor angiogenesis results from the secretion of angiogenic factors by the tumor cells (Folkman 1992) and by loss of physiological inhibition of endothelial cell proliferation. Angiogenic factors include growth factors such as fibroblast growth factors (FGF), platelet derived growth factor (PDGF),

vascular permeability or vascular endothelial growth factor (VPF/VEGF), tumor necrosis factor-alpha (TNF-alpha), a number of cytokines etc (Cockerill et al. 1995; Hormigo et al. 2007). There are more than twenty known endogenous angiogenesis stimulating factors. The angiogenic growth factors bind to specific receptors located on the endothelial cells of existing vessels, activating a cellular signalling cascade. The activated endothelial cells begin to proliferate and to produce enzymes that dissolve the basal lamina. Transmembrane adhesion proteins (integrins) and enzymes (matrix metalloproteases) further facilitate the migration of endothelial cells towards the tumor and the formation of new blood vessel tubes, which are then stabilized by pericytes (Cuenod et al. 2006).

The morphology of blood vessels in many solid tumors deviate markedly from the vessels in healthy tissue (Cuenod et al. 2006; Dewhirst et al. 1989), which leads to altered blood flow that is spatially more heterogeneous (Carmeliet and Jain 2000; Tozer et al. 1990). There is also an alteration in relative volumes of major tissue compartments, such as the vascular and extravascular extracellular compartments (Jain 1987). In addition, tumor capillaries often differ from those of the surrounding brain in their permeability (Cuenod et al. 2006).

3.6. Treatment modalities

Brain tumors are treated with surgery, radiation therapy and chemotherapy. Depending on the type, location, and size of the tumor, as well as the patient's age and general health status, a multimodal approach may be used. If surgery can not be performed or the resection is incomplete radiotherapy and chemotherapy are generally used as secondary or adjuvant treatments. Different radiotherapy techniques are available including external fractionated radiotherapy, implant radiotherapy, and stereotactic radiosurgery. Chemotherapy drugs prescribed for brain tumors include temozolomide, procarbazine, lomustine, vincristine, cisplatin, carmustine, and carboplatin. Carmustine is also given by polymer wafer implant during surgery (Ewend et al. 2007), and methotrexate may be administered intrathecally (injected directly into spinal fluid). Treating brain tumors with chemotherapy can be difficult because the blood brain barrier can prevent some chemotherapy drugs from entering the brain.
The identification of molecular markers associated with tumor but not with normal tissue has allowed the development of highly specific, targeted therapies for the treatment of cancer. Molecularly targeted therapy is designed to inhibit a molecule produced by cancer cells to promote their survival, proliferation or spread. This therapy is called "smart" because these

medications are specific to cancer cells and have fewer side effects than traditional chemotherapy drugs. For example, nanoparticles coated with gold and specifically targeted to cancer cells can absorb specific wavelength of light. Activated by a laser, the photothermal agent produces intense heat that kills the cancer cells (El-Sayed et al. 2006). Single dendrimers, a few nanometer in size, can carry a molecule that recognizes cancer cells, a therapeutic agent to kill those cells, and a molecule that can be detected by a medical imaging technique or that recognizes the signals of cell death. They are designed to release their contents only in the presence of certain trigger molecules associated with cancer, making the targeted therapy far more effective and less toxic than conventional chemotherapy. Successful treatment with such a vehicle loaded with the anticancer drug methotrexate, folic acid, and a fluorescent imaging agent has been reported in mice (Kukowska-Latallo et al. 2005). Cancer cells possess much more folate receptors on their surface than normal cells, and capture the whole complex, including the drug and the imaging agent. However, these works are still at a very early stage and problems like how to make these drugs cross the BBB have not been solved yet.

3.7. Antiangiogenic treatment

The amount of vascularization of brain tumors has been correlated to their prognosis (Abdulrauf et al. 1998; Assimakopoulou et al. 1997; Brem et al. 1972; Leon et al. 1996). In 1971 Judah Folkman has postulated that inhibition of tumor angiogenesis could cure cancer (Folkman 1971). In 1975 Judah Folkman and Henry Brem discovered the first natural angiogenesis inhibitor (Brem and Folkman 1975), and it was also Judah Folkman who managed to demonstrate suppressed tumor growth caused by a plasminogen fragment called angiostatin (O'Reilly et al. 1994). Today, there is a long list of known endogeneous angiogenesis inhibitors, and also a number of synthetic molecules that have shown a therapeutic potential in experimental studies or are tested in clinical studies.

One class of angiogenesis inhibitors being tested in cancer patients are molecules that directly inhibit the growth of endothelial cells, such as the endogeneous angiostatin and endostatin (collagen XVIII fragment) (Kirsch et al. 2001). Combretastatin A4, causes apoptosis of growing endothelial cells. Other drugs interact with the membrane protein integrin such as Vitaxin®, a monoclonal antibody directed against the alpha-v/beta-3 endothelial integrin. A second class are molecules that block or interfere with steps in the angiogenesis signalling cascade. Included in this category are epidermal growth factor receptor antibodies and anti-VEGF antibodies.

Bevacizumab (Avastin®), a monoclonal antibody, is the first anti-VEGF antibody to be FDA-approved. Interferon-alpha, is a naturally occurring protein that inhibits the production of FGF and VEGF, preventing these growth factors from starting the signalling cascade. Another type of approved treatment in this class are small molecules that inhibit enzymes called tyrosine kinases for receptors of multiple proangiogenic growth factors. A third class of inhibitors block the ability of endothelial cells to break down the extracellular matrix. Finally, other drugs with indirect antiangiogenic actions exist, although the exact mechanism is unclear. Thalomid® that has been used for its anti-inflammatory effect is one of them.

In contrast to antiangiogenic therapies (Folkman and Ingber 1992) which inhibit vascular proliferation, antivascular therapies aim to destroy mature vascular cells. Drugs of these two categories bring with them a need for an accurate means of assessing tumor angiogenesis and monitoring response to treatment.

3.8. Angiogenesis assessment

For planning the optimal treatment strategy and assessing prognosis, accurate histologic grading is essential, and for this, the evaluation of tumor vascularity is valuable (Aronen et al. 1994). Another motivation for assessment of tumor microvasculature is to evaluate the response to cancer therapies targeted at tumor microvasculature or that indirectly affect tumor microvasculature.

In clinical routine, two methods for angiogenesis assessment are used. One is the detection of proangiogenic factors or angiogenesis inhibitors by biochemical analysis of blood and urine. The second consists in taking a stereotactic needle biopsy for the evaluation of the microvascular density (Weidner et al. 1991). The regional heterogeneity of malignant tumors makes histopathological diagnosis a serious challenge when it is based solely on biopsies. A single tumor mass can be histologically heterogeneous, and at biopsy their grade might be underestimated if the tumor part of highest malignancy is not attained by the needle. In addition, owing to their invasive character, biopsies are not suited for follow-up studies.

Imaging modalities that cover the whole tumor mass are therefore necessary for correct evaluation of the patients. The ideal assessment method should be repeatable, reproducible across centers, robust and acceptable to patients (minimally invasive, without involvement of

ionizing radiation, not too long). It should produce meaningful parameters that have known statistical variations. Qualitative parameters are difficult to compare between patients. Semi-quantitative or relative parameters can be used for comparison between patients and across centers, but the reference value (often in healthy appearing tissue) has to be carefully chosen, documented and accurate (e.g. in MRI the nonuniformity of the RF field must be taken in account). Quantitative parameters with values being compared to normal ranges are therefore preferred and increase the sensitivity to changes associated with disease. The most stringent requirements are usually encountered in the assessment of therapeutic response to novel antiangiogenic or antivascular therapies.

Except for the need of CA injection for particular applications, MRI is a non invasive imaging technique combining high soft tissue contrast with an acceptable spatial resolution. MRI is now routinely available in many countries and has become the method of choice in particular in brain imaging.

3.9. Quantitative MRI

In contrast to other imaging techniques such as PET, the signal intensity from most MR pulse sequences does not relate directly to any physiological parameter. MRI is generally used by qualitatively interpreting the available soft tissue contrast. Although the image data is in numerical form, quantification is still difficult. Magnetic field strength, scanner parameters, sequence timing parameters, flip angle as well as image scaling, make the signal scanner dependent and serial or multi-center studies difficult.

Procedures for data collection have to be found which are insensitive to scanner, sequence and operator influence, and which are reliable and reproducible over time and between patients. The measured parameters have to be examined for their biological meaning and related to clinically relevant quantities. In this way, changes at the microscopic level such as in cellular or microvascular structures can be detected as changes in MR parameters, such as relaxation times or magnetization transfer ratio, or as changes in diffusion and perfusion parameters at typical MR image resolutions of about 1 mm.

As mentioned in the previous paragraph, heterogeneity is a hallmark of cancer and definition of regions or tumor boundaries can be problematic. Averaging values over an entire volume of

interest may result in insensitive parameters. Histogram analysis and parametric maps improve sensitivity.

The next paragraphs will review some MR techniques which provide valuable information about the pathophysiology of neoplasms.

4. MRI of cancer

For diagnosis and follow up of cancer, as well as for the study of fundamental biological processes that lead to the development of cancer, MRI offers several techniques, which provide various parameters that are related to the pathophysiology of cancer.

In 1971, Damadian suggested that T_1 and T_2 differences could be used to distinguish malignant from benign tumors (Damadian 1971). Unfortunately, these differences are too variable to be an effective indicator of cancerous tissue. However, Damadian's merit is the discovery of the difference between MR signals from different soft tissue types (normal tissue and cancer tissue), which is much larger than the contrast in CT.

T_1 and T_2 weighted MRI is used to firstly localize and delineate the tumor extent and to detect associated areas of hemorrhage and edema. T_1 weighted images of the brain are typically made for anatomic information, providing also high sensitivity for paramagnetic CA, fat, fluids with high protein content and subacute haemorrhage. T_1 weighted pre-contrast images are carried out to avoid confusion of bright signal on T_1 weighted images after CA administration. Gadolinium-enhanced T_1 weighted images are used for the diagnosis of all types of intracranial tumors (Edelman and Warach 1993a; Edelman and Warach 1993b). Post-contrast, lesions are classified as homogenous or heterogeneous, and necrotic or cystic components are seen more clearly. T_2 weighted images offer high sensitivity to most pathologic processes but is not specific, since a prolongation of tissue T_2 is seen with edema, infarction, demyelination, infection, inflammation, neoplasm and most fluid collections (Edelman and Warach 1993a; Edelman and Warach 1993b). The margin enhancement provides a gross measure of tumor extension, but the area of enhancement does not represent the outer tumor border because infiltrating cells can

often be identified beyond this margin. To detect this infiltration and to characterize the tumor and its subparts, functional physiologic parameters have to be measured.

Magnetic resonance spectroscopy (MRS) is much more disease specific than changes in T_1 and T_2 relaxation times. It provides a means for evaluating cancer metabolism along with its inhibition and regulation pathways. Particularly, the study of choline and its metabolites by ^{1}H MRS is a biomarker for tumor diagnosis and therapy assessment (Negendank et al. 1996; Preul et al. 1996; Wald et al. 1997). ^{1}H MRS demonstrates tumor specific changes in the choline, creatine, lactate and the N-acetylaspartate concentrations. MRS and MRI methods are also suited for the non-invasive assessment of the extent and distribution of hypoxia in tumor tissues (Robinson 2005), which is a cause of genetic instability, angiogenesis and resistance to radio- and chimiotherapy (Tatum et al. 2006).

In a pulsed gradient spin echo NMR experiment (PGSE-NMR), the incoherent movement of water in the brain is characterized by its apparent diffusion coefficient, giving insight into the existence of biological barriers impeding the free diffusion of water. Diffusion weighted and diffusion tensor imaging is sensitive to the tissue microarchitecture, because it determines the cellular density, the anisotropy of the tissue and the size of compartments. Diffusion weighted imaging can therefore detect edema, cellular density, or necrotic areas by way of quantification of water molecular mobility which is affected by these cellular features. The apparent diffusion coefficient increases in many disease processes that destroy the biological barriers for water diffusion, such as occurs in neoplasm but also in other brain pathologies. On the other hand, neoplasms can also decrease the water diffusion due to an increase in tissue cellularity. The response to anti cancer therapy is also measurable, because treatment results in tumor lysis, loss of cell membrane integrity, increased extracellular space and therefore in an increase in water diffusion.

A measure of the diffusion tensor is independent of the orientation of the tissue in the scanner. Quantitative analysis then derives the mean diffusivity, which is the apparent diffusion coefficient averaged over all directions, and the fractional anisotropy which decreases with barrier destruction in disease. However to be comparable between experiments, such parameters have to be acquired using the same diffusion time and magnetic field gradients intensities. The directional information contained in the diffusion tensor can lead to tractography identifying the path of larger nerve bundles. The nerve tracts can be altered by a space occupying lesion.

In conjunction with appropriate biomarkers, MRI can be used to visualize in vivo molecular alterations in tumor tissues, such as up- or downregulation of certain molecular targets (Weissleder and Mahmood 2001). Biomarkers are composed of a functional moiety and a magnetic label. For example, the early detection of apoptosis following therapy predicts long-term treatment outcome and allows timely optimization of the treatment protocol. Targeted probes are under development for revelation with MRI techniques (Hakumaki and Brindle 2003).

Since tumors are commonly associated with abnormal vascular density, angiogenesis and compromised vascular wall integrity, the ability to focus an imaging sequence on vascular characteristics provides a physiologically-specific approach to tumor delineation, offering utility in surgical (Sunaert 2006) and radiation therapy planning. Beyond this, the quantitative assessment of tumor vascularity and endothelial hyperpermeability is of utility in diagnosis and prognosis, as surrogates of histologically-assessed tumor grade (Aronen et al. 1994). It is also of value in distinguishing residual or recurrent tumor from treatment effects such as radiation induced necrosis (Sugahara et al. 2000). Furthermore, by quantitatively assessing tumor vascular characteristics, these approaches allow the assessment of novel anti-angiogenic therapies, guiding drug development through preclinical stages (Padhani 2003), and facilitate the inter- and intra-subject comparisons. They also offer early assessments of the biological activity of various treatments in the clinical setting (to distinguish potential responders from non-responders), before more traditional criteria, such as tumor size change, become apparent.

MRI techniques for the quantification of hemodynamic parameters are reviewed in detail in paragraph 9. Most of these techniques require the administration of a CA and rely on a particular CA kinetics and distribution in the tissue.

5. Compartment models of the brain tissue

In an MR image of a biological system the signal originates from all compartments containing water molecules. The MRI signal depends on numerous compartment specific intrinsic parameters such as the T_1 and T_2 relaxation times, magnetic susceptibility, proton density,

velocity or diffusion of water molecules, and it is mediated by water exchange between compartments.

The tissue water is modeled as being compartmentalized by physiological boundaries. In order to be an acceptable model, the compartments should be homogeneous for the properties, to which particular MR acquisition techniques are sensitive.

5.1. The intravascular and the extravascular compartment

In a first approach we distinguish the blood or intravascular (iv) and the extravascular (ev) compartment, separated by the structures that make up the BBB. This is a two-compartment model of the brain tissue which is generally used in perfusion MRI (Zhou et al. 2001), especially if CA are used.

5.2. The intracellular and extracellular compartments

The blood in the intravascular compartment is composed of plasma and a cellular component. Plasma contains a protein fraction of about 7% mainly consisting of albumin (~70 kD) and solutes (electrolytes, nutrients, gases). The cellular fraction of blood is mainly composed of erythrocytes, and to a negligible extent of leukocytes and thrombocytes. The erythrocytes carry the hemoglobin which can be dia- or paramagnetic in function of its oxygenation status. In strongly deoxygenated blood or in the presence of a CA compartmentalized in the plasma, susceptibility differences exist between erythrocytes and plasma (Gillis et al. 1995) affecting the transverse relaxation time of blood. However, the longitudinal relaxation times of plasma and of the cell fraction of blood are not very different (Kim and Kim 2005).

Similarly, the extravascular compartment is made up of neural and glial cells and interstitial fluid. The intracellular and the extracellular water contain different amounts of solutes and proteins, and are separated by the cell membranes. Interstitial fluid allows metabolites to be diffused between the capillaries and cells in the tissue. In the absence of CAs it is difficult to distinguish the intra- and extracellular compartments by MRI although diffusion weighted imaging has this potential.

Each of the four compartments is described by its volume, water density and MRI parameters such as the relaxation times. The intravascular compartment volume V_{iv} is only about 3 to 5 ml/100g brain tissue. The intravascular intracellular volume is called the hematocrit and makes up about 45% of the blood in humans. The volume of the extravascular intracellular compartment in the brain is in the order of 70 to 80 ml/100g (Quirk et al. 2003), leaving the remaining 15 to 25 ml/100g to the extravascular extracellular volume.

The water density differs slightly between intra- and extravascular compartment, expressed by the brain-blood partition coefficient for water λ. This is the ratio of the tissue water content to the blood water content $\lambda = \frac{w_{tissue}}{w_{blood}}$. Its average is probably slightly smaller than unity (Herscovitch and Raichle 1985), but it depends on the hematocrit and on tissue factors and varies spatially within the brain (Roberts et al. 1996). Formation of an edema within a brain lesion can increase λ above unity.

6. Water exchange

6.1. Intracellular - extracellular exchange

The boundary between intra- and extracellular compartments is constituted by cell membranes or cytolamma, which are lipid bilayers with a variable amount of membrane proteins. Water can move through the membrane driven by the transcapillary hydrostatic and osmotic pressure gradients. For some cell types, such as erythrocytes, this exchange is facilitated by aquaporins which are transmembrane water channels (Mathai et al. 1996). The average residence time (τ) of water in human erythrocytes is in the order of 10 to 20 ms (Andrasko 1976; Herbst and Goldstein 1989) depending on the temperature. The exchange rate across the cell membrane (τ_{exch}^{-1}) is given by

$$\tau_{exch}^{-1} = \tau_a^{-1} + \tau_b^{-1}$$

in terms of the water residence times in erythrocytes (τ_a) and plasma (τ_b). The exchange time τ_{exch} is therefore about 8 ms.

The plasma is regarded as a homogeneous compartment with respect to water relaxation rates, because the motion of water is free with a diffusion coefficient close to that in pure water (Gillis et al. 1995; Tanner 1983).

The transcytolemmal water exchange rate between the interstitial fluid and the extravascular intracellular compartment is in the order of 2 s^{-1} for brain tissue (Quirk et al. 2003) but may be different for other tissues (Donahue et al. 1994; Sobol et al. 1991).

6.2. Intravascular - extravascular exchange

The capillary wall is composed of two lipid bilayers each about 5 nm thick, separated by a 1 µm thick layer of cytoplasm. The BBB constitutes a mechanical and metabolic (enzymes) barrier impeding or slowing down the transport of various substances. This is also the case for water molecules, because the paracellular bulk flow along the osmotic gradient is reduced. In the brain, the junction size is only 7 Å, which is too small to allow crossing by sodium. The determinant factor of water exchange in the brain is mediated through the osmolality and not the oncotic pressure (Favre et al. 1996).

The exchange rate of water across the BBB has been estimated in the order of 0.6 to 2 s^{-1} (Donahue et al. 1997; Labadie et al. 1994; Orrison et al. 1995; Schwarzbauer et al. 1997). Recently, Shin et al (Shin et al. 2006) reported an exchange rate of 0.93 s^{-1} for white matter and 1.70 s^{-1} for gray matter. The endothelial permeability of intact brain capillaries to water is in the range of 2 to 60×10^{-6} m/s (Eichling et al. 1974; Herscovitch et al. 1987; Paulson et al. 1977). The permeability surface product PS_v of the brain microvasculature to water has been reported in the order of 2 to 4 ml $min^{-1}g^{-1}$ (Barbier et al. 2002; Ginsberg et al. 1985; Reid et al. 1983; Schwarzbauer et al. 1997) and being greater for gray matter than for white matter (Schwarzbauer et al. 1997).

6.3. Intravascular and extravascular residence times

The PS_v product and the intravascular compartment volume V_{iv} (= CBV) determine the average intravascular residence time of a water proton (τ_{iv}):

$$\tau_{iv}^{-1} = \frac{PS_v}{V_{iv}}.$$

The inverse of the average intravascular residence time τ_{iv}^{-1} is the water exchange rate from the intravascular to the extravascular compartment, often given the symbol $k_{iv\text{-}ev}$ or k_{iv} (cf. Fig. 0-4). Since the same equations relate the extravascular compartment volume V_{ev} and the average extravascular residence time (τ_{ev}), the following relation holds true:

$$\frac{\tau_{iv}}{\tau_{ev}} = \frac{V_{iv}}{V_{ev}}.$$

A pathologic breakdown of the BBB probably first increases the permeability to water before increasing the permeability to CAs. The short intercapillary distance allows for near instantaneous solute equilibration throughout the brain interstitial space for small molecules, once the BBB has been overcome. Therefore, in MRI, the interstitial or extravascular extracellular compartment can be regarded as homogeneous.

6.4. The exchange regime

The effect of the water exchange between compartments is the attenuation of the difference between the respective relaxation rates of the compartments (Donahue et al. 1997). The exchange between compartments a and b is slow, when

$$\tau_{exch}^{-1} << \left| T_{ia}^{-1} - T_{ib}^{-1} \right| \text{ for i = 1,2.}$$

The exchange is considered as fast when

$$\tau_{exch}^{-1} >> \left| T_{ia}^{-1} - T_{ib}^{-1} \right| \text{ for i = 1,2.}$$

The shutter speed, which is the relaxation rate difference between both compartments,

$$\Delta R_i = \left| T_{ia}^{-1} - T_{ib}^{-1} \right| \text{ for i = 1,2}$$

increases when a CA is administered and can change the water exchange regime between the intra- and the extravascular or between the extravascular intra- and extracellular compartments from the fast exchange limit ($\tau_{exch}^{-1} >> \Delta R_i$) to the intermediate exchange ($\tau_{exch}^{-1} \approx \Delta R_i$) or slow exchange ($\tau_{exch}^{-1} << \Delta R_i$).

If $\tau_{exch}^{-1} << \Delta R_i$, the observed signal is the sum of the signal from both compartments, weighted with the corresponding water fractions. Each compartment is relaxing with an apparent relaxation rate:

$T_{ij}^{app\,-1} = T_{ij}^{-1} + \tau_j^{-1}$ for i = 1,2 and j = a,b.

If $\tau_{exch}^{-1} >> \Delta R_i$, the signal relaxes monoexponentially with a weighted time constant $T_i^{-1} = p_a T_{ia}^{-1} + p_b T_{ib}^{-1}$, i = 1,2

where p_a and p_b are the water fractions of the compartments a and b.

Given the rather small average residence time τ for erythrocytes (10 to 20 ms) the fast exchange regime applies for the subcompartments of blood (Landis et al. 1999). Even for the usual plasma concentrations of typical extracellular CA, the relaxation of the whole intravascular compartment remains monoexponential (Donahue et al. 1997; Landis et al. 1999). This implies that blood can be considered as a homogeneous substance with respect to its relaxation behavior before and after injection of CA. Although the CA remains in the plasma compartment, most methods do not measure the cerebral plasma volume, but the CBV, unless very high plasma concentrations of CAs are achieved resulting in a slow exchange regime.

Fig 0-4: The BBB is the interface between the intra- (iv) and the extravascular (ev) compartment. The intravascular compartment can be subdivided into intracellular (erythrocytes, red) and extracellular compartment (plasma, pink). The extravascular compartment is made up of the intracellular (different brain cells) and extracellular (interstitium, blue) compartments. The exchange across the BBB is governed by the exchange rates $k_{iv\text{-}ev}$ and $k_{ev\text{-}iv}$, and across the cytolemma by k_{ie} and k_{ei}.

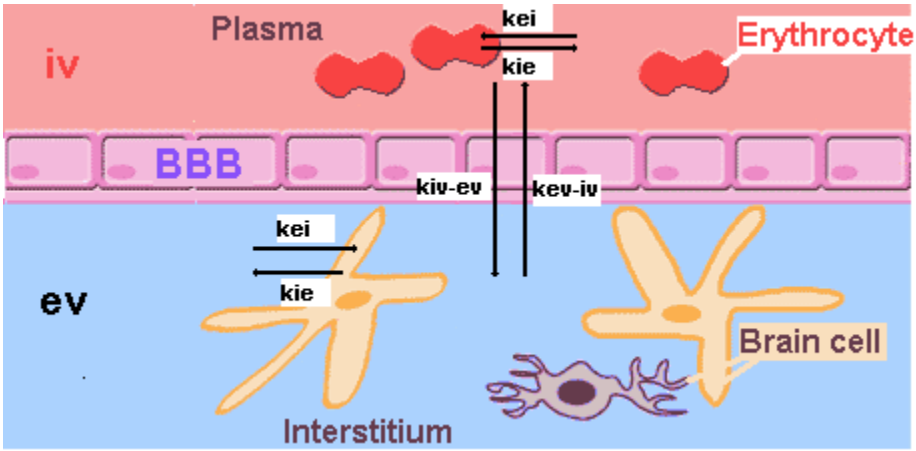

7. Contrast agents

Despite the multiparameter dependence of MRI contrast, the usefulness of CAs relies in their ability to increase both the inherent low signal to noise ratio (SNR) and the contrast between tissues. Unlike the situation in CT imaging, MRI CA are not imaged directly. Instead, the water proton spins that encounter the CA are imaged, via the catalytic effect the CA has on the relaxation of their MR signal. Neglecting the effect of intercompartmental water exchange, these are mainly the water molecules in the same physiological compartment as the CA.

7.1. CA relaxivity

It is usually assumed that the relaxation rates increase linearly with the CA concentration [CA] via

$$\Delta R_i = R_i - R_{i0} = r_i[CA], \; i = 1,2$$

where ΔR_i is the relaxation enhancement and

$$R_{i0} = \frac{1}{T_{i0}}, \; i = 1,2$$

is the intrinsic relaxation rate of the compartment in the absence of any CA. The term $r_i[CA]$ is the paramagnetic relaxation rate enhancement caused by the paramagnetic CA, where [CA] symbolizes the CA concentration. The efficacy of a CA is expressed by the longitudinal and transversal relaxivities r_1 and r_2, which are the proton relaxation rate enhancements induced by a 1 mM concentration of the CA.

The relaxivities measured in solutions are generally dependent on magnetic field and on temperature. In biological tissues, both the T_1 and the T_2 relaxation can additionally be influenced by CA compartmentalization and local field gradients, but the two relaxation mechanisms are affected in different ways as discussed further below. They can also be affected by the water exchange between compartments. The linearity may not hold for all ranges of CA concentrations and tissues (Kiselev 2001).

7.2. Paramagnetism

The relaxation rates of water can be increased by endogenous molecules or by administration of para- or superparamagnetic particles. Paramagnetism and superparamagnetism are characterized by a large electronic magnetic moment in the presence of an external magnetic field when microscopic permanent magnetic moments (dipoles) resulting from unpaired electrons in the atomic orbitals are magnetically ordered. Contrary to ferromagnetic substances which have remnant magnetic moment at zero field once magnetized, para- and superparamagnetic substances have no remnant magnetic moment. Gd^{3+} is the most widely used paramagnetic ion because it has seven unpaired electrons, a very high magnetic moment (S = 7/2), a relatively long electronic relaxation time and a symmetric electronic ground state $^8S_{7/2}$. Other ions with large electronic magnetic moments are Mn^{2+} and Fe^{3+} with five unpaired electrons and a spin S = 5/2. The hemoglobin protein is diamagnetic in oxygenated state and paramagnetic in deoxygenated state (Pauling and Coryell 1936), and is used as endogenous CA.

7.3. Chelating compounds

The metal ions in solution are relatively toxic (reported LD_{50} values for the metal chloride salts in aqueous solution are 1.4, 1.5 and 1.6 mmol/kg for gadolinium, manganese and iron, respectively, when administered to mice i.p. (Lauffer 1987)), and nothing controls the biodistribution of these ions.

A chelate is an organic chemical compound, which binds a metal ion in its central part, eg hemoglobin. Acyclic and macrocyclic polyaminocarboxylates ligands have been synthesized forming thermodynamically and kinetically stable complexes with Gd^{3+}. Their function is threefold:
they reduce the toxicity of the metal ion
they determine the CA distribution in the tissue and the pharmacokinetics of the compound
they modify the relaxivity of the metal ion

7.4. Proton relaxation in the presence of magnetic agents

Paramagnetic metal ions with one or more unpaired electrons, such as the lanthanides Gd^{3+}, Mn^{2+} and Dy^{3+} and metal ions, decrease the T_1 and T_2 relaxation times of nearby water protons through interactions between the unpaired electrons on the metal and metal-bonded (inner sphere), hydrogen-bonded (second sphere) and unbound (outer sphere) water molecules that are in fast exchange. The inner sphere and outer sphere contributions add linearly to the total relaxation rate change.

$\Delta R_i = R_i^{\text{inner sphere}} + R_i^{\text{outer sphere}}$, i = 1,2.

The relaxation enhancement ΔR_i is governed by dipolar interactions between the electronic moment of the ion and the nuclear moment of the water protons in the fluctuating local magnetic field around the paramagnetic center arising from the dipolar interactions. The relaxation enhancement strongly depends on the distance between the nuclear and the electron spin and on the residence time of the water molecule in the inner (first hydration) sphere of the metal complex. It further depends on factors such as the number of water molecules in the first coordination sphere, the rotational correlation time and the electronic spin relaxation time.

In the inner sphere, the longitudinal relaxation is governed by

$$\frac{1}{T_1} = qP_m \frac{1}{T_{1m} + \tau_m}$$

and the transverse relaxation by

$$\frac{1}{T_2} = \frac{qP_m}{\tau_m}\left[\frac{T_{2m}^{-2} + T_{2m}^{-1}\tau_{\mathbf{m}}^{-1} + \Delta\omega_{\mathbf{m}}^2}{\left(\tau_{\mathbf{m}}^{-1} + T_{2m}^{-1}\right)^2 + \Delta\omega_{\mathbf{m}}^2}\right]$$

where

q is the hydration number (bound water protons per metal),

P_m is the mole fraction of the bound water protons,

τ_m is the residence time of the coordinated water molecule in the first hydration sphere of the metal and

$\Delta\omega_m$ is the chemical shift difference between the bound water and the diamagnetic water in the absence of a paramagnetic metal.

The longitudinal and transverse proton relaxation rates of the bound water are the result of two relaxation mechanisms:

$$\frac{1}{T_{im}} = \frac{1}{T_i^D} + \frac{1}{T_i^S}, \; i = 1, 2$$

where the superscript D refers to the dipole - dipole relaxation mechanism and the superscript S refers to the scalar contact mechanism.

It is the dipole - dipole relaxation mechanism that strongly depends on the distance between the electron and the nuclear spin:

$$\frac{1}{T_i^D} \propto \frac{1}{r^6},$$

where r is the distance between electron and nuclear spin.

The relaxivity decay with increasing magnetic field strength is governed by factors such as

$$\frac{1}{1+\omega^2\tau_c^2}$$

where

ω symbolizes the Larmor precession frequency and

τ_c is the correlation time.

The scalar mechanism depends on the electron Larmor frequency only, whereas the dipole - dipole mechanisms depends on both, the electron and the nuclear Larmor frequency.

The correlation times are given by:

$$\frac{1}{\tau_c^D} = \frac{1}{T_{ie}} + \frac{1}{\tau_m} + \frac{1}{\tau_R}, \; i = 1, 2$$

for the dipole - dipole relaxation mechanism,

and

$$\frac{1}{\tau_c^S} = \frac{1}{T_{ie}} + \frac{1}{\tau_m}, \; i = 1, 2$$

for the scalar relaxation mechanism,

where

τ_R is the rotational correlation time and

$\frac{1}{T_{ie}}$ are the electronic relaxation rates which also decrease with increasing magnetic field.

At magnetic field strengths above 1 T, the relaxation of water protons are mainly governed by the rotational correlation time τ_R. The relaxation rates can therefore be described by simplified equations:

$$\frac{1}{T_1} \propto \frac{\tau_R}{1+\omega^2\tau_R^2}$$

$$\frac{1}{T_2} \propto \frac{2}{3}\tau_R + \frac{1}{2}\ \frac{\tau_R}{1+\omega^2\tau_R^2}.$$

The outer sphere mechanisms that are due to translational diffusion of the water molecules with respect to the chalate contribute much less to the total relaxation enhancement. They are mainly determined by the electronic relaxation rate $\frac{1}{T_{1e}}$, the minimum distance of approach between the outer sphere water molecules and the metal complex and the sum of the diffusion constants of the outer sphere water molecules and the complex.

At the usual clinical imaging fields of 0.5 to 1.5 T, the commonly marketed CAs reach only about 1/20th of the relaxivity predicted by the Solomon-Bloembergen-Morgan theory (Aime et al. 2005; Caravan et al. 1999; Livramento et al. 2006a; Livramento et al. 2006b; Vander Elst et al. 2003), if the electronic relaxation of the spin is slow and the rotational diffusion speed of the complex as well as the rate of water exchange between the inner sphere and the bulk have their optimal values. Novel applications in MRI require CA with higher efficacy.

7.5. NMRD profiles

Proton spin relaxivity measured as a function of magnetic field strength is called nuclear magnetic relaxation dispersion (NMRD). Proton T_1 NMRD profiles are informative tools to explore the dynamics of molecules, especially those complexes containing paramagnetic ions which drastically change the proton relaxation time at a certain range of magnetic field strength. The r_1 usually decreases with increasing field strength in a compound specific manner, while the r_2 can increase (Vander Elst et al. 2005). These profiles can be fitted to models (Caravan et al. 1999) to disentangle the inner sphere and outer sphere contributions to the relaxivity.

7.6. Types of CAs

The use of paramagnetic ions to enhance contrast was first introduced in 1982 (Brady et al. 1982; Goldman et al. 1982), and in 1984 the gadolinium chelate diethylenetriamine pentaacetic acid (Gd-DTPA), Magnevist®, was used for imaging human cerebral tumors (Carr et al. 1984).

When CAs are used for MRI perfusion imaging, from the methodological point of view three properties are important:
the compartmentalization in the blood pool, which strongly depends on the tissue type
the CA relaxivities and
the biologic elimination rate from the blood pool.
The last two properties determine the dose to be administered. For routine preclinical and clinical use other aspects become important such as adverse effects, cost, approval for clinical use.

For animal studies a large variety of CA types are available.

Small molecular CAs

Currently, all paramagnetic CA approved for clinical use in MRI are derivatives of the open chain DTPA or the macrocyclic chelate tetraazocyclododecane tetraacetic acid (DOTA) (Oudkerk et al. 1995) (Fig. 0-5). These clinically approved non-specific CAs are freely diffusible in the intra- and extravascular extracellular compartement with the exception of the brain where only BBB lesions enable the CA to pass. They do not enter the cells (Koenig et al. 1986). Gd-DTPA and Gd-DOTA are conventional small molecular CA with molecular weights of 560 and 547 Da, respectively, a diameter of 0.9 nm (Corot et al. 2000a) and a distribution volume of 0.266 l/kg, approximating the extracellular fluid volume (Brasch et al. 1984; Weinmann et al. 1984).

Blood pool CAs

In the field of brain tumor perfusion imaging, there is a need for CAs that do not leak across an interrupted BBB and can serve as blood-pool CA. Beyond diagnosis of tumor extension and vascular permeability, blood pool CA help in the classification and follow-up of tumors by MRI by virtue of quantifying microvascular parameters, such as CBV and CBF (Fig 0-6).

By selecting polymers of higher molecular-weight, extended blood pool retention during the postbolus phase can be achieved (Ladd et al. 1999), due to lower extravasation and/or a slower renal clearance (Corot et al. 2000b; Corot et al. 2002; Port et al. 1999).

Intermediate sized CAs

Intermediate sized CAs, such as P792, Vistarem®, 6.47 kDa (Weidensteiner et al. 2006), or P760, 5.29 kDa (Corot et al. 2000a)(Fig. 0-5), have improved contrast-enhanced magnetic resonance angiography (MRA) through prolonged imaging during the longer intravascular steady state concentration. Both CA are based on a Gd-DOTA core, which is substituted by rigid hydrophilic arms. P760 has a mean diameter of 2.8 nm (Corot et al. 2000a). Its relaxivities are five to seven times higher than those of Gd-DOTA (Table 0-2).

Fig. 0-5: size comparison of Gd-DOTA and P760

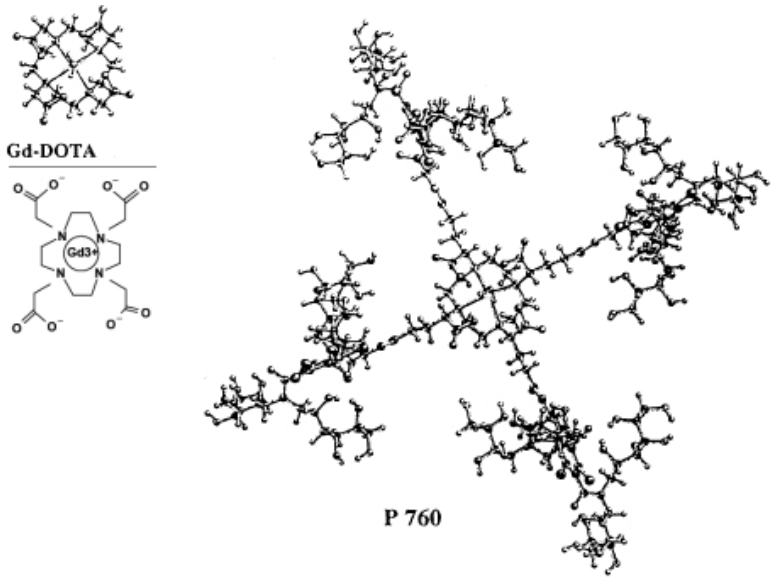

Fig. 0-6: indications for the use of extracellular Gd^{3+}-based and blood-pool CAs in oncology

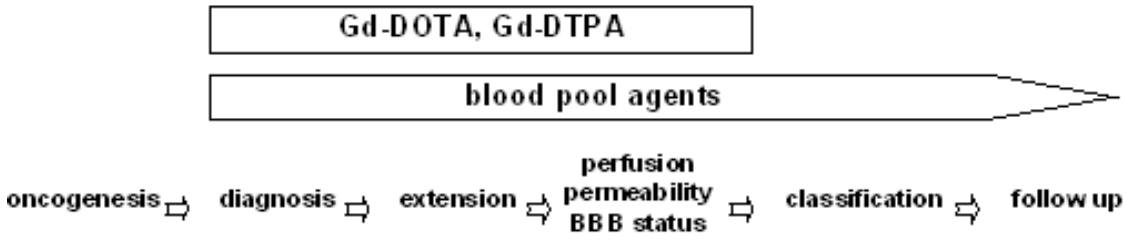

Macromolecular CAs

Macromolecular CAs typically range from 5 kDa to 90 kDA in molecular weight. MS-325, Vasovist® (international non-proprietary name: gadofosveset), binds human serum albumin reversibly in vivo coupling the blood pool retention of a macromolecule with the renal excretion properties of small molecules (Caravan et al. 2002; Grist et al. 1998; Lauffer et al. 1998; Turetschek et al. 2001).

Albumin-Gd-DTPA is a prototype macromolecular CA with a molecular weight of 92 kDa, a plasma half life of approximately 3h and an initial distribution volume of 0.05 l/kg, which closely approximates the blood volume (Schmiedl et al. 1987). It consists of human serum albumin, paramagnetically labeled with 19 Gd-DTPA groups.

Polymeric agents, e. g. dextran, have molecular weights above 15 kDa, but exhibit a high degree of polydispersity.

Dendrimers, such as polyamidoamine and diaminobutane core polypropylimine, are another class of macromolecular CA. These branched polymers, can be synthetically produced at different sizes, with different pharmacokinetic properties (Kobayashi and Brechbiel 2003). Viral particles and liposomes that incorporate either Gd^{3+} or iron particles are potential macromolecular CA that could also serve to vehicle therapeutic agents (Mulder et al. 2006).

Superparamagnetic CA

Another type of macromolecular CA are superparamagnetic iron oxide (Fe_2O_3 or Fe_3O_4) nanoparticles coated with dextran. Because of their crystalline structure and the large number of

non-paired spins, the nanoparticles have a high net magnetic moment exceeding that of typical paramagnetic ions, and preferentially shorten the T_2* in vivo. They exist in various sizes, which alter their pharmacokinetics. Superparamagnetic iron oxide (SPIO) particles have diameters of 50 – 150 nm, ultrasmall SPIO (USPIO) of 10 – 50 nm, and very small SPIO particles (VSOP) of 2 – 10 nm. Compared to SPIO, the USPIO are taken up more slowly by the reticuloendothelial and lymphatic systems, because they escape rapid recognition by the monocyte macrophage phagocytic system mainly of liver and spleen (Weissleder R, Guillermo E, Wittenberg J Radiology 1990). This results in a blood half life in the order of 1 h, 4 h and 24 h in mice, rats and humans, respectively. The distribution volume approximates the blood volume in rats (0.05 l/kg), but is also very species specific.

Molecular CAs

Molecular CAs are designed to target specific biologic molecules (e.g. genes and proteins) that are linked to disease processes (Weissleder et al. 2000), and to quantify physiologic molecular events. Molecular imaging has many applications in biology and medicine. Tumor angiogenesis could be evaluated by imaging with vascular targeting CAs (Guccione et al. 2004; Ocak et al. 2007; Winter et al. 2006).

Table 0-2 gives an overview focused on MRI CA that can be used as blood pool agents. The relaxivities in water at room temperature are given. Comparing these values with relaxivities measured in plasma or blood, it can be observed that they are often lower in water. For example, at 0.47 T, the r_1 relaxivity of P760 is about 28.7 $mM^{-1}s^{-1}$ and 29.2 $mM^{-1}s^{-1}$ in plasma and blood (Corot et al. 2000a), respectively. This is due to reversible binding to plasma proteins which slow down the rotational correlation time of the CA molecules resulting in increased relaxivity.

Table 0-2: Blood pool contrast agents. The relaxivities r_1 and r_2 ($mM^{-1}s^{-1}$) are given in water at room temperature.
f = free, b = bound form. The magnetic field strength is given in Tesla.

compound	ion	r_1	r_2	B_0	distribution	trademark®
Gd-DTPA	Gd^{3+}	3.4	3.8	1	intravascular (neuro), extracellular	Magnevist
Gd-DOTA	Gd^{3+}	3.4 2.9	4.8 3.4	1 2.35	intravascular (neuro), extracellular	Dotarem
Albumin-Gd-DTPA	Gd^{3+}	14.9		2	intravascular	
Gadodiamide Gd-DTPA-BMA	Gd^{3+}	3.9	4.3	1	intravascular, extracellular	Omniscan
Gadoteridol Gd-HP-DO3A	Gd^{3+}	3.7	4.8	1	intravascular, extracellular	ProHance
Gadobenate dimeglumine Gd-BOPTA	Gd^{3+}	4.6	6.2	1	intravascular, extracellular, hepatobiliary	MultiHance (phase III)
Gd-DTPA-17(and 24) cascade polymer	Gd^{3+}	11.9	16.5		intravascular	Gadomer-17 Gadomer-24 (preclinic)
Gadomelitol P792	Gd^{3+}	39 25		0.47 1.5	intravascular (neuro), extracellular	Vistarem
P760	Gd^{3+}	24.7 17.2	27.1	0.47 2.35	intravascular (neuro), extracellular	(preclinic)
MS-325	Gd^{3+}	6 (f) 33 (b)		0.47	intravascular	Vasovist
dextran coated Ferrumoxid, SPIO AMI-25	Fe^{2+} Fe^{3+}	40	160	0.47	Reticulo Endothelial System	Endorem, Feridex
Ferrumoxtran-10 USPIO, AMI-227	Fe^{2+} Fe^{3+}	25 10 6	160 88 90	0.47 1.5 3	intravascular, lymphatic system	Sinerem, Combidex (phase III)
MION	Fe^{2+} Fe^{3+}	3.7	6.5	0.47	intravascular, lymphatic system	(preclinic)

8. Fast MRI techniques

Owing to the developments that resulted in shorter acquisition times, MRI is a modality that can be used to monitor dynamic physiological processes (such as cardiac contraction, tracking the passage of a CA bolus, functional brain activation).

The technical developments that lead to fast MRI, include improvement of the speed of the gradient system and of the sensitivity of RF coils but it is essentially the result of improved sequence design.

The duration T_{Acq} of a two dimensional scan is determined by the repetition time TR, the number of phase encode steps n_{Ph}, which determines the spatial resolution, and the number of experiments n_{Ex} used to accumulate the signal to increase the SNR:

$$T_{Acq} = TR \times n_{Ph} \times n_{Ex} \qquad \textbf{Eq. 0-1}$$

The various techniques that have been developed to speed up acquisition, aim at reducing one of these factors:
reduce the repetition time
reduce the number of phase encoding steps
reduce the data that has to be acquired
reduce the number of experiments
increase data points per unit time

8.1. K-space

The K-space or Fourier-space is the reciprocal space of the real or Euclidean space (R-space). It is a two or three dimensional matrix of spatial frequencies **k.** In a MRI experiment the signal is spatially encoded with three orthogonal magnetic field gradients, which define the spatial frequencies:

$$k_i(t) = \frac{\gamma}{2\pi} \int_0^t G_i(t')dt' \text{ , } i = x, y, z$$

where γ is the gyromagnetic ratio of the proton, and G(t) is the intensity of the magnetic field gradient.

R-space and K-space are related by the Fourier Transform:

$$S(\mathbf{k}) = \int_V \rho(\mathbf{r}) \exp(-i2\pi \mathbf{k} \cdot \mathbf{r}) d\mathbf{r} \qquad \textbf{Eq. 0-2}$$

where S(**k**) is the frequency spectrum which is a complex value, **r** is the spatial position and ρ(**r**) is the spin density function. The two vectors **r** = (x, y, z) and **k** = (k_x, k_y, k_z) are the two conjugated variables. To go from K-space data to the desired image function ρ(**r**) requires using an inverse Fourier Transform. The center contains the spatial frequencies that determine the image contrast. The outer k-space defines the image resolution and therefore the details in the image.

Images can be created from the matrix using the discrete Fourier transform (DFT). The Fast Fourier Transform can be used if the K-space data is sampled on a Cartesian grid.

8.2. Conventional K-space sampling

To image 3D objects, tomographic imaging requires either 2D imaging with a suitable technique for defining a narrow slice within the object, or a 3D spatial encoding procedure. To reduce spatial encoding to two dimensions (K-plane), slice selection is accomplished by selectively exciting the magnetization of a slice with the aid of an oscillating $B_1(t)$ field perpendicular to the B_0 field and an RF pulse, characterized by a pulse envelope function, which defines its frequency bandwidth, and an appropriate excitation frequency, without perturbing the magnetization in the rest of the object. The subsequent signal originates only form this slice.

Common RF pulse envelopes are the rectangular, gaussian and the sinc function. A short (hard) rectangular pulse in the order of a microsecond excites spins over a wide frequency bandwidth. The RF pulse is therefore nonselective. A long (soft) rectangular pulse of a few milliseconds duration excites spins resonating over a narrow frequency bandwidth, and is therefore selective. In practical use, sinc pulses with truncated side-lobes and reduced side-lobe amplitudes yield better slice-selection profiles.

True 3D encoding necessitates a number of phase encode scans in the third direction in K-space before applying the 3D inverse Fourier transform. Equation 0-1 then has an additional factor n_{Ph} equal to the number of phase encoding steps in the third direction. The third

dimension can also be encoded by applying a gradient during the free induction decay (FID) or echo acquisition. If equilibrium has to be awaited after acquisition of each profile, total scan times increase by a factor equal to the number of encoding steps in the third direction. The larger number of independent measures for one single pixel during a 3D scan increases the SNR by the square root of the number of planes, compared to single or multiple slice imaging. Consequently, in 3D imaging, smaller pixels can be measured with similar SNR.

Figure 0-7 illustrates a K-space sampling scheme in a 2DFT or spin warp imaging experiment. In this and all following figures the frequency encoding is performed in the k_x-direction and the phase encoding in the k_y-direction. The total transverse magnetization of the excited slice is sampled n_S times during one echo, and these sample values provide a profile in the K-plane (horizontal line with constant k_y-value) per TR. The number of profiles in the K-plane equals the number of phase encode steps n_{Ph}. A conventional spin echo or gradient echo sequence acquires only one K-space line per TR. This is called a multiple shot technique. Total acquisition time for the spin echo sequence is given by Eq. 0-1.

Fig. 0-7: conventional K-space sampling pattern. The white dots on each profile represent the discrete sampling points. The time required to sample the whole K-plane is the repetition time TR times the number of phase encode steps.

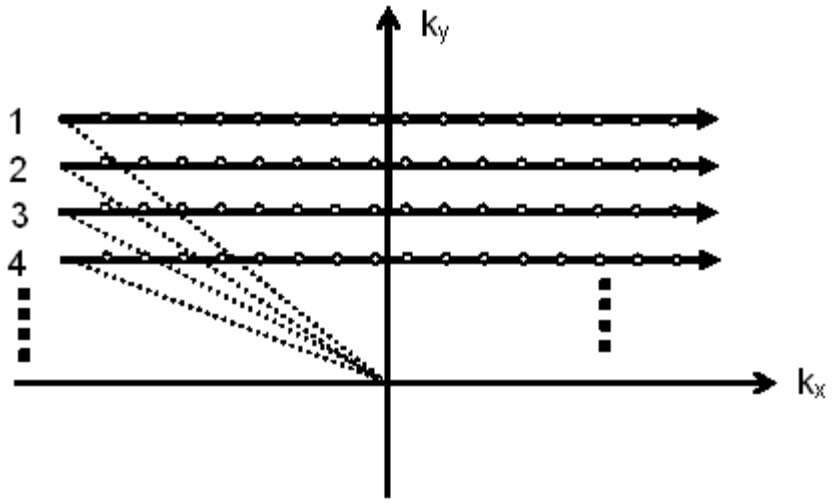

8.3. Strategies that reduce the repetition time

When TR << $5T_1$, the signal becomes T_1 weighted because the longitudinal magnetization has no time to recover before the next excitation pulse. With gradient echo imaging, it is possible to use smaller (< 90°) flip angles, and consequently the longitudinal magnetization requires less time to recover to thermal equilibrium. However, a low flip angle decreases the amount of magnetization tipped into the transverse plane, and the consequence is a lower SNR. The flip angle α for optimum SNR at a given TR depends on the T_1 of the tissue, and is given by the Ernst equation:

$\cos(\alpha) = \exp(-TR/T_1)$.

The image contrast relies on the three extrinsic parameters TR, TE and α. In opposite to spin echo images, gradient echo images are T_2* weighted as the transverse magnetization decay due to B_0 inhomogeneities is not inverted, and they are therefore more sensitive to susceptibility artefacts.

When TR < T_2*, the spins on the slice plane do not have enough time to dephase: the MR signal never decays completely. These sequences are called steady-state. The steady-state technique produces T_2*-weighted images very fast (in less than 1 second with TR < 10 ms) with a good SNR. Additional gradients or RF pulses can spoil or refocus any remaining transversal magnetization before the next readout pulse.

A typical spoiled gradient echo is the fast low angle shot (FLASH) sequence introduced in 1986 (Frahm et al. 1986). With fast (turbo) gradient echo sequences, such as snapshot FLASH (Frahm et al. 1990; Haase 1990), images can be acquired in less than one second.

As a result of the short TR, the longitudinal magnetization can not fully recover and after a few initial excitation pulses there is a dynamic equilibrium established between longitudinal magnetization recovery and reduction due to the excitation pulses. The signal intensity S of a spoiled gradient echo sequence is given by

$$S \propto \frac{M_0 \exp(-TE/T_2^*)[1-\exp(-TR/T_1]\sin(\alpha)}{1-\exp(-TR/T_1)\cos(\alpha)}\rho \qquad \textbf{Eq. 0-3}$$

where ρ is the proton density and M_0 is the longitudinal magnetization at thermal equilibrium. This is a multiple-shot technique since each image is acquired by applying a train of low flip angle pulses, each of which gives one phase encode line.

Technical improvements, such as stronger and faster switching gradients, further facilitate the task of reducing the TR.

8.4. Strategies that reduce the number of phase encode steps and speed up K-space sampling

A larger portion of the K-space data can be acquired after a single excitation during the decay of the transverse magnetization. Additional data profiles in K-space are acquired using multiple gradient echoes or spin echos. Other more efficient K-space sampling trajectories exist such as spirals and echo planar imaging (EPI). If the entire K-space is acquired after one excitation pulse and a long train of echoes then such a technique is called single-shot.

8.4.1. Fast Spin Echo

A multi spin echo sequence uses a 90° RF pulse followed by more than one refocusing pulse to create separate echoes at increasingly longer echo times. Fast spin echo (e.g. RARE) is accomplished by acquiring multiple echoes with successive 180-degree pulses, and uniquely phase encode each echo during a given TR. The number of echoes phase-encoded in a given TR is the factor by which the sequence is speeded up compared to a conventional spin echo sequence and is known as the turbo factor (or echo train length).

Fast spin echo images demonstrate more T_2-weighting making it difficult to obtain true proton density weighted images. Since all echoes have different TE, an effective TE is defined by the position of the echo belonging to the zero K-space line.

8.4.2. Echo planar imaging

In EPI (Pykett and Rzedzian 1987), multiple phase encoding lines are acquired from a single RF excitation instead of one single line. In single-shot EPI, all of k-space is sampled after a single set of RF pulses. A strong and rapidly switching/reversing readout gradient is used in combination with a weak phase encoding gradient (blip) at the end of the acquisition of each

line. Each traversal of K-space is achieved via one positive or negative readout gradient pulse, resulting in a meander trajectory (cf. Fig. 0-8). Instead of the blips in the phase encoding gradient, a small but constant phase encoding gradient can be used, such that oblique lines are described through the K-space, resulting in a zig-zag trajectory.

Since alternate lines of K-space are scanned in opposite directions, this must be taken into account in the reconstruction. The total trajectory through the K-space must be covered within T_2* (comprising T_2 decay and off-resonance effects), otherwise not enough signal is left at acquisition. The TE value for the center of K-space determines the contrast in the image. If T_2* is too short to allow acquisition of the entire K-space at once, segmentation is usually applied, meaning that the K-space is acquired using more than one excitation pulse (multiple-shot EPI).

Fig. 0-8: a single shot blipped EPI trajectory

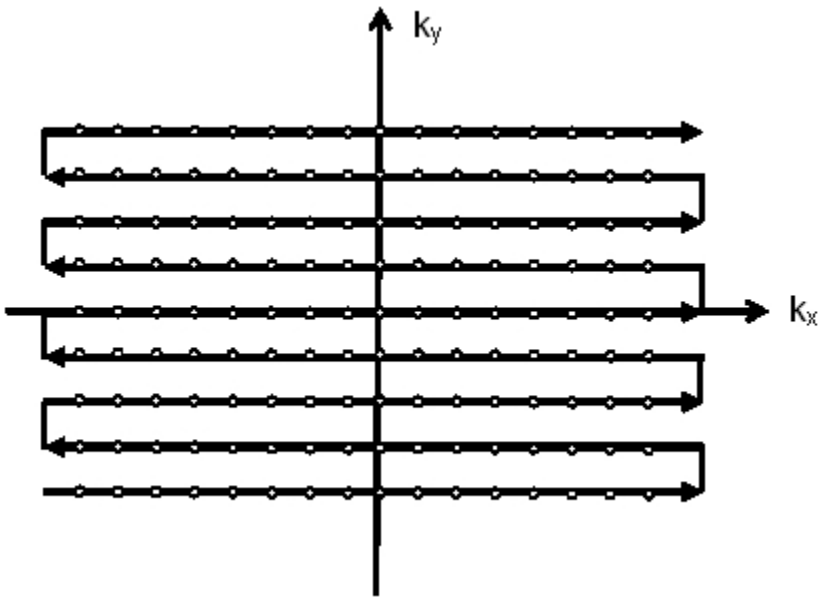

EPI is more sensitive to ghosting (variations in the phase encoding gradient cause alternating K-space shifts) than conventional imaging. In particular, it suffers from T_2* decay during the acquisition causing blurring, and from main magnetic field inhomogeneities causing resonance offset and distortions in the phase encoding direction. High gradient system performance is required, and instrumental imperfections can generate additional artifacts.

8.4.3. Spiral imaging

Non Cartesian K-space sampling trajectories are also possible. One such technique is spiral acquisition. A rotating magnetic field gradient is applied by a pair of increasing sinusoidal gradients, causing the trajectory in K-space to trace a spiral out from the center to the edge (Kim et al. 2003) (cf. Fig. 0-9) .

Fig. 0-9: spiral acquisition trajectory. The trajectory is smooth but the sampling points do not lie on a Cartesian grid.

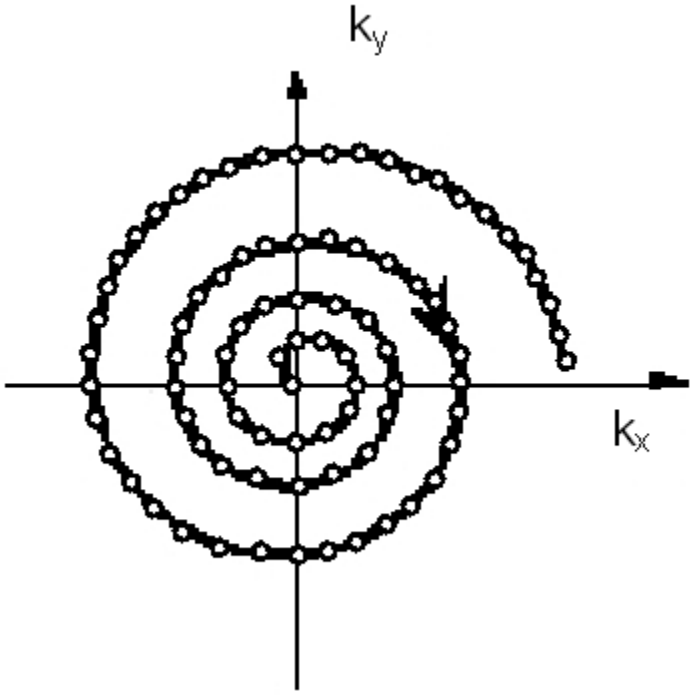

In spiral imaging the TE can be very short, because the trajectories start at the center of K-space. The signal is greatest at the start of the acquisition, while high spatial frequencies are acquired when the signal is attenuated due to T_2 and T_2 * decay. Hence acquiring the center of K-space first improves contrast to noise ratio (CNR) when compared to conventional acquisitions, especially in the presence of rapid movement. Effects such as flow, susceptibility

and T_2* decay, have no time to develop serious errors before essential information from large structures (low k values) is acquired.

A further difference from other fast methods is that the trajectory through the K-space is smooth and less demanding for the gradient system. T_2* decay and resonance offset occur mainly in the radial direction of K-space. Eddy currents, main magnetic field inhomogeneities and imperfections of the gradient field also distort the exact position of the sampling points in K-space.

For all non Cartesian sampling patterns, in order to use the efficient inverse fast Fourier transform for discrete data (Cooley and Tukey 1965) the sampled points in K-space must first be interpolated onto a Cartesian rectilinear grid. This method is called gridding (Noll et al. 1992).

8.5. Strategies that reduce the acquired data

8.5.1. Variable density sampling

Techniques that reduce the data that has to be acquired include those that undersample the high-frequency regions of the K-space. This often leads to acceptable image degradations, because, roughly speaking, the main contrast is determined by the magnetization acquired at the low spatial frequencies. K-space filling trajectories such as variable density Cartesian sampling, radials, or spirals, exploit this principle.

Projection reconstruction acquisitions

The earliest imaging technique used in MRI is projection reconstruction (PR) (Lauterbur 1973). Each acquisition starts at the origin of K-space and goes out on a radius at a polar angle $0 \leq \Theta < 2\pi$ (cf. Fig. 0-10) determined by the gradients in the x and y directions (G_x and G_y):

$$\Theta = \tan^{-1}\left(G_y / G_x\right).$$

The TE can be short since no phase encoding is necessary.

To encode the third dimension a gradient can be applied during signal acquisition in order to increment the azimuthal angle in the range $0 \leq \Phi < \pi$. This samples a sphere in K-space with radial profiles given by:

$$k_x = k\cos(\Theta(t))\sin(\Phi(t))$$
$$k_y = k\sin(\Theta(t))\sin(\Phi(t))$$
$$k_z = k\cos(\Phi(t))$$

Here

$$k = \frac{\gamma}{2\pi} G\,\Delta t\,,$$

with Δt being the time the gradient is applied.

Fig. 0-10: Projection reconstruction sampling pattern. The center of K-space is oversampled and the sampling points have a decreasing density from the center out to the periphery of K-space. The sampling points do not lie on a Cartesian grid.

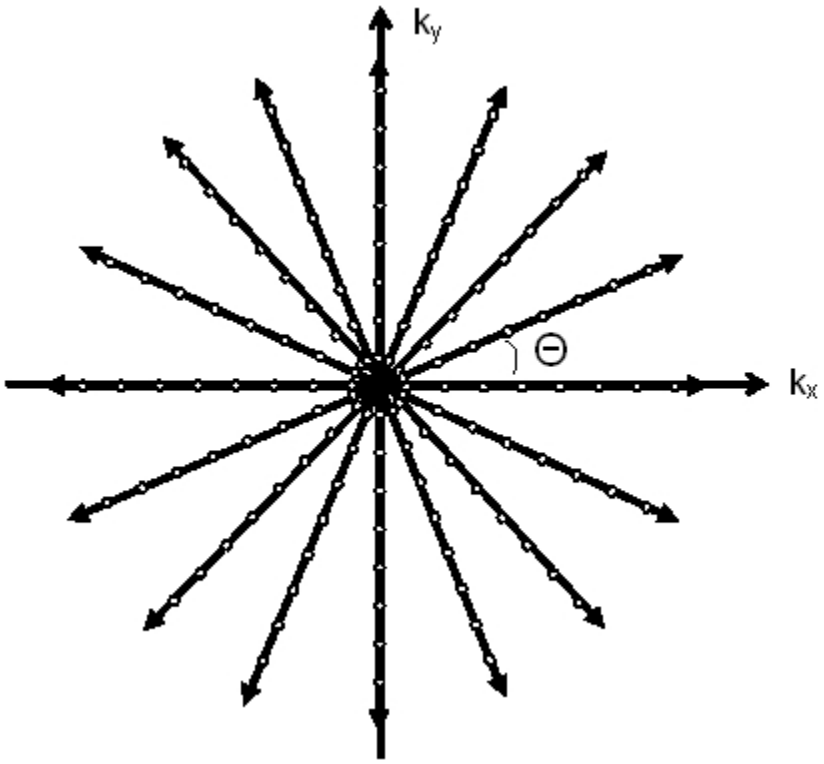

Acquisitions of radial profiles through the origin of the K-space have the advantage of oversampling the central region. This results in good sensitivity but relatively modest spatial resolution. Averaging of the low spatial frequencies also results in a reduction of motion and flow induced artifacts. Whereas with conventional Cartesian sampling techniques motion between the acquisitions of two lines in K-space causes ghosting artifacts in the phase encode direction,

more tolerable local blurring and streaking perpendicular to the direction of motion occurs at the periphery of the field of view (FOV) with radial sampling techniques (Glover and Pauly 1992).

Radial profiles can be acquired one by one after excitation from the equilibrium magnetization (long TR), or a T_1 weighting is introduced when TR < T_1. If a number of radial profiles (turbo factor) spanning an angular range is acquired after one excitation, eventually in an interleaving pattern, resonance offset and susceptibility artifacts as with spiral imaging or EPI are generated.

As with other non Cartesian sampling patterns a gridding procedure followed by the inverse fast Fourier transform can be used for image reconstruction. With radial sampling, filtered back projection can also be used for reconstruction similar to CT: each radial line can be inverse Fourier transformed and the obtained images (position dependent projections) superimposed (back-projected) to obtain the projection-reconstruction image. The 1/r blur has to be corrected by weighting the acquired K-space data before applying back projection.

Keyhole acquisitions

Keyhole imaging (van Vaals et al. 1993) is used for monitoring the passage of a CA in the vasculature (dynamic imaging) for which a very high temporal resolution is required.

The principle consists in acquiring a reference image before injection of the CA by sampling the K-space up to high spatial frequencies. However, during CA bolus passage, the low spatial frequencies are sampled at a higher rate than the peripheral regions of K-space because the details in the image are temporally invariant while the contrast is determined by the central K-space region which needs to be updated. Images are reconstructed at each sampling of the central K-space region using the temporally nearest samples from the peripheral K-space regions. Therefore the keyhole technique increases temporal resolution without loss of spatial resolution.

8.5.2. Half Fourier reconstruction

The NMR signals are detected using two phase detectors with orthogonal RF reference signals. The two channels, provide two time-dependent output signals u(t) and v(t) which behave as Cartesian components of a complex signal S(t) = u(t)+iv(t). According to equation Eq. 0-2, S(-**k**)

= S*(**k**), with the star denoting the complex conjugate. This means that there is a symmetry in K-space. One therefore needs to acquire S(**k**) only in slightly more than a suitably selected half of the K-space, resulting in equal spatial resolution. This technique is called Half-Fourier reconstruction. Drawbacks of this technique are a reduced SNR by a factor $\sqrt{2}$. In addition any artifacts during sampling of the first half of K-space are propagated to the second half.

8.5.3. Reduced FOV

Spatial resolution is an inverse function of the FOV. The smaller the FOV, the fewer data points are needed to sample it. A smaller image volume can be achieved by using local RF coils which pick up only signals arising from a limited area of a larger body, by using a non square shaped FOV and by outer volume suppression.

8.6. Strategies that increase the sampled data points per unit time

Strategies to acquire more data points per unit time include parallel imaging and pulse sequences that improve the duty cycle such that most of the time is spent acquiring data.

8.6.1. Parallel imaging

With parallel imaging or sensitivity encoding (SENSE), data are acquired simultaneously by individual receiver coils increasing the acquisition rate by a factor equal to the number of coils. The receiver coil elements have different sensitivity patterns in space, and these differences can be used to differentiate the spatial locations of signal sources for reconstruction.

8.6.2. Multiple slice acquisitions

A strategy that utilizes the time necessary to wait for longitudinal magnetization to recover (between the end of echo collection and the next 90° excitation pulse referred to as dead time) is the acquisition of multiple slices. Cross excitation between adjacent slices due to imperfect slice profiles is accounted for by interleaving slices, so that even slices are excited first followed by the odd ones.

8.7. Strategies to decrease the number of experiments

Signal has to be averaged over a large number of experiments, when the SNR is low. The SNR is always reduced when using low flip angles. It is also reduced when sampling as much data points of the K-space as possible after a single excitation pulse. The latter acquisition techniques are limited by the decay term

$$f_D = \exp(t/T_2^*) \qquad \textbf{Eq. 0-4}$$

where T_2^* is the apparent transverse relaxation time, which in addition to the intrinsic transverse relaxation time comprises diffusion and the dephasing effect due to local field inhomogeneity.

8.7.1. Increasing the SNR

The use of high-field magnets with field strength greater than 1.5T provides higher SNR, due to the increase in the nuclear polarization fraction. However, the disadvantages of high-field MRI are increased T_1, decreased T_2 and increased susceptibility based field inhomogeneity.

With the use of CAs, the recovery of the longitudinal magnetization can be accelerated and therefore the SNR improved.

8.7.2. Slowing down the transverse signal decay

Technological advances allow the construction of more homogeneous magnets. However, the object to be imaged is generally heterogeneous and induces local field inhomogeneities which accelerate the transverse decay of the signal. Local dedicated RF coils can be used to image a small volume of interest with improved SNR, thereby excluding irrelevant parts of the body that can be characterized by a greater field inhomogeneity.

8.7.3. Numeric correction for the decay term

The T_2^* can be considered spatially invariant if the magnetic field is homogeneous, since this is the dominating process for T_2^*. If the desired K-space data collection can not be accomplished while the decay factor (Eq. 0-4) is still close to one, a correction is theoretically possible before

reconstructing the image if for each data sampling point in K-space the delay TE at acquisition is known:

$$S(\mathbf{k}(0)) = f_D^{-1} \cdot S(\mathbf{k}(TE))$$

This correction implies that the decay rate $1/T_2^*$ is known and spatially invariant, and that this correction is not carried out for TE for which the SNR is already low, since this would amplify the noise component.

9. CBV measurements by MRI

The CBV can be measured using exogenous CAs, which remain confined to the vascular compartment in brain tissue. Two approaches for CBV quantification exist.

The so called steady state approaches for CBV measurement rely on the signal or relaxation rate change induced by a homogeneous distribution and stable concentration of the CA in the intravascular compartment.

The dynamic approaches either model the signal change during the first pass of the CA bolus through the tissue of interest (so called first pass or bolus tracking techniques) leading to the CBV, the CBF and the mean transit time (MTT), or afterwards including the CA distribution within different compartments and its elimination from blood, leading to the CBV, the extravascular leakage volume and a physiologic parameter related to the permeability of the BBB to the CA.

All MR relaxation mechanisms have been exploited for the measurement of CBV, and all approaches are based on a linear relation between CA concentration and relaxation rate change of blood (Boxerman et al. 1995; Rosen et al. 1990). Therefore the CBV can be derived from the relaxation rate change or from appropriately T_1 or T_2 weighted acquisitions. Any non-linearity between relaxation rate or signal change and CA concentration in tissue and blood will therefore introduce errors (Kiselev 2001).

Two MRI techniques exist, the Blood Oxygen Level Dependent (BOLD) technique and the Arterial Spin Labeling (ASL) technique, that do not rely on the injection of an exogenous CA and that measure a signal which is related to the CBV. Originally, they have not been conceived for

CBV measurement, but for the quantification of the CBF in the case of ASL techniques and for the detection of activated brain areas in functional MRI in the case of the BOLD technique.
Although they do not lead to the quantification of the total CBV, the origin of the CBV component to the signal acquired with these techniques will be briefly described in the last paragraph of this chapter.

9.1. Steady state methods

The compartmentalized presence of an intravenously injected CA reduces the longitudinal and transverse relaxation time of the vascular compartment and induces microscopic field gradients and susceptibility effects at the vessel wall, which shorten the T_2* relaxation time constant. With steady state approaches, the relaxation rate or signal change of the brain tissue induced by the CA is considered proportional to the intravascular CA concentration (Boxerman et al. 1995; Rosen et al. 1990) and is therefore related to its distribution volume in the tissue of interest: the CBV. A comparatively high CA dose is needed to assure a high and stable vascular concentration throughout the duration of the post-contrast acquisition. CAs with a long blood half life and high relaxivity are therefore preferred.

MRI acquisitions are performed before and after injection of the CA, and a difference image of the brain tissue is created from two T_1, T_2 or T_2* weighted acquisitions, or from the change in tissue relaxation rates ΔR_1, ΔR_2 or ΔR_2* before and after injection of a CA.

To quantify the CBV with all steady state techniques, information about the CA induced relaxation rate or signal change in the blood compartment is needed. The ΔR_2*-method under steady state conditions requires the knowledge of the blood susceptibility. Blood sampling becomes necessary, which is also the case using other acquisition techniques to determine the signal or relaxation rate difference of blood. If the spatial resolution of the images is sufficiently good to distinguish large vascular structures, this information can also be obtained from a vascular ROI. In this case blood sampling can be avoided but this method is limited by the partial volume effect.

9.1.1. CBV measurement in the slow water exchange regime

In the no-water exchange or slow water exchange limit, quantitative CBV is calculated as the ratio of the signal changes induced by the CA in tissue and blood (Kuppusamy et al. 1996; Lin et al. 1997):

$$CBV^{ss} = \frac{S_{pre}^{total} - S_{post}^{total}}{S_{pre}^{iv} - S_{post}^{iv}}$$

where S_{pre} and S_{post} are the signal intensity before and after CA injection, the superscript ^{total} refers to the signal in a tissue voxel (intravascular and extravascular), the superscript ^{iv} refers to the blood signal (intravascular) and the superscript ^{SS} refers to steady state methods.

T_1 weighted acquisitions are more adapted for this method because it is assumed that the longitudinal relaxation enhancement is dominant. However, with long TE times the CBV can be contaminated by T_2-effects. T_2 weighted acquisitions have also been used (Le Duc et al. 1999).

9.1.2. CBV measurement in the fast water exchange regime

In the fast water exchange limit, the T_1 values of all tissue compartments are shortened, although the CA remains intravascular, and the CBV can be obtained by calculating the ratio of R_1 change in the tissue to R_1 change in blood (Schwarzbauer et al. 1993).

$$CBV^{ss} = \frac{\frac{1}{T_{1post}^{total}} - \frac{1}{T_{1pre}^{total}}}{\frac{1}{T_{1post}^{iv}} - \frac{1}{T_{1pre}^{iv}}}$$

9.1.3. CBV measurement by the steady state ΔR_2^* method

Other studies (Payen et al. 2000; Tropres et al. 2004) have exploited the changes in R_2^* (Villringer et al. 1988). The CBV quantification by the steady state ΔR_2^* method is based on a simplified geometric model of the brain microvasculature and the approximation of static water protons. The compartmentalization of high magnetic susceptibility CAs, such as USPIO, within the randomly oriented capillary network of the brain results in localized microscopic field inhomogeneities in the tissue in which water protons diffuse, inducing a loss of transverse phase coherence with T_2^* signal loss in the perivascular space. As illustrated in Fig. 0-11, the

component of the magnetic field B(r) which is parallel to B_0 is inversely proportional to the square of the distance r form the vessel:

$$B(r) \propto \Delta M \left(R/r\right)^2 \sin^2(\Theta)$$

and it is a function of

ΔM: the magnetization difference between the intra- and extravascular compartment induced by the compartmentalized CA,

R: the radius of the vessel,

Θ: the angle between the direction of the main magnetic field B_0 and the axis of the vessel.

A static or quasi static water proton diffusion regime means that the diffusion coefficient D of the extravascular water protons is D ≈ 0, or equivalently that their mean diffusion length

$$d = \sqrt{D \cdot TE}$$

is short with respect to the vessel radius R. In this case, the water protons situated at different distances r from the vessel experience different magnetic field strengths B(r) and therefore diphase at different rates. Consequently the R_2* of the tissue signal is high after CA injection. The difference ΔR_2* between the relaxation rate before and after CA injection is shown to be proportional to the vascular volume fraction. Monte Carlo simulations show good agreement with in vivo results (Boxerman et al. 1995; Tropres et al. 2001).

Fig. 0-11: The ΔR_2^* method for CBV measurement models the capillary as an infinitely long and homogeneous cylinder containing the CA. The magnetic field gradient around the cylinder is a function of the cylinder radius R, of the magnetization difference between the intra- and extravascular compartment, of the cylinder orientation in the main homogeneous magnetic field B_0 and of the distance from the cylinder. The diffusion regime is said to be static or quasi static when the mean water proton diffusion length d is short with respect to R, in such a way that the water protons in the vicinity of the cylinder dephase at a faster rate than those situated further away.

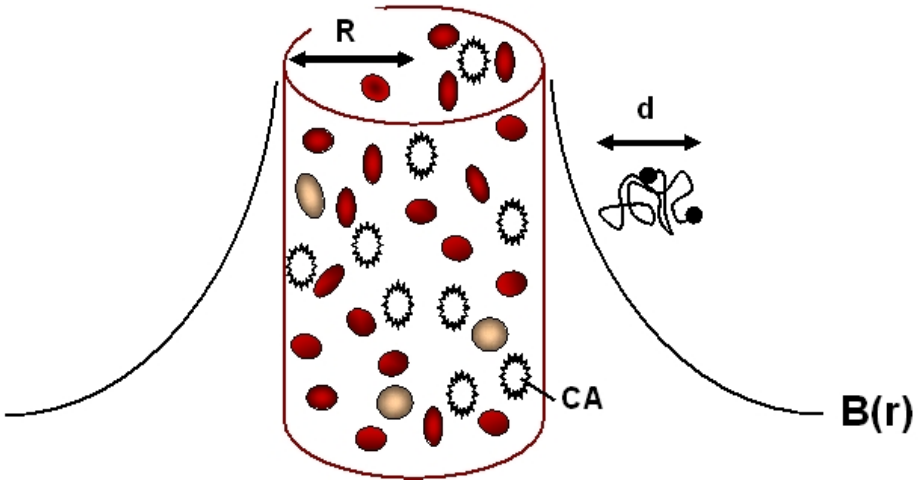

The proportionality factor between the vascular volume fraction and ΔR_2^* depends on the intra-extravascular susceptibility difference $\Delta\chi$, which has to be measured from peripheral blood samples, although $\Delta\chi$ is dependent on the hematocrit level, which is not the same in a large vein and the microvasculature (Bereczki et al. 1993a; Cremer and Seville 1983). Large CA doses are needed for an increased $\Delta\chi$.

The CBVf expressed in % is obtained in the following way (Yablonskiy and Haacke 1994):

$$CBVf = \frac{3}{4\pi}\frac{1}{\gamma \Delta X B_0}\Delta R_2^* \qquad \textbf{Eq. 0-5}$$

where γ is the gyromagnetic ratio and B_0 is the static magnetic field strength.

The ratio $\frac{\Delta R_2^*}{\Delta R_2}$ is dependent on the vessel size (Boxerman et al. 1995; Dennie et al. 1998). ΔR_2 is sensitive primarily to small vessels, while ΔR_2* is influenced by a broader range of vessel sizes.

By measuring $\frac{\Delta R_2^*}{\Delta R_2}$ using gradient echo and spin echo sequences, and the water diffusion coefficient D, it is possible to estimate a vessel size index (VSI) which can be interpreted as the weighted mean of the volume fraction of vessels with a particular radius r (Tropres et al. 2001):

$$VSI = 0.424\left(\frac{D}{\gamma \Delta X B_0}\right)^{1/2}\left(\frac{\Delta R_2^*}{\Delta R_2}\right)^{3/2}$$

9.1.4. Vascular space occupancy (VASO)

Relative CBV

The vascular space occupancy (VASO) technique (Lu et al. 2003) uses an inversion recovery sequence with timing parameters optimized to suppress the blood signal, while the extravascular tissue gives rise to a signal, which is not at its equilibrium value.

For functional MRI, images are acquired during task performance (regional CBV increase) and under rest conditions. It is assumed that the sum of intravascular and extravascular magnetization in a voxel is equal in the rest and in the activated condition.

In the rest condition,

$S^{rest} = (M_{0\,total} - M_{0\,blood}) \cdot f(TR, T_{inv}, TE)$

the extravascular signal is proportional to the extravascular magnetization at equilibrium $M_{0\,ev}^{rest}$:

$M_{0\,ev}^{rest} = M_{0\,total} - M_{0\,blood}$

where

$M_{0\,total}$ is the equilibrium magnetization of the voxel,

$M_{0\,blood}$ is the equilibrium magnetization of the blood compartment under the rest condition and

the factor

$f(TR, T_{inv}, TE)$

is a function of the sequence parameters used, where the inversion time T_{inv} is the delay between inversion pulse and excitation pulse that nulls the blood signal.

Since the CBV increases in an activated voxel, the extravascular tissue signal is given by

$$S^{activation} = \left(M_{0\,total} - (M_{0\,blood} + \Delta M_{0\,blood})\right) \cdot f(TR, T_{inv}, TE)$$

where $\Delta M_{0\,blood}$ is the magnetization difference due to the blood volume increase.

The signal difference between the rest and the activated condition is proportional to the CBV change:

$$S^{activation} - S^{rest} = \Delta M_{0\,blood} \cdot f(TR, T_{inv}, TE).$$

Under the experimental conditions (Lu et al. 2003) a signal decrease of about 0.7% has been detected. A signal decrease has also been observed for hypercapnia, while for hypocapnia the tissue signal increases, consistent with a vasoconstriction (Lu et al. 2003).

Absolute CBV

In a second version of this approach (Lu et al. 2005), the absolute CBV can be determined using the T_1 shortening effect of Gd-DTPA.

The signal before CA injection S_{pre} is only of extravascular origin since the blood signal is suppressed by the inversion recovery sequence using an appropriate T_{inv}:

$$S_{pre} = S_{ev}$$

where S_{ev} is the extravascular signal.

After CA injection the T_{inv} is sufficiently long to allow full relaxation of the blood water magnetization to thermal equilibrium, and the post-contrast signal S_{post} is given by:

$$S_{post} = S_{ev} + S_{0\,iv}$$

where S_{0iv} is the blood signal corresponding to the equilibrium magnetization of the blood compartment.

The signals in the difference image are proportional to the blood volume since the extravascular tissue cancels out.

$$S^{post} - S^{pre} = S_{0\,iv}$$

This method is similar to the steady state T_1 weighted approach, but the signal enhancement is maximized by blood nulling before CA injection, and it is not necessary to measure the signal enhancement in blood because it corresponds to the blood magnetization at thermal equilibrium. However, for CBV quantification, the resulting blood signal in the difference image has to be normalized by the signal corresponding to the thermal equilibrium magnetization of the total tissue (intra- + extravascular compartment) of the voxel. The normalization factor is obtained from a ROI containing CSF on a reference image with sufficiently long acquisition times or from a small ROI containing mainly blood on the postcontrast image.

In humans, mean CBV from 1.4 to 5.5 ml/100 g have been measured with this technique for white matter and cortical gray matter, respectively (Lu et al. 2005).

Drawbacks of the VASO method

The difficulties encountered with this technique are the following:
The repetition time (TR = 6 s) used is relatively long and therefore the blood T_1 has to be known precisely in order to determine the blood nulling inversion time ($T_{inv} \approx 1$s, depending on the field strength). A slightly inappropriate T_{inv}, reduced inversion efficiency or a change in blood T_1 (e.g. with hematocrit or oxygenation), does not only result in a non negligible blood signal, but this signal might also be negative before and positive after CA injection, resulting in an underestimation of the CBV if the difference image is calculated from absolute signal values.

Due to a relatively long T_{inv}, the water exchange between intra- and extravascular compartment will have a large effect. This will be quantified and discussed in detail in chapter I.

Finally, if the RF coil used for detection has an inhomogeneous sensitivity profile as can be the case with surface coils, the normalizing factor obtained from a small CSF containing ROI is not representative for a ROI in another location. If the normalization factor is obtained from a vascular ROI affected by the partial volume effect, the CBV might be underestimated.

9.2. Dymamic methods

Dynamic methods involve the rapid serial acquisition (< 1.5 s) of MR images before, during and after an intravenous injection of a CA. As the CA enters into the tissue under investigation, the T_1 and T_2 values of tissue water decrease to an extent that is determined by the concentration of the CA and the signal displays a characteristic intensity time course, which is related to the CA concentration. Such a characteristic signal intensity time course is illustrated in Fig. 0-12 as an example of a positive (T_1 weighted) signal change. Studies that exploit changes in T_1 are termed dynamic contrast enhanced (DCE) MRI, while those relying on T_2* changes are termed dynamic susceptibility contrast (DSC) enhanced MRI.

Fig. 0-12: Characteristic signal intensity time course during CA bolus passage. After the first high peak, the second peak corresponds to the second bolus passage after recirculation.

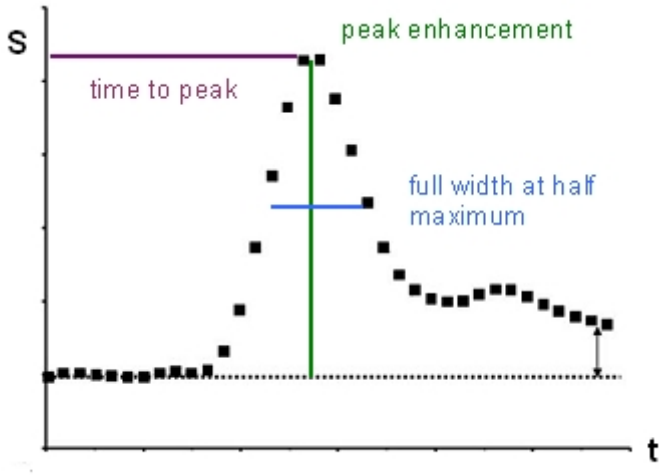

EPI sequences are typically used, because they allow a good temporal resolution. DCE MRI can be performed with a rapid FLASH sequence (Adam et al. 1994; Hacklander et al. 1996)

Tracer kinetic analysis (Meier and Zierler 1954) of the first bolus passage mainly provides estimates of blood flow, blood volume and mean transit time of the CA. This so-called bolus tracking method is described in paragraph 9.2.1.

If the CA diffuses into the extravascular compartment, the DCE MRI data that monitors the tissue signal change (referred to as CA uptake curve) over a longer time scale, can be fitted to an appropriate pharmacokinetic model. In this case other physiological parameters can be extracted that relate to, for example, microvascular vessel wall permeability and extracellular volume fraction, but also to the tissue perfusion. The main pharmacokinetic models are reviewed in paragraph 9.2.4.

9.2.1. Bolus tracking method

Characteristic descriptive parameters measured form the observed signal changes during bolus passage include for example “peak enhancement”, “time to peak” and "full width at half maximum" (cf. Fig. 0-12). In general, these have the advantage of being robustly estimated, but may depend on combinations of physiologic parameters, such as blood flow, fractional blood volume, and CA extravasation. However, the peak signal amplitude was shown to correlate with the CBV (Cha et al. 2000b).

For CBV quantification, the signal intensity during bolus passage is converted into a change in R_1 (Dean et al. 1992), R_2 or R_2* (Villringer et al. 1988) versus time reflecting the CA concentration. The proportionality constant between tissue relaxation rate change and CA concentration has to be known. This constant depends on CA properties, magnetic field strength and MR sequence parameters. It is generally assumed to be the same as the relaxivity of the CA in blood.

Relative CBV

In clinical routine, the CBV in the tissue of interest is given relative to a reference tissue. Maps of relative CBV are calculated by integrating the area under the curve over time. Since the CBV is calculated on the basis of signal recovery to the precontrast baseline, an adequate estimation of the baseline signal by signal averaging is essential. The accuracy of the CBV measure depends on the ability to fit a gamma variate function to the concentration versus time curve (cf. Fig. 0-12) to correct for CA recirculation (Thompson et al. 1964). When relative CBV values are reported, the assumption of identical arterial concentration profiles and of identical CA relaxivity in all compared tissue ROIs is made.

Absolute CBV

The absolute CBV can be determined from the ratio of the areas under the tissue $C_{tissue}(t)$ and arterial $C_a(t)$ concentration versus time curves:

$$CBV = \frac{\int_{-\infty}^{\infty} C_{tissue}(t)dt}{\int_{-\infty}^{\infty} C_a(t)dt}$$

The tissue concentration versus time curve is the convolution of the so-called tissue residue function $\Re(t)$ and the shape of the arterial concentration time curve $C_a(t)$ times the CBF:

$$C_{tissue}(t) = CBF \int_{-\infty}^{t} C_a(\tau)\Re(t-\tau)d\tau$$

$\Re(0)$ is equal to one at t = 0 when the CA enters the volume of interest. To calculate the CBF the impulse response CBF $\times$ $\Re(t)$ has to be determined by deconvolution, and then CBF is obtained as the initial (t = 0) height of the impulse response function.

The time dependent arterial CA concentration $C_a(t)$ is called arterial input function (AIF). It has to be specified from voxels within or next to the major feeding artery. The imaging of the time course of the vascular CA concentration requires that the acquisition mode is insensitive to flow, that it has an adequate spatial resolution to identify a vessel and a high temporal resolution to sample the shape of the initial bolus passage. In addition, signal saturation for the very high vascular concentrations during the bolus peak has to be avoided, otherwise the signal does not reflect the CA concentration correctly.

For accurate CBV and CBF calculation, the CA should be administered as a very short bolus. A slow injection (wide bolus) might also prevent accurate determination of the arrival time. The MTT is obtained by the central volume theorem:

$$MTT = \frac{CBV}{CBF}$$

9.2.2. Steady state versus bolus tracking MRI techniques

Drawbacks of the bolus tracking techniques

Bolus tracking techniques rely on very rapid acquisitions to accurately sample the first pass of the CA. The image acquisition time should be preferably < 1.5 s especially for the high heart rate of small laboratory animals or children. The spatial image resolution is therefore lower than for steady state techniques. Due to short TR for rapid sampling a T_1 weighting can appear with T_2* weighted acquisitions.

The main disadvantage of the bolus tracking method is the need of an AIF measurement, which is difficult to obtain in a reliable way, and which is the major source of error. The AIF can be influenced by variations in injection conditions and by physiologic or morphologic parameters of the vasculature. Delay and dispersion occurs from the site of the AIF measurement to the tissue ROI. Dispersion occurring in the larger vessels can be misinterpreted as a low tissue flow, although it is normal (Calamante et al. 2000; Ostergaard et al. 1996). The AIF measure is often affected by partial volume effects or suffers from saturation effects. Deconvolution methods (Calamante et al. 2002; Perthen et al. 2002) have been proposed to provide more reliable absolute quantifications. However, most studies using bolus tracking techniques report relative/semiquantitative results, because the determination of the AIF is considered too complex or inaccurate.

Drawbacks of the steady state techniques

One of the difficulties with the steady state techniques is the necessity of determining the signal change in the blood compartment, which either requires blood withdrawal and an additional acquisition, or a ROI reflecting exclusively the blood signal and therefore a good spatial resolution of the MRI acquisitions.

Another drawback of steady state techniques is the need of higher CA doses than for the bolus tracking techniques.

Since steady state CBV measurements can require long imaging times, they are subject to patient motion. For the same reason, water exchange and CA extravasation taking place during

the acquisition result in an overestimation of CBV when T_1 weighted imaging is used and in an underestimation when T_2 or T_2* weighted imaging is used.

9.2.3. T_1 weighted versus T_2 weighted MRI for CBV mapping

T_1 weighted acquisitions have a rather low SNR, because the relaxation enhancement is limited to the relatively small intravascular space. A higher SNR is achieved with T_2* weighted methods. Since the effects of the CA extend to the water protons of the extravascular compartment, the signal is derived from a larger fraction of protons than that contained in the vascular space. This indirectly renders the small capillary volume of about 3% significant on the signal intensity.

As mentioned in paragraph 9.1.4., spin echo T_2 weighted acquisitions provide a higher sensitivity for the microvascular perfusion than gradient echo T_2* weighted acquisitions (Boxerman et al. 1995) but have consequently a smaller SNR and necessitate higher CA doses. Similar to T_2* weighted acquisitions T_1 weighted acquisitions exhibit sensitivity to the total vascular pool, including large vessels. Therefore they correlate more closely with PET studies.

T_1 weighted dynamic MRI requires a smaller fraction of CA than the T_2* weighted and T_2 weighted methods do. In addition to the economic benefit, a smaller CA dose has the practical advantage of facilitating the injection as a narrow bolus.

If the CA leaks out of the vessels, such as occurs in extracerebral and in tumor tissue, the decrease of the compartmentalization reduces the local field inhomogeneities and the extravascular accumulation of CA causes a T_1 shortening. In DSC MRI, a small dose of CA injected a few minutes before the main bolus injection can compensate for the T_1 shortening effects of the leaking CA but cannot overcome the decrease in compartmentalization. CBV maps computed from T_2* weighted and T_2 weighted dynamic MRI tend to underestimate the CBV values in the presence of CA leakage, and may show false negative findings in the event of an active tumor recurrence (Aronen et al. 1994). Where T_1 weighted sequences are used, the presence of transendothelial CA leakage will act synergistically on signal intensity, causing artefactual CBV increases (Hacklander et al. 1996).
Attempts to separate the effect of CA leakage from the CBV measurement were made (Ostergaard et al. 1999), resulting in models that allow simultaneous estimation of CBV and permeability.

9.2.4. Pharmacokinetic models for BBB permeability and CBV estimation

Small molecular hydrophilic CAs diffuse readily across vascular membranes except in some organs such as the brain. Thus, imaging of the blood pool, such as with MR angiography or bolus tracking methods, must be accomplished within 20-30 s post injection, after which the CA has diffused into the extravascular extracellular compartment. Imaging the extravascular compartment by monitoring the CA uptake can take place over several minutes to hours until the CA is filtered and eliminated.

Kinetic analyses of such time-dependent MRI data, based on principles of solute diffusion across endothelial barriers, can derive quantitative parameters describing the microvascular permeability, the perfusion of the tissue and the compartment volumes accessible to the CA (among these the CBVf). The main recognized pharmacokinetic models will be reviewed (Tofts 1997).

Clinical studies using MR methods for measuring the uptake of CA in tumors have demonstrated the utility of these parameters for assessing malignancy and response to therapy in various tumors (Taylor and Reddick 2000). Measures derived from DCE MRI data correlate with surrogates of tumor angiogenesis.

Permeability to macromolecular CAs

Endothelial permeability depends upon both vascular morphology and the physicochemical characteristics of the CA molecule. Selective hyperpermeability to small molecular CA induced by a pathology can be exclusively studied in the microvessels of malignant brain tumors (since all other tissues in the body are also permeable under physiologic conditions). Kinetic modeling and interpretation is simplified by the assumption of a low extravasation rate compared to vascular flow rate (permeability limited model). When the CA extravasation rate is in the same order or higher than the blood flow rate in the vessel, the permeability limited model is no longer accurate. CAs of greater molecular weight allow this limitation to be overcome, because their extravasation rate is lower. By virtue of their blood pool properties macromolecular CAs also permit the study of extracerebral neoplasms analogous to MRI studies performed in brain tumors.

Semiquantitative parameters

A simple qualitative or semiquantitative analysis of the signal enhancement curve with time after CA injection (Parker et al. 1997) use descriptors, such as arrival time of the CA, maximum signal intensity or maximum intensity time ratio (Flickinger et al. 1993), initial gradient or washout gradient. These parameters have a link to the underlying tissue physiology and CA pharmacokinetics, but the link is complex and often undefined. Unless the CA concentration versus time curves are used for semiquantitative analysis, they also depend on MR scaling factors. Intra- and interpatient comparisons are therefore difficult.

Quantitative parameters

For quantification, the time-varying signal has to be translated into tissue CA concentration. This procedure is not without the risk of ignoring nonlinearities between signal and high CA concentrations, such as they occur in the vessels during the first passages.

Pharmacokinetic modeling sets up a simplified description of tissue as a multi-compartment system. CA transport between the compartments may then be modeled in terms of rate constants. Simplest approaches model unidirectional CA flux (from intravascular to extravascular (or interstitial) compartments). More detailed approaches recognize CA reflux in a bidirectional flux model. This enables the estimation of at least two parameters: the coefficient of endothelial permeability called K^{PS} or K^{trans} by different authors, and the fractional volume of the extravascular compartment into which the CA distributes (extravascular extracellular) called v_e (without unit):

$$v_e = \frac{V_e}{V_{total}}$$

where V_e is the volume of the extravascular compartment (ml) accessible to the CA and V_{total} is the total tissue volume (ml).

Permeability limited CA leakage

In general, the CA arrival in a voxel is by blood supply or by diffusion from nearby voxels, but the diffusion component is typically ignored in dynamic MRI.

The permeability limited model (Tofts and Kermode 1991) assumes that the flow is high enough and the vascular permeability low enough to prevent a decrease of the intravascular CA concentration. Arterial C_a and venous C_v concentrations remain equal, and the extraction fraction E, defined as

$$E = (C_a - C_v)/C_a$$

is practically null.

The change in extravascular CA concentration dC_e/dt is proportional to the vascular permeability P (cm/min), the vascular surface area S_v (cm^2/g) and to the difference between the blood plasma concentration $C_p(t)$ (mM) and the extravascular concentration $C_e(t)$ and inversely proportional to the fractional volume of the extravascular compartment. If the backflux of the CA from the extravascular into the intravascular compartment is assumed to be the same, the extravascular CA concentration change is described by:

$$\frac{dC_e}{dt} = \frac{PS_v\rho}{v_e}\left(C_p(t) - C_e(t)\right) \qquad \textbf{Eq. 0-6}$$

where ρ is the tissue density and approximately 1 g/ml.

The CA concentration in the tissue is composed of the concentrations in the plasma and in the extravascular compartment:

$$C_{tissue}(t) = v_p C_p(t) + v_e C_e(t) \qquad \textbf{Eq. 0-7}$$

where v_p is the fractional volume of the plasma compartment, and $C_{tissue}(t)$ the CA concentration in the tissue. The fractional plasma volume is related to the fractional blood volume (= CBVf) by:

$$v_p = (1 - Hct)\,CBVf$$

However, most models consider the plasma compartment negligibly small ($v_p << v_e$). With this assumption, the tissue concentration is:

$$C_{tissue}(t) = v_e C_e(t).$$

Therefore Eq. 0-6 becomes:

$$\frac{dC_{tissue}}{dt} = PS_v\rho\left(C_p(t) - C_{tissue}(t)/v_e\right).$$

Flow and permeability limited CA leakage

When the initial extraction fraction (before backflux into the vessel plays a role) is not negligibly small, the extravasation rate is also governed by the flow.

In this mixed flow + permeability limited case (Larsson et al. 1990) the extravasation rate is determined by

$$\frac{dC_{tissue}}{dt} = FE\rho\left(C_p(t) - C_{tissue}(t)/v_e\right),$$

where the extraction fraction is expressed as

$$E = 1 - \exp\left(-PS/F\right),$$

and F is the plasma flow.

Flow limited CA leakage

In the flow limited case, for which

$PS_v >> F$,

$E = 1$

the extravasation rate is

$$\frac{dC_{tissue}}{dt} = F\rho\left(C_p(t) - C_{tissue}(t)/v_e\right),$$

which is the model initially proposed by Kety for absorption of an inert gas (Kety 1951).

General form

In all three cases the factor of proportionality is the K^{trans} coefficient, which is

$K^{trans} = PS_v\rho$ in the permeability limited case,

$K^{trans} = FE\rho$ in the flow and permeability limited case

and

$K^{trans} = F\rho$ in the flow limited case.

In a generalized form, the extravasation rate can be expressed as

$$\frac{dC_{tissue}}{dt} = K^{trans}\left(C_p(t) - C_{tissue}(t)/v_e\right)$$

or

$$\frac{dC_{tissue}}{dt} = K^{trans}C_p(t) - k_{ep}C_{tissue}(t). \qquad \textbf{Eq. 0-8}$$

The rate constant

$$k_{ep} = K^{trans}/v_e$$

governs the backflux of CA into the vessel. K^{trans} and k_{ep} have the same unit, usually min^{-1}, because v_e is a volume fraction without unit. A time constant for CA transendothelial flow can also be defined (Gowland et al. 1992):

$$\tau_{ep} = k_{ep}^{-1}.$$

Estimation of the CBV

The fractional plasma compartment volume v_p can be estimated by respecting Eq. 0-7 (Daldrup et al. 1998). Inserting Eq. 0-7 into Eq. 0-6 results in the following differential equation describing the CA flux across the endothelium:

$$\frac{dC_{tissue}}{dt} - v_p\frac{dC_p}{dt} = PS_v\rho\left[C_p(t) - \frac{1}{v_e}\left(C_{tissue}(t) - v_pC_p(t)\right)\right].$$

If different permeabilities for the outflux P_{out} and the backflux P_{back} are used, the equation becomes:

$$\frac{dC_{tissue}}{dt} - v_p\frac{dC_p}{dt} = P_{out}S_v\rho C_p(t) - \frac{P_{back}S_v\rho}{v_e}\left(C_{tissue}(t) - v_pC_p(t)\right).$$

A solution to Eq. 0-8 is

$$C_{tissue}(t) = K^{trans}\int_0^t C_p(\tau)\exp\left[-k_{ep}(t-\tau)\right]d\tau \ .$$

with the initial condition $C_{tissue}(0) = v_eC_e(0) = 0$, since the plasma CA concentration has been neglected.

The tissue concentration corrected for the plasma concentration is therefore given by:

$$C_{tissue}(t) = K^{trans} \int_0^t C_p(\tau) \exp\left[-k_{ep}(t-\tau)\right] d\tau + v_p C_p(t). \quad \textbf{Eq. 0-9}$$

The parameters in this expression (including the fractional plasma volume) can be fitted to the corresponding DCE-MRI data (Daldrup et al. 1998).

The plasma concentration of the CA versus time

In all described cases, the CA uptake by the tissue is not only determined by the coefficient of endothelial permeability but by plasma concentration curves $C_p(t)$ as well. Therefore, to derive the physiological parameters K^{trans}, v_e and v_p, the plasma concentration versus time has to be measured or modeled.

Three main groups, Tofts and Kermode (Tofts and Kermode 1991), Larsson et al (Larsson et al. 1990) and Brix et al (Brix et al. 1991), used methods that differed mainly in the way they got access to C_p:

Tofts and Kermode assumed a typical biexponential decay of C_p, due to rapid leakage into the extravascular extracellular compartment anywhere in the body and to the slower filtration by the kidneys. Larsson et al measured it from blood samples, while Brix et al included the plasma clearance rate as a free parameter in the fit.

Tofts and Kermode assumed the CA relaxivity r_1 in tissue equal to that in water, while Larsson obtained r_1 by fitting the initial slope of the tissue relaxation rate to the model. Brix et al used a CA infusion at a constant rate instead of a bolus and assumed a linear relation between signal and tissue CA concentration.

Main assumptions of the pharmacokinetic models

A major assumption in the study of Tofts and Kermode (Tofts and Kermode 1991) is the description of the blood or plasma concentration of the CA.

Assumptions common to all models described here are the homogeneity of the compartments with respect to the CA distribution, a CA flux that is proportional to the concentration gradient between compartments, a negligible contribution from diffusion of CA from other voxels and a

time invariance of the compartment volumes and permeability coefficients. Further compartmentalization of the CA within the extravascular extracellular space is ignored. Finally the water exchange between compartments is assumed to be fast so that a single relaxation time constant T_1 can be measured for the tissue, although the CA is compartmentalized.

Each model makes assumptions that may not be valid for every tissue or tumor type in such a way that experimental data may not fit the model chosen. The analysis methods must monitor fit failures. For example, the Tofts and Kermode model (Tofts and Kermode 1991) fails in areas where contrast extraction from the vasculature is extensive (flow limited case) or negligible, such as in normal brain tissue.

Patlak method

The Patlak method (Patlak and Blasberg 1985; Patlak et al. 1983) is a graphical analysis technique of the CA uptake versus time. It is assumed that there is at least one irreversible tissue compartment in which the CA is trapped and any number of reversible tissue compartments in equilibrium with the plasma compartment. The tissue concentration C_{tissue} divided by the plasma concentration C_p of the CA is plotted on the y-axis against the time integrated plasma concentration divided by the instantaneous plasma concentration of the CA on the x-axis. The unit on the x-axis is sometimes called stretched or normalized time.

$$\frac{C_{tissue}(t)}{C_p(t)} = K_i \frac{\int_0^t C_p(\tau)\,d\tau}{C_p(t)} + v_p$$

This equation results from equation Eq. 0-9 assuming the exponential term is unity (i.e. $k_{ep} = 0$) and after dividing by $C_p(t)$. For tissues with irreversible compartments (unidirectional CA uptake) this plot becomes linear when all reversible compartments are in equilibrium with the plasma compartment, i.e. when the ratios of the CA concentration in plasma and in the reversible tissue compartments are stable. This happens when the plasma concentration decreases slowly enough for the reversible compartments to follow. The slope of the straight line fitted to the plotted data yields the so-called influx constant K_i (min^{-1}), which is the uptake rate and related to the endothelial permeability, and the intercept v_p with the y-axis yields the fractional plasma volume plus, if existing, the volume of the reversible compartments.

The method was originally developed to model the blood-brain exchange, assuming that the CA backflux from the tumor extravascular extracellular compartment into the vessel is negligible (Patlak et al. 1983). The model can be applied for the analysis of PET data such as with radiolabeled fluoro-deoxy-glucose, or for the analysis of CT (Leggett et al. 1999) or MRI (Ewing et al. 2003) data. In a later version, a correction for backflow from the former "irreversible" tissue compartment was implemented (Patlak and Blasberg 1985) yielding the transfer rates in both directions as in the generalized pharmacokinetic model (Tofts et al. 1999).

9.3. CBV estimations by ASL and BOLD MRI techniques

The aim of the following two paragraphs is to describe how the CBVf contributes to the signal acquired with the ASL (aimed at CBF measurement) and the BOLD technique (aimed at detecting the vascular response to brain activation). Attempts to disentangle the CBVf component of the signal have been reported.

Arterial Spin Labeling

ASL is a technique that focuses on measuring the CBF without the use of exogenous CA. It detects the inflow of magnetically labeled spins into the imaging slice. The labeling is performed upstream by inverting or saturating the blood water proton spins in a feeding artery, usually in the internal carotid arteries in the neck.

In the imaged voxel, the labeled blood spins flow through an arterial, a capillary and a venous segment of the microvessel. Only the capillary blood is assumed to freely exchange with the tissue, and therefore determines the microvascular blood flow. The venous blood magnetization is in equilibrium with the tissue and does not contribute to the signal. This is also assured by a sufficiently long TE, with respect to the short T_2 of venous blood.

The arterial blood in the imaged voxel does not always contribute to the perfusion of the same voxel. The signal component arising from arterial flowing spins is therefore considered to contaminate the measurement of the CBF and it is eliminated. It is usually dephased by the application of weak bipolar diffusion gradients.

In a couple of studies based on ASL techniques (Brookes et al. 2007; Kim and Kim 2005; Kim and Kim 2006; Thomas et al. 2001) attempts have been made to separate the arterial signal from the tissue signal instead of eliminating it. Dynamic ASL also gives access to the arterial CBVf by measuring CBF and arterial transit time (Barbier et al. 2001) related to the arterial CBVf by the central volume theorem (cf. paragraph 9.2.1)

Some of these approaches have lead to the measurement of the arterial CBVf, but not the total CBVf. The arterial CBVf in normocapnic rat gray matter is in the range of 0.7 to 1ml/100 g tissue (Barbier et al. 2001; Kim and Kim 2005; Kim and Kim 2006) and the arterial CBVf in human gray matter was reported to be about 2% (Brookes et al. 2007). Measurement of the total CBVf has been reported by Thomas et al (Thomas et al. 2001). CBVf values between 2 and 4% have been obtained in the gerbil brain under normothermic conditions.

BOLD

The BOLD technique (Ogawa et al. 1993) was developed for functional MRI studies but can also be used to assess the vascular reactivity in tumors following challenges with an inhaled gas (Ogawa et al. 1993). It is based on the process of neuronal vascular coupling and relies on the differences in magnetic susceptibility between oxyhemoglobin (diamagnetic) and deoxyhemoglobin (paramagnetic with respect to the surrounding tissue water), which can be regarded as an endogenous CA.

The mechanism of signal change is summarized in Fig. 0-13. As regional CBF and regional CBV are increased in an active brain region, a small signal increase is seen in the voxel of interest, caused simply by the increase in blood protons. Local oxyhemoglobin levels also rise because the increased blood flow more than compensates for any increase in oxygen extraction and consumption. As oxyhemoglobin displaces deoxyhemoglobin in an activated voxel, the local magnetic field in the voxel becomes more uniform, resulting in a greater signal in the vicinity of activated neural tissue. The resulting signal change is largely dependent on small blood vessels. The magnitude of the effects is relatively small and requires statistical analysis.

Fig. 0-13: The relationship between increased neural activity, tissue oxygen consumption, changes in regional CBF and the BOLD signal.

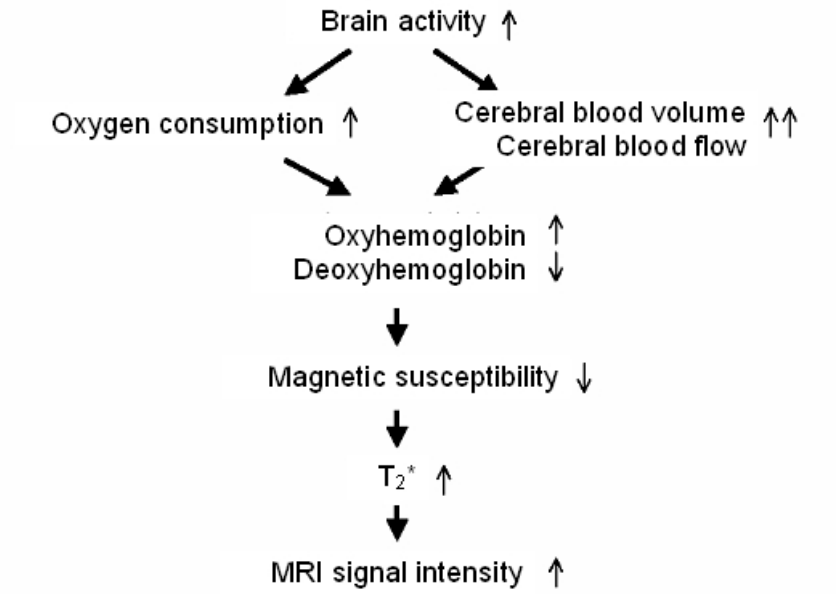

To distinguish and quantify the different mechanisms other imaging techniques such as DSC-MRI or Doppler ultrasound are used simultaneously with BOLD (Robinson 2006; Scheffler et al. 1999). As another example, the extravascular ΔR_2^* contributions to the BOLD effect have been quantified using the VASO technique (Lu and van Zijl 2005).

10. Other imaging techniques for CBV measurement

10.1. PET, SPECT and CT

Other imaging techniques that provide haemodynamic parameters include PET, single photon emission computed tomography (SPECT) and dynamic Xenon enhanced CT (Gur et al. 1989; Johnson et al. 1991).

For CBV and/or CBF measurement the ^{15}O isotop is used as a PET tracer. After intravenous administration of $H_2{}^{15}O$ or inhalation of $C^{15}O_2$ and $^{15}O_2$, and in combination with an arterial blood sampling measurement serving as AIF, the indicator-dilution model (Kety 1951) can be applied

for CBF quantification (Herscovitch et al. 1983; Raichle et al. 1983) similar to dynamic MRI. The CBV can be determined from the ratio of the radioactivity in brain to that in peripheral whole blood.

Dynamic perfusion CT is a technique that traces the first pass of an intravenous bolus of iodinated CA (Axel 1980; Kamena et al. 2007). The same analytic techniques as for dynamic MRI are used, including the need for signal deconvolution. Perfusion CT has the advantage of being widely available even in emergency departments.

Synchrotron radiation has also been used to quantify the CBV (Adam et al. 2003). The monochromatic radiation as well as the improved shape, homogeneity and flux of the radiation beam allow more accurate quantification of the attenuation induced by the iodinated CA compared to conventional radiation sources. Synchrotron radiation is only available in specialized facilities and mainly used for research.

The inherent radiation risk of these techniques prevents many repeated measures in sensitive subjects, such as children. PET and SPECT have lower spatial resolution and are less available than MRI and CT.

10.2. Optical techniques

Two photon laser microscopy

In two photon excitation fluorescence microscopy, two excitation photons from a pulsed laser combine to excite a fluorescent molecule. The resulting fluorescence emission is a photon of higher energy (typically visible light). The probability of simultaneous absorption of two photons being extremely low, the excitation will only occur at the focal point where the photon density is sufficiently high (0.1 - 10 MW/cm^2) and thereby provides a 3D resolution without out of focus blur. This optical section can be varied in depth, building up a stack of images. Radial and axial resolutions below 1 µm (depending on the wave length) are achieved. The advantage of two photon microscopy over confocal microscopy is the larger penetration depth in thick tissue such as the brain (Svoboda and Yasuda 2006) because of the use of longer wavelength excitation radiation, which at the same time reduces image deterioration.

Two photon laser scanning microscopy has been used to quantify in vivo the CBVf in the mouse cortex up to a depth of 600 µm (Verant et al. 2007). After injection of a fluorescent dye (Rhodamine B-Dextran) confined and uniformly distributed inside the blood pool, the CBVf was measured by integrating over the local intensity of the two photon fluorescence and normalizing at each depth by the maximum intensity in the image. With this technique the cortical CBVf in healthy mice was between 2% ± 0.3% and 2.4% ± 0.4% excluding larger vessels in the ROI. Figure 0-14 shows an image of the cortical microvasculature in mice obtained by this technique (Verant et al. 2007).

Fig. 0-14: 3D reconstruction of 121 images acquired in vivo from 0 to 600 µm in the parietal cortex of a nude mice. The scalebar has a length of 200 µm. Source (Verant et al. 2007)

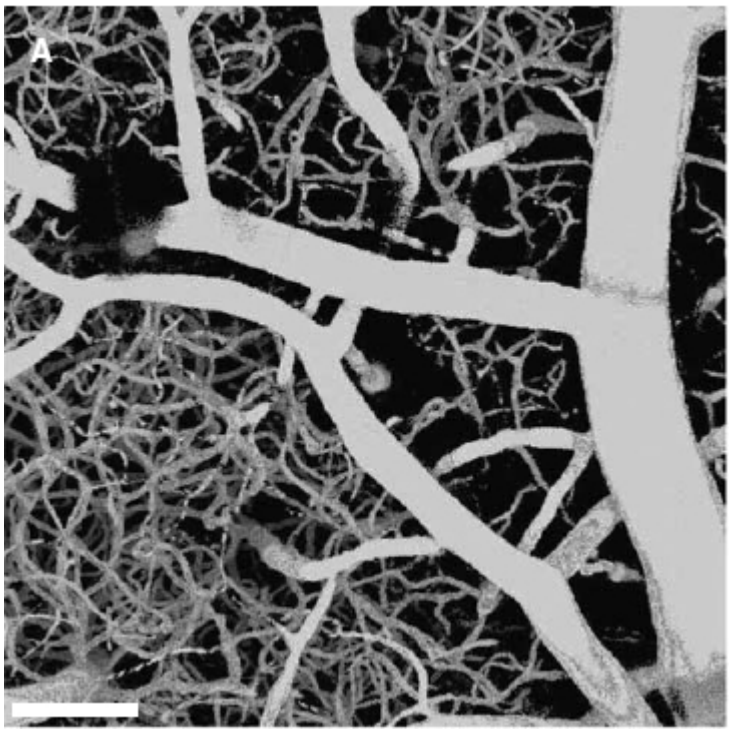

Histology

A more invasive technique for CBV estimation is histological analysis. It can be carried out on biopsies or post mortem. The advantage of histological images of tissues is that the vessel sections can be visualized individually, providing morphological parameters such as the microvascular density, the vessel radii and the intravascular distance. These parameters are

related to the blood volume, but none of these parameters can accurately represent it. To assess a 3D parameter such as the CBV or the blood volume of other tissues from histological sections, the vascular cross section area density, which is a 2D parameter, is often used as a first approximation (Weibel 1980). The technique for extracting a quantitative morphologic description of a 3D structure such as the vasculature from measurements made on 2D planar sections is called stereology.

Stereology

Microscopy is inherently a 2D technique because an unavoidable reduction in dimensionality is introduced by the sectioning process: the parameter of interest such as the vascular volume V_v (= CBV) or vessel surface S_v is only observable as a surface (vessel cross section) or a perimeter (vessel boundary), respectively, on the section. Stereology applies mathematics and probability theory to relate the observable parameters to the higher dimensional morphologic parameters of interest.

In order to extrapolate from a few plane sections to the three-dimensional object, the sections must be representative. Either the object is assumed to be completely homogeneous in such a way that any plane section is representative, or the plane sections are selected according to a specified random sampling protocol. Many stereological techniques, in addition to assuming homogeneity, also involve mathematical modeling of the geometry of the structures under investigation. The target quantities are relative densities: volume fraction, surface area per unit volume, or length per unit volume. If the reference volume is representative, total quantities such as the total capillary exchange surface area, or the total length of capillaries in an organ can be given.

In the study of the vasculature, stereology has been employed to access its three dimensional spatial framework (Dockery and Fraher 2007; Shortt et al. 2004). For example, the length density of capillaries can be calculated by modeling the capillaries as randomly oriented and curved cylinders, counting the number of profiles and determining their individual orientation (Adair et al. 1994). Pathak and coworkers (Pathak et al. 2001) showed that the vascular cross section area density correlated better with CBV measurements obtained by MRI after a stereological correction for the slice thickness.

11. Literature review: CBV in rats

The experimental CBV and CBVf values reported in Table 0-3 are obtained with different techniques and depend on the origin of the measured signals and on the available SNR. What is measured as "blood volume" by MRI techniques is in fact the blood water volume, where the NMR signal arises from, without the solid components of the blood which do not contribute to the signal. The signals used to quantify the blood volume with other techniques (PET, CT, autoradiography) do not arise from the blood water but from tracers injected into the blood pool. Histologic techniques measure the vascular surface fractions, sometimes extrapolated to "volume fractions".

Although comparison is not trivial, all average CBV or CBVf values for the whole brain reported in the literature are in the range of 1 to 5 ml/100 g or %. Often the CBV is reported relative to the CBV in white matter. This and some other CBV ratios are reviewed in Table 0-4.

Since volatile anesthetic drugs are known to be vasoactive (Archer et al. 1987; Artru 1984; Cenic et al. 2000; Cenic et al. 2002; Lorenz et al. 2001), the type of anesthesia is specified where appropriate.

Table 0-3:

Literature review: regional CBV (healthy regions) in normocapnic, normothermic, anesthetized rats. Decimal places and standard deviations are given as reported in the original work.

ROI	CBV value	unit	technique	reference
whole brain[a]	2.51	ml/100g	autoradiography[i]	(Todd et al. 1992)
whole brain[a]	2.96 ± 0.57	ml/100g	autoradiography[i]	(Todd et al. 1993)
whole brain[b]	2.77 ± 0.24	ml/100g	autoradiography[i]	(Todd and Weeks 1996)
whole brain	1.3 ± 0.1	ml/100g	autoradiography[j]	(Bereczki et al. 1992)
cortex	3.4	ml/100g	optical bolus tracking method	(Shockley and LaManna 1988)
whole brain[c]	2.40 ± 0.34	%	3D SS T_1 MRI	(Lin et al. 1997)
whole brain[c]	2.96 ± 0.82	%	3D SS T_1 MRI	(Lin et al. 1999)
whole brain[b]	3.14 ± 0.32	%	SS T_2 MRI	(Dunn et al. 2004)
cortex[b] **corpus callosum**[b] **thalamus**[b]	1.63 ± 0.18 1.22 ± 0.25 3.03 ± 0.36	ml/100g	SS T_1 MRI	(Schwarzbauer et al. 1997)
whole brain[b]	3.14 ± 0.32	%	SS ΔR_2*-MRI	(Dunn et al. 2004)
cortex[d]	4.3 ± 0.7	%	SS ΔR_2*-MRI	(Tropres et al. 2004)
striatum[e]	3.1 ± 0.7	ml/100g	SS ΔR_2*-MRI	(Julien-Dolbec et al. 2002)
striatum[f]	2.2 ± 0.6	ml/100g	SS ΔR_2*-MRI	(Julien et al. 2004)
cortex[a] **striatum**[a]	3.01 ± 0.43 2.94 ± 0.49	%	SS ΔR_2*-MRI	(Payen et al. 2000)
cortex[a] **striatum**[a]	4.07 2.87	%	SS ΔR_2*-MRI	(Tropres et al. 2001)
whole brain	1.89 ± 0.39	%	morphometry[k]	(Pathak et al. 2001)
whole brain without MV[g] **whole brain with MV**[g] **cortex**[g] **striatum**[g]	1.92 ± 0.32 4.18 ± 1.06 2.27 2.01	ml/100g	SRQCT	(Adam et al. 2003)
striatum[h]	5.6	ml/100g	SRQCT	(Adam et al. 2005)

[a]rats anesthetized with halothane

[b]rats anesthetized with isoflurane

[c]rats anesthetized with intraperitoneal pentobarbital

[d]contralateral to C6 glioma, under moderate hypoxia, rats anesthetized with halothane

[e]rats anesthetized with intraperitoneal thiopental

[f]contralateral to C6 glioma, rats anesthetized with intraperitoneal thiopental

[g]anesthetized by intraperitoneal infusion of chloral hydrate, MV = macroscopic vessels

[h]contralateral to F98 glioma (n = 1)

[i] ^{14}C-dextran labeled plasma and ^{99m}Tc labeled red blood cells

[j] ^{125}I- labeled serum albumin and ^{55}Fe labeled red blood cells

[k]with stereo correction for slice thickness, contralateral to 9L tumor

SS = steady state method

SRQCT = synchrotron radiation quantitative computed tomography

Table 0-4:

Literature review: regional CBV ratios in normocapnic, normothermic rats

ROI	CBV ratio	technique	reference
cortex/striatum[a]	1.43	SS susceptibility contrast MRI	(Payen et al. 1998)
cortex/striatum[a]	1.02	SS susceptibility contrast MRI	(Payen et al. 2000)
cortex/striatum[a]	1.42	SS susceptibility contrast MRI	(Tropres et al. 2001)
cortex/corpus callosum[b]	1.34	SS T_1 MRI	(Schwarzbauer et al. 1997)
GM/WM	1.52 ± 0.42	morphometry[d]	(Pathak et al. 2001)
parietal cortex/corpus callosum	1.47	morphometry[d]	(Pathak et al. 2003)
parietal cortex/corpus callosum	1.75 2.24	morphometry	(Schlageter et al. 1999)
cortex/striatum[c]	1.13	synchrotron radiation quantitative computed tomography	(Adam et al. 2003)

[a]rats anesthetized with halothane

[b]rats anesthetized with isoflurane

[c]anesthetized by intraperitoneal infusion of chloral hydrate

[d]with stereo correction for slice thickness, contralateral to 9L tumor

SS, steady state method; GM, gray matter; WM, white matter

Experimental studies

1. Chapter I: The Rapid Steady State T_1 method by IR-FLASH

1.1. Introduction

In this chapter, the theoretical background of the $RSST_1$ method is exposed and signal modeling is used to investigate the signal behavior during the proposed fast inversion recovery sequence. In vitro experiments on whole blood verify the conditions required by the $RSST_1$ method and demonstrate its feasibility for blood volume measurement. To determine the optimal CA dose, the signal from brain tissue is studied in an in vivo experiment on healthy rats. Two CA from Guerbet Laboratories are used: Gd-DOTA being a clinically approved small molecular size CA, and P760 an experimental intermediate size CA with a higher longitudinal relaxivity. Both CAs remain confined in healthy microvasculature. The CBVf is mapped in healthy rats under normocapnia and induced hypercapnia, and the measured regional CBVf is compared with reported values. Finally, factors that limit the accuracy of the CBVf measurement are evaluated, and the relative error is estimated.

French Introduction

Chapitre I : La méthode stationnaire Rapide par effet T_1 utilisant IR-FLASH

Dans ce chapitre, la théorie de la méthode stationnaire par effet T_1 "Rapid-Staedy state T_1 ($RSST_1$) est présentée. C'est une méthode rapide proposée pour mesurer le Volume Sanguin Cérébral (VSC) absolu c'est-à-dire la fraction volumique du sang dans un voxel, noté fVSC. Après une modélisation du signal dans le cas d'un système de spin soumis à une séquence Inversion Récupération rapide et une simulation du signal pour différents paramètres de la séquence, des expériences de faisabilité in vitro sont réalisées sur des échantillons de sang prélevé avant ou après injection d'un AC paramagnétique. Les premières expériences in vivo ont été réalisées chez le rat sain pour définir la dose à injecter nécessaire pour mesurer la fVSC. Deux AC paramagnétiques des Laboratoires Guerbet ont été utilisés, le Gd-DOTA, AC

largement utilisé en clinique et le P760, AC expérimental ayant une forte relaxivité r_1, 5 fois supérieure à celle du Gd-DOTA à 2.35T. Dans le cerveau sain ces deux AC sont intra-vasculaires. Les mesures du VSCf sont réalisées chez le rat sain en normocapnie et en hypercapnie. Dans ce dernier cas, des variations du VSC ont été détectées et ont permis d'évaluer la sensibilité de la méthode. Dans ce chapitre sont également décrits, les effets de certains paramètres sur la précision de la mesure comme les effets de relaxation transversale, de susceptibilité magnétique ou encore les effets de l'échange de l'eau entre les deux milieux intra et extravasculaires. Pour chacun de ces effets, l'erreur sur la mesure est donné.

1.2. Theory

1.2.1. The two compartment model

In this work, a two compartment model of the brain tissue without water exchange is used:

$$V_{total} = V_{iv} + V_{ev}$$

where V_{total} denotes the total volume of the voxel, and V_{iv} and V_{ev}, denote the volume of the intra- and extravascular compartment, respectively.

The CBVf is the relative volume fraction of the intravascular compartment and corresponds approximately to the relative fraction of the intravascular water protons with respect to the total number of water protons of the intra- and extravascular compartment:

$$CBVf = \frac{V_{iv}}{V_{iv} + V_{ev}} \approx \frac{n_{iv}}{n_{iv} + n_{ev}},$$

where n_{iv} and n_{ev} denote the number of water protons of the intra- and extravascular compartment, respectively.

In order to distinguish between the water protons of the two compartments, one must discriminate between MR signals arising from water in the intra- and extravascular compartments. To do so, different relaxation times in the two compartments are necessary. The $RSST_1$ method exploits the longitudinal relaxation differences between the intra- and extravascular compartments after homogeneous distribution of an intravenously injected blood pool CA. It reduces exclusively the relaxation times of the intravascular compartment, while the extravascular compartment remains characterized by long relaxation times.

The net magnetization at thermal equilibrium M_0 results from the relative alignment of magnetic dipole moments in an external magnetic field B_0 and is proportional to the difference of the relative numbers of spins in the two possible energy states:

$$M_0 = \frac{\gamma^2 \hbar^2 B_0}{4 k_B T} n_{ps} \quad ,$$

where γ is the gyromagnetic ratio of hydrogen, ħ is the reduced Planck constant, B_0 is the external magnetic field strength, k_B is the Boltzmann constant, T is the absolute temperature of the system and n_{ps} is the total number of spins of the system. In tissue and in particular in blood, these spins are mainly water protons. So the thermal equilibrium magnetization of a compartment is proportional to the concentration of water protons in this compartment, and the following ratio defines the CBVf:

$$CBVf \approx \frac{n_{iv}}{n_{iv} + n_{ev}} = \frac{M_{0iv}}{M_{0iv} + M_{0ev}} .$$

M_{0iv} and M_{0ev} are the equilibrium magnetizations of the intra- and extravascular compartments, respectively.

A heavily T_1 weighted fast inversion recovery (IR) gradient echo sequence is used to acquire a signal corresponding to the thermal equilibrium magnetization of the blood compartment M_{0iv} relaxing with a short T_1:

$$S_{iv} = S_{0iv} ,$$

while suppressing the signal from the extravascular compartment characterized by a long T_1:

$$S_{ev} \approx 0 .$$

S_{iv} and S_{ev} symbolize the signals originating from the intra- and the extravascular compartment, respectively. In this work, the subscript "0" is always used to denote a signal acquired when the magnetization is at thermal equilibrium, i. e. using a long TR and a TE ≈ 0.

The resulting arbitrary signal intensity S_{0iv} originating from the blood compartment is normalized by the total signal S_0 of the voxel being the sum of the signals at thermal equilibrium originating from the intra- (S_{0iv}) and the extravascular (S_{0ev}) compartment

$$S_0 = S_{0iv} + S_{0ev} .$$

This S_0 signal is acquired by an IR or saturation recovery gradient echo sequence with sufficiently long TR to allow full relaxation of both compartments prior to acquisition.

The ratio of these signals corresponds to the CBVf:

$$S^{norm} = \frac{S_{0iv}}{S_0} = \frac{S_{0iv}}{S_{0iv} + S_{0ev}} = \frac{M_{0iv}}{M_{0iv} + M_{0ev}} \approx CBVf ,$$

where S^{norm} is called the normalized signal.

The major assumptions of the $RSST_1$ method are:

1. complete suppression of the signal of the extravascular magnetization relaxing with a long T_1
2. acquisition of an intravascular signal corresponding to the magnetization at thermal equilibrium after injection of a CA reducing the T_1 of this compartment
3. no T_2 weighting
4. no water exchange between compartments

In this study, the validity and the limits of these assumptions in conjunction with Gd-DOTA and P760 are evaluated, and corrections for incomplete extravascular signal suppression, R_2-attenuation and water exchange between compartments are given.

1.2.2. Spin fraction or volume fraction?

In this work the normalized signal S^{norm} is said to correspond to the vascular volume fraction

$$S^{norm} \approx CBVf = \frac{V_{iv}}{V_{total}} = \frac{V_{iv}}{V_{iv} + V_{ev}} .$$

Strictly speaking, S^{norm} corresponds to the vascular spin fraction $S^{norm} = \frac{n_{iv}}{n_{total}} = \frac{n_{iv}}{n_{iv} + n_{ev}}$,

where n_{total} is symbolizing the total number of spins in the voxel. To convert from spin fraction to physical volume

$$CBVf = \frac{V_{iv}}{V_{total}} ,$$

the slight differences in spin density and water content between tissue and blood must be considered.

$$\frac{V_{iv}}{V_{total}} = \frac{n_{iv}}{n_{total}} \frac{\rho_{tissue}}{\rho_{blood}} \frac{w_{tissue}}{w_{blood}} = \frac{n_{iv}}{n_{total}} \frac{\rho_{tissue}}{\rho_{blood}} \lambda ,$$

where ρ_{tissue} and ρ_{blood} are the densities and w_{tissue} and w_{blood} are the water contents of tissue and blood, respectively, and λ is the brain-blood partition coefficient. In this work, "tissue" refers to the sum of the intra- and extravascular compartments.

With the values for density and water content cited by Herscovitch and Raichle (Herscovitch and Raichle 1985) (w_{tissue} is assumed to be 80 g/100g, a value within the reported ranges of white and gray matter tissue), the factor $\frac{\rho_{tissue}}{\rho_{blood}}\lambda$ is about 0.98. The relative error introduced by declaring the vascular spin fraction as vascular volume fraction is:

$$\frac{\rho_{blood}}{\rho_{tissue}}\frac{1}{\lambda} - 1 = 0.016.$$

As we will show later in this chapter, this underestimation of 1.6% is negligible compared with the under- and overestimations induced by the R_2 - and water exchange effects. Moreover, the water contents of blood and tissue used in the calculation of λ are mean values over the whole cerebral tissue, and are subject to change with hematocrit, vascular permeability, edema formation etc (Herscovitch and Raichle 1985). The uncertainty about the exact value of λ is much greater than the error induced by approximating the factor to unity. It is therefore acceptable to use the normalized signal value S^{norm} as vascular volume fraction. From now on we define:

$$S^{norm} = CBVf\ .$$

To convert the normalized signal corresponding to the vascular volume fraction into a CBV in units of ml blood/100g tissue the vascular signal has to be multiplied by the factor:

$$\frac{\lambda}{\rho_{blood}}100 \approx 93.75.$$

A numeric example:
a S^{norm} of 0.03 corresponds to a CBVf of 0.0295 ml/ml and to a CBV of 2.81 ml/100g tissue.

1.2.3. Principle of the $RSST_1$ method

After an inversion pulse (π), the tissue magnetization is inverted and relaxes back to its equilibrium value. At a particular time T_{inv} after the inversion pulse, the longitudinal tissue magnetization M_z is null. In brain tissue, the intra- and the extravascular compartment have

similar longitudinal relaxation times in the order of 1 to 2 seconds. When using a rapid IR sequence with a short TR with respect to the T_1 of brain tissue, a dynamic equilibrium installs after a couple of inversions, and suppression of the tissue signal can be achieved for a broad range of T_1 values. This will be shown by signal modeling and has also been confirmed experimentally.

For the same sequence, signals from compartments with shorter T_1 relaxation times in the order of TR will persist. The aim is not only to create a large T_1 difference between the intravascular (blood) and the extravascular compartment, in order to discriminate between the signals of these two compartments, but also to obtain a signal from the intravascular compartment which is proportional to its proton density and consequently to its volume. The signal intensity of the intravascular compartment is proportional to the number of intravascular water protons when they have a relaxation time < T_{inv} /5 and consequently are at thermal equilibrium at acquisition.

If the extravascular signal is completely nulled, the total tissue signal S is proportional to the intravascular water protons:

$$S = S_{iv} + S_{ev} = S_{0iv} + 0$$

When $S_{iv} = S_{0iv}$ and $S_{ev} = 0$, S is called the $RSST_1$ signal. The term $RSST_1$ conditions refers to an intravascular $T_1 < T_{inv}/5$ and an extravascular $T_1 >> TR$.

Our approach to measuring CBVf was to increase the intravascular concentration of a blood pool CA until the tissue signal amplitude becomes independent of concentration, which can be regarded as signal saturation. In a first approach, the relaxation of the extravascular compartment is considered to remain unchanged after CA injection.

1.2.4. A steady state MRI method?

Conventional steady state MRI methods for CBV mapping are based on a constant CA concentration in blood resulting in a constant signal, which is referred to as steady state signal, as opposed to the signal variation induced by the first passage of a CA bolus through the imaged voxel. With these methods, the steady state signal does not necessarily correspond to a tissue magnetization at thermal equilibrium.

The term "steady state" (= SS) in the acronym $RSST_1$ refers to a constant vascular signal corresponding to the blood magnetization at thermal equilibrium and is independent of the longitudinal relaxation of blood. Although the CBVf measurement in this study is carried out after CA injection when the CA concentration is homogeneous in the vascular compartment and approximately constant in time, instead of during the first bolus passage, the $RSST_1$ method is not based on a constant CA concentration. As will be shown in chapter VI, the $RSST_1$ method can also be used for dynamic imaging, with a tissue signal that changes due to CA accumulation in the extravascular compartment. However, the $RSST_1$ method requires a constant intravascular signal corresponding to the thermal equilibrium magnetization of the blood, even when used for dynamic imaging, and can therefore be regarded as a variant of the conventional steady state MRI methods.

1.3. Signal modeling

1.3.1. Longitudinal magnetization as a function of TR, T_{inv} and T_1

A sequence with a single inversion RF pulse followed by a train of short-TR FLASH segments acquiring the entire K-space to form one image was published as single point or snapshot IR-FLASH (Haase 1990; Larsson et al. 1994).

This sequence is illustrated in Fig. I-1 and has been used for the experiments described in this chapter. The FLASH module consists of a series of low angle readout pulses (α) and a gradient echo acquisition scheme enabling a short repetition time TR_{FLASH} between the α-pulses. The whole K-space is acquired after the π-pulse, starting with the $k_y = 0$ line at a particular T_{inv} and alternating positive and negative K-space lines from low to high k_y values (center out).

Fig. I-1: the inversion-recovery-Fast Low Angle SHot (IR-FLASH) sequence

a: the imaging module FLASH is started at a particular time T_{inv} after the inversion pulse, beginning with the acquisition of the central K-space line (center out). TR is the overall repetition time between two inversion pulses.

b: the pulse sequence timing diagram shows that the inversion pulse is nonselective. The FLASH module is a gradient echo sequence having a repetition time TR_{FLASH} = 10.5 ms. It is repeated Nk times defining the spatial resolution of the resulting image.

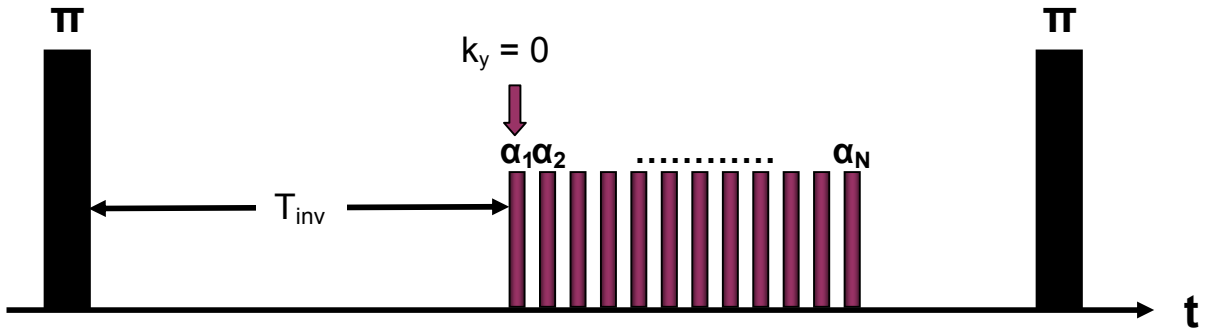

a

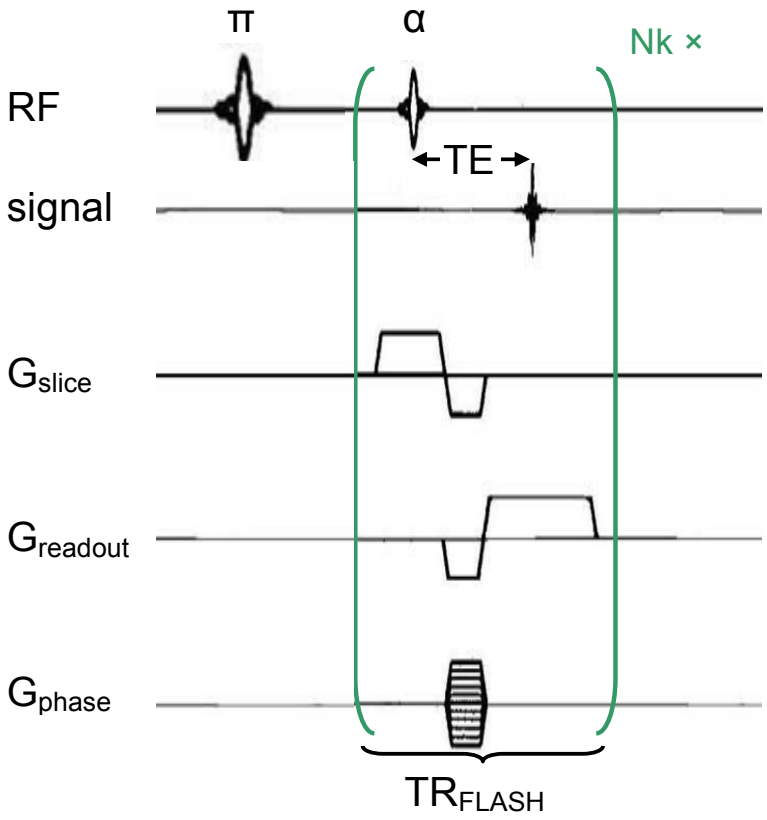

b

The signal evolution during this pulse sequence can be modeled (Jivan et al. 1997). The following equation for the longitudinal magnetization M_z is an approximation for low α flip angles, when dynamic equilibrium has installed.

$$\frac{M_z(T_{inv}, TR, T_1)}{M_0} = 1 - \frac{2\exp\left(-\frac{T_{inv}}{T_1}\right)}{1+\exp\left(-\frac{TR}{T_1}\right)} \qquad \textbf{Eq. I-1}$$

Suppression of the longitudinal tissue magnetization can be achieved for

$$T_{inv}(TR, T_1) = T_1 \ln 2 - T_1 \ln\left[1+\exp\left(-\frac{TR}{T_1}\right)\right]. \qquad \textbf{Eq. I-2}$$

Using Eq. I-1, the diagram in Fig. I-2a shows M_z in function of T_1 plotted for different T_{inv} and a fixed TR of 750 ms. For T_1 > TR, M_z approaches zero, most rapidly for a T_{inv} of about 325 ms. All tissues with T_1 > 1 s can therefore be effectively suppressed with a couple TR/T_{inv} such as 750 ms/325 ms.

The exponential function $\exp\left(-\frac{TR}{T_1}\right)$ can be expanded into a Taylor series and approximated to $1-\frac{TR}{T_1}$ for T_1 >> TR. Eq. I-2 then becomes:

$$T_{inv}(TR, T_1) = T_1 \ln 2 - T_1 \ln\left[2-\frac{TR}{T_1}\right].$$

This implies:

$$T_{inv}(TR, T_1) = T_1\left\{\ln 2 - \ln\left[2\left(1-\frac{TR}{2T_1}\right)\right]\right\} \text{ and}$$

$$T_{inv}(TR, T_1) = -T_1 \cdot \ln\left(1-\frac{TR}{2T_1}\right).$$

Substituting $1-\frac{TR}{2T_1}$ by $\exp\left(-\frac{TR}{2T_1}\right)$ results in:

$$T_{inv}(TR) = \frac{TR}{2}$$

In the limit of T_1 >> TR, the signal is suppressed at $T_{inv} = \frac{TR}{2}$. However, for TR = 750 ms and realistic tissue T_1, the best suppression is obtained at T_{inv} = 325 ms as shown in Fig. I-2a.

By plotting T_{inv} as a function of T_1 for different TR using Eq. I-2 such as in Fig. I-3, it can be seen that T_{inv} approaches $\frac{TR}{2}$ more rapidly for shorter TR. Therefore, the shorter the TR is with respect to T_1, the wider the range of T_1 that can be suppressed.

Figure I-2b is a zoomed part of Fig. I-2a for small T_1. For tissues having a $T_1 < T_{inv}/5$ a signal that corresponds to the equilibrium magnetization M_0 can be acquired at t = T_{inv}. The sequence acts like a low-pass filter for T_1. In this plot, TR was set to 750 ms. Using a T_{inv} of 325 ms to suppress the extravascular signal (1 s < T_1 < 2 s) requires a blood T_1 < 65 ms in order to acquire a blood signal corresponding to thermal equilibrium. For an IR-FLASH sequence with an analogue couple of parameters TR/T_{inv} = 500 ms/225 ms, a T_1 < 45 ms has to be achieved for the blood compartment.

Fig. I-2: Longitudinal magnetization M_z for an IR-FLASH sequence with TR = 750 ms in function of T_{inv} and of T_1. For T_{inv} = 325 ms, signal suppression occurs for tissues with long T_1 (a) and an equilibrium signal can be measured from tissues with $T_1 < T_{inv}/5$ (b). The sequence acts like a low-pass filter for T_1.

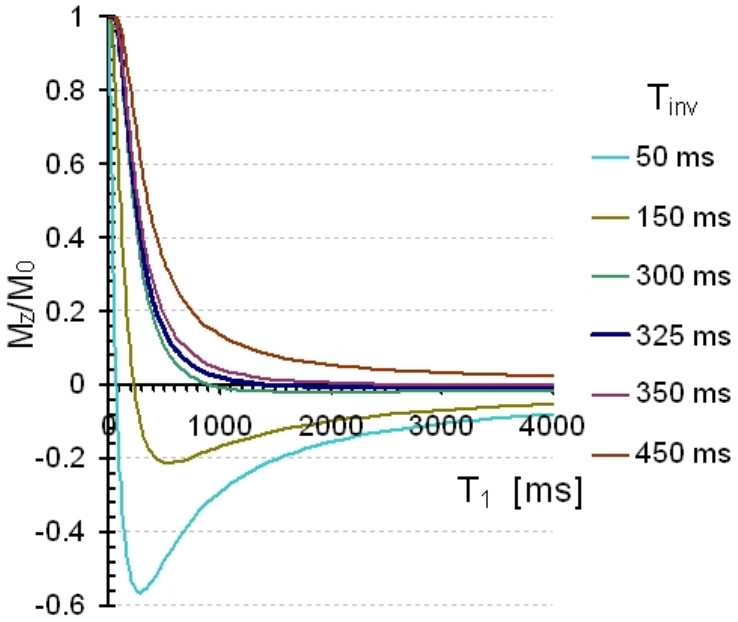

a

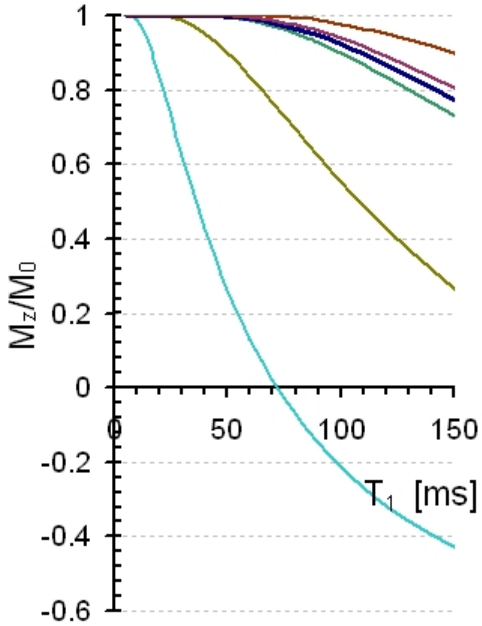

b

Fig. I-3: The T_{inv} for which the signal is nulled is plotted as a function of T_1 and TR. The shorter the TR is with respect to T_1, the wider the range of T_1 that can be suppressed.

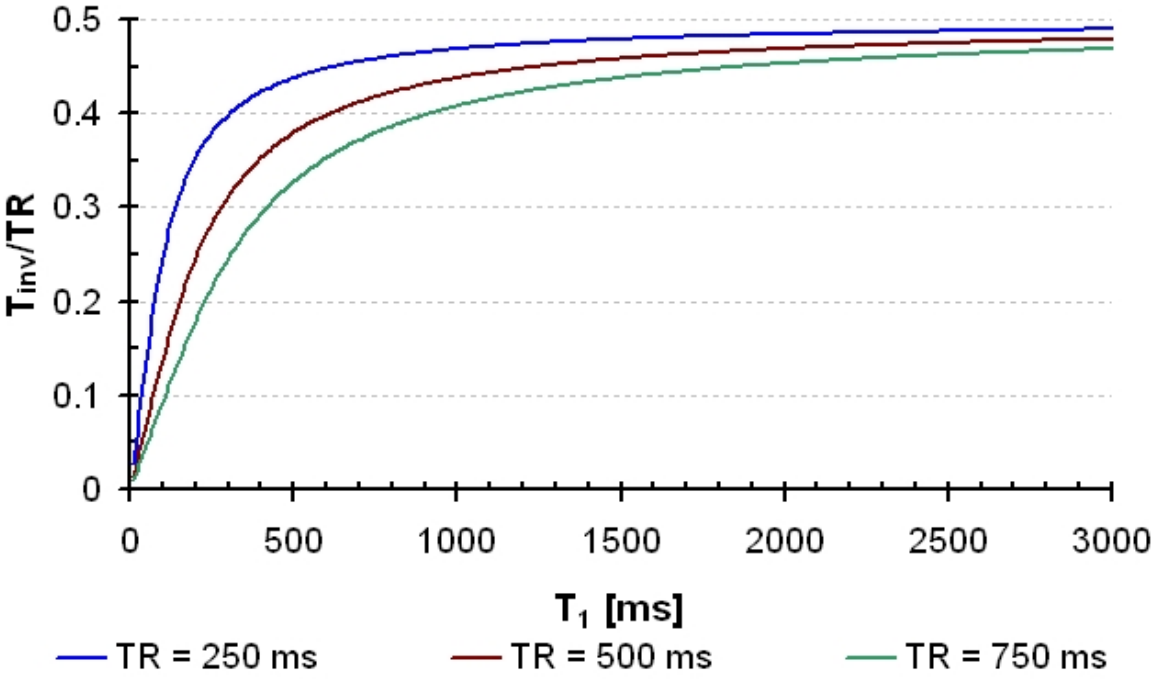

1.3.2. Longitudinal magnetization versus time during the IR-FLASH sequence

In Fig. I-4 the evolution of the longitudinal magnetization M_z/M_0 during the sequence is plotted for T_{1iv} = 50 ms, representative for the blood pool after CA injection, and for T_{1ev} = 1200 ms, representative for the extravascular compartment, when dynamic equilibrium has installed after a couple of repetitions. Here the exact equations (Jivan et al. 1997) are used with Nk = 16 α-pulses, α = 10° and TR_{FLASH} = 10 ms to show how the signal is perturbed by the successive α-pulses of the FLASH module used to acquire the k-space lines. Although this is of benefit for the suppression of the extravascular magnetization, the blood magnetization is at thermal equilibrium only when the k_y = 0 line is acquired. After Nk = 16 successive α-pulses with the FLASH timing parameters above, M_z of the blood compartment is reduced to 0.938 M_0 and after Nk = 32 α-pulses the M_z is 0.936 M_0. These values are the results of Eq. [4] in the paper by Jivan at al (Jivan et al. 1997), where $M_z^{(Nk\alpha+)}$ is the longitudinal magnetization after Nk α-pulses and $M_z^{(\alpha-)}$ is the magnetization at t = T_{inv} before the first α-pulse is applied. This equation is:

$$\frac{M_z^{(Nk\alpha+)}}{M_0} = \frac{M_z^{(\alpha-)}}{M_0}\left[\exp\left(\frac{-TR_{FLASH}}{T_1}\right)\cos\alpha\right]^{Nk} + \left[1-\exp\left(\frac{-TR_{FLASH}}{T_1}\right)\right]\left\{\frac{\left[\exp\left(\frac{-TR_{FLASH}}{T_1}\right)\cos\alpha\right]^{Nk}-1}{\exp\left(\frac{-TR_{FLASH}}{T_1}\right)\cos\alpha-1}\right\}$$

The difference between M_z for Nk = 16 and M_z for Nk = 32 is small because a dynamic equilibrium installs between the 16th and the 32 α-pulse. However, the M_z at the acquisition of the central k-space line contributes most to the signal intensity seen in the final image.

Fig. I-4: Longitudinal magnetization M_z in function of time during an IR-FLASH sequence with TR = 750 ms plotted for two representative T_1: T_1 = 1200 ms for the extravascular compartment and T_1 = 50 ms for the blood after CA injection. The symbol π denotes the inversion pulse at t = 0. α_1 to α_{16} are the successive low flip angle readout pulses (here α = 10°). The central k-space line is acquired at t = T_{inv} = 325 ms when the extravascular signal is nulled and the blood signal is at thermal equilibrium.

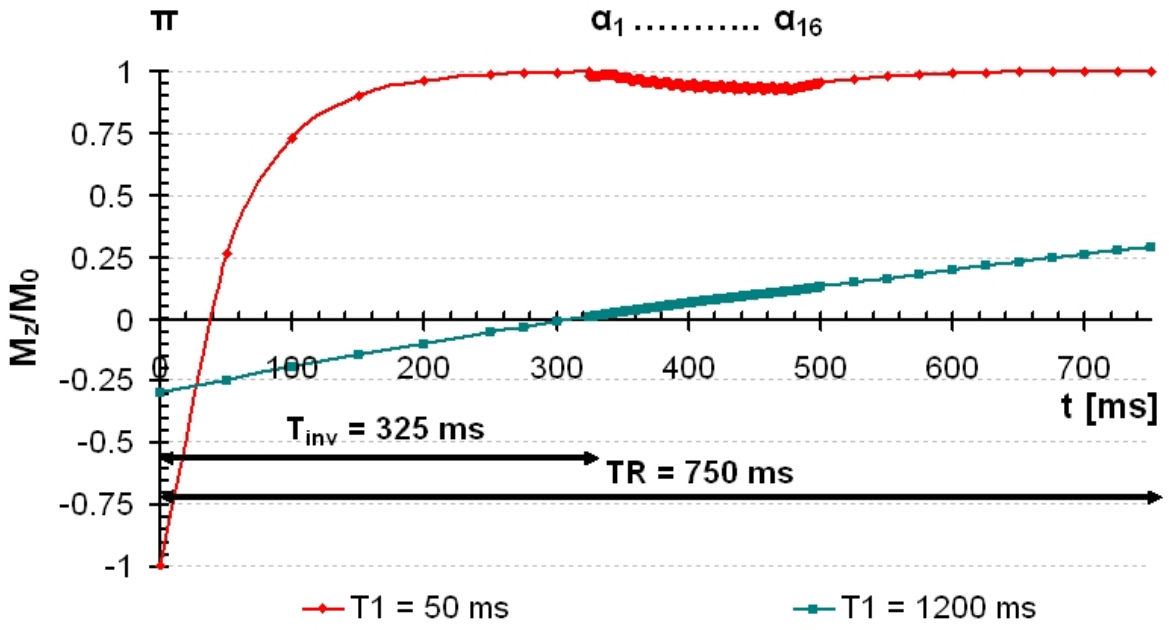

1.3.3. Blood signal as a function of the administered CA dose

T_1 based acquisitions require positive CAs with strong r_1 relaxation enhancement and minor accompanying r_2 relaxation effects, even at high magnetic fields where r_2/r_1 is generally higher. Since the r_2 relaxivity of all CAs is always higher than the r_1 relaxivity, the R_2-attenuation has to be minimized. Fast MRI acquisition techniques that acquire the entire k-space in a single-shot during the R_2^* decay after a single excitation pulse, such as EPI, are always T_2 weighted. Therefore a multiple-shot gradient echo sequence was preferred and the R_2-attenuation was minimized by a short TE. In this work, a TE of 3.2 ms was used unless another value is specified.

Both CAs used in this study are Gd^{3+} chelates. Gd-DOTA has a r_1 relaxivity of 3.37 $s^{-1}mM^{-1}$ and a r_2 relaxivity of 4.33 $s^{-1}mM^{-1}$ in plasma at 2.35T and 37°C. For P760 r_1 = 19.7 $s^{-1}mM^{-1}$ and r_2 = 33.9 $s^{-1}mM^{-1}$ under the same conditions (Fonchy et al. 2001). The Gd^{3+} concentration in the blood pool just after injection decreases at a slower rate for P760 than for Gd-DOTA. This is because, after intravenous injection, the pharmacokinetics of P760 is characterized by a lower diffusion into extracerebral tissues, but by a similarly rapid renal clearance from the blood pool compared to Gd-DOTA (Corot et al. 2002; Port et al. 1999). In normal brain with an intact BBB, the capillaries are not permeable for CA such as Gd-DOTA and P760, except for the choroids plexus which exhibits elevated permeability as a result of its involvement in cerebrospinal fluid production.

When a CA is administered intravenously at a particular dose (measured in mmol/kg), its blood concentration (mmol/L = mM) and its r_1 and r_2 relaxivities determine the relaxation rates R_1 and R_2 of the blood compartment via

$$R_i = R_{i0} + r_i \cdot [CA],$$

where i = 1, 2 and [CA] is the blood concentration of the CA. The total blood volume of rats ranges from 50 to 70 ml per kilogram body weight (Lee and Blaufox 1985). The blood relaxation rates R_1 and R_2 were computed as a function of the administered dose for total blood volumes of 50 and 70 ml/kg with the relaxivities mentioned above for plasma at 2.35T. The T_1 and T_2 of blood without CA, was set to 1350 ms and 200 ms.

The blood signal S_{iv}/S_{0iv} that can be acquired by the IR-FLASH sequence with $TR/T_{inv}/TE$ = 750 ms/325 ms/3.2 ms in function of the injected dose of Gd-DOTA and P760 is plotted in Fig. I-5 for

blood concentrations obtained just after injection. S_{iv}/S_{0iv} was computed using Eq. I-1 for the longitudinal magnetization multiplied by $\exp(-R_2 \cdot TE)$ to account for the R_2-attenuation. The signal corresponding to thermal equilibrium was set to $S_{0iv} = 1$. The factor sin(α) was omitted.

A magnetization at equilibrium M_{0iv} can theoretically be attained for CA doses that decrease the blood T_1 below $T_{inv}/5$, which is the case for Gd-DOTA doses above 0.2 mmol/kg and for P760 doses above 0.04 mmol/kg. However, the R_2-attenuation is already about 10 % at these doses and increases with increasing doses. The only way to decrease the R_2-effect is to use shorter TE times.

In practice, higher doses can be injected to obtain a steady state regime. This is to compensate for the loss of CA from the blood pool due to diffusion into extracerebral tissue, which starts immediately after CA injection, especially for Gd-DOTA, and due to renal clearance.

Fig. I-5: Modeling of the blood signal in an IR-FLASH experiment with $TR/T_{inv}/TE$ = 750 ms/325 ms/3.2 ms at 2.35T for different doses of Gd-DOTA and P760. In rats, the CA distribute in 50 to 70 ml blood per kg body weight.

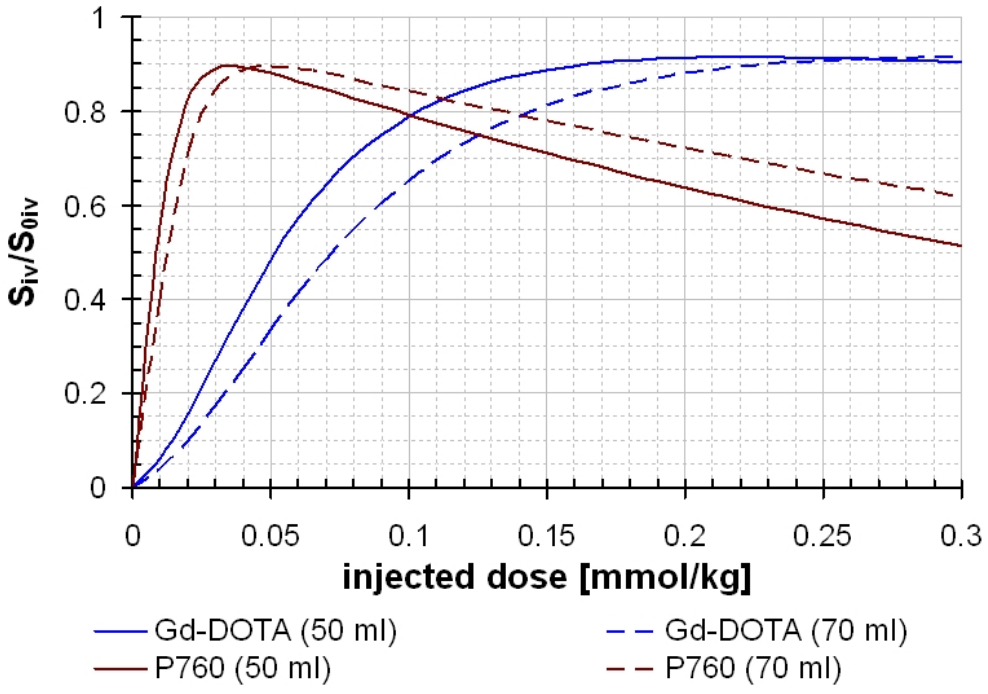

1.4. In vivo experimental setup (general)

1.4.1. Animals

All procedures related to animal care strictly conformed to the Guidelines of the French Government (decree 87-848, October 19, 1987, licenses 38 07 19 and A 38 516 10004).

Two rat strains, Fischer and Wistar, were used for CBVf mapping, because later experiments are carried out using two different tumor models, which only develop in the syngeneic host in which it had been originally induced. All rats were initially anesthetized with 5% isoflurane in a 2:1 mixture of air:O_2 gases. Once the animals were fully anesthetized, the isoflurane level was reduced to 2.5% for surgical preparation consisting of femoral vessel catheterization. The femoral artery was catheterized for blood pressure monitoring and blood gas sampling and the femoral vein was catheterized for fluid and CA administration. The arterial blood pressure and rectal temperature were recorded with a LabVIEW graphical interface (Laboratory Virtual Instrumentation Engineering Workbench, National Instruments).

In the magnet, the animal was positioned prone in a special plastic frame with its head secured by means of a bite bar and ear pieces. The animal's rectal temperature was maintained at 37.5°C with a warm circulating water pad, a rectal thermo-coupled probe and a feed-back unit. During MR experiments the isoflurane levels were reduced to 1.5 to 2%. Femoral arterial blood gas levels, hemoglobin, pH, and oxygen saturation were measured and corrected for rectal temperature before each CA injection with the use of a pH/blood gas analyzer (Radiometer Copenhagen ABL^{TM} 510) to confirm full oxygenation and a normocapnic arterial carbon dioxide tension ($PaCO_2$) (40 ± 5 mm Hg) as well as normal hematocrit (> 35%). At the end of the experiment, the rats were sacrificed by an intravenous overdose of chloral hydrate.

1.4.2. MRI equipment

Unless specified otherwise, all studies in this work were performed at B_0 = 2.35 T on a superconducting horizontal bore magnet of 40 cm diameter (Bruker Spectrospin, Wissenbourg, France), equipped with actively shielded gradient coils (Magnex Scientific Ltd, Adingdon, UK)

and interfaced with a SMIS console (Guildford, UK). The gradient system has a maximum gradient strength of 1500 Hz/mm and a rise time of 500 µs.

Earlier studies were carried out using a 30 mm diameter circular surface coil placed horizontally above the rats head for emission and detection. With this setup transverse planes were studied at a depth at which the sensitivity of the surface coil is still homogeneous. The full width at half maximum (FWHM) of the magnitude RF spectrum, which is proportional to $(\pi T_2^*)^{-1}$ and characterizes the inhomogeneity of the B_0 field, was in the order of 65 Hz after a global shimming procedure covering the entire brain, and of about 25 Hz after a shim performed on a 2 mm thick plane.

Later studies were carried out using a homogeneous birdcage coil of 12 cm inner diameter for emission and a separate decoupled double loop circular surface coil of approximately 3 cm diameter positioned above the rat's head for detection. With this setup a FWHM of about 50 Hz could be achieved for a volume covering the whole rat head (80 mm in the longitudinal (z) direction). For a 2 mm thick coronal slice the FWHM was in the order of 20 Hz.

1.4.3. Imaging protocol

Spin echo pilot images were first obtained to localize a coronal or transversal slice at the level of the basal ganglia. Magnetic field homogeneity was than adjusted on this slice. One image with anatomical contrast was obtained with a T_2 weighted spin echo sequence (TR/TE = 2000 ms/80 ms) and an acquisition matrix of 128 $\times$ 64. The FOV varied between 28 and 32 mm^2. The IR-FLASH sequence was used with the same FOV, a matrix size of 128 × 64, a slice thickness of 2 mm, a TE of 3.2 ms, a flip angle $\alpha = 10°$, a TR/T_{inv} = 3500 ms/325 ms, a TR_{FLASH} = 10.5 ms and a number of averages = 8. With these parameters a mixed T_1 and T_2 weighted tissue contrast is achieved allowing to distinguish anatomical details. This acquisition is referred to as high resolution image.
After acquisition of the T_2 weighted spin echo and the high resolution IR-FLASH image, the transmitter frequency and gain as well as receiver gain were kept constant for all acquisitions related to the CBVf measurement for each rat. The sequence parameters common to all single slice IR-FLASH acquisitions used for CBVf measurement are: TE = 3.2 ms, $\alpha = 10°$, slice thickness = 2 mm, matrix size 32× 32 and a FOV identical to that of the T_2 weighted spin echo and high resolution image IR-FLASH image. For spin inversion a nonselective adiabatic

sech/tanh RF pulse of 4 ms duration was used. The homogeneous range of the RF coil covered the upper part of the animals body including major cervical arteries, thus avoiding the inflow of noninverted blood proton spins. The acquisition starts with the central line of k-space, so the magnetization at the low k values is acquired at the nulling T_{inv}.

1.5. Preliminary experiments

1.5.1. T_1 determination of brain tissue

To verify the conditions necessary for signal suppression of the extravascular compartment before CA injection, the T_1 of water protons in the cerebral parenchyma of rats was measured in vivo with the use of the snapshot IR-FLASH sequence with an adiabatic hyperbolic secant π-pulse of 4 ms duration and slice selective α-pulses of 10°. The timing parameters for the Wistar rats were TR = 10 s with 13 different T_{inv} (range 50 ms to 9 s), number of averages = 4, and for the Fischer rats TR = 20 s with 15 different T_{inv} (range 15 ms to 15 s), number of averages = 2. The FOV was 32 × 32 mm^2 and the acquisition matrix 32 × 32, giving an in plane spatial resolution of 1 × 1 mm^2 at acquisition. The duration of the acquisitions were 9 to 10 min. Transversal planes with a slice thickness of 2 mm were imaged for the Wistar strain, and coronal planes of 1 mm for the Fischer strain. ROIs were drawn manually on the corpus callosum for white matter, and on the temporal (transverse planes) and parietal (coronal planes) cortex for gray matter. A ROI covering the whole brain slice was used for a global value. The signals from all pixels within the ROIs were averaged prior to fitting Eq. I-1 to the peak amplitudes using a least squares fit under Excel, leaving the inversion factor (= 2 in Eq. I-1) as an adjustable parameter to account for imperfect inversions in addition to the fitted parameters M_0 and T_1.

1.5.2. T_1 determination of blood

To ensure signal suppression from native (without exogenous CAs) blood, and a T_1 < 325 ms/5 = 65 ms after P760 injection, in vitro T_1 measurements of rat blood were performed at ambient temperature 21 ± 1°C. In vitro rather than in vivo measurements were preferred to avoid partial volume effects, and to use a standard spectroscopic IR sequence. The blood was sampled from

the femoral artery into heparinized syringes before and one minute after CA injection. The circular surface RF coil was used for transmission and reception and the syringes were positioned horizontally parallel to B_0. The spectroscopic IR sequence consisted of an adiabatic inversion and a 90° square hard readout pulse of 300 µs leading to a higher precision. In this case, the adiabatic RF pulse was not used for homogeneous excitation, but to avoid the systematic recalibration of the pulse for each new sample.
For comparison, the native blood T_1 was also measured with the snapshot IR-FLASH sequence on a 2 mm thick transverse slice through the syringe, using $\alpha = 10°$.

A TR of 20 s was used for both sequences and the eleven T_{inv} used to measure the T_1 of native blood ranged from 20 ms to 6 s. The T_1 of tap water was measured with the same timing parameters. The T_{inv} used for blood sampled after CA injection ranged from 2 ms to 1 s, and the TR was 2 s, being greater than $5 \cdot T_1$. Eq. 0-2 was fitted to the area under the peak of the signals acquired with the spectroscopic IR-sequence and Eq. I-1 was fitted to the peak signal amplitude acquired with the snapshot IR-FLASH sequence using a three parameter least squares fit. The three adjusted parameters were the inversion factor, M_0 and T_1.

1.5.3. In vitro blood volume experiment

An in vitro "blood volume" measure was carried out using the same syringes containing blood sampled prior (native blood) and one minute after injection of 0.1 mmol/kg P760. By acquiring the blood signal S_{iv} using the $RSST_1$ method, and normalizing it by a proton weighted acquisition S_{0iv}, the ratio S_{iv}/S_{0iv} should reflect the "blood volume" in the syringe, i. e. 100%.

The syringes were placed horizontally and parallel to each other and to B_0 at the same distance from the circular surface coil used for transmission and reception (Fig. I-6). To image the blood samples obtained from one rat simultaneously, the IR-FLASH sequence was used with a spatial resolution of $1 \times 1 \times 2$ mm^3 with two couples of TR/T_{inv} and a TE = 3.2 ms. The FWHM was in the order of 60 Hz (magnitude) after global shimming.

A TR/T_{inv} of 750 ms/325 ms was used to verify the efficiency of suppression of native blood and whether a signal corresponding to fully relaxed magnetization can be obtained from blood sampled after CA injection.
The signals acquired with these imaging parameters are referred to as:

S_{pre} when they originate from blood without CA, and as
S_{post} when they originate from blood drawn after CA administration.
In this experiment, 120 acquisitions corresponding to 90 s were performed, from which the first 20 were discarded before averaging.
S_{pre} is expected to be ≈ 0, and S_{post} is expected to be the signal S_{0iv} corresponding to the blood magnetization at thermal equilibrium.

A TR/T_{inv} of 10 s/8 s was used for a proton density weighted acquisition of native blood and of blood sampled after CA injection.
The signals acquired with these imaging parameters are referred to as:
S_{0pre} when they originate from blood without CA, and as
S_{0post} when they originate from blood drawn after CA administration.
Using these timing parameters, 10 acquisitions were performed and averaged.
S_{0pre} and S_{0post} are also expected to correspond to S_{0iv}. A "blood volume fraction" S_{post}/S_{0post} = 1 is expected. The ratio $S_{0post}/S_{0pre} = \exp\left(-\Delta R_2^* \cdot TE\right)$ will be used to quantify the R_2-attenuation occurring at a TE of 3.2 ms.

The signal to noise ratio is calculated as follows:

$$SNR = \frac{\frac{1}{N}\sum_{i=1}^{N} S_i}{\sigma_S} \qquad \textbf{Eq. I-3}$$

where S is the signal amplitude in blood, N the number of signals averaged and σ_S the standard deviation for N acquisitions. σ_S is not the standard deviation of the background noise but results from averaging the blood signal over N acquisitions. The SNR was calculated this way, to be compared to the SNR of later in vivo acquisitions used for CBVf measurement, on which almost no background was available.

Fig. I-6: In vitro setup. The syringes containing blood sampled before (pre) and after (post) injection of 0.1 mmol/kg P760 were imaged simultaneously using an IR-FLASH sequence. Red blood cells (RBC) accumulate in the lower part of the tube during shimming and RF calibration.

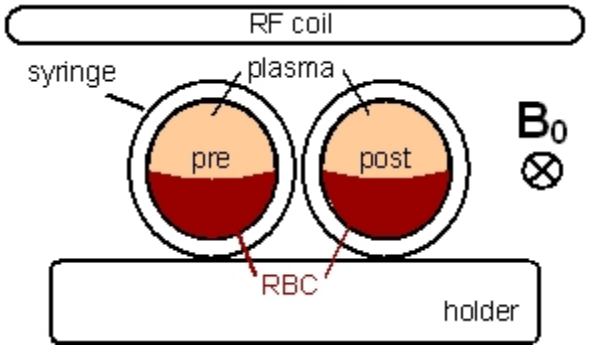

1.5.4. In vivo dose studies

To define the suitable CA dose that has to be injected to create the blood T_1 necessary for the $RSST_1$ regime and for in vivo CBV measurements, a series of IR-FLASH images (FOV 32 × 32 mm^2) with TR/T_{inv} = 750 ms/325 ms were acquired in three rats for 90 s before, during and after six incremental doses of Gd-DOTA ranging from 0.01 to 0.2 mmol/kg, and in other three rats for 210 s after 0.1 and 0.2 mmol/kg P760. The CA was injected manually as a short (< 1 s) bolus at t = 0 s. The concentration of the injected CA was identical, therefore the amounts varied. After each Gd-DOTA dose a 30 minutes washout interval was allowed prior to injection of the following dose. For P760, the washout interval between the two injections was one hour. The core temperature of the rats was controlled and prior to each CA administration the $PaCO_2$ of sampled arterial blood was measured. An identical experiment has been carried out for five Gd-DOTA doses from 0.01 to 0.15 mmol/kg and for five P760 doses from 0.002 to 0.035 mmol/kg but for less than 50 s after the bolus injection (c.f. Appendix II (Perles-Barbacaru and Lahrech 2007).

The signal obtained after homogeneous distribution of the CA in the blood pool is named S_{post} and is a function of time and of dose.

Data analysis

A custom-made IDL (Interactive Data Language, Research Systems Incorporated) program operating on a Sparc 20® work station (Sun Microsystems Inc., Mountain View, CA) was used for image processing and signal analysis. All images were reconstructed after zero filling to 256 × 256.

ROIs were drawn manually on the T_2 weighted or the high resolution IR-FLASH image. The duration of the steady state was determined at each dose from signals in a mainly vascular ROI (sagittal or cavernous sinus) plotted as a function of time.
Signals were also averaged over the whole cerebral tissue of the slice (referred to as "global brain ROI") and plotted against time. The steady state duration and the maximum signal amplitude for each dose were compared. For the dose experiment carried out with P760 as CA, the signal ratio $\frac{\langle S_{post}(0.2\text{mmol/kg})\rangle}{\langle S_{post}(0.1\text{mmol/kg})\rangle}$ averaged over a global brain ROI and over the first 50 s of the $RSST_1$ interval was computed.

1.5.5. Results of the preliminary experiments

T_1 of brain tissue at 2.35T

In rats of the Fischer strain (n = 6) the T_1 of white matter ranged from 1096 to 1203 ms with a mean of 1143 ± 35 ms, while the T_1 of the cortex ranged from 1210 to 1301 ms with a mean of 1264 ± 31 ms. The mean global T_1 was 1218 ± 29 ms for the Fischer strain and 1206 ± 214 ms for the Wistar strain (n = 7).

T_1 of blood at 2.35T

Native blood was found to have a T_1 of 1449,6 ± 34.0 ms (n = 5) using the spectroscopic IR-sequence and a T_1 of 1421.5 ± 44.5 ms (n = 5) using IR-FLASH, in accordance with literature (Thomas et al. 2001).

After injection of 0.1 mmol/kg P760 the blood T_1 was 49.43 ± 7.6 ms (n = 5). A single measure was carried out after injection of 0.2 mmol/kg P760 leading to a blood T_1 of 20.5 ms.

For tap water T_1 values ranging from 2.63 to 2.92 s were measured (n = 3).

In vitro signal ratios

The in vitro "blood volume measurement" yielded a mean S_{post}/S_{0post} value very close to unity: 0.997 ± 0.090 (n = 5). The ratio S_{post}/S_{0pre} is affected by the R_2 effect and resulted in lower values: mean 0.823 ± 0.103. The mean ratio of S_{0post}/S_{0pre} was 0.831 ± 0.111. The same signal intensities were obtained from ROIs in the bottom and in the top half of the syringes although a hematocrit gradient had installed during the time necessary for shimming and RF calibrations.

The average SNR were 15 ± 8, 202 ± 62 and 210 ± 56 for the S_{pre}, S_{post} and the S_{0pre} acquisitions, respectively.

In vivo dose studies

In Fig. I-7, the signals averaged over a global brain ROI are plotted against time.

The diagram in Fig. I-7a shows the signal evolution for selected Gd-DOTA doses. The response appeared to plateau at the top end of the concentration range used in this study. The signal intensities had not returned to baseline levels in each animal prior to administration of the second CA because of incomplete CA elimination. The first pass signal enhancement varies considerably because of different injected volumes and varying injection speed. The following steady state signal is completely independent of the injection mode (speed, volume, location) as long as the resulting CA concentration in blood is sufficiently high.

A steady state duration of almost 30 s can be obtained with 0.15 mmol/kg Gd-DOTA (Perles-Barbacaru and Lahrech 2007) and of more than one minute with 0.2 mmol/kg (Fig. I-7a). A dose of 0.1 mmol/kg yields a signal evolution that passes through the same maximum amplitude but for only a couple of seconds (Fig. I-7a and Appendix (Perles-Barbacaru and Lahrech 2007)) reflecting the rapid clearance of the CA from the blood.

Following a dose of 0.1 mmol/kg P760, a steady state duration of at least 2 minutes can be obtained, in some cases up to 5 minutes. The maximum signal amplitude following 0.1 and 0.2 mmol/kg P760 is the same although it is not reached at exactly the same time after injection. The higher the dose, the later the maximum amplitude is reached, and the longer it lasts (Fig. I-7b).

The mean ratio $\frac{\langle S_{post}(0.2\text{mmol/kg})\rangle}{\langle S_{post}(0.1\text{mmol/kg})\rangle}$ was 1.002 ± 0.063 (n = 3) with a minimum of 0.946 and a maximum of 1.070.

Fig. I-7: Signal versus time in an IR-FLASH experiment for different doses of Gd-DOTA and P760 (other signal versus time plots as a function of CA dose can be found in the Appendix (Perles-Barbacaru and Lahrech 2007) as Figure 2).

a: A RSST$_1$-regime can be achieved for more than 30 s with a Gd-DOTA dose of 0.2 mmol/kg, while a dose of 0.1 mmol/kg reaches the equilibrium signal and decays immediately.

b: Doses of 0.1 and 0.2 mmol P760 result in the same signal amplitude. The higher the dose, the later the maximum amplitude is attained.

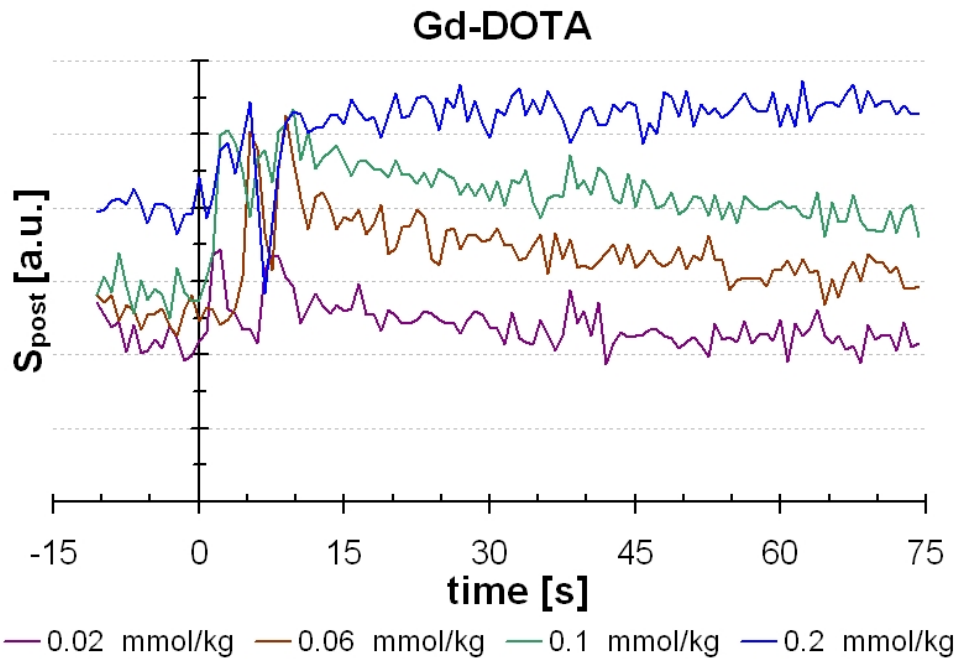

a

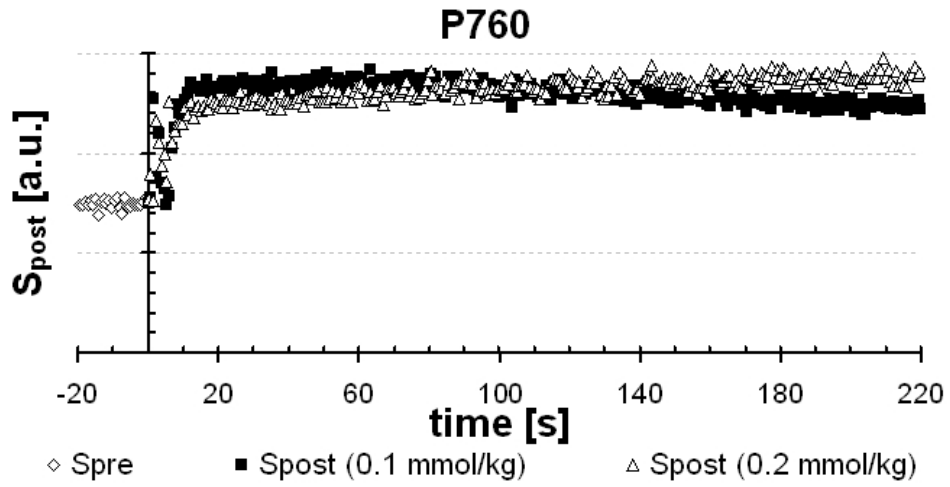

b

1.5.6. Discussion of the preliminary experiments

Blood and tissue signal suppression

The inversion time T_{inv} was chosen to null the signal from brain tissues for a T_1 range as large as possible. The T_1 measurements of brain parenchyma and of blood prior to CA injection show that the T_{inv} that nulls the brain tissue, simultaneously nulls the blood signal. This provides maximum contrast in magnitude to changes in signal intensity caused by a T_1 reduction following CA administration.

For TR = 750 ms, the optimal T_{inv} for suppression of blood with a T_1 of 1450 ms would be 327 ms (Eq. I-2). The blood T_1 in vivo at 37°C might be slightly higher, in which case it can be suppressed more easily. For a brain tissue characterized by a T_1 of 1206 ms, Eq. I-1 predicts a residual longitudinal magnetization of 0.006 M_0 at T_{inv} = 325 ms. The T_1 of the extravascular water can be approximated as the T_1 of the tissue since the blood contribution is small.

R_2-effect and intra-/extracellular water exchange

The in vitro S_{post}/S_{0post} ratio close to unity confirms full relaxation of the blood magnetization after 0.1 mmol/kg P760 at T_{inv} = 325 ms. The S_{post}/S_{0pre} ratio is lower due to the R_2 effect induced by the presence of the CA.

In an in vivo experiment where the vascular and the extravascular compartment contribute to the S_{0post} and S_{0pre} signals, the ratio S_{0post}/S_{0pre} corresponds to the factor $\exp(-\Delta R_2^* \cdot TE)$. The transverse relaxation enhancement ΔR_2^* has two origins:
First, it is the result of the transverse relaxivity of the CA and depends on the CA concentration in blood. In the in vitro studies this effect plays the major role and $S_{0post}/S_{0pre} = \exp(-\Delta R_2 \cdot TE)$.
Second, for the in vivo S_{0post} acquisitions where the signal arises from the intra- and the extravascular compartment, the susceptibility gradient at the vessel wall due to the presence of a compartmentalized CA, could have an additional accelerating effect on the dephasing of the transverse magnetization.
After an intravenous injection of P760 at a dose of 0.1 mmol/kg the blood concentration ranges between 1.4 and 2 mM. The factor $\exp(-\Delta R_2 \cdot TE)$ therefore theoretically ranges between 0.80 and 0.86 in close agreement with the experimental value of 0.83. Under the experimental conditions of the in vitro study we therefore have to account for an average R_2 attenuation of 17%, which cancels out if we use the ratio S_{post}/S_{0post} instead of S_{post}/S_{0pre}.

For each syringe, the signals were identical for ROIs drawn on accumulated erythrocytes or on the plasma above. This is a confirmation of the fact that the water exchange rate between the erythrocyte and the plasma is fast enough to consider the blood as a homogeneous compartment with respect to the relaxation times.

The $RSST_1$ signal and the minimum CA dose

The T_1 of blood after injection of 0.1 mmol/kg P760 confirms that with TR/T_{inv} = 750 ms/325 ms the conditions of the $RSST_1$ regime are fulfilled for the blood compartment for at least the first minute after injection. The in vivo dose studies show that a steady state signal of about one minute can be achieved with a dose of 0.2 mmol/kg Gd-DOTA or 0.035 mmol/kg P760, which are approximately isoefficient ($\frac{r_1(P760)}{r_1(Gd\text{-}DOTA)} \approx 5.8$). This closely agrees with the optimum theoretical CA doses (Fig. I-5). The blood signal S_{iv} is independent of the definite T_{1iv} value of the blood compartment obtained after CA administration, as long as it is smaller than $T_{inv}/5$. During a couple of repetitions, although the blood T_1 slowly increases with time due to CA

pharmacokinetics, the signal acquired at T_{inv} = 325 ms remains constant masking the T_1 increase in blood. This condition is referred to as a $RSST_1$.

Signal intensity in vessels continued to increase with increasing dose up to 0.15 mmol/kg Gd-DOTA. The increase is non-linear, reflecting both the non-linearity in the gradient echo signal intensity versus R_1 relationship and the increasing influence of CA-induced R_2* effects, which can mitigate the positive enhancement. As expected, CA doses exceeding 0.2 mmol/kg Gd-DOTA or 0.035 mmol/kg P760 lengthen the duration of the steady state without increasing the signal amplitude. However increasing R_2-attenuation becomes evident at higher doses, reflected by the fact that the signal reaches the maximum amplitude at a later time point, when the CA concentration in blood decreases to the optimal value.

A ratio $\frac{\langle S_{post}(0.2\text{mmol/kg})\rangle}{\langle S_{post}(0.1\text{mmol/kg})\rangle}$ close to unity was found by averaging over three experiments, indicating that a possible underestimation due to the R_2 attenuation in the early part of the steady state when R_2 effects are high is masked by the variability between subjects and between successive measures with an one hour interval. In fact, since the signal amplitude is linearly related to the blood water content under these experimental conditions, CBVf variations between measures would also have an influence on the signal amplitude and therefore on the ratio $\frac{\langle S_{post}(0.2\text{mmol/kg})\rangle}{\langle S_{post}(0.1\text{mmol/kg})\rangle}$.

The comparison of two measures carried out at different time points is not without difficulty, since the CBVf depends on a number of parameters. The time invariance of only a few physiologic parameters can be controlled during the experiment. One of the most important parameters in this context is the $PaCO_2$ of blood. Although all three rats injected with 0.1 and 0.2 mmol/kg P760 had a $PaCO_2$ in the normocapnic range [35 - 45 mmHg] prior to administration of both doses, the $PaCO_2$ was closer to the upper limit (range 42 to 45 mmHg) prior to the 0.2 mmol/kg dose. This might have had an increasing effect on the CBVf attenuating the signal loss due to the higher R_2-effect expected for the double CA dose.

1.6. CBVf measurement under normo- and hypercapnia

The minimal CA dose for the establishment of the $RSST_1$ conditions had been determined in vivo by maintaining a $RSST_1$ signal for a time interval of at least 30 s. The in vitro experiments confirmed that the $RSST_1$ conditions were fulfilled in blood. Subsequent experiments were carried out either with P760 at a dose of 0.1 mmol/kg or Gd-DOTA doses above 0.2 mmol because of a convenient duration of the SS, and because it has been shown that the R_2 effects are not yet pronounced. P760 was mainly used because of its high relaxivity, while Gd-DOTA was used to demonstrate that a CBVf measurement with the $RSST_1$ method is possible with a CA approved for clinical studies.

The $RSST_1$ method was now applied for CBVf mapping in healthy rats. In order to confirm that the expected physiological parameter is measured, the known physiological variation of the CBVf with the $PaCO_2$ level was monitored.

1.6.1. Imaging protocol

Normocapnic CBVf

The in vivo CBVf measurements were carried out on Wistar rats using the same surgical procedures, positioning and physiological monitoring as described in the general setup for in vivo experiments (paragraph 1.4.), including arterial blood gas analysis prior to CA injection. After shimming and RF calibrations, high resolution single slice transversal and coronal images were acquired with the spin echo and the IR-FLASH sequence with a FOV of 32×32 mm^2 and the imaging parameters described in paragraph 1.4.3.

Prior to CA injection 40 acquisitions were recorded with TR/T_{inv} = 10 s/8 s and 160 acquisitions with TR/T_{inv} = 750 ms/325 ms. These acquisitions are referred to as S_{0pre} and S_{pre}, respectively. Using the latter rapid timing parameters, continuous imaging was commenced 10 to 30 s prior to the intravenous bolus injection of CA, which was carried out manually in approximately 1 to 2 s. For 0.2 mmol/kg Gd-DOTA injections, a total of 160 images (corresponding to 120 s) were acquired to monitor the $RSST_1$ signal of about one minute duration. For P760 injected at a dose of 0.1 mmol/kg, 400 images (300 s) were acquired because the $RSST_1$ interval exceeds two minutes. These acquisitions are referred to as S_{post}. In two rats, five minutes after injection,

another series of 40 images was acquired using TR/T_{inv} = 8/10 s, and this acquisition is named S_{0post}.

Continuous CA infusion

To further lengthen the post injection $RSST_1$ interval, the initial P760 bolus was followed by a continuous CA infusion at a rate calculated to compensate for the loss of CA from the blood pool. An electric power injector was used for the continuous infusion. Owing to ferromagnetic components it had to be positioned far from the magnet outside the Farady cage. The intravenous line was approximately 3 m long and connected to the usual line of 40 cm length accessible from the open end of the magnet. Bolus doses of 0.3 mmol/kg for Gd-DOTA and of 0.1 mmol/kg for P760 were administered manually as usual through the 40 cm long line and the infusion was connected immediately after completed bolus injection. These CA doses ensured a $RSST_1$ of at least 3 minutes, the time necessary for the arrival of the continuous infusion.

The infusion rates were 63 µmol kg^{-1} min^{-1} for Gd-DOTA and 7.8 µmol kg^{-1} min^{-1} for P760. The plasma clearances for these CA reported in Corot et al (Corot et al. 2000b) were used to calculate the elimination rate. The infusion rate of P760 was chosen so as to maintain a plasma concentration of 1.3 mM theoretically leading to a blood T_1 of approximately 40 ms. The infusion rate of Gd-DOTA that would maintain a plasma concentration of 8 mM, such as achieved immediately after bolus injection of 0.2 mmol/kg is 53.6 µmol kg^{-1} min^{-1}. However, in practice this is not sufficient to obtain a $RSST_1$ signal. The infusion rate of 63 µmol kg^{-1} min^{-1} was finally established experimentally.

Prior to CA administration and during the 40 to 60 minutes of CA infusion, series of images with TR/T_{inv} = 750 ms/325 ms and 500 ms/225 ms were acquired for up to 20 minutes, and series of images with TR/T_{inv} = 10 s/8 s for up to 5 minutes. In between the acquisition series, 0.5 ml arterial blood was withdrawn and preserved for T_1 measurement. Spectroscopic T_1 measurements were carried out at the end of the infusion experiment as described for the preliminary experiments in paragraph 1.5.2.

CBVf measures under induced hypercapnia

To verify whether the MRI method is sensitive to CBVf variations as they occur physiologically in order to adapt to transitory metabolic changes, in vivo CBVf measures were performed in rat brain under increasing $PaCO_2$ levels. The described technique of continuous CA infusion would have been appropriate for this experiment. However, to economize CA, in particular P760, successive injections of 0.3 mmol/kg Gd-DOTA (n = 3) or 0.1 mmol/kg P760 (n = 5) at each hypercapnia level were used in this experiment.

In addition to the surgical procedure described above, for this experiment, the rats were tracheotomized and intubated for mechanical ventilation (respiratory frequency 60 min^{-1}, inspiration time 0.4 s, pressure < 12 mmHg) with a mixture of 70% air and 30% oxygen. The pulmonary pressure was monitored in addition to the arterial pressure.

Once the scanner calibrations and the S_{0pre} (N = 40) and S_{pre} (N = 400) image acquisitions were performed, the animals were paralyzed with an intravenous injection of 2 ml pancuronium bromide (0.1 mg/ml) to prevent hyperventilation. This amount was usually sufficient for about one hour. Increasing amounts (up to 7%) of CO_2 were added to the air/oxygen mixture. The $PaCO_2$ was measured 15 min after increasing the CO_2 fraction and a CBVf measure was performed if the $PaCO_2$ had risen. S_{post} (N = 400) acquisitions were performed under three to four of the following conditions: normocapnic ($35 < PaCO_2 < 45$ mmHg), slight hypercapnic ($45 < PaCO_2 < 65$ mmHg), severe hypercapnic ($PaCO_2 > 65$ mmHg), and after recovery to a $PaCO_2$ level within or close to the normal range (30 to 45 min after CO_2 removal). The imaging protocol is illustrated in Fig. I-8.

Fig. I-8: Imaging protocol for the CBVf monitoring under normocapnia and various hypercapnia levels induced by increasing the inspired CO_2 fraction (blue plot).

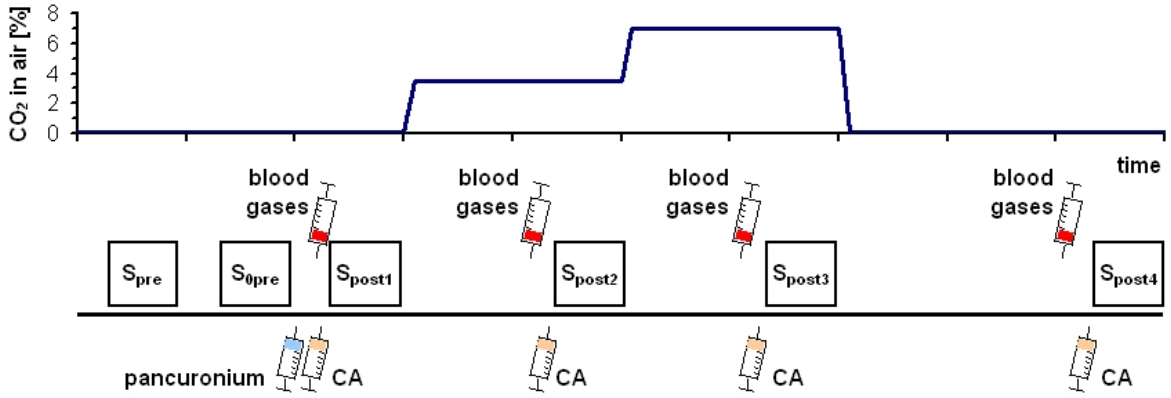

1.6.2. Image analysis

Under IDL, a vascular signal versus time plot was used to determine the beginning and the end of the $RSST_1$ interval which is defined by a signal having a constant and maximum amplitude. For all CBVf calculations signals were averaged over at least one minute. The CBVf maps are given in a linear gray scale (0 - 255). White (255) corresponds to the maximum CBVf encountered which is specified for each map. For convenience, CBVf is often given in % ± standard deviation.

Only coronal brain slices were used to investigate regional CBVf variations by averaging the CBVf over large visible brain structures. White matter values were obtained from the corpus callosum. Gray matter values are given for the cortex (mainly parietal) and subcortical structures. Subcortical gray matter is composed of all deep gray matter structures such as striatum and thalamus (basal ganglia). The cortical ROIs were delineated at a reasonable distance from the brain surface to avoid inclusion of the pial vasculature.

Statistical significance of CBVf differences between cerebral structures were tested using one-way analysis of variance for repeated measures, followed by a Bonferroni multiple comparison test.

When CBVf results are reported for one animal, the standard deviation reflects the temporal fluctuation of the signal, unless a mean CBVf value from the CBVf map for a particular ROI is reported, in which case the standard deviation reflects the spatial heterogeneity within the ROI. When mean CBVf values over a group of animals are reported, the standard deviation reflects the interindividual variability. Cerebral blood volume fraction ratios are calculated for each individual rat, before averaging over all rats.

The SNR of the signal averaged over the brain tissue and over 90 acquisitions before CA injection (S_{pre}) and during the $RSST_1$ interval following CA administration (S_{post}), and over 40 S_{0pre} acquisitions was computed according to Eq. I-3. The σ_S is not the standard deviation of the background noise but of the temporal variation of the brain signal, because with few exceptions, the FOV was entirely filled by tissue. The SNR of the S_{pre} acquisition was measured to quantify the efficiency of suppression of brain tissue signals. Where possible (n = 6), the background signal was also averaged over 90 S_{pre} acquisitions and compared to the S_{pre} from brain tissue.

The CBVf changes under hypercapnia are given relative to the normocapnic CBVf, calculated for each rat from the experimental data for a $PaCO_2$ value of 40 mm Hg.

$$\Delta CBVf[\%] = \frac{CBVf(PaCO_2) - CBVf(40\ mmHg)}{CBVf(40\ mmHg)} \cdot 100$$

A linear relationship between the global CBVf and the $PaCO_2$ was assumed and the experimental data was fitted separately for the three experiments carried out with Gd-DOTA and the five experiments carried out with P760. For regional CBVf changes, the rats injected with both CAs were pooled.

1.6.3. Results of the in vivo CBVf measurements

Determination of the $RSST_1$ interval

Theoretically, the $RSST_1$ interval has to be determined from the signal evolution in a vascular ROI, either the sagittal or cavernous sinus or another similar vein draining blood from the brain. In practice, all signals from ROIs on cerebral tissue yielded an equivalent $RSST_1$ interval, since Gd-DOTA and P760 are confined to the blood pool in healthy brain tissue. With the temporal resolution available, the signal enhancement in the brain tissue occurred simultaneously with the enhancement in the venous structure. The signal peaked rapidly, but in many cases the initial

signal showed a transitional drop, demonstrating the effect of a first pass of the bolus, until the CA concentration reached a homogeneous distribution. The first pass is accompanied by a signal loss due to a high T_2 and T_2* effect of a transitory high CA concentration. The $RSST_1$ installs after several recirculations, as soon as the CA is homogeneously distributed.

R_2* effect in tissue

From acquisitions performed after bolus injections and under CA infusion, the mean ratio S_{0post}/S_{0pre} equalled 1.020 ± 0.025 for signals averaged over the whole brain slice.

The blood T_1 during continuous CA infusion

The infusion rates were chosen as to maintain a blood T_1 in the order of 40 ms throughout the infusion duration. However, about 5 to 10 minutes after the initial bolus injection, the blood T_1 was rather around 65 ms with P760 and 100 to 200 ms with Gd-DOTA. Forty minutes to one hour after the initial bolus, the blood T_1 was decreased to about 20 ms by both CA.

In vivo SNR

The SNR for signals from global ROIs averaged over 15 rats was 27 ± 11, 40 ± 18 and 276 ± 96 for the S_{pre}, the S_{post} and the S_{0pre} acquisitions, respectively. In the images acquired prior to CA injection, in which the signal from cerebral tissue including native blood is suppressed (S_{pre}), the SNR was analyzed to quantify the quality of suppression. The residual cerebral signal on S_{pre} images was also compared to the background noise: the ratio was 2.1 ± 0.8 (n = 6).

The SNR of the S_{pre} acquisitions being almost twice as high as in the in vitro experiment (i.e. in the absence of any extravascular water), it was concluded that the extravascular compartment is the origin of the residual signal. Therefore, the regional variations of the S_{pre} signal amplitude were investigated in detail. The signal S_{pre} was found to account for 2 to 3% of the corresponding S_{0pre} value (instead of the theoretical 0.6%), with a value systematically higher in white matter (characterized by a lower T_1) than in the cortex. Studies performed under CA infusion demonstrated that with TR/T_{inv} = 500 ms/225 ms, the suppression of the extravascular signal is more efficient (2.4 ± 0.4% instead of 2.9 ± 0.4% of S_{0pre}, n = 3), although theoretically it should account for only 0.07% of S_{0pre} for a mean tissue T_1 of 1200 ms.

Although even white matter T_1 was never measured to be below about 1100 ms, the $RSST_1$ method is unable to suppress the extravascular tissue as theoretically expected. Only one half of the S_{pre} signal can be contributed to the statistical background noise. Another contribution to the S_{pre} signal might arise from the fact that only the central k-space line is acquired at T_{inv} = 325 ms, while the $k_y \neq 0$ lines are acquired later, when the extravascular magnetization is $\neq 0$ (cf. Fig. I-4).

Correction for incomplete tissue signal suppression

To correct for this residual signal which arises from insufficiently suppressed extravascular water, the mean signal acquired before CA injection $\langle S_{pre} \rangle$ was subtracted from the S_{post} signal. For each acquisition, the normalized signal S^{norm} was calculated according to the following equation:

$$S^{norm} = \frac{S_{post} - \langle S_{pre} \rangle}{\langle S_{0pre} \rangle} \qquad \textbf{Eq. I-4}$$

The mean signals $\langle S_{pre} \rangle$ and $\langle S_{0pre} \rangle$ are obtained by averaging over all available acquisitions, typically a number of 160 for S_{pre} and 40 for S_{0pre}.

Since in vivo the S_{0post} and S_{0pre} signals do not differ greatly, the S_{0pre} signal was used for normalization because it is acquired while the tissue T_2 is constant. As indicated by the blood T_1 reached several minutes after Gd-DOTA and even after P760 bolus injection, the blood concentration of the CA is changing rapidly. Relatively constant blood relaxation times after CA administration can only be guaranteed for CAs having a long blood half life or during continuous CA infusion. Different errors will be introduced by trying to measure S_0 when the CA concentration is changing.

During the $RSST_1$ interval defined as a constant vascular signal amplitude, the S^{norm} amplitude corresponds to the CBVf. The CBVf maps were calculated by averaging each voxel over N images acquired during the $RSST_1$ interval, which has the effect of reducing the background noise and enhancing the SNR:

$$CBVf_{voxel} = \frac{1}{N}\sum_{i=1}^{N} S_i^{norm} \qquad \textbf{Eq. I-5}$$

For CBVf mapping following bolus injections, N was 90 (about 70 s). In the experiments carried out under continuous CA infusion, up to 1600 images were averaged corresponding to 20 minutes.

CBVf under normocapnia

For experiments carried out with 0.1 mmol/kg P760 a mean global CBVf of 3.29 ± 0.69% was measured (n = 15). For experiments carried out with 0.2 mmol/kg Gd-DOTA the average global CBVf was 3.37 ± 0.41% (n = 4). As reviewed in the Introduction chapter (Table 0-3), this value is within the range of published values for normocapnic rat CBVf.

A typical coronal CBVf map from a single representative rat is shown in Fig. I-9 together with an anatomical section at the same level. Extracerebral vascular structures are excluded from the map for better contrast within the low CBVf range of brain tissue. The border of the map has strong intensities, possibly due to the presence of large vessels at the surface of the cortex, therefore the cortical ROIs were delineated at an acceptable distance from the brain surface. In the CBVf maps, the highest volume is observed at the location of the anterior cerebral artery in the interhemispheric fissure. At the base of the brain the two spots with elevated CBVf correspond to the middle cerebral arteries. In the center of the brain slice, the symmetric spot with high blood volume in the region of the lateral and third ventricles is likely to correspond to the choroids plexus. Since it is involved in the production of cerebrospinal fluid, this structure is composed of a large quantity of microvessels and is in addition more permeable than typical brain capillaries.

Fig. I-9: coronal section through a rat brain depicting anatomical details and a CBVf map obtained with the $RSST_1$ method after injection of 0.1 mmol/kg P760.

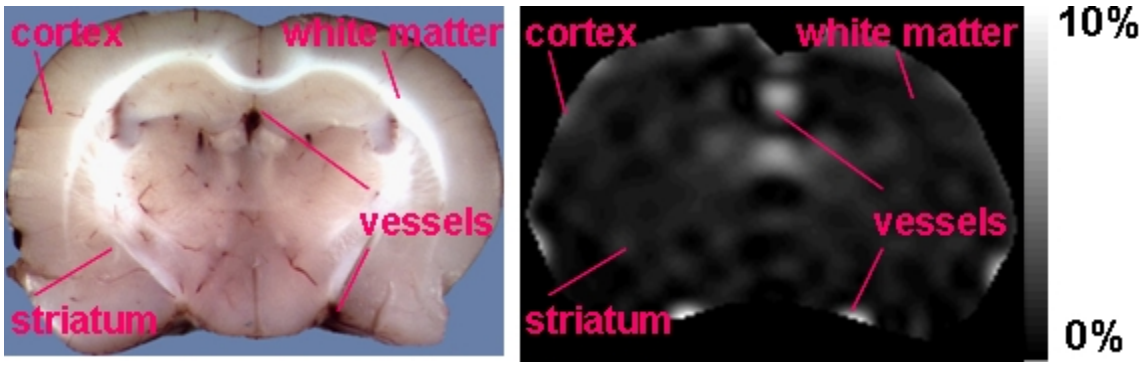

Large CBVf differences between brain structures such as white matter and cortex result in a distinguishable contrast. The histogram in Fig. I-10 shows the regional CBVf values averaged over six rats. Since the CBVf is in the order of 2 to 3 % it is susceptible to noise resulting in a large scattering of data, especially in small ROIs. In addition, these measures are subject to partial volume effects. However, regional CBVf values appear consistent. White matter has a significantly ($P < 0.05$) lower CBVf than the gray matter structures. The striatum is a mixture of gray and white matter as it is traversed by thalamocortical projection fibers. This might explain its slightly lower CBVf compared to the cortex and is in accordance with Adam et al (Adam et al. 2003).

The ratios of regional CBVf between cortex and striatum $\frac{CBVf_{cortex}}{CBVf_{striatum}}$ as well as between gray matter and white matter $\frac{CBVf_{gray\ matter}}{CBVf_{white\ matter}}$ were 1.11± 0.18 and 1.59 ± 0.51, respectively. Similar ratios were reported and are reviewed in Table 0-4.

Fig. I-10: mean CBVf in different brain structures

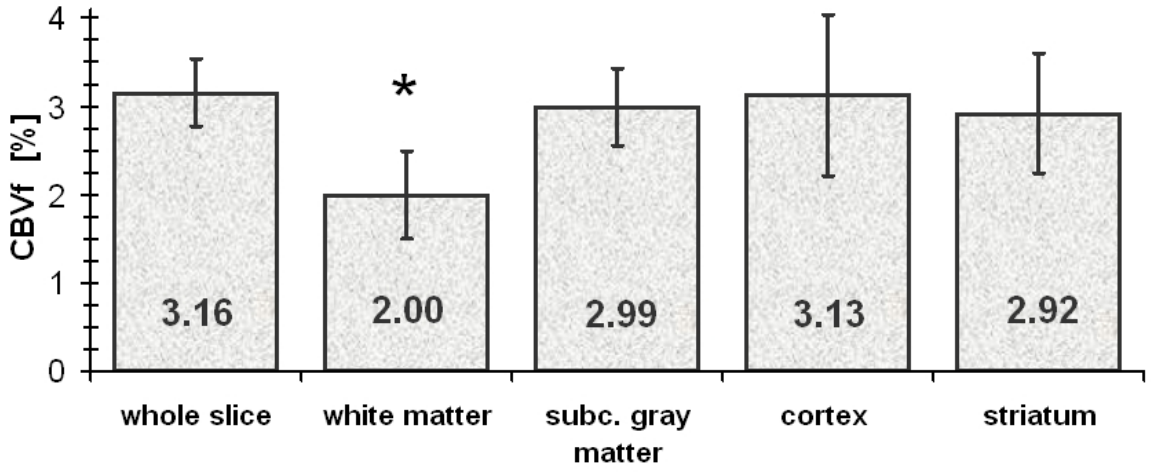

Deep gray matter structures have a similar mean CBVf as the cortex but with a larger spatial variability. The CBVf histograms in Fig. I-11 illustrate the heterogeneity of the CBVf in the cortex (Fig. I-11a) and the striatum (Fig. I-11b). In general, a larger range of CBVf values including values below 2% is encountered in the subcortical gray matter with respect to the cortical gray matter. Figure I-11c shows the CBVf map with the corresponding ROIs.

Fig. I-11: Histograms of the CBVf in the cortex (a) and in the striatum (b) and the delineation of the corresponding ROIs on a coronal CBVf map (c).

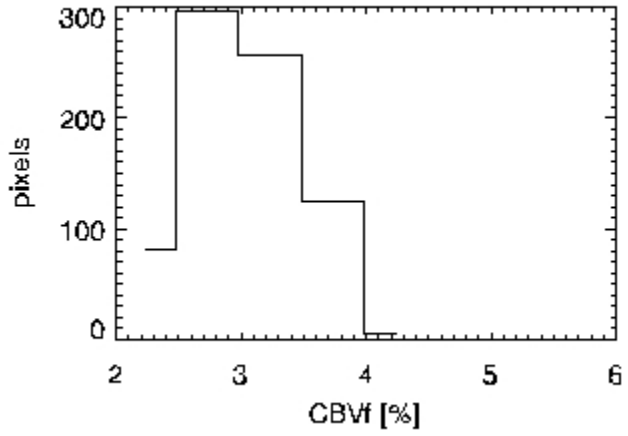

a

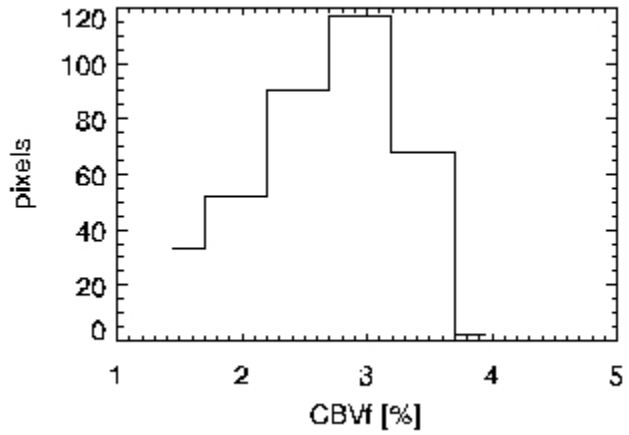

b

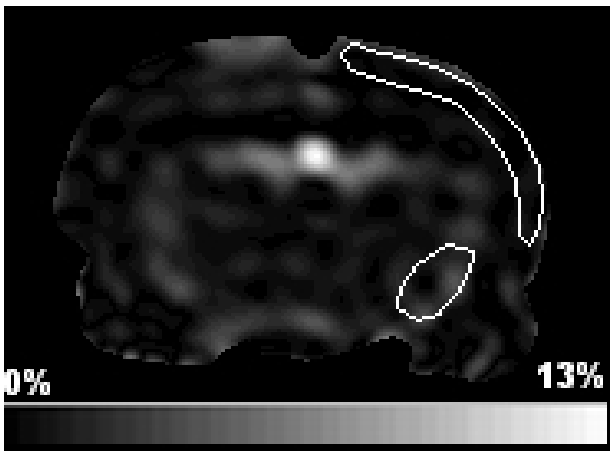

c

For this particular rat in Fig. I-11, the global CBVf was 3.28 ± 0.24%. The average cortical and striatal CBVf for the depicted ROIs were 3.12 ± 0.88% and 2.77 ± 1.51%, respectively. Here the standard deviations reflect the CBVf heterogeneity within the ROI.

Depending on the degree of partial volume effect, the mean blood volume measured in vascular structures ranged from 50 to 80%. A value of 100% was never obtained.

Under normocapnic conditions, CBVf measurements at different time points during the steady state created by a continuous CA infusion revealed fluctuations within 9% of the mean CBVf value. This can be due to physiologic variations or to a temporally varying T_2 effect. As revealed

by the T_1 measurements at different time points during the infusion, we were not able to maintain the CA concentration in blood perfectly stable.

CBVf increase under hypercapnia

The results of the CBVf measurements as a function of the $PaCO_2$ level are shown in Fig. I-12a. The linear regression for experiments with Gd-DOTA (dashed line) and P760 (solid line) bolus injections yield practically identical slopes (Gd-DOTA: 0.99%/mm Hg, R^2 = 0.67; P760: 0.98%/mm Hg, R^2 = 0.85). Regional analysis reveals that CBVf increases under hypercapnia are steepest for the cortex, i.e. 1.30% per mmHg (n = 8, Gd-DOTA and P760 experiments combined).

The CBVf increase under hypercapnia is in the range of those reported in the literature (Payen et al. 1998; Shockley and LaManna 1988). The hypercapnia induced CBVf response of microvessels was lower in studies in which the CBVf was determined post mortem by autoradiography (Bereczki et al. 1993b; Keyeux et al. 1995). In contrast to these studies, the $RSST_1$ technique is not only sensitive to microvessels but includes vessels of various radii. The use of volatile isoflurane anesthesia might have an effect on the vascular response, too (Archer et al. 1987).

Figure I-12b shows the result of an experiment in which recovery has been allowed after three increasing levels of hypercapnia, showing the reversibility of the CBVf change. While the $PaCO_2$ measured during recovery is still higher than the normocapnic one, the CBVf decreases to a lower value than under normocapnia. A similar undershoot of CBVf has been observed in rats by Payen et al (Payen et al. 1998) predominantly for the striatum during recovery after inhalation of CO_2, and in cats by Hamberg et al (Hamberg et al. 1996) after transient ischemia.

Fig. I-12: Global CBVf (expressed in percent of the normocapnic CBVf) as a function of $PaCO_2$ (a). CBVf during hypercapnia and recovery (b)

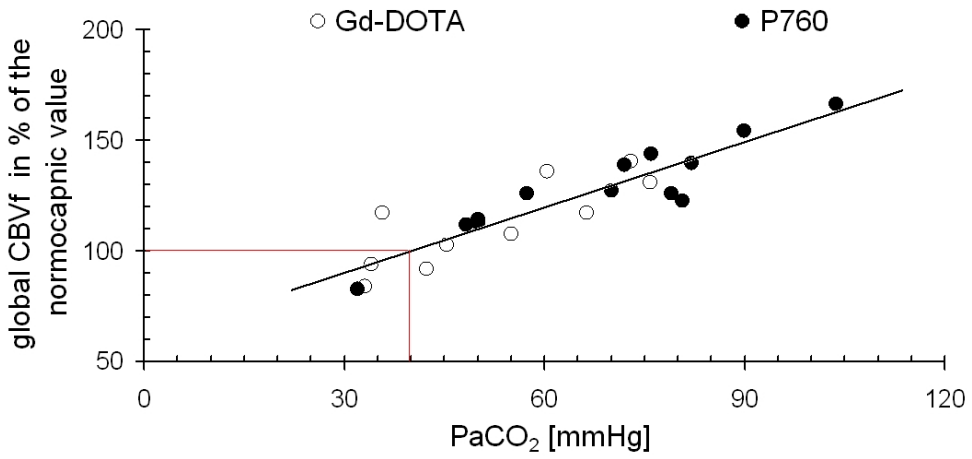

a

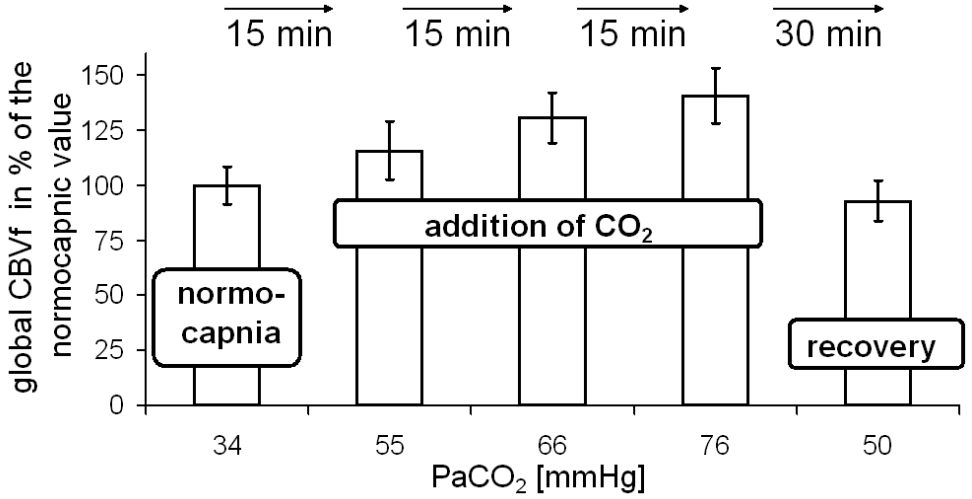

b

1.7. Discussion

The $RSST_1$ method is based on a number of assumptions that will be discussed.

Using IR-FLASH with TR << T_1 progressively suppresses the longitudinal magnetization of tissue and native blood. After CA injection, only the blood T_1 will be reduced below $T_{inv}/5$ for a

particular time interval, allowing the acquisition of a signal corresponding to the equilibrium magnetization of blood. This signal amplitude divided by the signal corresponding to the equilibrium magnetization of all water protons in the ROI or voxel represents the vascular volume fraction. To simplify the calculation, a tissue density of 1 g/ml was assumed for both compartments. This is an acceptable approximation as shown in the beginning of this chapter.

1.7.1. R_2 attenuation

This MR technique is based on T_1 effects, but changes in T_2 will also influence the measured signal. Estimates of the blood concentration of CAs and of their relaxivity in blood show that the T_2 reduction will cause a signal attenuation, while T_2* effects caused by susceptibility differences at the vascular wall can be neglected due to suppression of the signal from the extravascular tissue compartment.

The subtraction of the S_{pre} signal has the disadvantage that the factor $\exp(-\Delta R_2 \cdot TE)$ can no longer be eliminated, whether the equilibrium signal used for normalization is measured before (S_{0pre}) or after (S_{0post}) CA injection. The attenuation factor due to transverse relaxation given by

$$\exp\left(-\left(\frac{1}{T_{2pre}} + r_2 \cdot [CA]\right) TE\right)$$

is 0.78 to 0.83 for 0.1 mmol/kg P760 and 0.92 to 0.93 for 0.2 mmol/kg Gd-DOTA, for a total blood volume range of 50 to 70 ml/kg (Lee and Blaufox 1985). For this estimation, an average T_{2pre} of 100 ms has been used since venous and arterial T_2 were reported to be 70 and 150 ms, respectively (Thomas et al. 2001).

The signal from large blood structures did not allow measuring a blood volume of 100%. In addition to the partial volume, the transverse relaxation effect could play a role. In blood, transverse relaxation is predominantly due to the diffusion of water through the field gradient arising from the susceptibility difference $\Delta\chi_{ery/plasma}$ between erythrocytes and plasma. The $\Delta\chi_{ery/plasma}$ depends on the oxygenation, on the hematocrit and on the susceptibility of the plasma modified by the CA injection. Although the attenuation was shown to be negligible in the microvasculature, the transverse relaxation effect is probably more pronounced in large veins or in the blood samples, because the blood oxygenation is lower and the hematocrit is higher than in the microvasculature (Cremer and Seville 1983; Iannotti et al. 1987).

1.7.2. Advantages of acquiring the normalizing factor before CA injection

As mentioned in the previous paragraph, the difference signal ΔS in the numerator of Eq. I-4

$$\Delta S = S_{post} - S_{pre}$$

contains a factor related to the transverse relaxation in the vascular compartment:

$$\Delta S \approx S_{0iv} \exp(-TE/T_{2iv})$$

where S_{0iv} is the signal corresponding to the thermal equilibrium magnetization of the blood water protons and T_{2iv} is the transverse relaxation time of the blood after CA injection.

The measured difference signal is normalized by a signal S_0 which is proportional to

$$M_{0iv}\left[1-\frac{2\exp(-T_{inv}/T_{1iv})}{1+\exp(-TR/T_{1iv})}\right]\exp(-TE/T_{2iv})+M_{0ev}\left[1-\frac{2\exp(-T_{inv}/T_{1ev})}{1+\exp(-TR/T_{1ev})}\right]\exp(-TE/T_{2ev})$$

M_{0iv} and M_{0ev} are the fully relaxed magnetizations of the intra- and the extravascular compartments, and T_{1iv} ,T_{2iv}, T_{2ev} and T_{1ev} are the longitudinal and transverse relaxation time constants of the intra- and the extravascular compartments, respectively.

Before CA injection, T_2 is about 63 ms, 70 ms and 150 ms for brain tissue, venous and arterial blood, respectively (Thomas et al. 2001). T_1 of tissue and blood is in the range of 1000 to 1300 ms. For these values and a TR/T_{inv} = 10 s/8 s, both expressions in square brackets ($1-\frac{2\exp(-T_{inv}/T_{1iv})}{1+\exp(-TR/T_{1iv})}$ and $1-\frac{2\exp(-T_{inv}/T_{1ev})}{1+\exp(-TR/T_{1ev})}$) as well as the factors $\exp(-TE/T_{2iv})$ and $\exp(-TE/T_{2ev})$ equal one.

If S_0 is acquired after CA injection, the extravascular parameters are not changed and the blood T_1 surely is sufficiently low to render the term $1-\frac{2\exp(-T_{inv}/T_{1iv})}{1+\exp(-TR/T_{1iv})}$ equal to one. However, the blood T_2 value is reduced, unknown and changing during the acquisition.

Since in vivo the S_{post} and the S_0 acquisition can not be performed simultaneously as it was done in vitro, the factor $\exp(-TE/T_2)$ can not cancel out. Therefore, normalizing by the S_{0post} signal acquired after CA injection is of no benefit. On the other hand, normalizing by the S_{0pre} signal

acquired prior to CA injection allows estimating and correcting for the R_2-attenuation occurring in blood.

Under our in vivo experimental conditions, with a TE = 3.2 ms and a P760 blood concentration of about 2 mM, the signal ratio S_{0post}/S_{0pre} was still about unity. Obviously, this is due to the small volume fraction of the blood compartment which experiences the transverse relaxation effect resulting in a signal attenuation small enough to be masked by the noise. A 15% signal reduction in the vascular compartment, with a CBVf of 3%, results in a total signal reduction of only 0.45%, thus theoretically in a S_{0post}/S_{0pre} ratio of 0.995. The hypothesis is supported by the fact that the signal amplitude during the early part of the steady state was equal for a P760 dose of 0.1 and 0.2 mmol/kg. Another hypothesis is that at the time the S_{0post} signal was acquired (from 5 to 10 minutes after bolus injection), the CA concentration in blood was already low. A third possibility is that another effect compensates for the CBVf underestimation. Such an effect could arise from exchanging water protons between the intra- and the extravascular compartments. A method to estimate the water exchange effect will be described in paragraph 1.7.5.

If for any reason the TE of the sequence is rather long, or the CA employed has a very high transverse relaxivity, the blood R_2 can be measured from withdrawn arterial blood and used to correct the CBVf measure for the R_2 attenuation.

1.7.3. The normalization factor S_0

The signal acquired during the $RSST_1$ interval arises from the intravascular water protons. The intensity varies between voxels because the blood volume fraction varies. However, a second mechanism is responsible for this inter-voxel variability. This is the inhomogeneous sensitivity profile of the RF coils, in our study in particular the sensitivity profile of the surface RF coil used for signal reception. Therefore, the S_0 signal, measuring the thermal equilibrium magnetization of the intra- and extravascular compartment, has been acquired with the same RF coils and identical RF pulse calibrations and receiver gains. The S_{post} signal from each voxel can therefore be normalized with the S_0 signal from the same voxel, canceling out any non uniform sensitivity of the RF coils.

However, even for voxels for which an equal RF coil sensitivity can be assumed, it has been observed that the S_0 signal is not the same. In fact, it depends on the proton density within the voxel. Although the intravascular compartment can be considered to have a water density of 1 g/ml, it appears that the proton density of the brain varies between different structures, due to variable amount of lipids and proteins. This variability is likely to be even more pronounced in diseased tissues, which can be characterized by areas of high cellular density, hemorrhage, edema or necrosis. For this reason we chose to normalize the vascular signal of each voxel by the S_0 signal from the respective voxel.

This choice has not been made by all investigators. One can also normalize with respect to the equilibrium signal from a region for which a density of 1 g/ml can be assumed. For example, Lu et al (Lu et al. 2005) who developed the VASO method for CBVf mapping used the signal from a region containing mainly cerebrospinal fluid for normalization. However, in this case the heterogeneous sensitivity of the RF coils has to be accounted for.

1.7.4. Blood flow effects

The effects of the blood velocity on the signal in a turbo-FLASH sequence have been studied by Dean et al and Ludemann et al (Dean et al. 1992; Ludemann et al. 2000). Flow related effects can appear for velocities above 1 cm/s and low CA concentrations.

At the capillary level, the blood flow velocity is too low (≈ 0.3 mm/s) to have any effect. Flow effects in the brain sinus appear to be negligible in our experimental conditions, since the CA doses are high (>2 mM) during the $RSST_1$ interval used for the CBVf measure. The advantage of the $RSST_1$ method is that it does not require acquisition of the AIF which might be influenced by the described flow effect, because of the high blood flow in arteries and rapidly varying CA concentrations during the first pass of the CA bolus.

In addition, the $RSST_1$ technique was made insensitive to the inflow of noninverted spins by inverting magnetization in a spatially nonselective manner.

1.7.5. Water exchange

1.7.5.1. Intra-/extravascular water exchange

The permeability surface area product (PS_v) of the capillary wall and therefore the water exchange rate τ_{exch}^{-1} between the blood and the extravascular compartment, are physiologic parameters and time invariant for a given tissue (Li et al. 2005). In general, ASL methods, are based on a single compartment model, which makes the assumption that the capillary wall has an infinite permeability to water. However, in some studies a two compartment model was considered (Parkes and Tofts 2002; Zhou et al. 2001) even when no exogenous CA was administered. The assumption of rapid water exchange does not hold for techniques that necessitate the injection of CA, since the exchange regime (slow or fast) depends on the difference between the longitudinal relaxation rates of the intravascular T_{1iv}^{-1} and extravascular T_{1ev}^{-1} compartment (the shutter speed), in addition to τ_{exch}^{-1} (Li et al. 2005; Moran and Prato 2004).

In our study, a two-compartment model of the cerebral tissue was used, the water exchange was considered low, and the CA dose was chosen to create a large difference between the two compartments.

Slow water exchange regime

Assuming an approximate microvascular blood volume of CBVf = 3%, and an intracapillary residence time τ_{iv} of 500 (Orrison et al. 1995) to 650 ms (Labadie et al. 1994), the extravascular residence time

$$\tau_{ev} = \frac{V_{ev}}{V_{iv}} \cdot \tau_{iv}$$

is in the order of 16 to 21 s, respectively. The water exchange rate

$\tau_{exch}^{-1} = \tau_{iv}^{-1} + \tau_{ev}^{-1}$

is thus in the range of 1.6 to 2.1 s^{-1}. After CA administration, the difference of the longitudinal relaxation rates between the two compartments is in the order of 20 s^{-1} ($T_{1ev}^{-1} \approx 1200$ ms and $T_{1iv}^{-1} \approx 50$ ms from the experimental data), fulfilling the condition for the slow exchange regime

$\tau_{exch}^{-1} << T_{1iv}^{-1} - T_{1ev}^{-1}$.

Therefore, the two-compartment model without exchange is an acceptable approximation.

Measurement error due to inter-compartmental water exchange

The exchange effect on the CBVf measure can be evaluated using the model described in (Moran and Prato 2004). This model defines an exchange regime as

$$K = \left(1 + \frac{\tau_{exch}}{m}\right)^{-1},$$

where

$$m = \left(\frac{1}{T_{1(iv)}} - \frac{1}{T_{1(ev)}}\right)^{-1}$$

is the characteristic time of the two relaxing compartments. The impact of the exchange regime (K = 0 no exchange, K = 1 fast exchange) modifies the intrinsic T_1 of either compartment resulting in apparent relaxation times T_1^{app}. These are calculated according to

$$\frac{1}{T_{1(a)}^{app}} = \frac{1}{T_{1(a)}} + Kv_{(b)}\left(\frac{1}{T_{1(b)}} - \frac{1}{T_{1(a)}}\right) \qquad \textbf{Eq. I-6}$$

where a and b denote the compartments and $v_{(a)}$ or $v_{(b)}$ are the corresponding compartment volume fractions.

In Fig. I-13a, the ratios M_z/M_0 of the intra- and extravascular compartments are compared in the absence (K = 0) and in the presence of exchange (K = 0.0765, reflecting experimental conditions). The plots are derived from Eq. I-1 as a function of T_{inv} with TR = 750 ms, and using the corresponding apparent relaxation times T_1^{app} instead of T_1 in the presence of exchange. The different T_1^{app} are computed according to Eq. I-6 for T_1 values comparable to those obtained experimentally for each compartment before and after CA injection (T_{1ev} = 1200 ms, T_{1iv} = 1450 ms before and T_{1iv} = 50 ms after CA administration). The K value used in this simulation results form τ_{exch} = 630 ms. For K = 0.0765, the apparent extra- and intravascular T_1 values are T_{1ev}^{app} = 1140 ms and T_{1iv}^{app} = 54 ms. The simulations were performed for an intravascular volume fraction of 3%.

The plot in Fig. I-13a demonstrates that the intravascular magnetization is not affected by the water exchange, while the extravascular magnetization is less suppressed when exchange takes place. The intravascular magnetization at T_{inv} = 325 ms increases from M_{ziv}/M_0(325ms) = $4.2\ 10^{-5}$ before CA administration to M_{ziv}/M_0(325ms) = 0.0299 after CA administration.

In order to show directly to which extent the CBVf is overestimated for K = 0.0765, the sum of the intra- and extravascular longitudinal magnetization

$M_z = M_{ziv} + M_{zev}$

is plotted in Fig. I-13b. The magnetization values resulting for the apparent longitudinal relaxation times of the intra- and extravascular compartment at T_{inv} = 325 ms in the presence of exchange were computed according to Eq. I-1, and yield a total tissue magnetization of M_z/M_0(325ms) = 0.0388. Without exchange, the total tissue magnetization is M_z/M_0(325ms) = 0.0361. Before injection, the exchange regime is characterized by K = 0.9170, but the longitudinal magnetization M_z/M_0(325ms) = 0.0062 (measured as a residual signal in the S_{pre} acquisition) is practically identical with or without exchange.

According to Eq. I-4 the CBVf is given by the difference of the tissue magnetization before and after CA administration. For an exchange time of τ_{exch} = 630 ms this yields an apparent CBVf of 3.27%, which corresponds to an overestimation of less than 10%. For an exchange time of τ_{exch} = 500 ms the overestimation is less than 12%.

Fig. I-13:

a: A model of the fractional longitudinal magnetization of the intra- and the extravascular compartment as a function of time in the absence (K = 0.0) and in the presence of exchange (K = 0.0765). The exchange affects only the signal of the extravascular compartment.

b: Total fractional longitudinal magnetization calculated in the case of exchange and without exchange before and after CA injection. According to Eq. I-1, the computed CBVf value in the presence of exchange (K = 0.0765) is overestimated by approximately 10%.

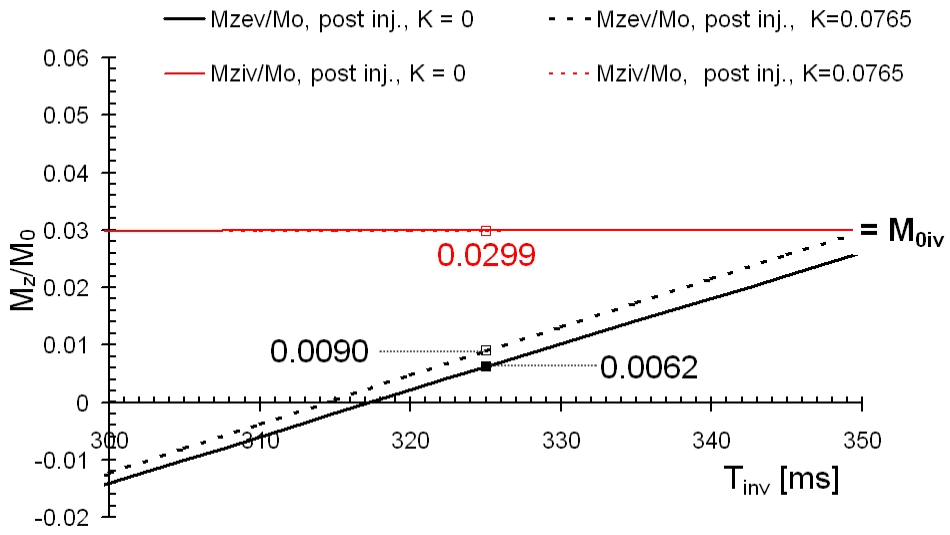

a

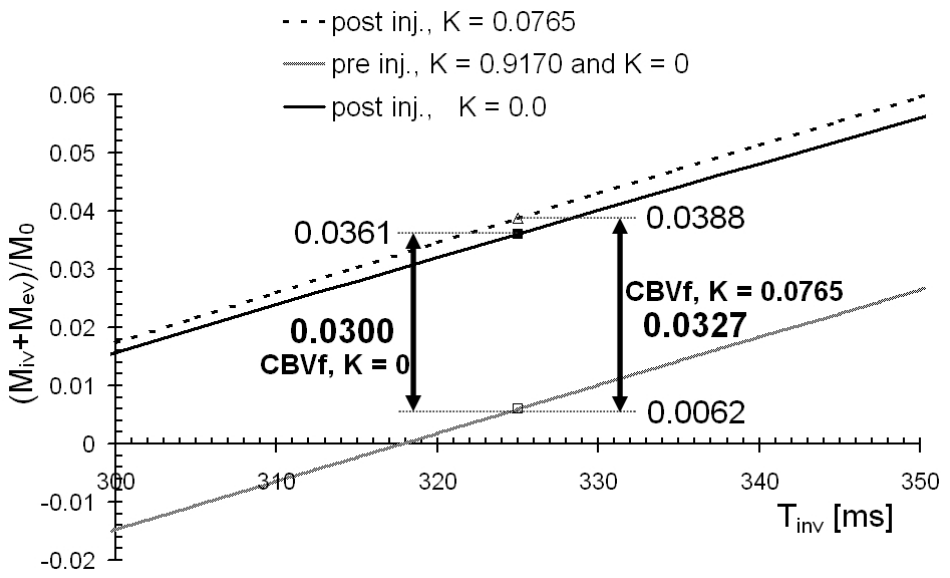

b

For the VASO method (Lu et al. 2005), a rough estimation of the water exchange impact using the reported intrinsic and extrinsic MRI parameters for 1.5 T indicates that for τ_{exch} = 630 ms (K = 0.2841 after CA administration) the CBVf is overestimated by almost 75% (5.2% instead of 3% for T_{1ev} = 1000 s).

Since the permeability of the BBB to water increases for several brain pathologies, it is important to minimize the sensitivity of the $RSST_1$ method to transepithelial water exchange. The water exchange effect can be reduced by shortening T_{inv}, allowing the system less time to exchange water across the vascular boundary (Donahue et al. 1996; Larsson et al. 2001). For example, with the couple of parameters TR/T_{inv} = 500 ms/225 ms, the overestimation would be reduced to less than 4% for $T_{1iv} = T_{inv}/5$ = 45 ms and τ_{exch} = 630 ms.

1.7.5.2. Intra-/extracellular water exchange in blood

The blood itself forms a two compartment system. The volume fraction occupied by erythrocytes, the hematocrit, varies between individuals (between 0.38 and 0.50 in healthy subjects) as well as within the same subject. In the normal cerebral microvasculature, the hematocrit drops to 85 % of the macrovascular hematocrit (Cremer and Seville 1983; Iannotti et al. 1987) but in pathological tissue, such as in tumors, the microvascular hematocrit varies greatly. At the CA doses and relaxivities used in this study, the shutter speed was still one order of magnitude lower than the water exchange rate between erythrocytes and plasma ($\tau_{exch}^{-1} \approx 125\ s^{-1}$). In this fast exchange limit, the water of the whole blood compartment is affected by the presence of the CA, and it is the CBV that is measured and not the plasma volume. It is therefore not necessary to know the regional hematocrit.

1.7.6. SNR

The CBVf in rats being very small, only about 3% of the total tissue water contributes to the signal with the $RSST_1$ technique. The SNR is therefore rather low, compared to techniques that do not suppress the extravascular tissue. Noise decreases with the square root of the total integration time. Signal accumulation over at least 40 s is necessary to obtain a correct contrast of the CBVf map. Signal accumulation over up to 20 min during continuous CA infusion did not

improve the image quality significantly. Averaging over one to two minutes appears to be a good compromise.

In the in vivo MRI experiments using the $RSST_1$ method in combination with the IR-FLASH sequence that are subject of the following chapters, the same experimental setup as described in paragraph 1.6.1 was used, and the SNR was the same as reported in paragraph 1.6.3 (about 40).

Strategies for increasing the $RSST_1$ duration were demonstrated in this study. A long $RSST_1$ duration does not only allow CBVf mapping with increased SNR but can also be utilized for increasing the spatial resolution or the volume coverage.

1.7.7. Dynamic imaging using the $RSST_1$ method

The data are obtained in an imaging mode that not only permits detection of regional but also of temporal variations of the CBVf, which can be the result of changes in the animal's physiological condition, pharmacological stimuli or functional activation studies. However, these changes are superimposed upon signal changes that include a drift of the signal intensity back to its pre-contrast value, as the CA is gradually eliminated from the vascular system, or a signal increase due to CA extravasation in case of a BBB lesion.

The S_{pre} and the S_{0pre} signals acquired before CA injection are temporally invariant (Eq. I-4). The S^{norm} signal in Eq. I-4 is a function of time and can be used to monitor the temporal evolution of the CBVf during the $RSST_1$ interval observable as a constant signal from a ROI located in a large vessel and under the condition of vascular confinement of the CA:

$$S^{norm}(t) = CBVf(t) \qquad \textbf{Eq. I-7}$$

A long $RSST_1$ duration would therefore also be of benefit for functional MRI to compare regional CBVf variations induced by cerebral activation. The study of the CBV response to hypercapnia confirms the sensitivity of the method to physiologic CBVf variations. Its advantage in comparison to the BOLD technique is to provide absolute CBVf values, but its drawback is the need of exogenous CA injection.

If the vascular signal is in the $RSST_1$ regime and the CA leaks out of the microvasculature into the brain tissue, $S^{norm}(t)$ is a measure of the distribution volume of the CA.

1.7.8. Sensitivity to motion

The acquisition time for one slice with the FLASH technique is 750 ms, which leaves little time for head motion artifacts. Movement can easily be detected as a shift between two images (within the limits of the spatial resolution of the image). If movement occurs, the shifted images can be discarded, before averaging over the remaining ones to compute the CBVf map. In case of in plane motion, image registration methods are applicable to avoid discarding, taking advantage of extracerebral tissue inside the FOV that provides a sufficient SNR on the images acquired after CA injection.

1.7.9. Multiple-slice acquisitions

Depending on the CA relaxivity, its blood concentration and the injection mode a steady state of one to 60 min was achieved. During this steady state, instead of acquiring the same slice every TR to improve the SNR, acquisitions with higher spatial resolution, multi-slice or 3D acquisitions could be performed. Knowing the duration of the $RSST_1$ interval available after injection of a CA, acquisition of multiple slices can be achieved by acquiring a series of images of one slice, then by changing the frequency of the RF excitation pulse in order to acquire the same number of images of a different slice and so on. The slices could also be acquired in an alternating way (slice 1 - slice 2 - slice 3 - slice 1 - slice 2 - slice 3 …).

The signal has been modeled for alternating acquisitions of two and three slices using the exact equations without approximation for low α flip angles as in paragraph 1.3.2. Although the non slice selective inversion pulse inverts the magnetization of all slices every TR, were they acquired or not, allowing to globally maintain the dynamic equilibrium of the magnetization of all slices during the rapid MRI sequence, the slice selective α-pulses do not perturb the magnetization of the other slices, resulting in the following consequences:

1. while the blood magnetization is immediately (after the first inversion) in a dynamic equilibrium, the dynamic equilibrium of the tissue magnetization takes more inversions to install. Consequently more dummy scans are needed at the beginning of the acquisition.

2. at t = T_{inv}, the blood magnetizations of all slices have fully relaxed to their thermal equilibrium M_{0iv}, whether the slice is being acquired or not. However, the suppression of the tissue magnetization is less good (M_{ev}(325 ms) = 0.015 M_{0ev}) when the slice is being acquired compared to the suppression obtained with single slice acquisitions (M_{ev}(325 ms) = 0.006 M_{0ev}).

During a typical time window of five minutes after injection of 0.1 mmol/kg P760, up to 5 slices can be acquired, allocating one minute for each slice, corresponding to 80 images. From 50 images upwards (≈ 40 s) CBVf maps with a reasonable SNR can be obtained.

The $RSST_1$ technique uses a short TR. Fig. I-14a shows that almost half of the TR = 750 ms is exploited by the FLASH module when 32 phase encoding steps are acquired. As illustrated in Fig. I-14b, the acquisition of multiple slices during the TR of 750 ms would only be feasible for a lower spatial resolution. In addition slice selective inversion pulses are needed in this case. After CA injection, slice selective inversion is compatible with the $RSST_1$ technique without inflow-outflow effect, because the blood of the entire body has a T_1 < 1/5 T_{inv}. The blood magnetization is completely relaxed to M_{0iv} prior to the FLASH acquisition, whether the blood water protons have experienced the inversion pulse or not. However, before CA injection, optimal suppression of the blood compartment could not be achieved because of the inflow of noninverted spins.

Fig. I-14:

a: Timing diagram of the IR-FLASH sequence with TR = 750 ms (time interval between two successive π pulses) , T_{inv} = 325 ms, TR_{FLASH} = 10.5 ms (time interval between two successive α-pulses) and α = 10°. N_k = 32 k-space lines are acquired. RF = radio frequency transmission, GS = slice selection gradient, GP = phase encoding gradient, GR = readout gradient.

b: Two or more slices can only be acquired within one TR interval, if the spatial resolution is reduced and the inversion pulses are slice selective.

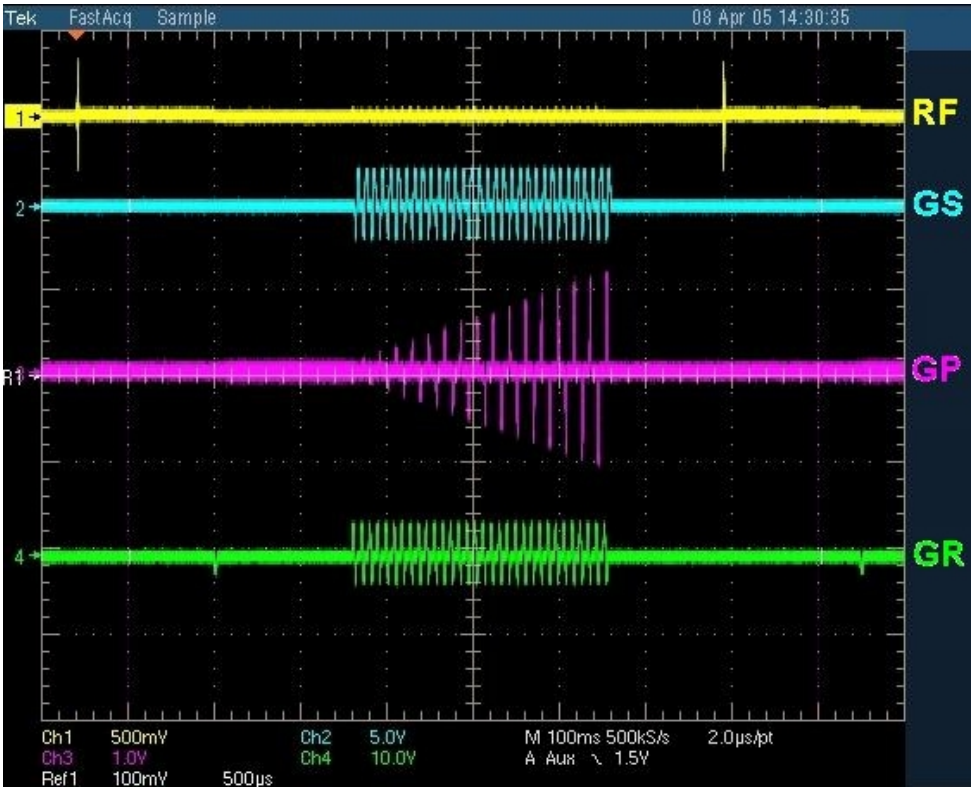

a

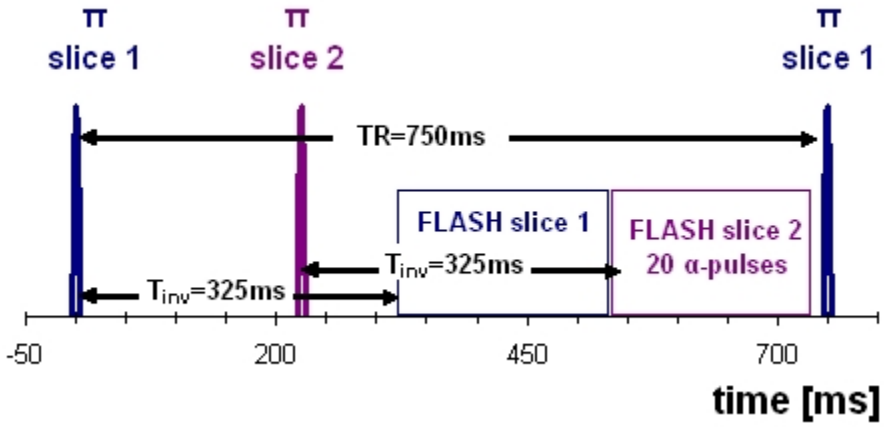

b

2. Chapter II: CBVf mapping in healthy rat brain using the $RSST_1$ method with SINEREM

2.1. Introduction

In this chapter it will be shown that the $RSST_1$ method can be used in combination with superparamagnetic iron oxide particles having a high transverse relaxivity. Since the $RSST_1$ method for CBVf quantification is based on the longitudinal relaxation of blood water protons, the sensitivity of the method to transverse relaxation effects has to be minimized. This can be achieved by shortening the echo time using nonselective hard RF pulses. Here, the blood signal is acquired in a three dimensional projection reconstruction mode. This development is aimed at the use of the CA SINEREM® from Guerbet Laboratories, which has interesting pharmacokinetic properties and is approved for clinical use.

French Introduction

Chapitre II : Mesure de la fVSC par la méthode $RSST_1$ sur des cerveaux de rat sain utilisant le SINEREM

Dans ce chapitre, on montre dans quelles conditions, le SINEREM est utilisé comme AC superparamagnétique dans la méthode $RSST_1$. La motivation de ce travail vient du fait que cet AC est déjà utilisé pour des applications chez l'Homme et que des études sur des modèles de tumeurs C6 ont montré que son extravasation est limitée dans la tumeur caractérisée par une rupture de la barrière hématoencéphallique (BHE). Comme cet AC a une très forte relaxivité transversale, une séquence Projection Rétroprojection à 3 dimensions ayant un temps d'écho extrêmement court a été développée. Dans ce chapitre, l'ensemble de ces développements, incluant des expériences de validation et des mesures de comparaison avec la méthode ΔR_2^* stationnaire sont présentées.

2.2. Characteristics of SINEREM

SINEREM (AMI-227) from Guerbet, Aulnay-sous-Bois, France, an USPIO, is a nanoparticle with a hydrodynamic diameter of 20–50 nm, mean 30 nm, (≈ 1 nm for Gd-DOTA), which consists of an iron oxide crystalline core of 4 to 6 nm, containing > 3000 Fe^{3+} ions, and a hydrophilic dextran coating. It is not initially recognized by the macrophage monocyte phagocytic system. Consequently, SINEREM is a blood pool CA with a long blood half life of 2 to 4 hours in the rat (Chambon et al. 1993) and in the order of 24 to 30 hours in man (Kooi et al. 2003). The half life is dose dependent. The distribution volume of SINEREM in rats is 52 to 55 ml/kg.

The use of SINEREM for CBV measurements is motivated by the following reasons:

1. owing to its long blood half life the blood concentration rapidly becomes independent from the injection pattern and may be considered to be constant throughout the imaging procedure
2. it is already available for human use, although angiogenesis assessment is not currently an approved clinical indication (macrophage imaging in atheroma, metastatic lymph node detection, multiple sclerosis, blood pool angiography)
3. a couple of studies (Julien et al. 2004; Le Duc et al. 1999; Tropres et al. 2004; Valable et al. 2006) suggest that SINEREM remains confined to the blood pool in some tumor types

2.3. The $RSST_1$ method in conjunction with SINEREM

SINEREM reduces both T_1 and T_2 relaxation times with a high r_2/r_1 ratio of 8.8 at 1.5 T and of 15 at 3 T, respectively. In addition, as described in Villringer et al (Villringer et al. 1988), the presence of a compartmentalized (super)paramagnetic CA creates magnetic field gradients within a voxel, causing accelerated loss of coherence of the MR signal and thus a signal intensity decrease. This T_2* effect is very pronounced with SINEREM and can be exploited for T_2* weighted first pass (Belliveau et al. 1990; Simonsen et al. 1999) or steady state CBV measurements (Payen et al. 2000) (cf. paragraph 9 in the literature review).

However, in T_1 weighted acquisitions, in order to produce a positive enhancement, a SINEREM injection has to be combined with a MR sequence optimized for low sensitivity to T_2 and T_2* effects.

In an in vivo imaging experiment at 2.35T using the IR-FLASH sequence for CBVf measurement such as described in chapter I, the signal arising from the brain microvasculature after injection of 200 µmol/kg SINEREM to a rat was not sufficient, even with a TE reduced to 1.6 ms, which is the minimum value.

To make use of the longitudinal relaxation effect of SINEREM for the CBVf quantification by the $RSST_1$ method we sought to implement an acquisition mode with reduced TE compared to the 2D IR-FLASH acquisition mode. Three dimensional acquisition modes do not require slice selective RF pulses and consequently the TE can be shorter. The projection reconstruction (PR) technique samples spatial frequencies on radial trajectories. By acquiring the center of K-space first, the effective TE can be kept short. A three dimensional projection reconstruction acquisition mode (PR3D) has therefore been implemented for image acquisition, to allow the use of SINEREM for CBVf mapping with the $RSST_1$ method. The PR3D sequence employed acquires one radial k-space line for each TR interval after a 90° readout RF pulse.

2.4. Preliminary experiments

2.4.1. Relaxivity of SINEREM at 2.35T in normal saline solution

The relaxivities of SINEREM at 2.35T in normal saline solution were measured to estimate the dose necessary for sufficient reduction of the blood T_1 to allow full relaxation to thermal equilibrium of the blood water during the $RSST_1$ acquisitions.

Relaxometry

After reconstitution in normal saline (NaCl 0.9%), the mother solution of SINEREM has a Fe^{3+} concentration of 357 mM ≈ 20 mg Fe^{3+}/ml. The T_1 and T_2 relaxation times were measured for seven SINEREM concentrations (0.5, 1.0, 1.5, 2.0, 3.0, 4.0, 6.0 mM ± 0.5%) and for normal saline (0.0 mM SINEREM) in NMR tubes filled with 0.2 ml solution. In this and all following experiments the homogeneous RF coil was used for emission and the double loop circular surface RF coil for detection. A custom-built holder for NMR tubes and 1 ml syringes was used.

After global shimming a FWHM of 5 Hz was obtained in normal saline solution. For the SINEREM containing solutions the FWHM (magnitude) was 20 Hz (0.5 mM) to 187 Hz (6.0 mM).

The longitudinal relaxation times T_1 of the samples were measured with a spectroscopic inversion recovery sequence. The TR was 20 s and the 15 T_{inv} were ranging from 100 ms to 19 s for 0.0 mM SINEREM. For all other concentrations the TR was set to 2 s and the 15 T_{inv} were in the range 12 ms to 1.8 s.

Single echo T_2 measurements were performed with a conventional spectroscopic single spin echo sequence using hard pulses. For the 0.0 mM concentration the TR was 20 s and 15 TEs ranged from 100 ms to 18 s. For all other concentrations the TR was set to 2 s and the 15 TEs ranged from 2 to 30 ms.

All measures were repeated three times. The temperature in the magnet was 19.2 ± 0.4 °C.

Using Microsoft Excel, a least squares procedure was used to fit the integrated spectral signal to a relaxation model. For the T_1 measure the equation was

$$S(T_{inv}) = S_0 \left| 1 - inv \cdot \exp(-T_{inv}/T_1) \right| \quad \text{(cf. Eq. 0-2)}$$

with S_0, inv and T_1 as free parameters. S_0 is the signal corresponding to the magnetization at thermal equilibrium and inv is the inversion factor, which is close to inv ≈ 2. For the T_2 measure the data was fitted to

$$S(TE) = S_0 \left(1 - \exp\left(-TR/T_1 \right) \right) \exp\left(-TE/T_2 \right)$$

with S_0 and T_2 as free parameters.

The r_1 and r_2 relaxivities were obtained by fitting a linear equation to the relaxation rate differences

$$\Delta R_i = R_i - R_{i0}, \quad i = 1,2,$$

where R_i are the relaxation rates obtained at the seven different SINEREM concentrations and R_{i0} is the relaxation rate of normal saline solution.

Results

For normal saline solution, T_1 = 2.879 ± 0.016 s and T_2 = 1.265 ± 0.006 s. A linear dependence of the relaxation times with SINEREM concentration was observed. The result of the relaxivity measurements of SINEREM in normal saline solution is shown in Fig II-1. The ratio r_2/r_1 is 17.7.

Fig. II-1: Relaxation rates versus SINEREM concentration in normal saline solution at room temperature. The slopes of the linear regressions correspond to the relaxivities of SINEREM.

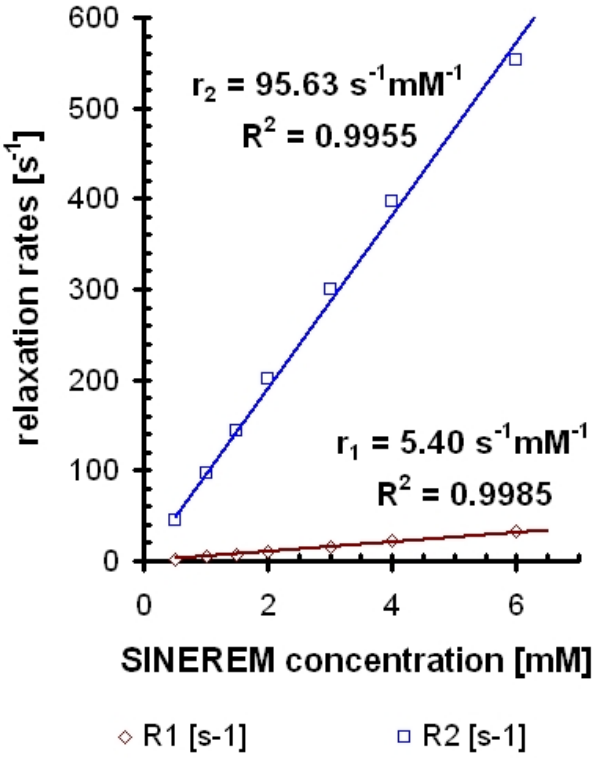

Assuming similar relaxivities of SINEREM in blood, it can be calculated that a blood concentration of 3.6 mM SINEREM is necessary to reduce the blood T_1 to about 50 ms. This blood concentration reduces the blood T_2 to less than 3 ms. A 3.6 mM blood concentration necessitates the injection of a SINEREM dose in the range of 0.18 to 0.25 mmol/kg, since rats have total blood volumes between 50 and 70 ml per kilogram body weight.

2.4.2. In vitro doses studies

Determination of blood T_1 and T_2

Accurate knowledge of the relationship between CA concentration and blood relaxation is a critical requirement for quantitative CBV assessment using classical contrast-enhanced MRI. For CBVf measurements using the $RSST_1$ technique it is sufficient to assure a blood $T_1 < T_{inv}/5$ if the attenuation due to transverse relaxation effects is negligible. However, since the r_2 relaxivity of SINEREM is high, the transverse relaxation effects (R_2 and R_2*) will play a role, and it is important to know the blood T_2 to estimate these effects.

A blood $T_1 < 65$ ms is necessary for CBVf mapping using the $RSST_1$ method with the sequence parameters TR/T_{inv} = 750 ms/325 ms, and a blood $T_1 < 45$ ms for the couple TR/T_{inv} = 500 ms/225 ms. A rough estimation using the relaxivities in normal saline solution, shows that SINEREM doses of about 200 µmol/kg and 300 µmol/kg have to be injected for sufficient reduction of the blood T_1. We wanted to know the transverse relaxation of blood resulting after injection of these doses, and for how long after injection the longitudinal relaxation of blood remained sufficiently low to satisfy the $RSST_1$ conditions. Instead of conceiving an in vivo experiment to investigate the pharmacokinetics of SINEREM in rats, blood was sampled at various time points after SINEREM injection to measure the relaxation times of blood in vitro.

0.5 ml of arterial rat blood was drawn into heparinized syringes before and 5, 15, 30, 60 and 120 minutes after intravenous injection of 200 and 300 µmol Fe^{3+}/kg. After each blood sampling, the cannula was flushed with a small amount (0.1 to 0.2 ml) of heparinized normal saline to avoid blood clotting, without replacing the sampled blood or rehydrating the rat. Relaxometry using whole blood is difficult, since it depends on the hematocrit, the oxygenation and the accumulation of the erythrocytes in the lower part of the syringe during the measure. To verify the measures on whole blood with measures on plasma, one additional milliliter blood was drawn with the first (before SINEREM injection) and the last (120 min post injection) blood sample, and centrifuged at 4000 rpm at 4°C for 10 minutes to obtain 0.5 ml plasma. Three rats were used for each dose.

The T_1 and T_2 measures were carried out as described for the relaxivity measurements of SINEREM in normal saline. Since the presence of SINEREM in the blood results in a large width of the water signal (the FWHM was several hundreds Hertz), the shimming procedure was only performed on blood without SINEREM with a resulting FWHM of 13 to15 Hz (magnitude). Using the custom-made holder, the syringe containing native blood could be replaced by the other syringes containing SINEREM in exactly the same position and without removing the setup from the magnet. For blood without SINEREM a TR of 10 s, 15 T_{inv} in the range of 4 ms to 9 s and 15 TE in the range 2 ms to 1 s were used. For blood and plasma sampled after the SINEREM injection the TR was 500 ms. Fifteen T_{inv} in the range of 4 to 450 ms and 15 TE in the range of 2 to 100 ms were used.

In vitro blood volume experiment

During the same experiment, the RF sequence used for the PR3D acquisition mode was used without projection gradients and with the typical timing parameters of the $RSST_1$ method for CBVf measurement. The purpose of this measure was to evaluate the transverse relaxation effect of blood at the TE used for later in vivo CBVf measurements.

The first acquisition was performed with TR/T_{inv} = 750 ms/325 ms using an adiabatic inversion pulse followed by a 90° read out pulse. This acquisition was supposed to suppress the signal from blood sampled before injection and this signal is referred to as S_{pre}. Performed for blood sampled after SINEREM injection, the signal (named S_{post}) was supposed to be proportional to the thermal equilibrium magnetization of blood.

The second acquisition was performed with a TR = 8 s and a 90° readout pulse without inversion. The signals acquired are referred to as S_{0pre} and S_{0post} for signals from blood sampled before and after SINEREM injection, respectively. Twenty repetitions were averaged for both acquisitions.

The signal from the first acquisition was divided by the signal from the second acquisition for each syringe, $\frac{S_{pre}}{S_{0pre}}$ and $\frac{S_{post}}{S_{0post}}$ for the blood sampled before and after SINEREM injection, respectively. Since the $\exp\left(-TE/T_2\right)$ factor cancels out, the $\frac{S_{post}}{S_{0post}}$ ratio should be about one

for all blood samples having a T_1 < 65 ms corresponding to the "blood volume fraction" of the syringe. The ratio $\frac{S_{pre}}{S_{0pre}}$ should show the efficiency of the blood signal suppression with the RF sequence.

These measurements were performed on whole blood. To verify whether the precipitation of red blood cells during the measurements had an effect, in one experiment, both spectroscopic acquisitions were repeated on the same syringe at approximately 1, 5, 15, 25 and 35 min after rotating it 180° around its axis.

Results

In this study, the relaxation times of blood sampled before CA injection of (n = 6) are T_1 = 1323 ± 45 ms (range 1249 to 1380 ms) and T_2 = 174 ± 27 ms (range 133 to 206 ms) consistent with those reported previously (Thomas et al. 2001). The difference with the mean T_1 of whole blood measured in Chapter I, may be the result of different hematocrit or oxygenation (which was not measured in this experiment).

The blood T_1 after injection of 200 µmol Fe^{3+}/kg SINEREM was about 60 ms for the first four samples (up to one hour). The T_2 ranged from 2.51 ms at 5 min to 3.62 ms at 120 min post injection. After 300 µmol Fe^{3+}/kg SINEREM the T_1 was about 40 ms for all five blood samples (up to two hours). The blood T_2 ranged from 1.97 ms at 5 min to 2.58 ms at 120 min post injection.

The T_1 of plasma and whole blood is similar before CA injection. For the sampling point at 120 min post injection, the mean plasma R_1 was a factor of 1.5 times higher than the R_1 of blood, consistent with a hematocrit of about 33%.

The signal ratios $\frac{S_{pre}}{S_{0pre}}$ and $\frac{S_{post}}{S_{0post}}$ (given in %) are presented in Fig. II-2a for the 200 µmol Fe^{3+}/kg dose and in Fig. II-2b for the 300 µmol Fe^{3+}/kg dose, together with the respective results

of the T_1 measurements. The signal ratios $\frac{S_{post}}{S_{0post}}$ for the measurements on plasma were equal to one within 1%.

The precipitating blood cells had indeed an effect on the signal. The signals from both acquisitions (TR/T_{inv} = 750 ms/325 ms and TR = 8 s) were lower after agitation of the blood sample. The signal increased with time and became constant for the acquisitions performed more than 15 min after the agitation.

Fig. II-2: Signal ratios $\frac{S_{pre}}{S_{0pre}}$ and $\frac{S_{post}}{S_{0post}}$ (left axis) and mean T_1 of blood (right axis) before and up to two hours after injection of 200 µmol/kg SINEREM (n = 3) (a) and after 300 µmol/kg SINEREM (n = 3) (b). The ratio $\frac{S_{pre}}{S_{0pre}}$ quantifies the efficiency of the blood signal suppression with the sequence parameters TR/T_{inv} = 750 ms/325 ms. The ratio $\frac{S_{post}}{S_{0post}}$ is ideally equal to one and corresponds to the "blood volume fraction" in the syringe.

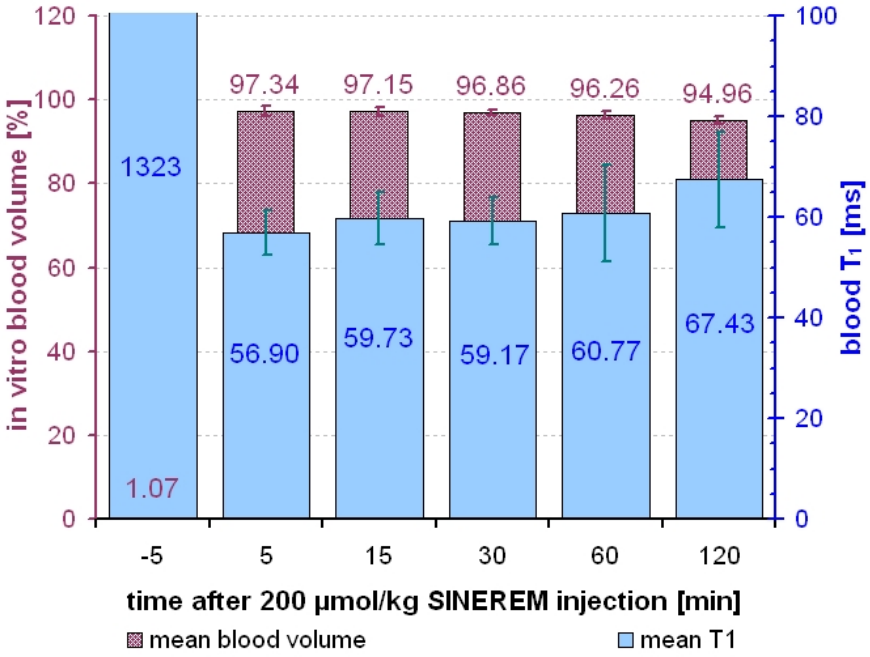

a

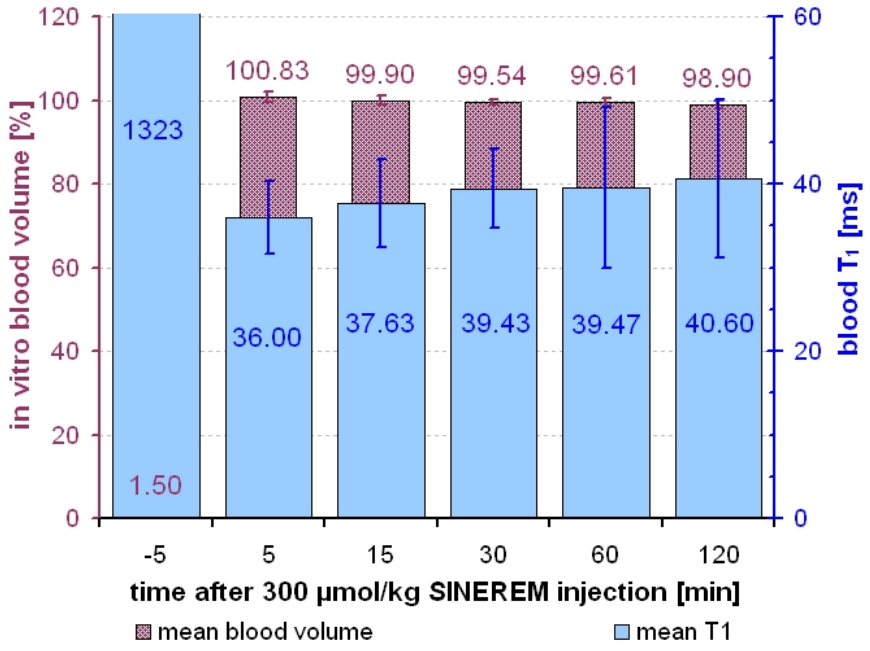

b

2.4.3. Discussion

Accuracy of blood relaxation time measurements

The purpose of this in vitro experiment was to determine for how long the $RSST_1$ conditions are satisfied after injection of SINEREM at two different doses. Only the first blood sample correctly reflects the relaxation times expected in vivo after SINEREM injection, since the following blood samples were affected by progressive dilution due to successive blood sampling within approximately two hours (5 ml in total) and to dehydration of the rat. From the second blood sample onwards, the T_1 and T_2 are overestimated with respect to the blood T_1 and T_2 in the rats if no blood had been sampled. For this reason, sampling for the measurements on plasma was avoided for the first time points after injection.

A T_1 < 65 ms was measured for the blood drawn up to 60 min post injection of 200 µmol/kg SINEREM. However, even the blood drawn two hours after injection has a T_1 only slightly higher than 65 ms, despite progressive dilution of the SINEREM concentration. With an injection of 300 µmol/kg SINEREM the $RSST_1$ method could also be applied with a TR of 500 ms and a T_{inv} of 225 ms, since the blood T_1 is lower than 225 ms/5 = 45 ms for all time points. However, the

blood T_2 is less than 2 ms after injection and necessitates an acquisition with very short TE. From these results it can also be concluded that the blood half life of SINEREM at both doses is at least two hours.

In vitro signal ratios

With the timing parameters TR/T_{inv} = 750 ms/325 ms, the signal of blood sampled before SINEREM injection could be suppressed to less than 0.015 M_0.

After injection of 300 µmol/kg SINEREM the $\frac{S_{post}}{S_{0post}}$ ratio was unity within 1% error. Although the $\frac{S_{post}}{S_{0post}}$ signal ratios are slightly lower than expected for the blood sampled after 200 µmol/kg SINEREM injection, the error of the "blood volume" measure was within 3 to 4% for the blood samples having a T_1< 65 ms. The signal attenuating factor is related to precipitating or unevenly distributed erythrocytes in whole blood, as demonstrated by the fact that the $\frac{S_{post}}{S_{0post}}$ ratio obtained from plasma (in which this factor is removed) was unity. This signal attenuating factor is without importance in an in vivo experiment since the blood flow maintains a homogeneous distribution of erythrocytes.

2.5. Theory

2.5.1. The three dimensional projection reconstruction acquistion

As can be seen in Fig. II-2a, an injection of 200 µmol Fe^{3+}/kg SINEREM decreases the blood T_1 to < 65 ms for at least one hour. This time interval can be exploited for CBVf measurements with the $RSST_1$ technique.

The signal during the PR3D sequence can be modeled. To verify whether the tissue signal at the time of acquisition t = T_{inv} is effectively nulled and whether the blood signal is at thermal

equilibrium, the longitudinal magnetization M_z was calculated for four time points during the sequence (Jivan et al. 1997):

1. just before the π pulse (π-) (Eq. [5] in (Jivan et al. 1997)):

$$\frac{M_z^{(\pi-)}}{M_0} = 1 - \exp\left(-\frac{TR - T_{inv}}{T_1}\right) + \frac{M_z^{\left(\frac{\pi}{2}+\right)}}{M_0}\exp\left(-\frac{TR - T_{inv}}{T_1}\right)$$

2. just after the π pulse (π+):

$$M_z^{(\pi+)} = -M_z^{(\pi-)}$$

3. just before the π/2 pulse (π/2-) (Eq. [3] in (Jivan et al. 1997)):

$$\frac{M_z^{\left(\frac{\pi}{2}-\right)}}{M_0} = 1 - \exp\left(-\frac{T_{inv}}{T_1}\right) + \frac{M_z^{(\pi+)}}{M_0}\exp\left(-\frac{T_{inv}}{T_1}\right)$$

4. just after the π/2 pulse (π/2+):

$$M_z^{\left(\frac{\pi}{2}+\right)} = 0$$

The longitudinal relaxation time of the intra- and extravascular compartments after CA injection was set to T_1 = 50 ms and T_1 = 1200 ms, respectively, and the longitudinal magnetization at dynamic equilibrium was calculated for the couple TR/T_{inv} = 750 ms/325 ms. At $t = T_{inv}$, the extravascular magnetization has 0.98% of its thermal equilibrium value and the intravascular magnetization has 99.7% of its thermal equilibrium value. Theoretically, a signal relaxing with 1323 ms < T_1 < 1450 ms, such as the intravascular magnetization before CA injection would be suppressed to less than 0.29% of its thermal equilibrium value.

2.5.2. Acquisition of the thermal equilibrium signal of the cerebral tissue

Since with the PR3D imaging mode one K-space line (projection) is acquired during each TR interval, the acquisition is rather slow. In particular, this is a problem for the acquisition of the thermal equilibrium signal of the cerebral tissue, used for signal normalization (S_{0pre}, Eq. I-4).

The sensitivity of the RF coils covers a large volume. To avoid aliasing, a large FOV, in particular in the axial direction of the animal, has to be chosen, and the acquisition of an image with acceptable spatial resolution in all three dimensions requires a large number of projections. A 3D acquisition with a similar spatial in-plane resolution as obtained using the FLASH mode in TR = 750 ms ($1 \times 1 \times 2$ mm^3) takes 24 minutes. This is compatible with the duration of the $RSST_1$ interval obtained after 200 µmol Fe^{3+}/kg. The acquisition of the thermal equilibrium signal of the cerebral tissue (S_{0pre}) performed with a TR of 10 s as before would take several hours even if the π-pulse is omitted.

If the TR is shortened, the resulting T_1 weighting has to be accounted for. The equilibrium signal can be determined from a T_1 weighted acquisition if the T_1 of the tissue voxels generating this signal is known. Global T_1 values for the brain tissue were measured in Chapter I. Single slice T_1-maps could be easily calculated from the IR-FLASH acquisitions performed in about 10 minutes. The acquisition of multiple slices or a 3D T_1 map would again take a lot of time.

Another possibility to shorten this acquisition time is to reduce the flip angle of the read out pulse, because the longitudinal magnetization takes less time to approach the thermal equilibrium value M_0.

Computing the longitudinal magnetization for TR = 1.2 s, α = 10° and a tissue T_1 in the range of 1 to 2 s using

$$\frac{M_z^{(\alpha-)}(TR,T_1)}{M_0} = 1 - \exp\left(-\frac{TR}{T_1}\right) + \frac{M_z^{(\alpha+)}}{M_0}\exp\left(-\frac{TR}{T_1}\right)$$

for the longitudinal magnetization just before the α-pulse, yields the following results: $M_z^{(\alpha-)}$=0.9935 M_0 for T_1 = 1 s, and

$M_z^{(\alpha-)}$ = 0.9818 M_0 for a T_1 = 2 s.

The difference is only one percent. This shows that for very low α-pulses, the tissue magnetization is almost independent of the tissue T_1. For a large range of possible tissue T_1, the acquired signal corresponds to S_0 with less than 2% error.

The transverse magnetization after the α pulse is:

$M_{xy} = M_0 \sin\alpha$.

Therefore, the acquired signal has to be divided by sin 10° = 0.174.

2.5.3. CBVf calculation

Denoting S_{0iv} and S_{0ev} the signals that could be measured for the thermal equilibrium magnetization of the intra- and extravascular compartments, respectively, $S_0 = S_{0iv} + S_{0ev}$ the signal that could be measured for the thermal equilibrium magnetization of the cerebral tissue, the equations describing the signals that can be acquired in an IR experiment with a TR/T_{inv} = 750 ms/325 ms, α = 90° before (S_{pre}) and after (S_{post}) CA injection and in a simple (without preparatory π-pulse) gradient echo experiment with a TR = 1.2 s and α = 10° before CA injection (S_{0pre}) are:

$$S_{pre} = 0.0098 \cdot S_{0ev} \cdot \exp\left(-\frac{TE}{T_{2\,ev}}\right)\sin(90°) + 0.0029 \cdot S_{0iv} \cdot \exp\left(-\frac{TE}{T_{2\,iv\,pre}}\right)\sin(90°)$$

$$S_{post} = 0.0098 \cdot S_{0ev} \cdot \exp\left(-\frac{TE}{T_{2\,ev}}\right)\sin(90°) + 0.9970 \cdot S_{0iv} \cdot \exp\left(-\frac{TE}{T_{2\,iv\,post}}\right)\sin(90°)$$

$$S_{0\,pre} \geq 0.9818 \cdot S_0 \cdot \exp\left(-\frac{TE}{T_{2\,tissue}}\right)\sin(10°)$$

And the normalised signal $S^{norm} = \frac{S_{post} - S_{pre}}{S_{0pre}}$ is:

$$S^{norm} = \frac{0.9970 \cdot S_{0iv} \cdot \exp\left(-\frac{TE}{T_{2\,iv\,post}}\right) - 0.0029 \cdot S_{0iv} \cdot \exp\left(-\frac{TE}{T_{2\,iv\,pre}}\right)}{0.9818 \cdot S_0 \cdot \exp\left(-\frac{TE}{T_{2\,tissue}}\right)\sin(10°)}$$

Neglecting the term to be subtracted in the numerator (< 0.3% of the blood signal), and approximating the remaining numeric factors to 1, results in:

$$S^{norm} = \frac{S_{0iv} \cdot \exp\left(-\frac{TE}{T_{2\,iv\,post}}\right)}{S_0 \cdot \exp\left(-\frac{TE}{T_{2\,tissue}}\right)\sin(\alpha)} \qquad \textbf{Eq. II-1}$$

Where α = 10°.

Using the PR3D with the timing parameters employed for signal modeling results in a normalized signal S^{norm}, which is equal to the CBVf after correction for the factor sin(α) if a signal attenuation

due to the transverse relaxation can be neglected for very short TE. However, due to the very short blood T_2 after injection, a R_2-attenuation of the S_{post} signal can not be avoided and has to be accounted for.

2.6. In vivo CBVf measurements

2.6.1. The steady state ΔR_2^* MRI technique for comparison

To validate the $RSST_1$ method, the CBVf measurements it provides should be compared to a standard technique for measurement of CBVf in the same animals. The "standard" techniques available in the laboratory are limited to other MRI techniques for CBVf measurement. Alternatively histological validation could be used.

In this study SINEREM is used for the CBVf measurement by the $RSST_1$ method. This opens the possibility of using a R_2^*-based MRI method for CBVf mapping immediately afterwards on the same animal without repeated CA injection, taking advantage of the long blood half life of SINEREM. The steady state susceptibility contrast (steady state ΔR_2^*) MRI method developed in the laboratory (Payen et al. 2000) is well established and frequently implemented in the research projects of the laboratory (Julien-Dolbec et al. 2002; Julien et al. 2004; Tropres et al. 2004). The steady state ΔR_2^*-method does not rely on a particular blood concentration or blood relaxation times. Instead, the CBVf measure with this technique necessitates additional measurements on sampled blood to determine the susceptibility difference ΔX induced in blood by the SINEREM injection.

The physiologic conditions (temperature, arterial blood pressure and blood gases) of the animal have to be maintained as constant as possible between the two measures, otherwise the CBVf might be altered for “biological” reasons. In the previous study using P760 for the CBVf measure by the $RSST_1$-method, the steady state ΔR_2^*-technique has not been used for comparison because the time interval necessary for at least partial elimination of the first CA, to avoid interference between the two different CAs, is no less than 2 hours. Intraindividual CBVf variations risk being as large as interindividual ones.

2.6.2. Animals

Eight healthy rats, four rats of the Fischer strain (weighting 222 to 276 g) and four of the Wistar strain (weighting 265 to 444 g) were imaged in this study using the PR3D $RSST_1$ method followed by the steady state ΔR_2^* method. CBVf measurements by the steady state ΔR_2^* method alone are available for four additional Wistar rats (277 to 388 g). All rats were obtained from Charles River.

The rats were anesthetised, prepared and positioned as described in chapter I. This and all following experiments were carried out under spontaneous breathing. The rectal temperature and the mean arterial blood pressure were monitored throughout the experiment, and blood gases were analyzed just before the CBVf measure by the $RSST_1$-method. A single SINEREM injection was used for the CBVf measure by both MRI methods.

2.6.3. CBVf by the $RSST_1$ method

The PR3D acquisition was performed in a gradient echo mode with hard excitation pulses, the duration of which was approximately 50 µs. To minimize the duration of the excitation pulses they were calibrated for the maximum pulse amplitude available. The K-space is sampled radially in m $\times$ n projections beginning with the center of K-space as illustrated in Fig. II-3, first in one plane by incrementing the θ-angle in m steps (projections) up to 360°. After completion of one plane, the Φ-angle is incremented in n steps (cf Fig. II-3 c), up to 180° in order to acquire planes in the 3rd dimension of K-space.

Fig. II-3:

a: sequence timing diagram of the inversion recovery projection reconstruction acquisition for the first five radial lines in the central k_x-k_y plane of K-space. Green arrow = TR = 750 ms, blue arrow = T_{inv} = 325 ms, violet arrow = TE = 0.7 ms.

b: representation of the acquired radial trajectories in the k_x-k_y plane of K-space

c: a sphere in K-space is acquired by varying the gradient in the third dimension

$$G_z = G\cos(\Phi(t))$$

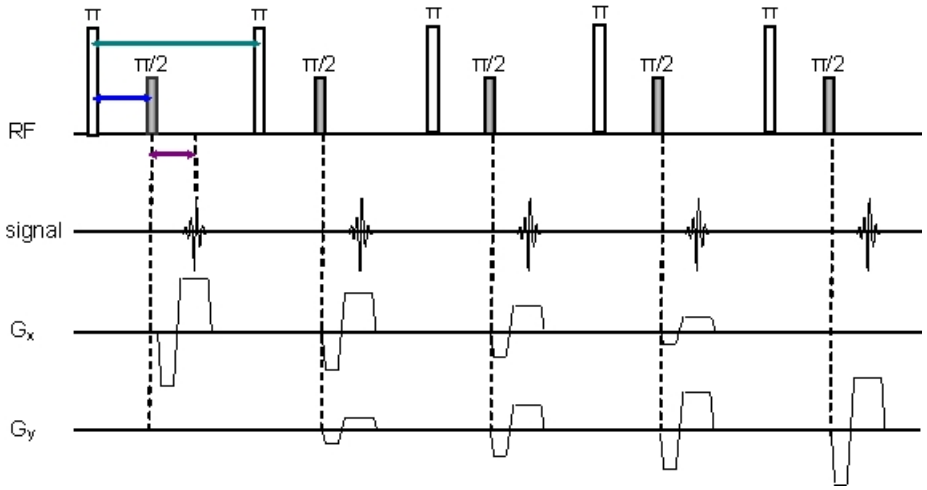

a

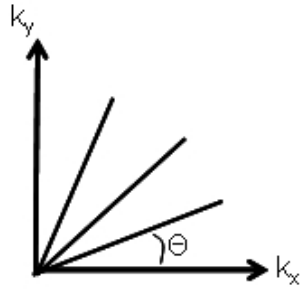

b

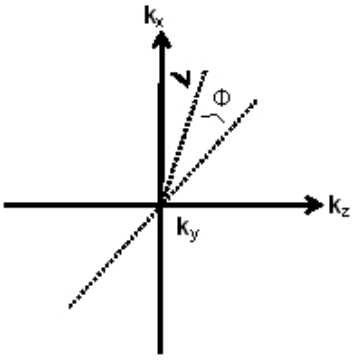

c

An adiabatic inversion pulse was used for the S_{pre} and S_{post} acquisitions. Transmitter and receiver gains were kept constant for all PR3D acquisitions. The FOV was 108 × 108 × 216 mm^3 (factor 2 along z-axis), the number of samples 2048 and the TE = 0.7 ms. The other sequence parameters were as follows:

- For the proton density weighted acquisition (S_{0pre}): 31 × 61 projections, no inversion, TR = 1.2 s, α = 10°, 15 dummy scans, duration ≈ 38 min

- For the IR-PR3D (S_{pre}, S_{post}): 31 × 61 projections, TR = 750 ms, T_{inv} = 325 ms, α = 90°, 15 dummy scans, duration ≈ 24 min

- For a high resolution PR3D acquisition with soft tissue contrast: 63 × 123 projections, no inversion, TR = 100 ms, α = 23° (Ernst angle), 30 dummy scans, duration ≈ 13 min

2.6.4. CBVf by the steady state ΔR_2^* method

The multi-slice multi gradient echo spin echo (MGESE) sequence is a hybrid gradient echo spin echo sequence which acquires a series of gradient echo images at different TE to estimate T_2^* values and a spin echo image to estimate T_2 values simultaneously. For each phase encode gradient, multiple refocusing of the readout gradient after a 90° RF pulse generate the echos. A spin echo is then generated by a 180° refocusing RF pulse.
Five adjacent coronal slices of 2 mm thickness were acquired using the MGESE sequence with the following parameters: FOV 32 × 32 mm^2, matrix 128 × 66, TR = 6 s, 7 gradient switches, TE = 6, 12, 18, 24, 30, 36, 42 ms for the gradient echo and 102 ms for the spin echo, 1370 samples, 2 averages, duration ≈ 13 min.

2.6.5. Imaging protocol

The timing diagram in Fig. II-4 summarizes the imaging protocol. Global field inhomogeneity was reduced to a FWHM of 45 to 50 Hz (magnitude) by shimming on the signal from a volume of interest 80 × 80 × 30 mm^3. The MGESE acquisition was performed followed by a first blood sample for the susceptibility measurement. The blood was immediately centrifuged as described before in paragraph 2.4.2 and the plasma was frozen. The PR3D sequence was then

used to acquire the proton weighted image (S_{0pre}), and the IR-acquisition with TR/T_{inv} = 750 ms/325 ms before SINEREM injection (S_{pre}). A 0.1 ml arterial blood sample was taken for blood gas analysis to verify whether the rat was under normocapnia.

SINEREM was manually injected as a bolus at a dose of 200 µmol Fe^{3+}/kg. The IR-acquisition with TR/T_{inv} = 750 ms/325 ms (S_{post}) was started 4 minutes after injection in order to allow equilibrium distribution of the CA throughout the blood pool. The post-injection MGESE acquisition was started as soon as the PR3D image was terminated (28 min post injection). A last blood sample was taken, centrifuged and the plasma frozen.

Finally, the high resolution PR3D image was acquired to help delineation of ROIs. Rats were then euthanized as described in chapter I.

Fig. II-4: Timing diagram showing the acquisitions performed with PR3D and MGESE

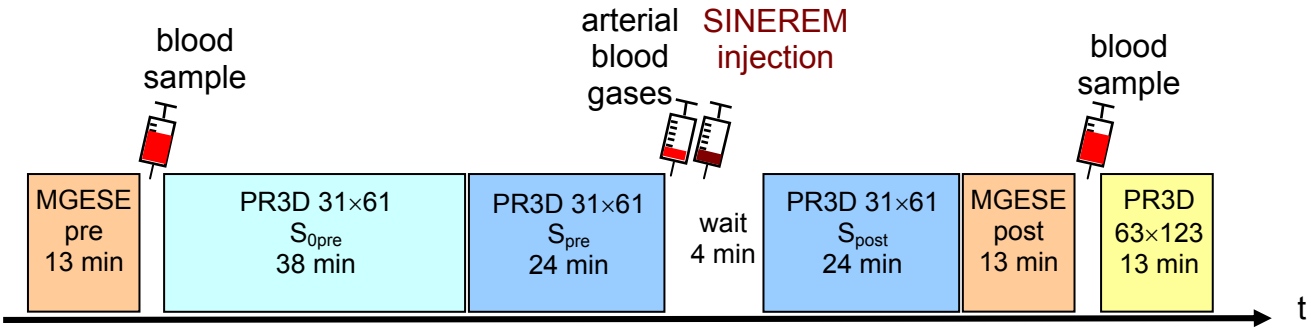

2.6.6. SINEREM induced blood susceptibility difference

The plasma samples were analyzed to determine the ΔX induced by the presence of iron particles in the blood pool. The iron concentration was deduced by measuring the R_2 difference of the plasma before and after SINEREM injection.

The pre-contrast and the post-contrast plasma samples were diluted in normal saline solution by a factor 8 and 20, respectively. The Carr-Purcell-Meiboom-Gill (CPMG) multiple spin echo pulse sequence consisting of a hard 90° RF pulse of 100 µs duration followed by an echo train induced by a series of hard 180° pulses was used for measuring T_2. For the diluted pre-contrast

samples, 600 echos were acquired with a first TE of 8 ms, for the diluted post-contrast samples, 400 echos with a first TE = 1 ms. Three acquisitions were performed on each sample for averaging. The signal arising from the plastic of empty Eppendorf microcentrifuge tubes was subtracted prior to fitting the echo amplitudes to

$$S(TE) = S_0 \exp(-TE/T_2),$$

using a custom-made Matlab (version 7.0.1) code.

The measured R_2^{pre} and R_2^{post} values were converted to the blood iron concentration $[Fe^{3+}]$ using the linear relation between R_2 and $[Fe^{3+}]$ previously established by inductively coupled plasma atomic emission spectrophotometry, and corrected for the respective dilution factor:

$$[Fe^{3+}] = \left(0.01055 \frac{\mu mol}{ml} s \cdot R_2 - 0.00024 \frac{\mu mol}{ml} \right) \cdot \text{dilution factor}$$

The magnetization induced by a 1 mM Fe^{3+} concentration in rat blood at 2.35T is 0.396 µT (Vaeth 1998). To convert this magnetization into a susceptibility difference ΔX in CGS units it has to be multiplied by the factor 0.4254:

$$\Delta X = 0.396\ \mu T\ mM^{-1} \cdot \Delta[Fe^{3+}]mM \cdot 0.4254$$

2.6.7. Image processing

PR3D data

The PR3D samples K-space data on a sphere. The image reconstruction of the PR3D acquisitions is achieved by a gridding interpolation of the K-space data onto a $36 \times 36 \times 72$ grid, a zero filling by a factor 4 in the x, y, and z direction, followed by a 3D discrete Fourier transform.

Two gridding algorithms were used:
The nearest neighbor (NN) algorithm, simply assigns the intensity value of the NN to the 3D Cartesian grid point.
The "averaged nearest neighbor" (ANN) algorithm uses the average intensity of the 16 nearest neighbors.

The reconstruction requires less than two minutes on a workstation (Xserve G5, Apple Inc).

The normalized signal $S^{norm} = \frac{S_{post} - S_{pre}}{S_{0pre}}$ was calculated voxel by voxel from the three PR3D acquisitions.

According to Eq. II-1, the S_{0pre} acquisition has to be corrected for the factor sin(10°) = 0.174. Before CA administration, the T_2 of blood and tissue is > 80 ms. Consequently, the term $\exp\left(-\frac{TE}{T_{2\,tissue}}\right)$ in Eq. II-1 is > 0.99 for a TE of 0.7 ms.

However, as shown in Eq. II-1, the intravascular signal component in the S_{post} acquisition has to be corrected for the R_2-attenuation. The mean T_2 of blood in the time interval from 5 to 30 min after 200 µmol Fe^{3+}/kg SINEREM injection was 2.83 ± 0.06 ms. Therefore, in this experiment, the factor $\exp\left(-\frac{TE}{T_{2\,iv\,post}}\right)$ = 0.78.

Thus, CBVf maps were calculated from the S^{norm} map by:

$$CBVf = S^{norm}\frac{\sin(10°)}{0.78}. \qquad \textbf{Eq. II-2}$$

Using ImageJ software (http://rsb.info.nih.gov/ij), the 3D data can be viewed in three orthogonal planes. Extracerebral tissue and background noise were masked and the CBVf values occurring in cerebral tissue were represented on a greyscale from 0 to 255. In the third dimension the planes had a thickness of only one voxel. Therefore ROI analysis was carried out on three transversal and three coronal planes on which the corpus callosum could be distinguished.

The SNR was evaluated on the S_{post} and on the S_{pre} acquisitions according to

$$SNR = \frac{S_{post}}{\sigma_S}$$

where S_{post} is the signal from a ROI in the brain, and σ_S is the standard deviation from a ROI of identical size outside the rat. Here, σ_S is the standard deviation resulting from the spatial variation of the noise while in chapter I (Eq. I-3) the SNR calculation was carried out using the temporal standard deviation over N acquisitions.

Steady state ΔR_2^* data

The gradient echo and spin echo images were reconstructed after zero-filling to a 256 × 256 matrix. A R_2^* map was calculated by fitting the data from each TE, on a pixel by pixel basis, to an exponential decay curve of the form $S(TE) = S_0 \exp(-TE \cdot R_2^*)$, using Matlab. The S_0 values obtained by this fit were used to calculate the R_2 map from the single spin echo image. The ΔR_2 difference map could be calculated directly from the pre-contrast S_{pre}^{MGESE} and the post-contrast S_{post}^{MGESE} image by

$$\Delta R_2 = \frac{1}{TE} \ln\left(\frac{S_{pre}^{MGESE}}{S_{post}^{MGESE}}\right).$$

A CBVf map can then be obtained from the ΔR_2^* difference map by using Eq. 0-2 with the corresponding ΔX.

ROI analysis was carried out with Matlab on one of the three central slices which approximately corresponded to the coronal slices used for the CBVf analysis of the PR3D data.

Since different image processing software was used for CBVf analysis of MGESE and PR3D acquisitions, the ROIs were not identical. The position and the thickness of the coronal slices were not identical, neither. Therefore regional CBVf values are only expressed as an average over all available rats of one strain, without correlating the CBVf values obtained by each technique rat by rat. Statistical analysis was carried out with GraphPad Prism (version 5.00, San Diego California USA, http://www.graphpad.com).

2.6.8. Results

Due to technical problems related to instabilities in the RF pulse transmission three experiments had to be excluded (one on a Fischer rat and two on Wistar rats).

Steady state ΔR_2* data

The susceptibility difference ΔX in plasma before and after injection of 200 µmol Fe^{3+}/kg was obtained for each animal individually. The mean $\Delta[Fe^{3+}]$ was 4.7 ± 0.9 µmol kg^{-1} and the mean ΔX was 7.9 ± 1.5·10^{-7} in CGS units (n = 9).

Coronal images of one representative rat obtained with the MGESE and the PR3D sequences are shown in Fig. II-5. The gradient echo images acquired with the MGESE sequence at TE = 6 ms before and after SINEREM injection are shown in Fig. II-5a and b, respectively. The image in Fig. II-5c is the ΔR_2*-map obtained from the MGESE acquisition. The intensities on this map are proportional to the CBVf. The mean global CBVf obtained with the ΔR_2*-method are 1.68 ± 0.16% for the Fischer strain (n = 3) and 2.25 ± 0.55% for the Wistar strain (n = 6). Regional CBVf are given in the histogram in Fig. II-6.

PR3D data

A CBVf map obtained by the PR3D-$RSST_1$ method is shown in Fig. II-5d. It is a CBVf map from the same animal as shown in Fig. II-5a, b and c, in approximately the same coronal slice. It was generated by calculating the normalized signal intensity according to Eq. II-2.

The SNR in the PR3D acquisitions was 79 ± 21 for the S_{post} acquisitions and 8 ± 5 for the S_{pre} acquisitions. The global CBVf is 2.07 ± 0.43% (n = 3) for the Fischer strain and 2.12 ± 0.55% (n = 2) for the Wistar strain, using the NN algorithm, and 2.20 ± 0.45% for the Fischer strain and 2.13 ± 0.62% for the Wistar strain, using the ANN algorithm. The global CBVf and the regional CBVf obtained with the two gridding algorithms are not significantly different (Wilcoxon matched pairs test). Therefore, in the histogram in Fig. II-6, only the regional CBVf obtained with the NN algorithm are summarized.

The mean CBVf obtained from a ROI in the cavernous sinus is 46 ± 2% (after correction for the R_2-attenuation). This value is lower than the blood volume measured in large blood structures such as the sagittal sinus in CBVf maps obtained by the IR-FLASH acquisitions. Values up to 80% had been found. Given the low spatial resolution of the CBVf maps obtained by PR3D acquisitions, it is not surprising that a blood volume of 100% could not be obtained from the cavernous sinus.

Fig. II-5: T_2-weighted images before (a) and after (b) SINEREM injection from one representative rat (TE = 6 ms). The gray levels in the ΔR_2*-map (c) are proportional to the CBVf as obtained by the steady state ΔR_2*-method. The CBVf map in (d) was obtained by the $RSST_1$ method according to Eq. II-2.

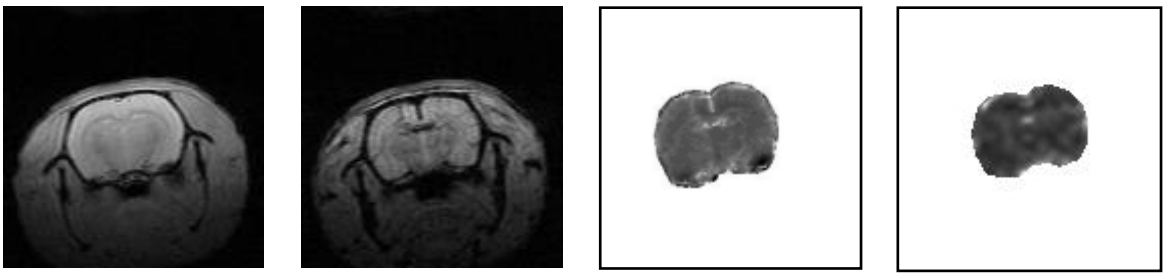

a **b** **c** **d**

Fig. II-6: regional CBVf obtained with the steady state ΔR_2* and PR3D-$RSST_1$ methods using SINEREM as CA. GM = gray matter, WM = white matter, subc. = subcortical

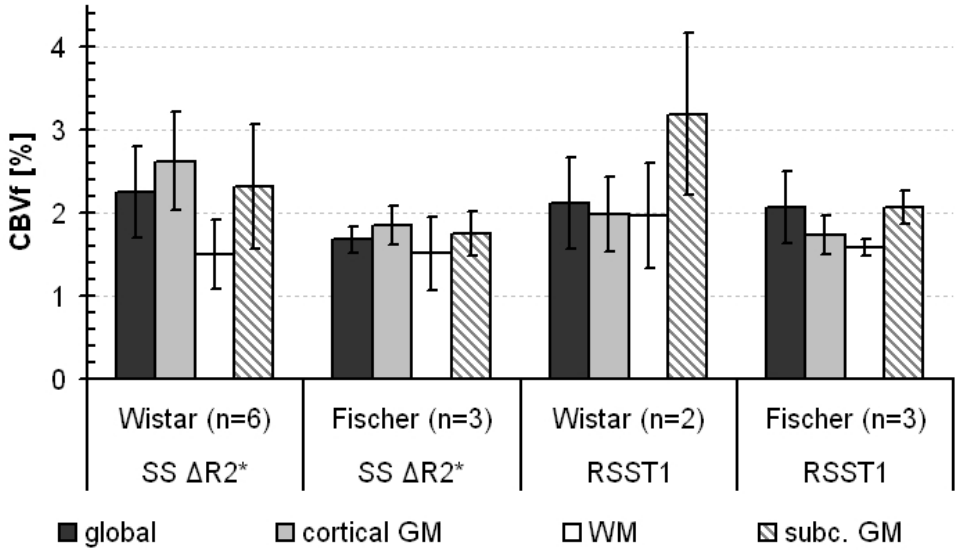

Statistical analysis

No significant different means were found for the global and regional CBVf when comparing the CBVf measurement methods and the rat strains, neither using the nonparametric Kruskall-Wallis

test, nor the one-way analysis of variance (ANOVA). Neither was there a significant difference between mean CBVf obtained with the two methods when both rat strains were grouped together (Mann-Whitney test). The number of experiments is small, so a difference might not be noticeable because of the few samples, but this is already an encouraging result, meaning that both methods result in comparative measures.

When comparing the mean regional CBVf, using the repeated measures ANOVA the white matter CBVf is significantly lower than the CBVf in both gray matter ROIs in the measures carried out with the ΔR_2^* method (n = 9) as well as with the $RSST_1$ (n = 5) method, with exception of the white matter versus cortical gray matter difference in the data obtained with the $RSST_1$ method. When using the nonparametric Friedman test for repeated measures, a significant difference was only found between the white matter CBVf and the cortical CBVf when using the ΔR_2^* method (P = 0.006), but the power of nonparametric tests is known to be very low for such small samples.

Although the mean global CBVf for the Fischer strain was lower than for the Wistar strain, 1.82 ± 0.51% (n = 6) and 2.22 ± 0.40% (n = 8), respectively, when the measurement methods were pooled, the difference was not significant (P = 0.08, Mann-Whitney test).

The global CBVf values are lower than those obtained with Gd-DOTA and P760 in Chapter I, but they are still in the range of CBVf values reported in the literature obtained by different techniques: autoradiography (Todd et al. 1992), MRI (Lin et al. 1997), synchrotron radiation quantitative computed tompgraphy (Adam et al. 2003), and histology (Pathak et al. 2001).

2.6.9. Discussion

Advantages and disadvantages of SINEREM for the $RSST_1$-method

Using SINEREM as blood pool CA the blood concentration may be considered constant throughout the imaging procedure which lasts 24 minutes for the post-contrast PR3D acquisition since this time scale is short in comparison to the plasmatic half life of SINEREM. The disadvantage of SINEREM when used with an MRI acquisition mode exploiting the positive contrast mechanism, i.e. the T_1 effect, is its high r_2-relaxivity. The TE of 0.7 ms still induced an attenuation grater than 20%.

The $RSST_1$-technique does not acquire the extravascular tissue water signal and is therefore insensitive to the susceptibility gradient at the vascular wall created by the compartmentalized CA. Only the transverse relaxation in blood plays a role.

Possible improvements

There are many ways to improve the PR3D acquisitions, especially their spatial resolution and the total acquisition time for a 3D volume.

To reduce acquisition time, a small surface RF coil could be used. Alternatively, the technique of outer volume suppression could be applied to suppress the signal from extracerebral tissue. However, care has to be taken, not to induce an inflow effect, by suppressing the signal from inflowing blood. The $RSST_1$ technique is based on a global inversion of the magnetization, in order to ensure that even blood flowing into the volume or slice of interest is suppressed before CA injection and relaxed to thermal equilibrium after CA injection.

The TE could certainly be shortened using a harder (shorter) excitation pulse. This would be a great advantage, because if the R_2-attenuation is negligible, such as with the IR-FLASH technique in conjunction with Gd-DOTA or even P760, knowledge of the blood T_2 would not be necessary, thus blood sampling or estimating blood T_2 could be avoided.

More accurate reconstruction techniques, which make use of the oversampling of the central K-space are in development, and are expected to lead to more reliable CBVf maps.

The use of SINEREM at a clinically approved dose

SINEREM is approved for clinical applications in humans up to a dose of 45 µmol Fe^{3+}/kg. At 2.35 T, an intravenous injection of this dose to a rat reduces the blood T_1 to about 180 to 240 ms and the blood T_2 to 10 to 14 ms. A T_{inv} of at least 900 ms would be necessary to measure the thermal equilibrium of the blood compartment. On the other hand, to suppress extravascular tissue having a T_1 of 1.2 s with an IR sequence a $T_{inv} \leq 830$ ms is necessary. At this T_{inv} the blood T_1 should not exceed 166 ms. This requires a SINEREM blood concentration of > 1 mM, which can be achieved with an injection of 50 to 70 µmol Fe^{3+}/kg to a rat and with a dose of

about 70 µmol Fe^{3+}/kg in men (Cameron 1999). The $RSST_1$-technique could therefore be used with adapted timing parameters of the IR sequence, but not for doses lower than 70 µmol Fe^{3+}/kg at 2.35T.

At lower magnetic field strength, the relaxivities of SINEREM are higher and the r_2/r_1 ratio lower and therefore more convenient for T_1 weighted acquisitions. Knowing the tissue T_1 at the desired field strength, the sequence can be adapted for the use of lower CA doses. For example, at 1.5T, the range of brain tissue T_1 is 780 ms (white matter) to 920 ms (gray matter). Using Eq. I-1 and Eq. I-2 it can be calculated that an IR sequence with TR/T_{inv} = 1680 ms/500 ms would suppress gray matter quite well, while white matter would keep a residual signal which had to be subtracted. In general, the larger the TR interval is, the smaller the range of T_1 that can be suppressed.

However, the use of SINEREM is still very interesting in animal models because of its increased intravascular retention compared to clinically approved Gd^{3+}-based CA, even in a number of pathologies. It has been successfully employed to assess hemodynamic and vascular morphologic parameters in a C6 brain tumor model using the steady state ΔR_2^*-technique (Julien et al. 2004; Tropres et al. 2004). Other USPIO of smaller size (MION, hydrodynamic diameter ≈ 17 nm) have also been used for CBVf measures in brain tumor, without significant extravasation (Dennie et al. 1998; Packard et al. 2003; Pathak et al. 2003; Pathak et al. 2001; Zimmer et al. 1995).

In general malignant tumors are distinguished from healthy brain tissue by the accumulation of CA in the extravascular compartment. So far, clinical tumor imaging is usually performed before and about 24 hours after SINEREM infusion (Enochs et al. 1999), because of its slow leakage from the blood pool and because of its long plasma half life of 21 to 30 hours. For other medical indications MRI is even performed up to 72 hours post injection (Kooi et al. 2003). It might be worthwhile to add an imaging protocol directly after injection giving rather information on blood volume instead of tissue infiltration.

3. Chapter III: CBVf mapping using $RSST_1$ with SINEREM as blood pool agent in tumor tissue

3.1. Introduction

In neuroimaging by magnetic resonance, lesions are detected with the use of diffusible CAs such as Gd-DTPA and Gd-DOTA because they do not remain intravascular in regions where the BBB is broken down. On the contrary, to assess brain perfusion by measuring blood flow or blood volume parameters, the CAs need to be confined to the intravascular compartment during the measure.

In the following experiment, it was tested whether SINEREM could be used to accurately measure the CBVf in tumor tissue. From literature (Le Duc et al. 1999) and experiments in our laboratory (Julien et al. 2004; Tropres et al. 2004; Valable et al. 2006) it is known that SINEREM does not extravasate in C6 tumors, and an accurate measure can be expected. In addition to the C6 tumor model a second malignant brain tumor model, RG2, was used. The vascular confinement of SINEREM in an RG2 tumor model had not been studied yet.

French Introduction

Chapitre III : Mesure de la fVSC avec le SINEREM dans des modèles de tumeur cérébrale

En neuroimagerie, avec les techniques de résonance magnétique, il est possible de détecter les lésions cérébrales en utilisant des AC comme le Gd-DOTA ou le Gd-DTPA qui diffusent en présence de rupture de la BHE. En revanche, pour des mesures de la perfusion cérébrale utilisant des AC de contraste, mesure du débit sanguin ou du volume sanguin, les méthodes utilisées sont basées généralement sur le confinement de l'AC dans le système vasculaire durant la mesure.

Comme il a été montré que l'extravasation du SINEREM est limitée dans les tumeurs (Julien et al. 2004; Tropres et al. 2004; Valable et al. 2006), les travaux de ce chapitre sont menés pour évaluer la faisabilité de cet AC pour mesurer la fVSC dans la tumeur en comparant les deux

méthodes $RSST_1$ et ΔR_2* chez le même animal. Deux modèles de rat ont été expérimentés : le modèle C6 et le modèle RG2. La biodistribution du SINEREM dans le modèle RG2, n'avait encore jamais été étudiée.

3.2. Tumor cell culture

The C6 glioma cell line was established by Benda et al (Benda et al. 1971; Schmidek et al. 1971) by repeated intravenous injection of N-methylnitrosourea to adult Wistar rats, followed by cloning of the developing tumors (Benda et al. 1968; Pfeiffer et al. 1969). It is a tumor model of astrocytoma.

The RG2 glioma cell line was induced in the progeny by a single intravenous injection of N-ethyl-N-nitrosourea to pregnant CD Fischer rats (Ko et al. 1980; Swenberg et al. 1972) and established following cloning by Wechsler et al. Histologically it has been classified as a grade III to IV astrocytoma.

The C6 and RG2 cells (purchased from American Type Culture Collection) were cultured at 37°C in Dulbeco's modified Eagle's medium (DMEM, GilboBRL, Lifes technologies, Scotland) supplemented with 10% foetal calf serum (GilboBRL, Lifes technologies, Scotland), 2% L-glutamin, 1% penicillin and streptomycin. The day of implantation the cells were trypsinized (trypsin/EDTA), centrifuged (1500 rpm for 5 minutes) and $2 \cdot 10^7$ C6 cells ml^{-1} or 10^6 RG2 cells ml^{-1} were suspended in the culture medium and stored in a refrigerator until implantation.

3.3. Tumor cell implantation

With the help of stereotactic coordinates, the cells were implanted in the right caudate nucleus of rats according to a method derived from Kobayashi et al (Kobayashi et al. 1980). These cell lines grow in their syngeneic host, therefore C6 cells were implanted in rats of the Wistar strain and the RG2 cells in rats of the Fischer strain.

Rats weighting 160 to 180 g were fully anesthetized with 5% isoflurane in air. Isoflurane was then reduced to 2.5 % and the rats were mounted on a stereotaxic head frame. After disinfection with Betadine, a middle scalp incision was made and the skin was removed until the bregma could be identified. A burr hole was drilled 3.5 mm to the right from the midsagittal line at the level of the bregma using either a 26G needle or an electric drill bit of 1 mm diameter (cf. Fig. III-1). Five microliter of the cell suspension (10^5 C6 tumor cells or $5 \cdot 10^3$ RG2 cells) were slowly injected into the right caudate nucleus at 5.5 mm depth under the skull bone using a 5 µl-Hamilton syringe with a 26G needle. The needle was slowly raised one minute after cell injection to allow for complete diffusion and to minimize suction of the injected solution back into the needle or along the created channel in the brain tissue. The burr hole was sealed with Horsley wax, and the scalp was sutured. After removing the rat from the stereotaxic device it was placed slightly inclined (with head up) within its cage at ambient temperature for recovery.

All rats implanted with the described amounts of C6 and RG2 cell suspensions developed rapidly growing tumors. The survival time ranged from three to four weeks for the C6 tumor bearing rats and from two to three weeks for the RG2 tumor bearing rats.

Fig. III-1: a rat's skull with the major interosseous sutures as landmarks. The bregma is the midline point where the coronal and sagittal sutures intersect. The glioma cells were implanted through a burr hole located 3.5 mm right to the bregma (red cross) in the caudate nucleus at 5.5 mm depth from the skull bone.

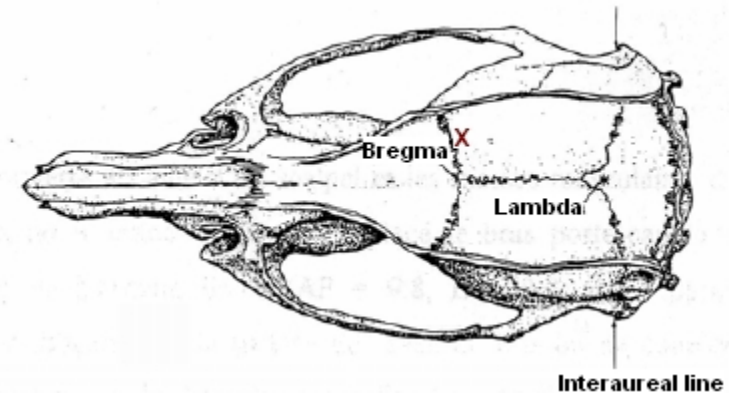

3.4. Imaging protocol

The imaging experiments were carried out 14 to 15 days after implantation of C6 tumor cells and 16 to 19 days after implantation of RG2 tumor cells, on five Wistar rats and five Fischer rats. The Wistar rats weighted 240 to 279 g and the Fischer rats weighted 263 to 283 g, the day of imaging. The femoral artery and vein were cannulated as described in Chapter I.

The imaging protocol and the sequence parameters were identical to the ones described in chapter II (paragraph 2.6.5) for healthy rats. The $RSST_1$ method and the steady state ΔR_2* method were used with a single SINEREM injection at a dose of 200 µmol Fe^{3+}/kg. Blood was sampled for later in vitro ΔX measurement, necessary for the CBVf quantification with the steady state ΔR_2* method.

3.5. Data analysis

Due to technical problems, only four experiments performed on RG2 tumor bearing rats were exploitable, and it was not possible to repeat the experiments on C6 tumor bearing rats, yet.

Image reconstruction of the PR3D and the MGESE acquisitions was performed as described in paragraph 2.6.7. Image analysis was performed under ImageJ for the PR3D data and with Matlab for the MGESE data. Statistical analysis was carried out using GraphPad Prism.

3.5.1. PR3D acquisitions

The ROIs were drawn on three transverse and three coronal planes of the PR3D acquisitions. The tumors were easily visible on the high resolution PR3D image (TR = 100 ms, α = 23°, matrix 63 × 123) and on the IR-PR3D acquisition performed during the $RSST_1$ interval after injection (S_{post}). One ROI comprised the whole tumor as visible on both images (cf. Fig. III-2). This ROI was subdivided in a smaller ROI drawn in the central part of the tumor, and in a peripheral ROI which was obtained by subtraction of the central ROI from the ROI comprising the whole tumor. The central ROI was drawn on the S_{post} image, which exhibited a different degree of contrast enhancement than the ring-like periphery of the RG2 tumor. In some cases the median line was

deviated and a ROI of the same size and shape as the whole tumor ROI could not be drawn on the contralateral side at the location corresponding to the tumor. Therefore, a large ROI was drawn comprising the contralateral hemisphere.

Only the CBVf values obtained from the reconstruction performed using the nearest neighbor algorithm will be presented in the Results section, because - as for the healthy rats imaged in chapter II - the difference with the averaged nearest neighbor algorithm was not significant (Wilcoxon matched pairs test). The standard deviations for regional CBVf given for individual rats result from averaging over the CBVf values in six ROIs (on three transverse and three coronal planes).

3.5.2. MGESE acquisitions

For regional analysis of the ΔR_2^* map obtained from the MGESE acquisitions the central slice was used, because it contained the largest tumor extension. The tumor extension was best visible in the T_2^* weighted pre-contrast image as a heterogeneous structure. After SINEREM injection, the RG2 tumors were hypointense compared to the surrounding normal brain tissue on the T_2^* weighted images. In general, the contrast between the tumor center and the ring like peripheral part was less pronounced than on the PR3D acquisitions. However, two ROIs were drawn in each tumor, a peripheral and a central one (cf. Fig. III-4) similar as for the PR3D acquisitions. For this data only one plane had been analyzed for each rat, therefore the standard deviations of the regional CBVf given for each rat individually result from averaging over all pixels within a ROI.

3.6. Results

3.6.1. CBVf obtained by the $RSST_1$ method

The mean CBVf obtained from the ROIs comprising the whole tumor varied between 4 and 21%. In the contralateral hemisphere CBVf ranging from 0.85 to 2.03 % were found with a mean of 1.49 ± 0.49% for the four rats. This is lower than the CBVf in healthy Fischer rats (cf. Chapter II),

but not significantly (neither with the nonparametric Mann-Whitney test, nor with the unpaired T test).

Fig. III-2 shows a representative example of the PR3D acquisitions obtained in a RG2 tumor bearing rat brain 19 days after implantation. Fig. III-2a is a transverse image acquired with high resolution about 45 min after SINEREM injection, and in this case reveals a ring shaped hyperintensity in the tumor periphery. Fig. III-2b and c are a transverse and a coronal plane of the CBVf map, respectively, clearly showing the typical enhancement pattern in this tumor type. The mean CBVf of the whole tumor was 21.19 ± 5.86% for this rat.

Fig. III-2: Representative example of a RG2 tumor bearing rat brain. The transverse high resolution PR3D image (a), as well as the transverse (b) and coronal (c) CBVf maps depict a hyperintense ring-like contrast due to SINEREM extravasation in the tumor periphery. The transverse plane is displayed from the top, the coronal plane from caudal.

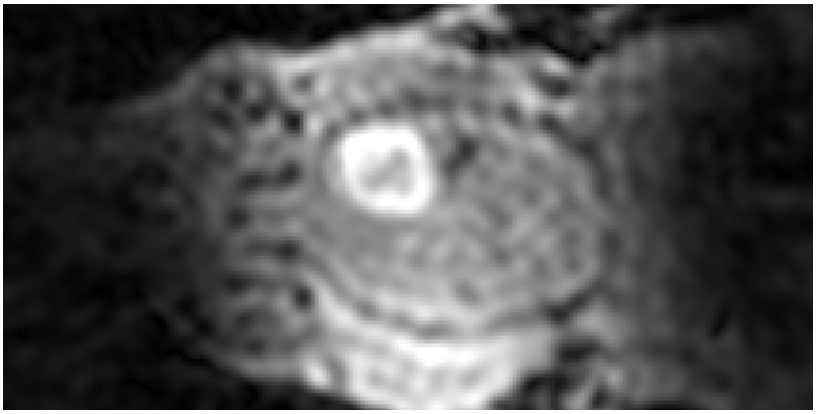

a

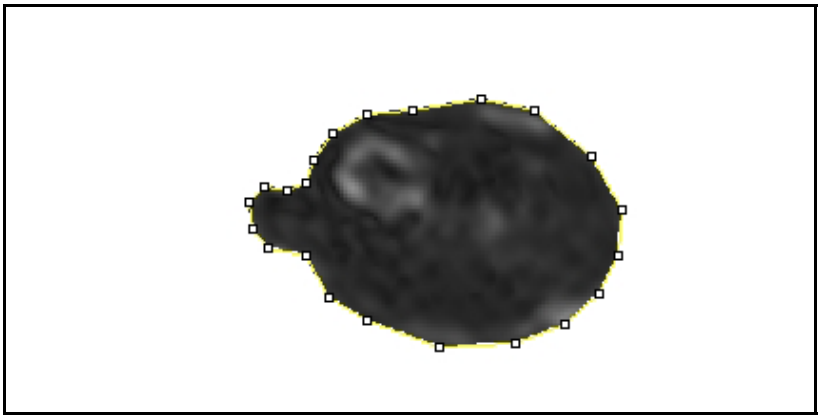

b

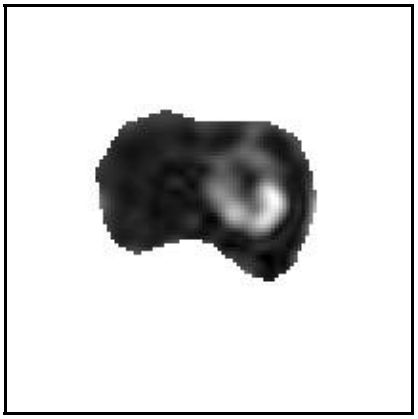

c

Since the CBVf in the tumors vary much between the rats, it makes little sense to present a mean value, especially for a small number of rats. Therefore, the histogram in Fig. III-3 gives the regional CBVf as measured by the $RSST_1$ method individually for each rat. The time interval between tumor cell implantation and CBVf mapping is given in days for each rat.

In three out of four rats, the CBVf measured in the tumor ROIs using SINEREM is by a factor of nine to fourteen higher than in the contralateral brain tissue. Ferrier et al reported a CBVf of less than 5% in an RG2 tumor model nine to eleven days after implantation (Ferrier et al. 2007). Even in one week older RG2 tumors such high degrees of vascularisation are unlikely. These findings suggest extravasation of SINEREM in this tumor model. The degree of extravasation varies between tumors, since little or no extravasation was observed in one rat for which the CBVf in the tumor was only about twice as high as the contralateral CBVf. The degree of extravasation also varies within a tumor as could be observed on the CBVf-maps. For example on the coronal CBVf map in Figure III-2c, the ventral (lower) half of the tumor has a higher CBVf than the dorsal part and the tumor center. The heterogeneity within tumors can also be deduced from the error bars in Fig. III-3. The extravasation was found larger in the tumor periphery than in the center for two rats and vice versa for the other two rats. Such heterogeneous distributions in intratumor permeability have been reported for various tumor types (Cuenod et al. 2006; Peterson et al. 1984; Yankeelov et al. 2003).

The CBVf for the tumor ROIs (whole tumor, center, periphery) were tested for correlation with the day post implantation using the nonparametric Spearman test, but no significant correlation

was found. However, for the central tumor CBVf the Spearman coefficient was r_S = 1, and almost significant (P = 0.083).

Fig. III-3: regional CBVf obtained by the $RSST_1$ method using SINEREM and PR3D acquisitions. The four rats where imaged on day (d) 16 to 19 after RG2 cell implantation

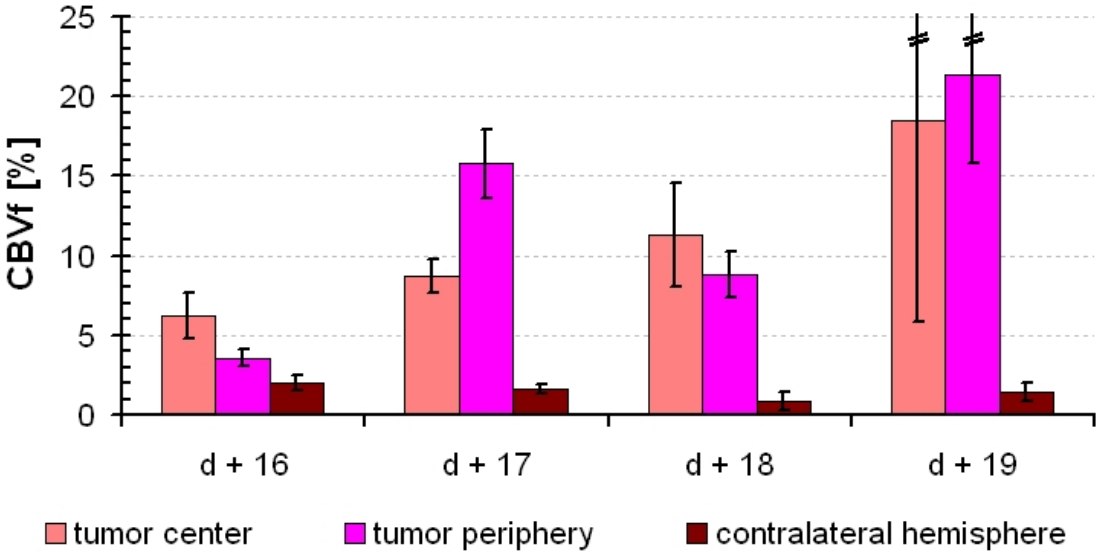

3.6.2. CBVf obtained by the steady state ΔR_2* method

The mean $\Delta[Fe^{3+}]$ in rat blood after an injection of 200 µmol Fe^{3+}/kg was 4.9 ± 1.3 µmol kg^{-1}. The mean ΔX was 8.2 ± 1.9·10^{-7} (n = 4).

The mean CBVf in the contralateral tissue is 1.76 ± 0.28% (n = 4), and not significantly different from the CBVf in healthy Fischer rats. Neither is it different from the CBVf contralateral to the tumor obtained with the $RSST_1$ technique.

Figure III-4a shows a coronal T_2 weighted pre-contrast image (spin echo, TE = 102 ms) of an RG2 tumor bearing rat brain with typical tumor and contralateral ROIs. The image in Fig. III-4b is a T_2* weighted acquisition (gradient echo, TE = 18 ms) of the same slice performed about 30 minutes after SINEREM injection. For this particular rat, the tumor appears hypointense in the center and slightly hyperintense in the periphery with respect to the surrounding brain tissue on

the post-contrast gradient echo and spin echo images. The image in Fig. III-4c is the ΔR_2*-map for the corresponding slice, on which the gray levels are proportional to the blood volume fraction in tissues in which the CA is confined to the intravascular compartment. The ΔR_2* is highest in the tumor center despite CA extravasation. The measured CBVf values are 1.73 ± 0.70% for the contralateral hemisphere, 3.30 ± 1.66% for the central tumor region and 2.67 ± 1.39% for the peripheral tumor region. The standard deviation given here results from spatial averaging, and reflects the heterogeneity of the CBVf in the respective ROI.

Fig. III-4: coronal images of a RG2 tumor bearing rat brain
a: T_2 weighted (TE = 102 ms) image obtained before CA injection
b: T_2* weighted (TE = 18 ms) image obtained after intravenous injection of 200 µmol/kg SINEREM
c: ΔR_2*-map. Despite probable CA leakage, the tumor center has the highest ΔR_2*-values in the image

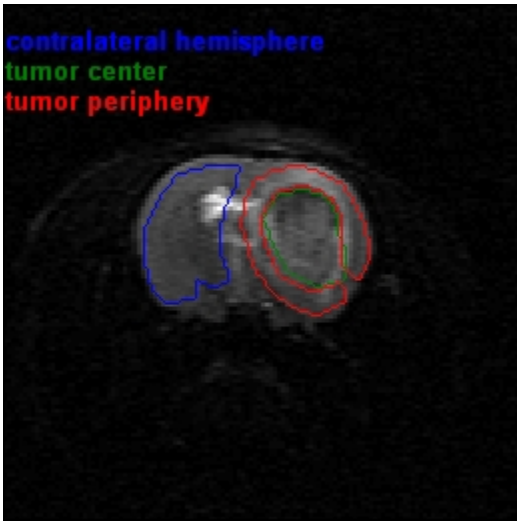

a

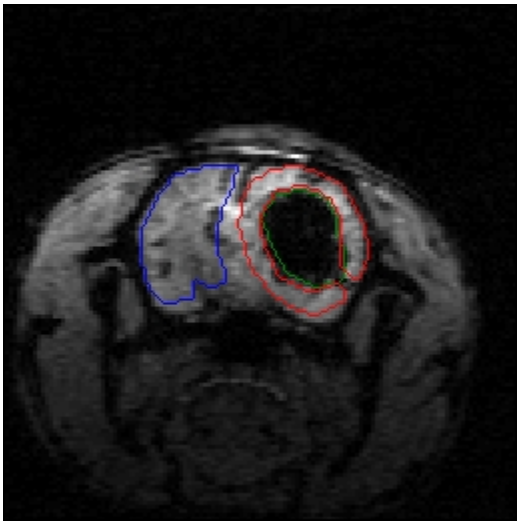

b

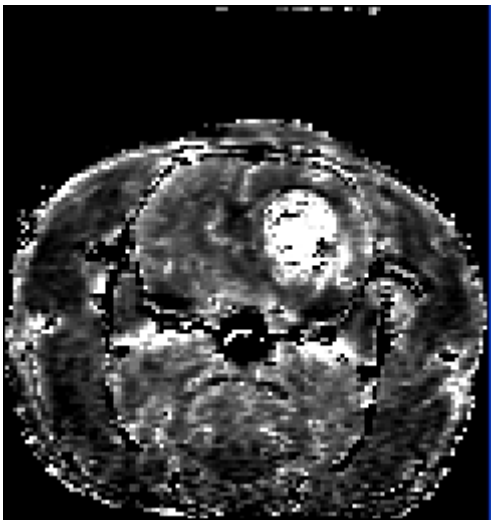

c

The histogram in Fig. III-5 illustrates the CBVf values obtained by the steady state ΔR_2* method. The CBVf values measured in tumor ROIs with the steady state ΔR_2* method are much lower than those measured by the $RSST_1$ method and only slightly higher than in the contralateral brain tissue.

Fig. III-5: regional CBVf obtained by the steady state ΔR_2^* method using SINEREM and MGESE acquisitions for four RG2 tumor bearing rats imaged 16 to 19 days after tumor cell implantation.

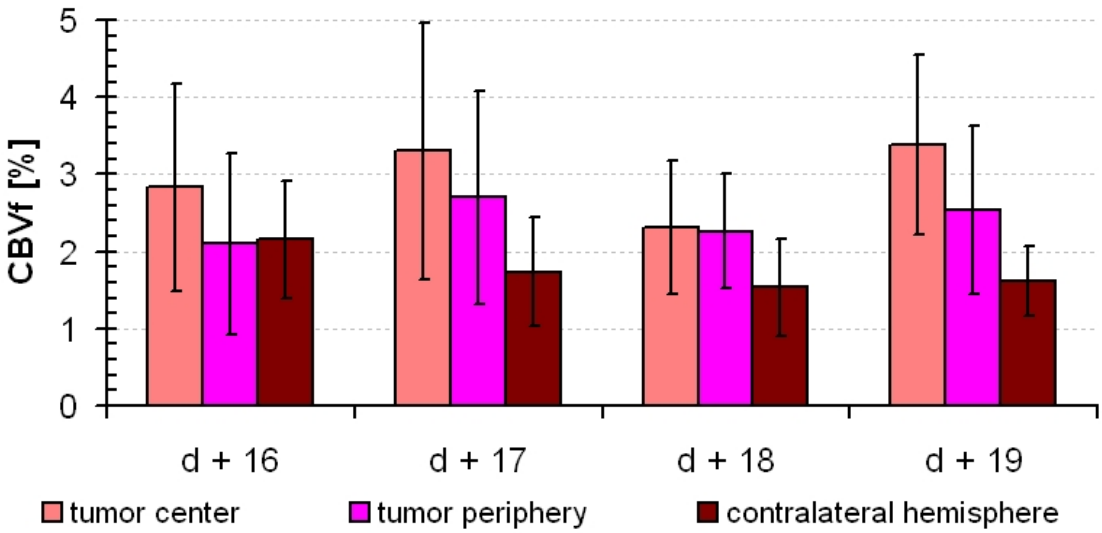

The MGESE acquisitions were performed immediately after the PR3D acquisitions. It is therefore unlikely that the different CBVf in tumor tissue obtained by the $RSST_1$ and the steady state ΔR_2^* method result from a significantly modified distribution of SINEREM between the PR3D and the MGESE acquisitions. If the CA leaked out of the tumor microvasculature as suggested by the findings of the $RSST_1$ measure, the CBVf obtained by the steady state ΔR_2^* method is underestimated. The ΔR_2^* methods are based on susceptibility differences in tissue created by compartmentalization of the CA such as in the network of healthy microvasculature. If SINEREM leaks out of the vascular compartment, half an hour after injection a significant quantity might be present in the extravascular compartment of the tumor tissue. Owing to the more homogeneous distribution of SINEREM in the tumor tissue, the susceptibility differences will be greatly reduced and the assumptions of the model, on which the ΔR_2^* methods are based, are not valid any more.

3.7. Discussion

3.7.1. CBVf overestimation in case of CA leakage

Direct confirmation for CA leakage can not be obtained neither with the $RSST_1$ acquisition nor with the steady state ΔR_2^* acquisition because, with such slow acquisition modes (13 min for steady state ΔR_2^* and about 25 min for the $RSST_1$ method in this study), it is not possible to monitor the CA leakage. The $RSST_1$ method just provides evidence for a several fold increased CBVf, while the steady state ΔR_2^* method provides evidence for low to normal CBVf within the tumor. It is rather the contradictory result obtained with both methods that evoke the possibility of CA leakage.
Neither the steady state ΔR_2^*, nor the $RSST_1$ method can measure the CBVf in case of CA extravasation, when slow acquisitions are used. Faster acquisitions can provide information about the leakage rate which can be used to correct the measured CBVf for the CA leakage (cf chapter VI).

If the BBB maintains its barrier function to a certain extend and the extravasation rate is small with respect to the blood flow rate, the CA extravasation is said to be diffusion limited. In this case, first pass techniques are better suited to estimate the microvascular CBVf, since the CA has little time to extravasate. However, T_1-based first pass techniques will still overestimate the CBVf because the presence of the CA in the extravascular compartment lowers its T_1, while T_2^*-based techniques are known to underestimate the CBVf due to the loss of CA compartmentalization.

In case of CA extravasation, the S^{norm} signal (Eq. II-1) rather represents the distribution volume of the CA provided there is an equilibrium between CA outflow from and backflow into the vasculature during the entire acquisition time. Using the PR3D acquisition mode, the signal is averaged over an acquisition time of about 25 min and it is impossible to tell at which rate the extravasation occurs and whether the equilibrium between CA extravasation into the interstitium and backflow into the vasculature installs during the acquisition. Such a long acquisition can only reflect the distribution volume of the CA correctly under the condition that the extravasation occurs rapidly, that the equilibrium installs before the acquisition is started and that the CA washout from the leakage compartment is negligible during the acquisition time. Given the long half life of SINEREM in the body, rapid elimination from brain tissue is unlikely, since

extravascular Fe^{3+} can also be phagocytised (Weissleder et al. 1990a; Weissleder et al. 1990b) slowing down its backflow into the intravascular compartment.

As discussed above, the $RSST_1$ method using a slow acquisition mode such as the PR3D mode in this study is a true steady state technique, because the first pass of the CA bolus can not be monitored, and the signal is acquired when the CA has more or less completely occupied its distribution volume. However, serial acquisitions using faster acquisition modes such as the FLASH mode, can either be used to monitor the first pass of a CA in the tissue of interest, or they can be used with a high r_1-relaxivity CA at a sufficient dose to create the conditions for the $RSST_1$ method. Fulfilling the $RSST_1$ conditions has the consequence that the S^{norm} signals represent the distribution volume of the CA. Therefore, dynamic monitoring of the S^{norm} signal as a function of time, such as defined in Eq. 0-5, might allow to study the behavior of the CA diffusion in tissues and calculate the extravasation rate. Such an attempt will be shown in the last chapter.

3.7.2. Water exchange in tumor tissue

Yet another mechanism that can aggravate the overestimation of the CBVf in tumor tissue with T_1 based techniques is the water exchange across the BBB. The water exchange rate has been estimated by different methods (Donahue et al. 1997; Labadie et al. 1994; Orrison et al. 1995; Schwarzbauer et al. 1997) and the reported rates are within a relatively limited range in healthy brain tissue (cf. paragraph 6.2). As illustrated in chapter I (paragraph 1.7.5), the impact on the CBVf measure can be estimated using an appropriate exchange model, when the exchange rate is known.

In many brain pathologies, and particularly in neoplasms, the presence of mediators of inflammation and angiogenic factors (i.e. VEGF) cause the BBB to become generally more permeable to solutes, metabolites and even CA. This also facilitates the transport of water across the BBB. The exchange rate is given by:

$$\tau_{exch}^{-1} = \tau_{iv}^{-1} + \tau_{ev}^{-1} = PS_v\left(\frac{1}{V_{iv}} + \frac{1}{V_{ev}}\right)$$

where P is the endothelial permeability to water, S_v is the vascular surface and V_{iv} and V_{ev} are the volumes of the vascular and extravascular compartment, respectively.

The water exchange rate depends on the permeability itself, but also on the vascular surface participating in the exchange, and on the vascular and extravascular volume, all of which are altered in diseased tissue with respect to healthy tissue (Dewhirst et al. 1989). In addition, all these parameters and with them the exchange rate vary spatially within a lesion (Kim et al. 2002). It is therefore very difficult to quantify the CBVf overestimation caused by the water exchange in brain pathologies.

When CA leakage from the vascular compartment is large, the difference between the relaxation times of the intra- and extravascular compartments is attenuated, i.e. the shutter speed decreases. In this case, the contribution of the water exchange effect does not play the principal role in the CBVf overestimation.

On the other hand, since the BBB first becomes permeable to solutes and small molecules before it is permeable to larger CA such as dextran coated Fe^{3+}, the effect of an increased water exchange in diseased tissue may be particularly large, when the CA is still confined in the vasculature. The water exchange than extends the relaxation enhancing effect of the intravascular CA to the extravascular tissue, decreasing the relaxation rate difference between compartments. This can also lead to over- or underestimations of the CBVf, with T_1 based and T_2* based MRI techniques, respectively.

4. Chapter IV: CBVf mapping using the $RSST_1$ method with Gd-ACX in a C6 tumor model

4.1. Introduction

Still in the search for CAs that can be used to assess brain hemodynamics and function in Gd-DOTA permeable tumor microvasculature, a new prototype CA, composed of an α-cyclodextrin derivative (ACX) complexed to Gd^{3+} was investigated for the use in combination with the $RSST_1$-method. Following biocompatibility studies the relaxation properties and the biodistribution of the complex were investigated. In a C6 tumor model, no generalized diffusion of Gd-ACX could be detected on T_1 weighted images, contrary to Gd-DOTA. The vascular retention was confirmed using the $RSST_1$-technique. Accurate CBVf measurements could be performed using Gd-ACX in this tumor model. The CBVf-maps were compared to the microscopic vessel distribution and density.

French Introduction

Chapitre IV : Mesure de la fVSC dans le modèle tumoral C6 utilisant le Gd-ACX

Dans ce chapitre, il est montré dans quelles conditions la complexation du gadolinium avec une nouvelle molécule α-cyclodextrine modifiée (ACX) conduit au Gd-ACX, un nouvel AC paramagnétique. Des mesures de relaxométrie (relaxivités longitudinales et transversales, profils NMRD) à différents champs magnétiques sont réalisées. Une grande partie de ce travail a concerné d'une part la biocompatibilité de cette nouvelle molécule et d'autre part sa bio-distribution dans un modèle de tumeur cérébral C6 en le comparant au Gd-DOTA où il est montré que cet AC est purement vasculaire même en présence d'une lésion de la BHE. Ce résulat a permis de réaliser avec succès des mesures quantitatives de la fVSC dans la tumeur, résultats confrontés aux données histologiques par microscopie optique.

4.2. Gadolinium complexed to an α-cyclodextrin derivative: Gd-ACX

The hexakis(2-O-carboxymethyl-3,6-anhydro)-α-cyclodextrin, a hexaacid $ACXH_6$ cyclodextrin derivative named ACX (Fig. IV-1), was synthesized by chemical modification of the natural α-cyclodextrin (ACD, Wacker, Société de Chimie, France) by the team of Andrée Gadelle (French Atomic Energy Commission: CEA, Laboratoire de Reconnaissance Ionique, Service de Chimie Inorganique et Biologique) (Gadelle and Defaye 1991). Acidic derivatives of modified cyclodextrins form a hydrophilic cavity carrying oxygen atoms capable of coordinating several kinds of metal cations (Fauvelle et al. 2002) and particularly Gd^{3+}, resulting in a potential MRI CA. The ACX molecule has a disc shape and a molecular weight of 1212 Dalton. The hydrated compound of formula $ACX.nH_2O$ ($n \approx 14$) has a molar mass of 1464 Dalton. The biochemical and physical properties of ACX and the Gd-ACX complex were investigated at the French Atomic Energy Commission. The first batches of Gd-ACX were examined by microanalysis (Service Central de Microanalyse du CNRS, Solaize, France) to check the basic chemical formula of ACX, assess the number of hydration water molecules attached to it, and control the absence of iodine which might have been introduced with the starting compound as a residual synthesis impurity. ^{1}H-NMR and ^{13}C-NMR were also employed to assess the purity of the product (AVANCE 200 Bruker spectrometer).

4.3. First studies with ACX and Gd-ACX

Biocompatibility studies were carried out at the French Research Center of the Army Health Services (CRSSA, Laboratoire de Biophysique Cellulaire et Moléculaire) under the direction of Jean-Claude Debouzy. They consisted in the measurement of the hemolytic activity in human blood, and the determination of the median lethal dose (LD_{50}) in mice, the LD_{50} being the dose that is lethal for 50% of the animals. These experiments are briefly summarized in this chapter. In vivo MRI after intravenous injection of Gd-ACX had been carried out in our laboratory and revealed a strong signal enhancement in the vascular structures and a negligible enhancement in C6 tumor tissue. Since the C6 tumor model is known to have microvasculature which is highly permeable to Gd-DOTA, this observation suggested a vascular retention of Gd-ACX. Before Gd-ACX was used for CBVf measurement in rats, the longitudinal and transverse relaxivities were measured and the biodistribution study by MRI was repeated.

Fig. IV-1: hexakis(2-O-carboxymethyl-3,6-anhydro)-α-cyclodextrin composed of six glucose units forms a hydrophilic cavity capable of coordinating Gd^{3+}

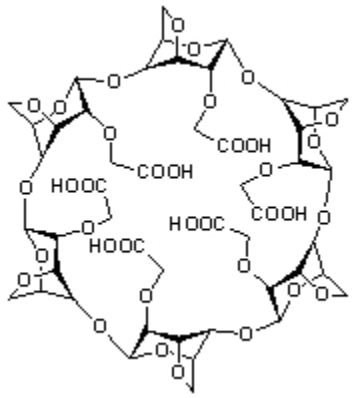

4.4. The Gd-ACX solution

4.4.1. Gd-ACX complexation

The lyophilized ACX received from Andrée Gadelle was washed twice in ethyl ether in order to remove iodine residues, and dried under vacuum. To prepare 1:1 Gd-ACX complexes appropriate amounts of gadolinium chloride ($GdCl_3.6H_2O$ from Sigma, La Verpillere, France) and $ACX.nH_2O$ were dissolved in normal saline solution at room temperature. The resulting solution is transparent with a slight yellow color. An excess of ACX (1.5 to 2 times Gd^{3+}) was used in order to minimize the presence of free Gd^{3+} in the solution. The ACX aqueous solubility was found to be limited to 45 mM, therefore the Gd^{3+} concentrations of the mother Gd-ACX solutions do not exceed 27 mM.

4.4.2. Gd-ACX concentration in solution

Particular attention was paid to the preparation of the Gd-ACX solutions assigned to the relaxivity studies, so as to obtain Gd-ACX concentrations accurate to within 1%. For that purpose, the exact volumes of the volumetric flasks were determined by weighing the

corresponding quantities of pure water and dividing the obtained masses by the water density. The volumes of the solutions to be mixed were also carefully checked by dividing their masses by their densities. The masses of the compounds and solutions were measured with a Mettler Toledo precision balance operating with an accuracy of 0.01 mg.

For all the biological investigations, the solutions were systematically filtered (Swinnex Millipore isopore membrane filters, type 0.8 µm ATTP) to remove any macroscopic impurities. Finally, the pH of the solution was measured using an InLab®423 Combination pH Micro Electrode (Mettler Toledo) and adjusted to 6.9 to 7.4 by adding a few drops of 10 M NaOH solution. The absence of free Gd^{3+} was confirmed by standard complexometric titration using xylenol orange as indicator (Lyle and Rahman 1963), which forms a distinctively colored red-violet complex with Gd^{3+}.

4.5. Biocompatibility studies

4.5.1. Hemolytic effect

Hemolysis is a classical side effect of natural cyclodextrins (Djedaïni and Perly 1991). Therefore, hemolysis in the presence of ACX alone and of the complex Gd-ACX was evaluated and compared to the hemolytic activity of ACD.

Isotonic NaCl solution (100 µl) containing human erythrocytes at a hematocrit of 10% was added to solutions (4 ml) containing concentrations of 0 to 50 mM ACD, and 0 to 41 mM ACX or Gd-ACX (in terms of ACX concentration). The samples were kept at 37°C for one hour before centrifugation. Absorption measurements were performed at 540 nm on a Shimazu MCS - 2000 absorption spectrometer (Debouzy et al. 1998). To calibrate the absorption, absence of hemolysis (0%) was evaluated by addition of isotonic NaCl solution, while total hemolysis (100%) was induced by addition of triton X-100 or sonication of the samples.

As in former studies carried out at the French Research Center of the Army Health Services (Debouzy et al. 2002), it was found that a 12 mM ACD concentration induces 50 % hemolysis. At this and lower concentrations (typical CA concentrations in blood after intravenous injection are

< 2 mM) no hemolysis could be detected, neither with ACX nor with Gd-ACX. The hemolysis occurring with ACX never exceeds 5% even at an ACX concentration of 41 mM, and is even lower for Gd-ACX than for ACX alone.

4.5.2. Median lethal dose of Gd-ACX

As a primary evaluation of ACX and Gd-ACX, toxicity experiments were carried out on CD1 mice from Charles River, France, weighting 20 to 30 g. Besides assessing mortality, a general survey was performed daily for one week, including weighting, observation for behavioural anomalies with special attention for prostration, spontaneous locomotor activity and tegumental alterations (yellow colored mice skin suggests significant stress (Harkness and Wagner 1989)). All substances were administered as intraperitoneal injections of the same volume per weight: 20 µl/g.

In a preliminary experiment to determine whether toxicity occurs if an ACX solution at a 45 mM ACX concentration (corresponding to the maximum solubility of ACX) is injected, five animals received ACX, five animals received a Gd-ACX solution having a stoichiometry 1:1.66 (27 mM $GdCl_3$, 45 mM ACX) and five control animals received normal saline solution. In view of the volumes of the administered injections, these concentrations corresponded to doses of 0.54 mmol Gd^{3+}/kg and 0.9 mmol ACX/kg.
No adverse effect could be observed after intraperitoneal injection of ACX alone. However, an intraperitoneal injection of a Gd-ACX solution at the maximum ACX concentration, lead to the death of three out of five mice within one day and one of the surviving mice of this group showed a 20% weight loss along with major behavioral anomalies such as prostration.

The second set of experiments was a quantitative determination of the $LD_{50\%}$ for Gd-ACX, carried out on eight groups of five animals each using the economic statistical floating mean method (Weil 1952). All concentrations and injected doses of the complex Gd-ACX are expressed in terms of Gd^{3+}. For the first group of mice the Gd-ACX solution was administered at a concentration of 21 mM corresponding to a Gd-ACX dose of 0.42 mmol/kg. Starting with this concentration, six successive dilutions by a factor of three were made, and administered to the other mice groups. The last group was used as a control and received the same volume of normal saline solution.

No death occurred in this experiment. During the first two days, transient weight loss accompanied by prostration and porphyrin-wet pillosity, indicative of a general health status alteration, could be observed within the two mice groups subjected to the two highest doses 0.42 and 0.14 mmol/kg, corresponding to injected concentrations of 21 and 7 mM of Gd-ACX, respectively. This weight loss was followed by recovery and normal growth. Neither abnormal locomotor activity nor trembling was observed.

Since the first two sets of experiments did not allow obtaining the $LD_{50\%}$ precisely, a final experiment was performed on ten mice by administering an intraperitoneal injection of a 25 mM Gd-ACX solution, which corresponds to a Gd-ACX dose of 0.50 mmol/kg. Normal saline solution was injected to ten other mice for control.
Transient weight loss, but no mortality occurred in the rats subjected to Gd-ACX at a dose of 0.50 mmol/kg. After the 7-day observation period, all mice had the same percentage of weight gain. From these three experiments, it was concluded that the $LD_{50\%}$ of Gd-ACX is higher than 0.50 but lower than 0.54 mmol/kg which correspond to Gd-ACX concentrations of 25 and 27 mM, respectively.

As heavy metals and lanthanides in particular are known to be nephrotoxic (Galle 1997; Johanson 1994), all animals of the first and last sets of experiments underwent histological examination of both kidneys seven days after injection. Histology was performed with a hematein-phloxin-safran staining on six frontal slices of 10 µm for each kidney. The glomerular and tubular system of the kidneys did not reveal any evidence for nephrotoxicity, neither for the surviving animals, nor for the three mice that died after injection of the 27 mM Gd-ACX solution at a dose of 0.54 mmol/kg.

4.6. In vitro relaxometry

Before deciding at which dose Gd-ACX can be used in vivo its relaxivity has to be known. Nuclear magnetic relaxation dispersion (NMRD) profiles are proton relaxivities plotted against the field strength and help understand the dynamics of CA relaxivity.

4.6.1. Materials and methods

For relaxometry, sealable NMR Young tubes of 5 mm diameter were filled with 0, 0.126, 0.233, 0.286, 0.414, 0.643, 0.965, 1.910, 2.840 and 3.830 mM concentrations of Gd-ACX in normal saline solution. The solutions were degased from their paramagnetic oxygen by gently bubbling argon for at least 20 minutes. NMR tubes with Gd-ACX concentrations of 0, 0.284, 0.421 0.636, 0.964 and 1.445 mM were also prepared in human plasma.

Relaxometry at low magnetic field

The low-field NMRD profiles were recorded at the CEA using a Stelar FFC - 2000 relaxometer operating between 10 kHz and 35 MHz. The profiles were obtained at 25 ± 1°C for the four Gd-ACX concentrations 0.965, 1.91, 2.84, and 3.83 mM in normal saline solution. The temperature dependence of the r_1 relaxivity was studied for the 0.965 mM sample by recording a profile at 37 ± 1°C. The temperature regulation was provided by a current of dry nitrogen heated by a resistor.

Relaxometry at 9.4 T

The T_1 were also measured at 9.4 T (400 MHz) in a high resolution small bore magnet of a Varian-U400 spectrometer. This system was equipped with a dedicated probe for which the temperature was regulated at 25 and 37°C by an air flow controlled by a Varian VT (variable temperature) unit. The T_1 values were measured with a saturation recovery pulse sequence using 12 to 15 different delay times between the two RF pulses ranging from 10 ms to 10 s and TR ranging from 1 to 12 s depending on the concentration of Gd-ACX.

Relaxometry at 2.35 T

The relaxivity experiments at 2.35 T (100 MHz) were performed at room temperature (20-21°C) on the Bruker spectrometer of the Department of Functional and Metabolic Neuroimaging using the homogeneous RF coil for emission and the surface coil for signal reception. As for former spectroscopic T_1 measures described in chapter I and II, an inversion recovery sequence with a nonselective adiabatic π pulse and a square hard readout pulse was used. The 15 T_{inv} ranged from 5 ms to 10 s and the TR from 1 s to 20 s depending on the Gd-ACX concentration of the

sample. Each experiment was repeated three times and the T_1 values were averaged. The T_1 relaxation measurements were repeated eleven weeks later for the Gd-ACX samples in normal saline solution. In order to evaluate the transverse relaxation effect on the signal in the in vivo studies, the r_2 relaxivity was measured as described before with a spin echo sequence, on the samples prepared in normal saline solution. The T_2 values were measured using 15 TE ranging from 2 ms to 10 s and TR as for the T_1 measure. Each measurement was repeated twice.

Data analysis

The T_1 value was taken to be the characteristic relaxation time of the function $M_0\left[1-\text{inv}\cdot\exp\left(T_{inv}/T_1\right)\right]$,

obtained by a least-squares fit of the three parameters M_0, inv and T_1 to the evolution of the measured peak area vs. the relaxation delay T_{inv}. The T_2 value was fitted as described in chapter 2.4.1. Piecewise linear fitting was used to obtain adequate estimations of the longitudinal and transverse relaxivity and the separating concentration of Gd-ACX in normal saline solution, since the corresponding relaxation rates were not well described by one rectilinear regression. The equations in the low and high concentration ranges were of the form

$R_i - R_{i0} = r_{i(low)} \cdot [Gd - ACX]$ and **Eq. IV-1a**

$R_i - R_{i0} = r_{i(low)} \cdot C + r_{i(high)} \cdot ([Gd - ACX] - C)$, **Eq. IV-1b**

respectively, where i = 1, 2 and $r_{i(low)}$ and $r_{i(high)}$ are the slopes or relaxivities in the low and high concentration range, respectively, separated by the concentration C. Relaxivities were also computed individually for each available data point to illustrate the dependence on the concentration. In the case of the low-field ^{1}H NMRD curves, the T_1 value at each field was determined by a three-parameter least-squares fit of the measured first points of the FID vs. the relaxation delay.

4.6.2. Results: Relaxivities of Gd-ACX

^{1}H NMRD profiles

The NMRD profiles (the magnetic field dependence of R_1) measured at 25°C for four different Gd-ACX concentrations in normal saline solution are shown in Fig. IV-2a. The NMRD profiles of

Gd-ACX differ greatly from those of standard clinical Gd^{3+}-based CAs, which either decrease rapidly beyond 1 MHz or exhibit prominent peaks around 20 MHz (Caravan et al. 1999). The NMRD profiles of Gd-ACX are surprisingly flat up to frequencies of 100 MHz. Almost no temperature dependence can be observed at the available Larmor frequencies.

r_1 and r_2 relaxivities at 2.35 T

The longitudinal relaxation enhancement $\Delta R_1 = R_1 - R_{10}$ in normal saline solution at 2.35 T and at 21°C is displayed in Fig. IV-2b versus the Gd-ACX concentration. This relaxation enhancement can not be approximated by a straight line passing through the origin, but it can be roughly approximated by low- and high-concentration linear regimes of notably different slopes 11.3 and 8.3 $s^{-1}mM^{-1}$, respectively. The partitioning concentration giving the best piecewise-linear fit is C = 0.414 mM. In Fig. IV-2c, this difference in slope is further investigated by plotting the r_1 relaxivity of Gd-ACX versus each studied Gd-ACX concentration. This relaxivity has a smooth behavior, which is an indication of the accuracy of the concentration and relaxation measurements. It shows a significant continuous decrease from 13.3 to 8.6 $s^{-1}mM^{-1}$ as [Gd-ACX] increases from 0.126 to 3.83 mM. At 2.35T and for concentrations above 3 mM, it is still 8.6 $s^{-1}mM^{-1}$, about twice as high as the r_1 of Gd-DOTA at the same temperature (Powell et al. 1996). The Gd-ACX complexes in solution were found stable for several months by repeating the relaxivity measurements. In human plasma at 20°C, the r_1 relaxivity was measured in the concentration range 0.3 to 1.5 mM, where it shows a slight overall decrease from about 11.6 to 10.7 $s^{-1}mM^{-1}$ as the Gd-ACX concentration increases.

The transverse relaxation enhancement $\Delta R_2 = R_2 - R_{20}$ in normal saline solution at 2.35T and 20°C is plotted versus the Gd-ACX concentration in Fig. IV-2d. The overall transverse relaxivity, which is 12.4 $s^{-1}mM^{-1}$ in the low-concentration regime below 0.414 mM, decreases to 10.4 $s^{-1}mM^{-1}$ in the high-concentration regime above 0.414 mM. In both concentration ranges, it is also more than twice as high as the transverse Gd-DOTA relaxivity of 4.3 $s^{-1}mM^{-1}$ at 2.35 T (Fonchy et al. 2001). The r_2 dependence on the Gd-ACX concentration is shown in Fig. IV-2e. The r_2 decrease with concentration is less pronounced than that of r_1.

Fig. IV-2: Relaxivities of Gd-ACX in normal saline solution at 2.35T: NMRD profiles for four different Gd-ACX concentrations and temperature dependence (a). Piecewise-linear fit for the longitudinal relaxation giving r_1 = 11.3 $s^{-1}mM^{-1}$ for lower concentrations and r_1 = 8.3 $s^{-1}mM^{-1}$ for higher concentrations (b). Dilution dependent longitudinal relaxivity of Gd-ACX computed individually for each data point (c). Piecewise-linear fit for the transverse relaxation giving r_2 = 12.4 $s^{-1}mM^{-1}$ for lower concentrations and r_2 = 10.4 $s^{-1}mM^{-1}$ for higher concentrations (d). Dilution dependent transverse relaxivity of Gd-ACX computed individually for each data point (e).

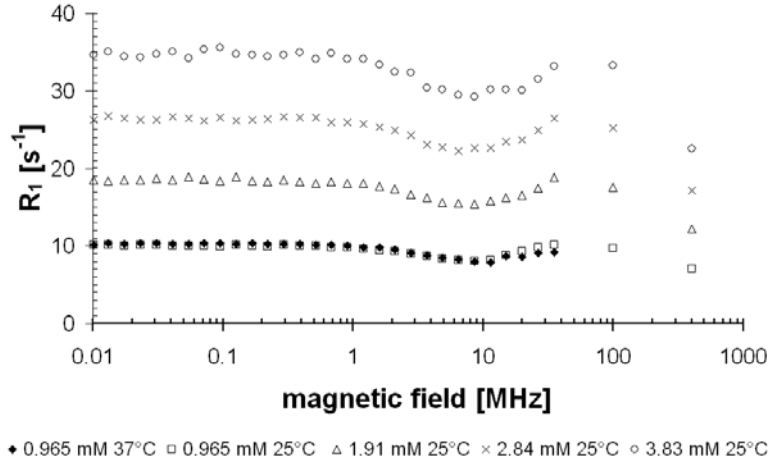

a

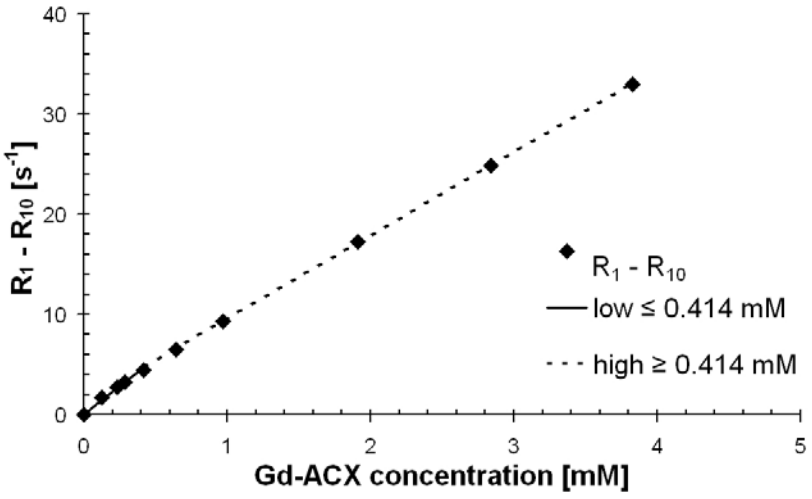

b

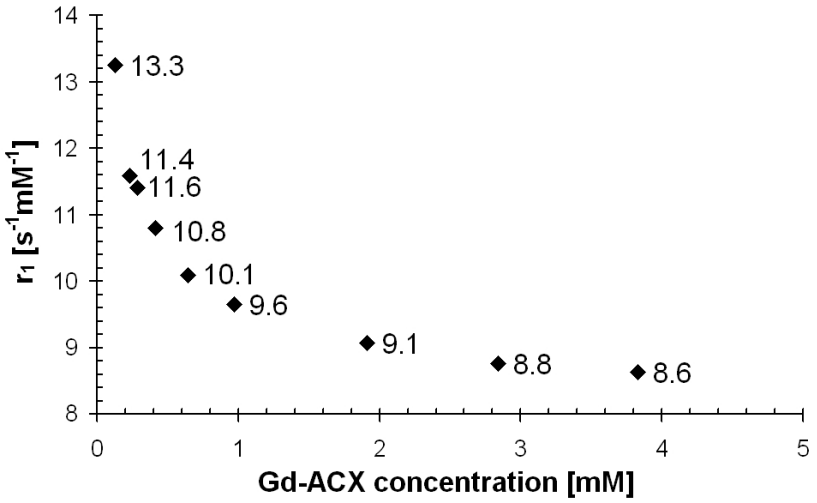
13.3
11.4
11.6
10.8
10.1
9.6
9.1
8.8
8.6
r1 [s-1mM-1]
Gd-ACX concentration [mM]

c

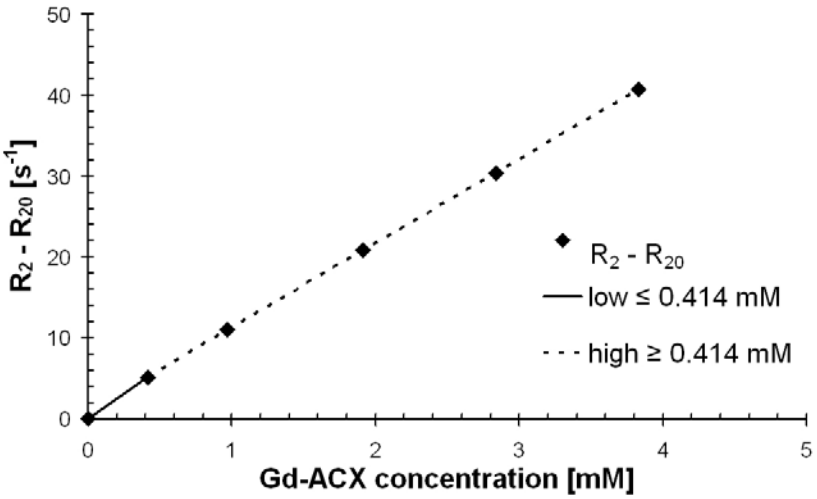
R2 - R20
low ≤ 0.414 mM
high ≥ 0.414 mM
R2 - R20 [s-1]
Gd-ACX concentration [mM]

d

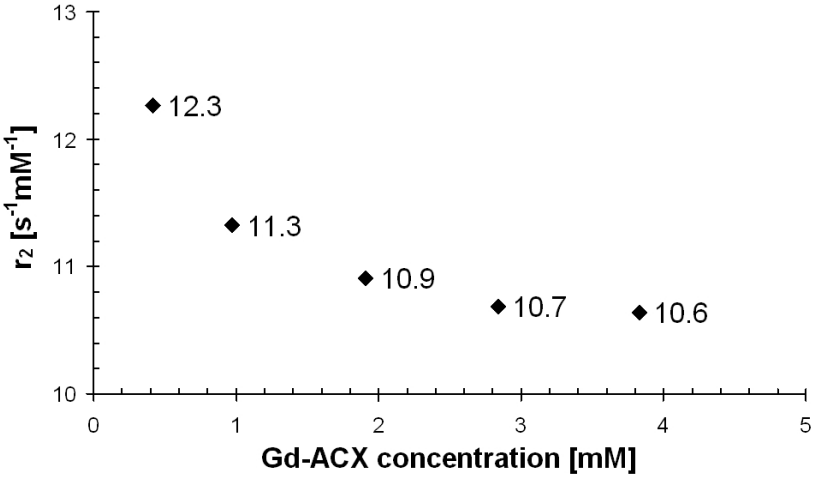
12.3
11.3
10.9
10.7
10.6
r2 [s-1mM-1]
Gd-ACX concentration [mM]

e

The concentration dependence of the r_1 and r_2 relaxivities was confirmed by multiple experiments in which particular care was taken to obtain solutions with highly accurate Gd-ACX concentrations. A precise interpretation of this unusual relaxation property in terms of structural and dynamic molecular factors necessitates a much deeper physico-chemical characterization. For the purpose of this study, the experimental characterization of the relaxivity was sufficient to assess the contrast efficacy of Gd-ACX. At the standard dose of MRI blood pool CAs, resulting in a vascular CA concentration of 1.4 to 2 mM just after injection, the average r_1 relaxivity of Gd-ACX is 9.1 $s^{-1}mM^{-1}$ in normal saline solution and 10.7 $s^{-1}mM^{-1}$ in human plasma, i.e. 2.5 to 3 times larger than that of Gd-DOTA (Fonchy et al. 2001; Powell et al. 1996).

4.7. In vivo MR imaging

The biodistribution of Gd-ACX and the CBVf were studied by MRI at 2.35T in nine male C6 tumor bearing Wistar rats 20 and 21 days after implantation. The C6 cell implantation was carried out as described in the previous chapter, with the exception that the rats (weighting 200 to 250 g) were anesthetized with an intraperitoneal injection of 400 mg/kg chloral hydrate obtained from Aldrich Chemical Company, instead of isoflurane inhalation.

The CBVf was also measured in five healthy Wistar rats.

4.7.1. Imaging protocol on C6 tumor bearing rats

For the imaging experiment, the rats, weighing 310 to 400 g, were anesthetized with isoflurane, equipped with a venous and an arterial cannula and placed in the plastic head frame as described in Chapter I. The homogeneous RF coil was used for emission, and the surface coil for reception. All images were obtained in the coronal plane with a FOV of 24 x 24 mm^2. A timing diagram of the imaging protocol is shown in Fig. IV-3.

Fig. IV-3: timing diagram of the in vivo imaging experiment for the simultaneous measurement of the biodistribution of Gd-ACX and of the CBVf in a C6 tumor model.

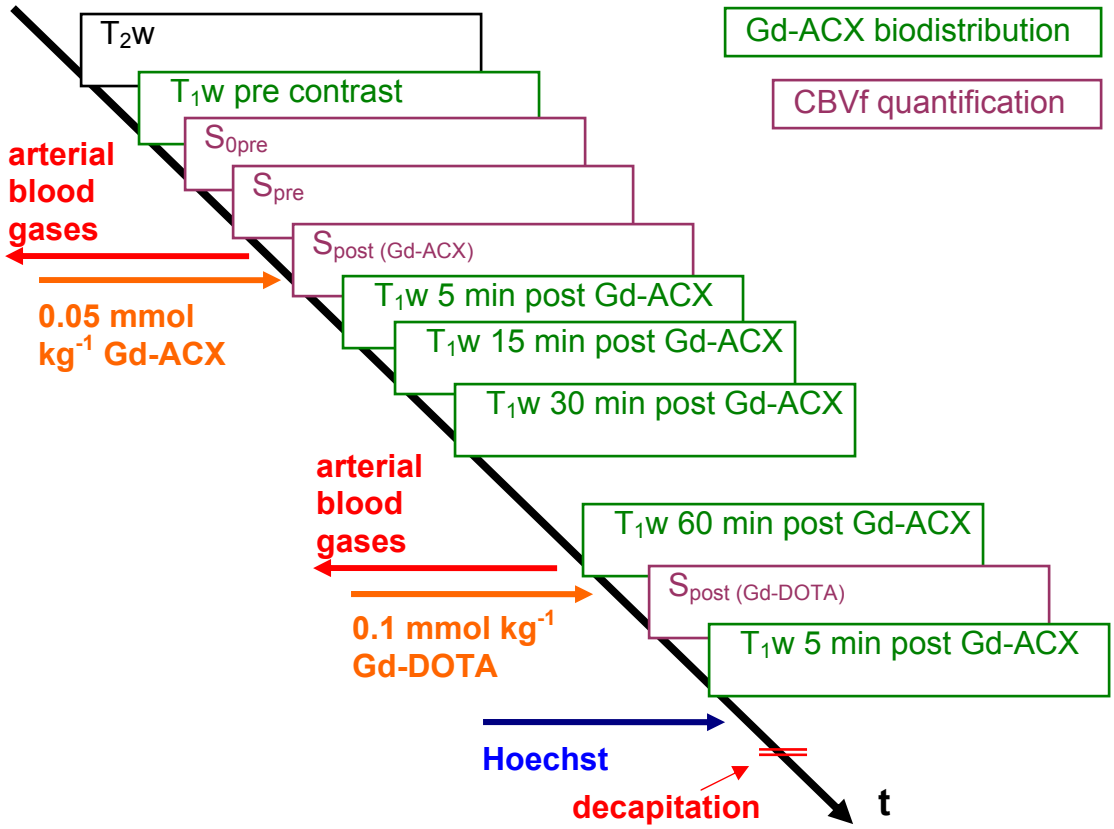

Biodistribution imaging protocol in C6 tumor bearing rats

The acquisition of high resolution T_2 weighted images for delineation of the spatial extent of the tumor was performed with a multi-slice spin echo sequence with TR/TE = 2000 ms/80 ms. Seven contiguous coronal and transverse slices of 1 mm thickness were acquired with a 128 x 66 matrix size. With two averages, the total acquisition time was 4 min and 48 s. To monitor the regional signal enhancement induced by the Gd-ACX injection in the seven coronal slices, T_1 weighted images with TR/TE = 500 ms/20 ms and the same acquisition matrix were acquired before injection and 5, 15, 30, and 60 min after Gd-ACX injection. With four averages the total acquisition time was 2 min and 15 s.

CBVf-mapping protocol in C6 tumor bearing rats

For the CBVf map, the single slice IR-FLASH sequence was used. The image plane corresponded to the central (fourth) slice acquired with the spin echo sequence but the slice thickness was 2 mm. Before CA injection, 40 proton weighted acquisitions with $TR/T_{inv}/TE$ = 10 s/8 s/3.2 ms (S_{0pre}) and 400 pre-contrast $RSST_1$ acquisitions with $TR/T_{inv}/TE$ = 750 ms/325 ms/3.2 ms (S_{pre}) were performed. Arterial blood gases were analysed. The Gd-ACX solution (25 mM in terms of Gd^{3+}) was slowly manually injected at a rate of about 1 ml/min and at a dose of 0.05 mmol/kg (2 ml/kg) body weight and was immediately followed by 400 post-contrast $RSST_1$ acquisitions ($S_{post\ (Gd\text{-}ACX)}$). The signal enhancement on T_1 weighted images was then monitored at the time points mentioned above for one hour. A 50 mM Gd-DOTA solution was then injected at a dose of 0.1 mmol/kg (2 ml/kg) followed by a second post-contrast $RSST_1$ acquisition ($S_{post\ (Gd\text{-}DOTA)}$) and a last T_1 weighted acquisition. The dose studies in Chapter I showed that after this Gd-DOTA dose the thermal equilibrium signal is reached but not maintained. However, one hour after a previous CA agent injection, the signal after 0.1 mmol/kg Gd-DOTA injection remains in a steady state for more than one minute.

Histological sections

After the last acquisition, four tumor bearing rats were intravenously injected with 0.2 ml Hoechst 33342 (6 mg in normal saline solution, Sigma, St. Louis, MO, USA), a vital DNA specific bis-benzimidazole fluorescent dye, a marker for perfused microvessels, followed by decapitation one minute later. The brains were immediately excised, frozen in liquid nitrogen and stored at -90°C, to stop the diffusion of the Hoechst dye into the perivascular tissue. Eight to twenty coronal sections of 10 µm thickness located within the 2 mm thick MRI slice for CBVf mapping were cut on a cryotome (Microm HM 560, Germany). To locate this coronal plane, the distance of the center of the MRI section from the base of the olfactory bulb, which is the most rostral part of the rat brain, was measured on transversal T_2 weighted images. Using the cryotome, this plane can be found with less than 0.5 mm inaccuracy. The cutting procedure has to be performed as fast as possible, because exposure to white light degrades the Hoechst fluorescent intensity. In addition, the cut brain sections have to be kept in the cryo chamber of the cryotome (about -18°C) to avoid thawing. The sections were stored at - 90°C until further

processing. One additional section was cut for standard histologic analysis of the tumor regions with nonspecific Hematoxylin-Erythosine (HE) staining.

The Hoechst immunofluorescent sections were scanned with an Olympus DP50 Microscope Digital Camera System (ColorView CCD color camera) mounted on a Nikon Microscope Eclipse E600 equipped with a 340 – 380 nm exciter filter and a 335 – 485 nm barrier filter. A composite image was reconstructed from the individual processed fields to cover the tumor extension (AnalySIS 5.0, Soft Imaging System GmbH).

4.7.2. CBVf-mapping protocol on healthy Wistar rats

Additionally, five healthy control Wistar rats (380 to 450 g) underwent the MRI CBVf measurement. Two of them were imaged using Gd-ACX only, and three of them were imaged with Gd-ACX and one hour later with Gd-DOTA. The imaging protocol for these rats was identical to the one described, with the exception that no T_1 weighted imaging was performed, no Hoechst was administrated and that a dose of 0.3 mmol/kg Gd-DOTA was used. The Gd-ACX solution had to be prepared several times, and different batches were used.

4.7.3. Data analysis

MR image processing was performed using IDL. The signal enhancement E(t) following CA injection was calculated as:

$$E(t) = 100 \frac{S_{post}(t) - S_{pre}}{S_{pre}} \qquad \textbf{Eq. IV-2}$$

where S_{pre} and S_{post} (t) correspond to the signal obtained before and at time t after CA administration, respectively. The kinetic signal enhancement was calculated on three ROIs located in the lumen of the cavernous sinus (≈ 10 pixels), covering the whole tumor area (≈ 200 pixels), and in the periphery of the tumor (≈ 50 pixels).

The CBVf map was calculated using Eq. I-4. In this experiment N = 200 images were averaged corresponding to 2.5 minutes during which the S_{post} signal amplitude is in a steady state.

4.7.4. Results

CBVf in healthy rats

The images in Fig. IV-4 show a coronal CBVf map and the corresponding T_2 weighted image of a healthy rat. The average CBVf of the whole slice was 2.7 ± 0.2% for this rat. The standard deviation of 0.2% reflects the temporal instability of the signal during 2.5 minutes. The white matter of the corpus callosum has a blood volume fraction of 1.6 ± 0.9% and the cortical gray matter 2.8 ± 0.7%. The value obtained from a small ROI in the sagittal sinus is 78 ± 7%. Averaged over five healthy rats, the global CBVf obtained with Gd-ACX is 2.2 ± 0.4%.

Fig. IV-4:
a: CBVf map of a healthy rat obtained with Gd-ACX and
b: the corresponding T_2 weighted image of the brain slice.
Medially, the anterior cerebral artery (red arrow) and the choroids plexus (yellow arrow) can be distinguished.

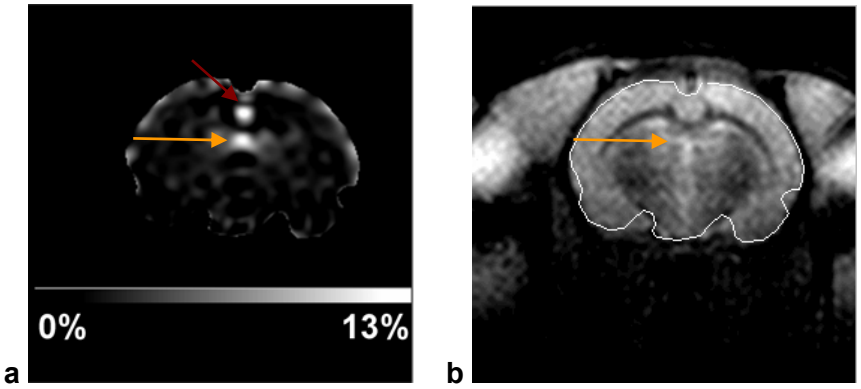

In this study the signal was averaged over 2.5 min. However, the signal obtained by the $RSST_1$ method after 0.05 mmol/kg Gd-ACX bolus injection remains constant for at least 5 min (duration of the entire MRI experiment), while following a bolus injection of 0.1 mmol/kg Gd-DOTA without previous CA injection it is known to drop immediately (cf. chapter I). Since 0.05 mmol Gd-ACX and 0.1 mmol Gd-DOTA are isoeffective just after injection, the duration of the steady state suggests a longer blood half life of Gd-ACX and thus a slower extravasation of Gd-ACX in extracerebral tissues compared to Gd-DOTA.

Histological examination of C6 tumors

Histological examination of the HE stained C6 tumor bearing sections revealed large areas of necrosis, predominantly in the central part of the tumor, containing very few but enlarged and deformed vessels, cystic formations (liquid filled cavities without any vessels) and a relatively narrow band of viable pleomorphic proliferating cells in the tumor periphery. In some cases, the tumor size and outline exceeded the one of the corresponding T_1 and T_2 weighted images. A substantial shift of the median line was observed in all brains, but was particularly pronounced for two brains (called J2 and J5). The $PaCO_2$ in most tumor bearing rats measured before both CA administrations was slightly higher than in the series of healthy rats. Values up to about 50 mmHg were measured with a mean of 47.0 ± 6.8 mmHg. One rat with a particularly large tumor was excluded due to a $PaCO_2$ of 70 mmHg, a low blood pressure and a low body temperature throughout the imaging experiment.

Biodistribution of Gd-ACX in C6 tumors

Figure IV-5a shows T_1 weighted coronal images of a C6 glioma bearing rat before and at different time points after intravenous injection of 0.05 mmol/kg Gd-ACX and also after injection of 0.1 mmol/kg Gd-DOTA. After Gd-ACX injection, the signal enhancement appears immediately in large vessels, but not in the tumor, while injection of Gd-DOTA reveals disruption of the BBB since an extensive signal enhancement is observed inside the tumor area. A quantitative analysis of the biodistribution of both CAs is given in Fig. IV-5b, in which the temporal evolution of the relative signal enhancement with Gd-ACX is plotted for three different ROIs. A sudden signal enhancement appears in the vascular ROI after injection of Gd-ACX and is similarly high with Gd-DOTA. In the tumor as a whole, no enhancement is observed during the first hour after Gd-ACX injection. The C6 tumor model is known to be vascularized in the tumor periphery. In such an ROI, the mean signal enhancement after Gd-ACX injection is about 20%. The enhancement appears as rapidly as that in the vascular ROI, indicating a vascular origin. The enhancement is much greater with Gd-DOTA. From the T_1 weighted acquisitions, Gd-ACX extravasation can not be ruled out but it is clearly limited and negligible with respect to Gd-DOTA extravasation.

Fig. IV-5:

a: T_1 weighted acquisitions at different time points after intravenous Gd-ACX and Gd-DOTA administration and

b: corresponding percentage signal enhancement in a vessel (left axis) and in tumor tissue (right axis).

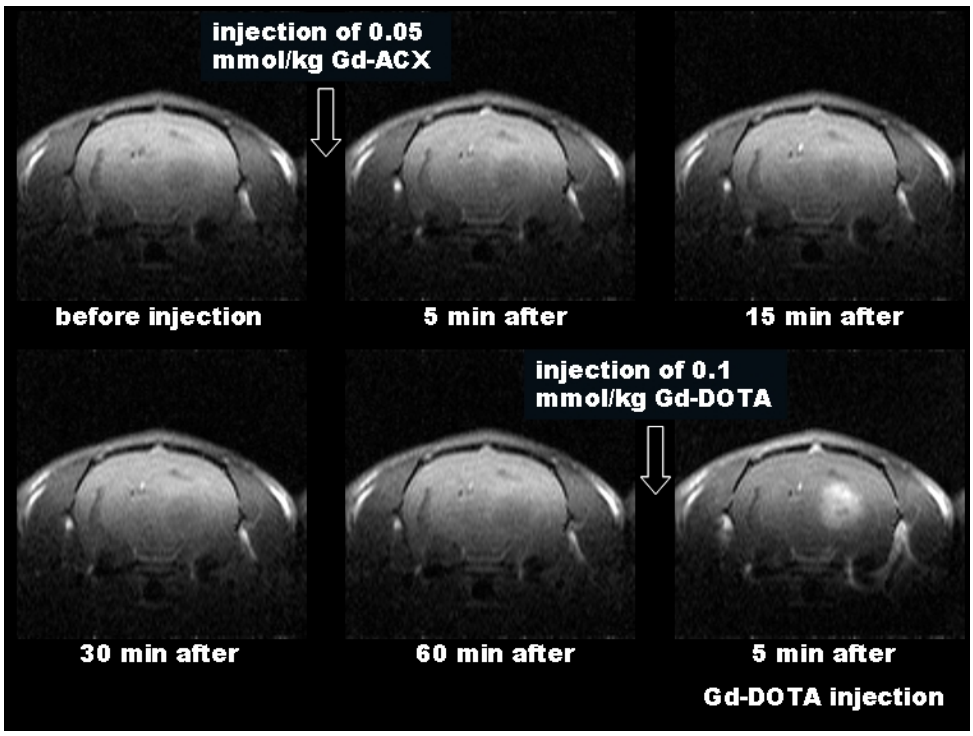

a

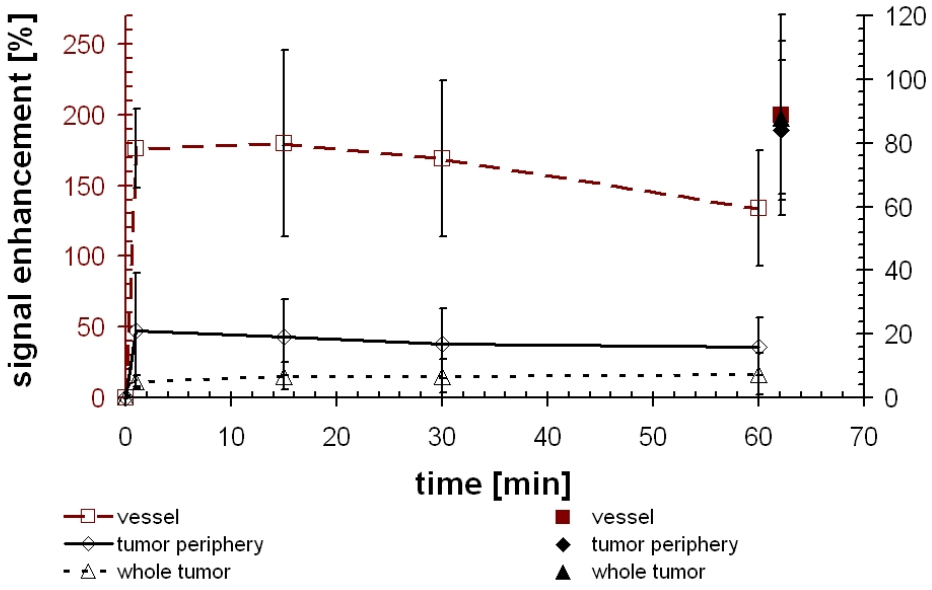

b

CBVf in C6 tumor bearing rats

The signal versus time plots obtained by the $RSST_1$ method in Fig. IV-6a and b are from one representative rat. Figure IV-6a shows the signal from a tumor ROI. After Gd-ACX injection, it remains perfectly constant for about 5 min, while after Gd-DOTA injection the signal increases continuously, reflecting CA accumulation in the tissue due to a BBB leakage for this CA. Figure IV-6b shows the identical signal behavior in cerebral tissue contralateral to the tumor after injection of Gd-ACX and Gd-DOTA. The constant signal enhancement obtained with the $RSST_1$ technique during the first five minutes confirms the absence of immediate Gd-ACX extravasation. In this case, the tumor signal enhancement must reflect the tumor blood volume even in the presence of a compromised BBB. Therefore, all CBVf measures in tumor tissue were obtained from measurements following Gd-ACX injection.

Figure IV-6c illustrates the CBVf values obtained in various ROIs, averaged over the eight rats. A mean CBVf value of 0.98 ± 0.34% was obtained in the tumor ROIs, which in average covered 46 ± 11% of the whole brain section. In the contralateral hemisphere similar CBVf values were obtained with both CA: 0.94 ± 0.16% with Gd-ACX and 1.03 ± 0.23% with Gd-DOTA. The ROIs placed in vascular structures revealed similar maximal values (70%) as obtained with P760 (chapter I). A value of 100% is never attained due to partial volume and transversal relaxation effects.

In all eight cases the CBVf in the tumor center was low corresponding to a necrotic region as confirmed by microscopy analysis with HE staining. The CBVf in the tumor periphery was 1.32 ± 0.40%, which is significantly different ($p < 0.05$, Wilcoxon signed rank test and Student T test for paired comparisons) from the mean CBVf values in all other ROIs including the contralateral tissue.

Fig. IV-6:

Normalized signal versus time curve for tumor tissue (a) and contralateral tissue (b) from one representative rat.

c: Mean (n = 8) regional tumor CBVf obtained with Gd-ACX and contralateral CBVf obtained with Gd-ACX and Gd-DOTA.

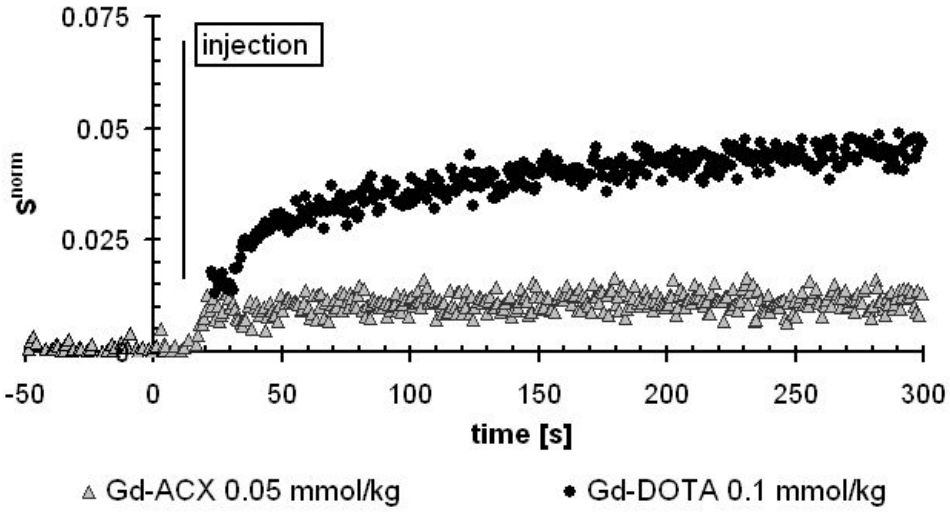

a

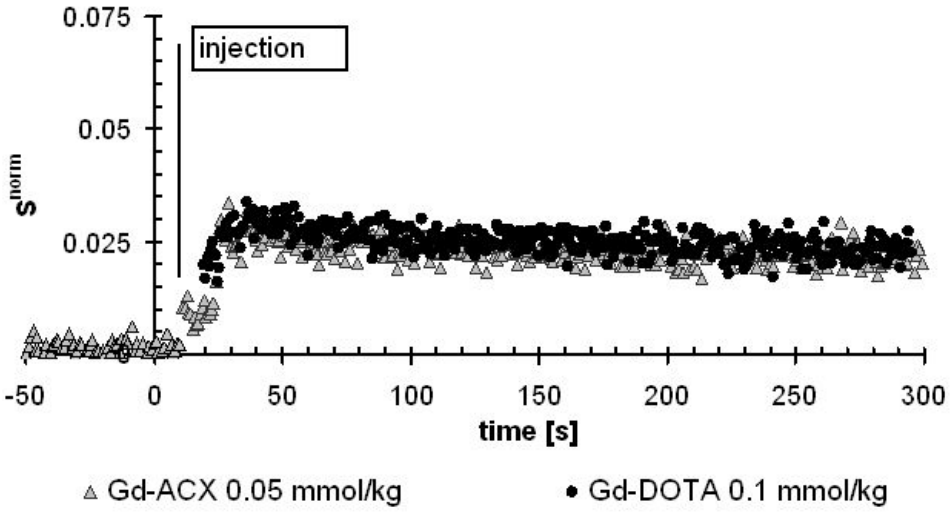

b

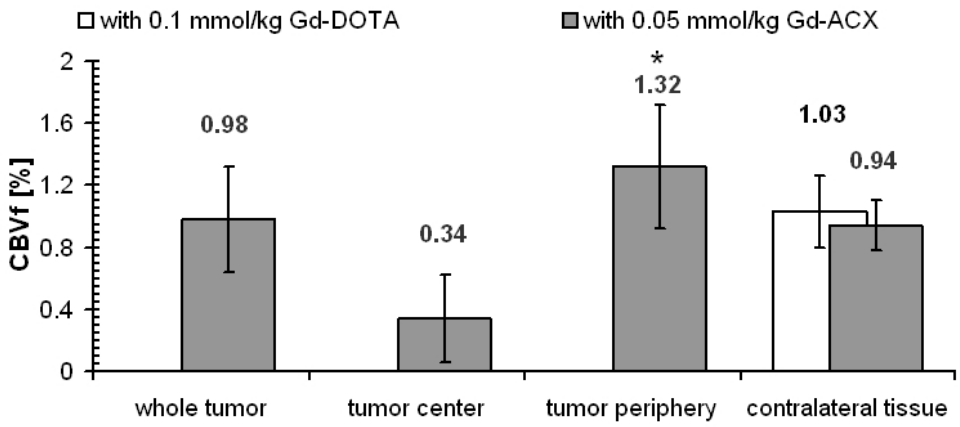

c

In Fig. IV-7 images of a tumor bearing rat are shown. The area enhanced by Gd-DOTA on the T_1 weighted image (Fig. IV-7a) is outlined. The corresponding CBVf map is given in Fig. IV-7b together with a corresponding microscopic Hoechst stained image covering a large part of the tumor (Fig. IV-7c). This advanced stage C6 tumor model is characterized by a large CBVf heterogeneity. The CBVf map exhibits low blood volume in the center of the tumor ROI and some areas characterized by a higher blood volume in the periphery. The HE stained section of this tumor revealed large necrotic areas in the tumor center. The Hoechst staining confirms a low vessel density in this ROI. Only few but enlarged vessels that are highly permeable to the Hoechst dye are visible. Interestingly, this typical vascular pattern for high grade tumors extends well beyond the region enhanced by Gd-DOTA, showing that the tumor extend can be easily misinterpreted using contrast enhanced MRI only. At the spatial resolution used to display the microscopy image, normal Hoechst stained microvasculature which is small and dense, gives a cloudy aspect such as encountered on the left border of the image.

Fig. IV-7: Coronal images from a C6 glioma bearing rat.

a: T_1 weighted image,

b: CBVf map and

c: the corresponding Hoechst fluorescent image.

The ROI corresponds to the tumor extension as revealed by the signal enhancement on a T_1 weighted image after Gd-DOTA injection. The Hoechst staining reveals rather sparse enlarged and leaky vessels within this ROI but also beyond.

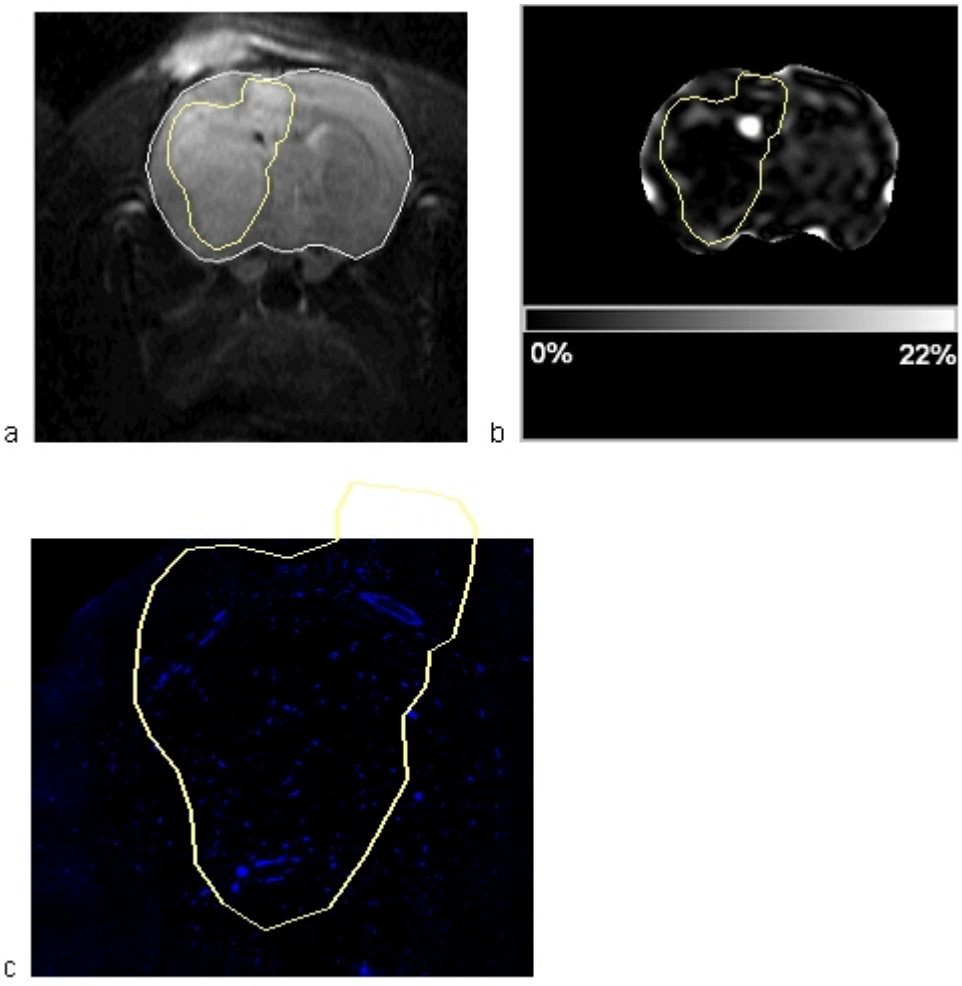

4.8. Discussion

4.8.1. Advantages of Gd-ACX

The relaxivity due to Gd-ACX was found to be particularly high, without notable decrease at imaging fields above 1.5 T, contrary to the Gd^{3+} complexes of high molecular weights (Aime et al. 2005; Caravan et al. 1999; Livramento et al. 2006a; Livramento et al. 2006b; Vander Elst et al. 2003). These observations were a strong encouragement to undertake detailed in vitro and in vivo studies of this potential CA, particularly suited for high field MRI. Gd-ACX presents two major advantages with respect to unspecific small molecular CA: it has a twofold longitudinal relaxivity at 2.35T and there is reasonable evidence that, despite its low molecular weight, Gd-ACX does not extravasate, even in a C6 brain tumor model for which the BBB is known to be permeable to Gd-DOTA and P760 (Fonchy et al. 2001). The experiments show, that Gd-ACX remains confined to the intravascular space during at least one hour. Therefore Gd- ACX has properties of blood pool CA such as macromolecular complexes. An MR paramagnetic contrast agent that does not extravasate throughout the period of an MRI examination, even in very leaky vascular beds, can lead to more accurate measurements of hemodynamic parameters in pathologic microvasculature.

4.8.2. Reason of Gd-ACX confinement to the blood pool

The origin of the vascular confinement of Gd-ACX is not yet understood and only speculations can be made. It is certainly not the size of the complex alone that impedes its leakage through an impaired BBB. The disk-shape, charge, and hydrophilicity are other properties that can limit its diffusion. The polarity of the Gd-ACX complex is currently under investigation since it is probable to play a role in the vascular confinement. Moreover it is not excluded that it binds to a serum protein. This hypothesis has not been investigated in detail, yet, but the slight relaxivity increase of Gd-ACX in plasma is a first finding in this context since the binding to a blood compound can affect rotational motion, and overall relaxivity. However, the longitudinal relaxation rate increase at 2.35T and 1 mM Gd-ACX concentration is only about 15% ($\frac{R_{1(\text{saline solution})}}{R_{1(\text{plasma})}} = \frac{9.3\ s^{-1}}{10.7\ s^{-1}} = 0.81$). If there is an interaction between Gd-ACX and blood proteins, the rotational correlation time of the paramagnetic center is not significantly modified by the binding.

4.8.3. CBVf in tumor, contralateral and normal brain tissue

The global CBVf values in healthy rats obtained with Gd-ACX are in the same order as those found with SINEREM (cf. Chapter II and III). However, the contralateral brain tissue in the tumor bearing rats exhibits a significantly lower CBVf. Since the three week old tumors are of considerable size, the low contralateral CBVf is probably the result of compression and consequently of increased interstitial pressure. An impaired metabolism, as well as decreased blood flow and blood volume in the hemisphere contralateral to high grade gliomas have also been observed by other authors proving that contralateral and peritumoral tissue is affected by the tumor presence. Different explanations were given such as a generalized immune response, edema, redistribution of blood flow, mass effect, or microscopic tumor infiltration (Beaney et al. 1985; Ito et al. 1982). Recently, Julien et al (Julien et al. 2004), using the steady state ΔR2* technique for CBVf mapping, also found a decreased blood volume contralateral to a C6 glioma in rats.

Even in the absence of CA extravasation, the CBVf in tumor tissue might be overestimated due to non negligible intra-/extravascular water exchange. Even for the intact blood brain barrier, the range of water exchange rates given in the literature is large: 1 to 2 s^{-1} (Labadie et al. 1994). In case of malignant glioma, which is a very heterogeneous tumor, the water exchange rate surely varies across the tumor extension. It is therefore impossible to estimate the error included in the cerebral blood volume measure. For CBVf measurements in tumor tissues it is even more important to minimize the water exchange effect by using short sequence time parameters.

4.8.4. Problems encountered with Gd-ACX

Although biocompatibility in mice and absence of hemolysis was shown, the use of a prototype CA like Gd-ACX is not always without experimental problems. The synthesis of ACX is a very time consuming process and at each synthesis only small amounts of ACX were dedicated to in vivo MRI experiments. Many different batches of ACX have therefore been used to carry out all the experiments described and microanalysis and ^{1}H-NMR spectroscopy could not be repeated on all batches to exclude impurities. Despite the intravenous use of $1/10^{th}$ of the LD_{50} (0.05 mmol/kg Gd-ACX), no effects on vital parameters and the arterial blood gases were observed in

any of the rats. Moreover, before the CBVf study, a couple of preliminary experiments have been performed using a dose of 0.1 mmol/kg without observable adverse effects.

Once, after synthesis and complexation of a new batch of ACX, a drop of the arterial blood pressure was observed when Gd-ACX was administered as fast intravenous injection at 0.1 mmol/kg. The blood pressure returned to normal values within a couple of seconds as soon as the injection was interrupted. By injecting the CA at a slower rate, the blood pressure drop could be prevented. Such an effect on the blood pressure had not been observed with other ACX batches, where the injection had been carried out at a rate usually used when administering P760, SINEREM or Gd-DOTA. Although the synthesis, complexation and filtration had been carried out exactly as before, and the products were purchased from the same companies, this effect on the blood pressure was reproducible with a variable degree in different rats.
Finally it was decided to use the remaining amount of ACX from this batch to test the tolerance of intravenous Gd-ACX injections at a dose of 0.1 mmol/kg in more detail. This experiment included cardiac monitoring and laboratory analysis of blood withdrawn five minutes after injection.

4.8.5. Intravenous tolerance of Gd-ACX

Protocol

Gd-ACX solutions with a Gd/ACX concentration of 25/50 mM were prepared and filtered as described above. Six male healthy Wistar rats (240 to 300 g) under isoflurane anesthsia were used. Cannulas were inserted into the femoral artery and vein. The intravenous injections were carried out manually at a dose of 0.1 mmol/kg Gd-ACX. The electrocardiogram and blood pressure was monitored on the LabVIEW interface during and for 15 minutes after completed injection. A recently custum-built electrocardiogram device was used. The electrocardiogram electrodes were attached to the forepaws and to the left hindpaw. Only one derivation was recordable.
The injections were interrupted if the blood pressure fell below 60 mmHg, until it became constant or rose again. The total duration of the injections (volume 0.92 to 1.1 ml) was about 4 min.
A volume of 2.75 ml arterial blood was withdrawn five minutes after injection for blood gases and biochemical parameters. Since reliable laboratory values for Wistar rats are sparse in the

literature and interindividual differences might be large, the same amount of arterial blood was also sampled before Gd-ACX injection to monitor the changes individually. Blood films were also performed with blood sampled before and after injection to examine the erythrocyte fragility and morphology.

Results

The electrocardiogram recordings were difficult to analyze due to 50 Hz and breathing artifacts. No changes of the QRS complex could be identified after injection.

Nevertheless in all cases a reversible blood pressure decrease during injection could be observed. The blood pressure continuously rises after completed injection and reaches normal values within two minutes. The blood pressure amplitude decreased in three out of five rats. The normal range of systolic and diastolic blood pressure is 88 – 184 mmHg and 58 – 145 mmHg, respectively.

No systematic modification of the heart rate could be observed before and after injection. In three rats it decreased and became irregular but remained within the normal range (123 – 480 min^{-1}, mean 205 min^{-1}). In the other two rats it remained unchanged. The respiratory frequency clearly accelerated during injection. However, no effects on the arterial blood gases were observed in any of the rats.

The Prothrombin Time (PT) and the Thrombin Time (TT) were slightly longer after injection but still within the range of reference values from literature. However, the Activated Partial Thromboplastin Time (APTT) became three to six times longer after Gd-ACX injection, suggesting a defect in the intrinsic pathway of the hemostasis (deficiencies in prekallikrein, factors XII, XI, IX or VIII, or combinations thereof).

Inspection of the blood films after routine May-Grunwald-Giemsa staining revealed no morphologic changes of the erythrocytes. The lactic dehydrogenase (LDH) did not change significantly after injection but both values (before and after injection) were higher than the literature reference values found. This is probably the result of iatrogenic hemolysis during sampling. The alkaline phosphatase was slightly lower after injection. Reference values for rats were not available. Total serum calcium levels rose by more than 40 %. Elevated serum calcium

can be a sign of renal failure or muscle damage. Serum chloride rose by about 4 %, urea by 12 % and serum phosphate was more than two-fold higher after injection. This can also be a sign of renal failure and muscle damage. Creatinin levels rose by more than 70 %, indicative of impaired renal function, congestive heart failure or shock. Other blood parameters were not significantly different before and after injection.

Conclusion

From these findings it can be concluded that the immediate effect of an intravenous injection of Gd-ACX is a decrease of the arterial blood pressure due to depression of both diastolic and systolic myocardial function, sometimes accompanied by a decreasing cardiac frequency. These are clinical signs indicative of a systemic shock syndrome. If the injection is carried out rapidly as a bolus, the cardiovascular collapse might lead to ischemic organ dysfunction, but an intermittent or slow injection allows the peripheral vasomotor tone to recover and the acute shock signs are reversible. Such acute adverse effects during CA injection at high speed have been observed in other studies and are attributed to osmotic expansion of the plasma volume and failure of the cardiovascular circulation (de Haen et al. 1994). There is no strong evidence for primary cardiac dysfunction. The biochemical analysis of the blood after injection indicates an acute renal failure. The high serum Ca^{2+} level is responsible for the cardiac arrhythmia observed in some cases.
The outcome of this experiment neither confirms nor excludes dissociation of the Gd-ACX complex with liberation of toxic Gd^{3+} ions.

Contrary to what one might expect, not many papers studying the effects of a unique intravenous administration of $GdCl_3$ to rats have been published. Spencer et al (Spencer et al. 1997) described mineral emboli and depositions composed of gadolinium, calcium and phosphate in the capillary bed of, predominantly, lung and kidneys, and hepatocellular and splenic necrosis. In addition, this study also revealed decreased platelet numbers and increased prothrombin time and activated partial thromboplastin time.

4.8.6. Dissociation of Gd^{3+}

The stability constant of a lanthanide Ln^{3+}-ACX inclusion complex was obtained with the lutetium ion Lu^{3+} (Bonnet et al. 2005) and is log $K_{Lu\text{-}ACX}$ = 7.5 (≈ log $K_{Gd\text{-}ACX}$), which is much smaller than for Gd-DTPA or Gd-DOTA (log K ≥ 20) (Caravan et al. 1999).

The NMRD profiles of Gd-ACX exhibit only a modest dispersion with frequency. This is consistent with the absence of free Gd^{3+} ions in the solution, since the profiles are very different from that of the free aquo Gd^{3+} ion (Powell et al. 1996). The Gd-ACX complex in solution stored in sealed tubes at 4°C are chemically stable for a few months as shown by the fact that strictly the same r_1-relaxivity values were obtained just after complexation and two months later. In particular, this result indicates that no substantial concentration of free gadolinium ions has appeared in normal saline solution during this period. Although this is an encouraging finding, it might not be a sufficient proof for the in vivo stability of Gd-ACX. The xylenol orange test could be used on blood sampled after Gd-ACX injection to detect whether free Gd^{3+} ions appear in blood.

4.8.7. Transmetallation

The selectivity of ACX for some endogeneous ions Cu^{2+}, Ca^{2+}, Na^{+}, K^{+} was evaluated in vitro (Fauvelle 1999). The association constants for K^{+} or Cs^{+} with ACX were in the order of log K ≈ 2, low compared to that of Lu-ACX and even lower for Cu^{2+}, Ca^{2+} and Na^{+} such that no complex formation with ACX was detectable with NMR spectroscopy. The transmetallation by endogeneous Zn^{2+} ions has not been investigated yet. In vitro proton relaxometry could be used to determine whether plasma anions compete with ACX for the Gd^{3+} ion. If transmetallation occurs, the released Gd^{3+} ions form complexes with the plasma anions and the relaxation rate of plasma would decrease.

4.8.8. In vivo use of Gd-ACX

Despite the moderate formation constant of ACX and Gd^{3+}, the Gd-ACX complex can be administered to animals at the dose of 0.05 mmol Gd^{3+} kg^{-1} body weight, which is R_1 and R_2 isoefficient to the standard doses (0.1 mmol/kg) of small molecular CA such as Gd-DOTA. Knowing that the safety factor (ratio of LD_{50} to effective dose) is between 50 and 100 for Gd-DOTA (ref: Brochure DOTAREM, Le macrocycle de l'IRM, Guerbet), Gd-DTPA and other CAs that recently entered clinical trials (e.g. MS-325), the use of Gd-ACX at $1/10^{th}$ of the median lethal dose can only be envisaged in animal studies. Applications of the $RSST_1$ method in combination with Gd-ACX are the preclinical evaluation of the therapeutic effect of new antivascular or antiangiogenic drugs.

4.8.9. β-cyclodextrin derivative

The recently synthesizeḍ β-cyclodextrin derivative (BCX) is analog to ACX with seven instead of six glucose units and is characterized by a greater solubility. The longitudinal relaxivity of its complex with Gd^{3+} in water is 28.0 ± 1.0 $s^{-1}mM^{-1}$ at 2.35T and 18.5 ± 0.5 $s^{-1}mM^{-1}$ at 7T. The transverse relaxivity is 32.0 ± 1.0 $s^{-1}mM^{-1}$ at 2.35T (Chieze 2005). If its biocompatibility can be confirmed, Gd-BCX could be an even more promising CA than Gd-ACX.

5. Chapter V: Histological vascular morphometric analysis

5.1. Introduction

Histological methods are the "gold standard" for measuring many vascular parameters. A correlation should exist between data obtained by other imaging techniques and histological data. In the clinical setting, histological validation is required especially in the presence of tumors, in which the CA distribution is relatively unspecific. The standard histological parameter for angiogenesis assessment is the microvessel density, but several investigators point out that the microvessel density is not a direct correlate of the blood volume (Hawighorst et al. 1998). It does not contain information about vessel diameter and length and the perfusion status. Particularly in tumors the vessel architecture is chaotic. The vessels are characterized by a large diameter distribution, tortuosity and incomplete perfusion (Bernsen et al. 1995). Some tumors even develop a microcirculation without typical endothelial cells (Folberg et al. 2000), and staining of endothelial cells only would miss these areas of vasculogenic mimicry.

This chapter presents an evaluation of a stereological technique for the CBVf assessment from histological sections through brain tumors imaged by MRI for CBVf quantification. The findings from histology and MRI are compared.

French Introduction

Chapitre V : Analyses histologiques de la morphologie vasculaire

Les analyses histologiques sont considérées comme ″méthodes standards″ pour de nombreux paramètres vasculaires. Les données vasculaires obtenues par IRM doivent en toute rigueur être corrélées aux données histologiques, et cette validation est très souvent nécessaire car la distribution de l'AC dans la tumeur n'est pas seulement liée à une vascularisation. Le paramètre standard mesuré par histologie et qui est corrélé au VSC est la densité de micro-vaisseaux. Ce paramètre est en revanche controversé par certains des auteurs (Hawighorst et al. 1998) car il ne contient aucune information relative au diamètre, tortuosité, distribution ou encore l'état de perfusion. Dans les tumeurs, l'architecture des microvaisseaux est justement chaotique

(Bernsen et al. 1995). De plus, il existe des tumeurs qui développent une microcirculation sans la présence de cellules endothéliales (Folberg et al. 2000) et par conséquent une méthode basée sur la coloration des cellules endothéliales conduit dans ce cas à des mesures erronées.

Dans ce chapitre, une technique de ″stéréologie″ est utilisée pour mesurer le VSC à partir de coupes histologiques obtenues au niveau de la tumeur. Cette technique est confrontée aux mesures réalisées chez le même animal utilisant la méthode $RSST_1$ avec le Gd-ACX comme AC.

5.2. CBVf by epifluorescent microscopy

Although the CBVf is a three-dimensional parameter and not directly quantifiable from a histological section, the goal of this study was to develop an approach by which CBVf measurements by MRI and histology can be directly correlated. For this purpose morphometric analysis of immunohistochemically stained brain vessels was carried out. Stereological methods help estimating parameters defining the three-dimensional form of vessels from two-dimensional sections.

5.3. The CBVf as vascular volume density V_v

The vascular structures confined in a reference volume V_{ref} enclose the vascular volume V, given as a volume ratio

$$V_v = V / V_{ref} .$$

Assuming vessels to be some kind of flexible cylinders, their volume can be obtained from the total vessel length L (the sum of the lengths of each vessel independent of vessel size and number) and the average vessel diameter $\bar{d}$ as follows:

$$V = \frac{\pi}{4} \bar{d}^2 L .$$

The length density L_v is defined as

$$L_v = L / V_{ref}$$

and used to derive V_v, named the vascular volume density:

$$V_v = \frac{\pi}{4} \bar{d}^2 L_v$$

In order to estimate L_v from a certain number of parallel sections within V_{ref} with random distances between each other, some information about the shape, the orientation and the tortuosity of these vessels needs to obtained from the available vessel cross-sections.

In a model, in which vessels are perfect cylinders arranged parallel to each other (total anisotropy) appearing as circular cross-sections on a plane perpendicular to their axis, L_v is simply the number of cross-sections in the section surface multiplied by the length of the side of V_{ref} which is parallel to the vessel axis and divided by V_{ref}. The resulting dimension is therefore $mm/mm^3 = mm^{-2}$. In this case, the numerical value of L_v is equal to the vessel density N_{2D} [mm^{-2}], which is expressed as the number of vessel cross-sections per section surface. As soon as the section is not perpendicular to all vessel axes, this equality does not hold any more. This is the case when the section is not perpendicular to the vessel bundle, when the vessels are no longer parallel, or when the vessels are no longer straight but winding.

5.4. Adair's stereological method for the estimation of the vascular length density

Adair et al (Adair et al. 1994) presented the following stereological method:

The intersection of a cylindrical vessel with a plane is an ellipse whose major axis a and minor axis b define the angle α of intersection of the vessel with the plane:

$$\sin\alpha = b / a .$$

The greater the angle of intersection, the greater the probability that a random section intersects the vessel segment (cf. Fig. V-1).

$\frac{1}{\sin\alpha}$ is therefore used as a weighting factor in the count of vessel cross-sections.

For α = 90°, $\frac{1}{\sin\alpha}$ equals 1.0,

for α close to 0°, $\frac{1}{\sin\alpha}$ approaches infinity.

L_v is therefore a weighted sum of vessel cross-sections in the test area A_t (or ROI) within one plane. In practice, several parallel sections within V_{ref} at regular or irregular distances are used and the L_v is the weighted sum of all vessel cross-sections within all test areas:

$$L_v = \frac{\sum_{\text{vessel cross-sections}} a/b}{\sum_{\text{test areas}} A_t}. \qquad \textbf{Eq. V-1}$$

The vascular area density A_V, which represents the fraction of the total tissue area occupied by the vessel wall and lumen, depends on the overall number, length, and size of vessels. According to the Delesse principle, stating that the profile area of a random section through a number of objects is proportional to the expected value of the objects' volume (Delesse 1848), A_V is often used to estimate the blood volume although it contains only two-dimensional information.

Fig. V-1: The vessel sections are ellipses. The ratio of major and minor axis (a and b respectively) depends on the angle of intersection with the vessel: $\sin\alpha = b/a$. In Adair's stereological algorithm the inverse of this ratio is used as a weighting factor. Circular vessel sections are weighted with the factor 1, elliptical sections with a factor > 1.

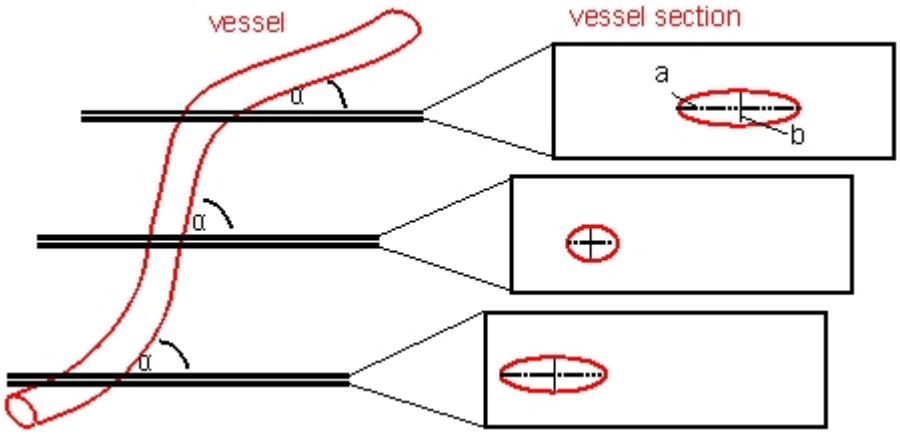

5.5. Material and methods

In this study, we compare the tumor CBVf obtained by the $RSST_1$ method with Gd-ACX as CA with the vascular volume density that can be measured by histological vascular morphometric analysis. Therefore, the rat brains used in this study are those of the C6 tumor bearing rats used for the CBVf measurement described in chapter IV. The microvasculature of seven rats enrolled in the MRI experiment was analyzed by epifluorescent microscopy. Four of these rats had received an injection of the fluorescent Hoechst dye. Their brains were removed, frozen and cut as described in Chapter IV (paragraph 4.7.1). The aim was to obtain 20 approximately equally spaced sections of 10 µm thickness from the same location as the MR image (2 mm thickness) for quantitative analysis of the microvasculature. Due to technical problems during the cutting process and due to inappropriate storage of some histological slides, not all sections were fully exploitable for the correlation of MRI results with histology.

5.5.1. Anti-collagen IV and Hoechst staining

All sections were stained with goat anti-collagen IV (Southern Biotechnology Associates, Inc., ref 1340-01, USA) and a second anti-goat antibody labeled with Alexa Fluor 546 (Molecular Probes, Inc., ref A11056, USA). The staining procedure with the anti-collagen IV antibody (diluted 1/100 in phosphate-buffered saline (PBS)) takes 12 h in a humid chamber at 4°C. Then slides are rinsed in PBS and exposed for 1 h at room temperature and in the dark to the secondary antibody conjugated to Alexa 546 (diluted 1/100). After a last rinse with PBS the slides were refrozen at -90°C.

This fluorescent marker stains the endothelium of all microvessels since collagen IV is the major constituent of the basal lamina. The DNA-intercalating Hoechst dye stains the nuclei of endothelial cells in blood vessels which are perfused at the moment of injection. In tumors, adjacent cells are also stained because the dye diffuses across a ruptured BBB into the tissue, similar to Gd-DOTA.

5.5.2. Image acquisition

The tissue sections were scanned with a Nikon Eclipse E600 microscope equipped with a Olympus DP50 microscope digital camera system and interfaced with a digital image processing software (AnalySIS). The Hoechst dye is ideally excited with UV light at approximately 350 nm. A filter was used which is optimized for the DAPI dye. Fluorescence emission can be detected at about 450 nm (blue channel) and with very low intensity at about 675 nm (red channel). A TRITC filter was used for the excitation and detection of the Alexa Fluor 546 fluorescence. The absorption maximum of Alexa Fluor 546 is 556 nm and the emission wavelength about 573 nm.

Each slice was scanned twice, during the same session, at a 10× magnification using the DAPI filter first, followed by the TRITC filter. The slides were moved by a high precision motorized scanning stage controlled by the image processing software. This procedure avoids the necessity of image registration when the images have to be matched (Rijken et al. 1995).

For all acquisitions the gamma factor had a value of 1, the saturation factor a value of 0 and the red, green and blue color channels had their maximum sensitivity value of 20. Only the exposure time varied between 50 and 100 ms for acquisitions with the DAPI filter and between 0.5 and 2.5 s with the TRITC filter in function of the fluorescent staining intensity. The pixel size of the resulting digital image was 0.767 µm.

Due to computer limitations only a maximum array of 6 x 6 or 5 x 7 images could be scanned, representing a total area of 9146 x 6865 μm^2 or 10664 x 5727 / 7628 x 8002 μm^2. In most cases this hardly covered the massively enlarged right hemisphere on the coronal slices, almost entirely occupied by the tumor. Little healthy appearing surrounding tissue is included on these images.

The composite image was computed from the individual images by the AnalySIS software. The acquisition and image processing time for one composite image was 20 minutes with each filter, i.e. 14 hours for one brain. For this reason only the ipsilateral tumor bearing hemisphere has been processed. In addition, the individual images were not always perfectly aligned. This process is based on image registration for overlapping image borders. In these cases, either the whole acquisition was repeated using a larger overlapping border, resulting in a smaller image with slightly lower SNR but with satisfactory alignment at visual inspection, or the section was

not used for quantitative analysis. This is another reason why less than 20 sections were analyzed for some rats.

5.5.3. Data analysis

The intensities of fluorescent images were analyzed with ImageJ software. A custom-made semiautomatic macro (included in the Appendix) was used for image segmentation and feature extraction. A flow chart of the macro is given in Fig. V-2. The anti-collagen IV stained images were processed first.

Fig. V-2: Flowchart of macro structure for semiautomated quantitative analysis of vascular structures from histological images

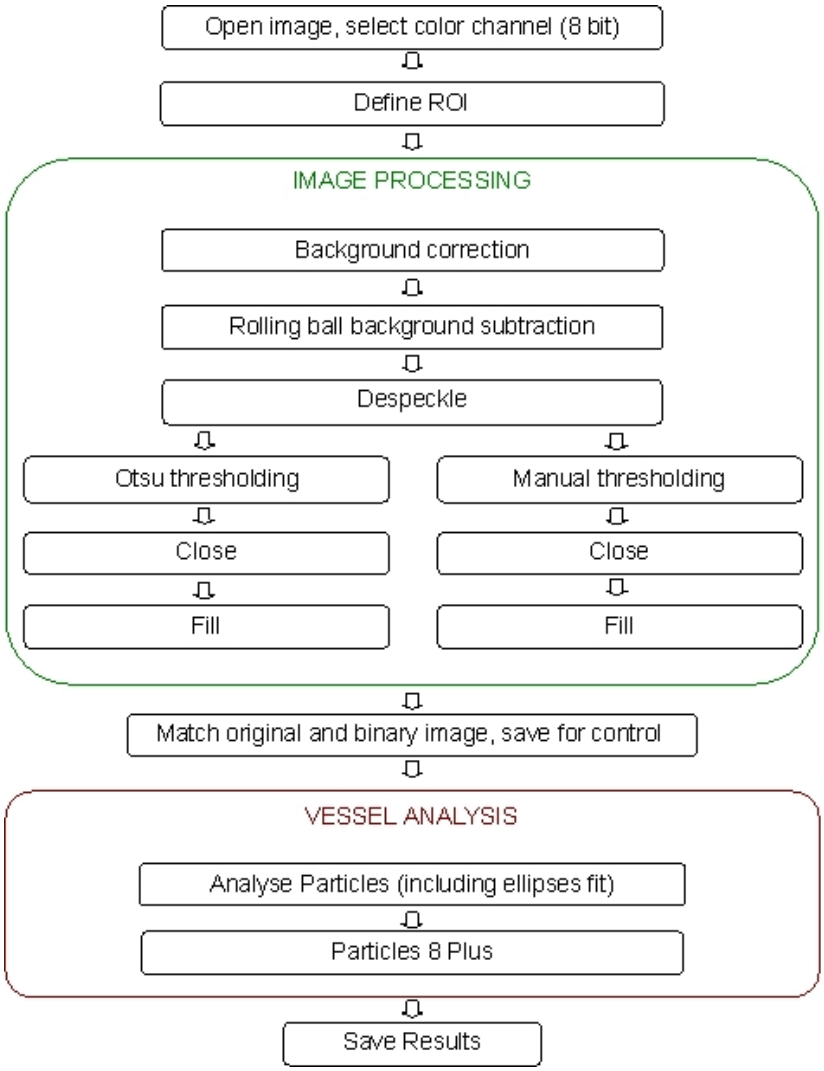

RGB images were converted to 8-bit gray scale images. ROIs were defined in the periphery of the tumor and in its central part. As much tumor tissue as possible was included in the ROIs, as had been done when analyzing the MRI data, but when the tumor size exceeded the borders of the composite image, the ROIs were smaller than those on the MRI-based CBVf-maps. Where available, ROIs were also defined in the ipsilateral (mainly parietal) cortex and the ipsilateral corpus callosum (appearing normal on HE images). Care was taken to exclude large vessels, which surely belong to the "macrovasculature" such as the anterior and middle cerebral artery.

A plugin for background correction was systematically used. This plugin corrects an uneven image illumination and contrast enhances the resulting image. Optionally, the "rolling ball background subtraction", an algorithm provided by ImageJ, could be used. One concern with setting a threshold manually is the potential to introduce user-bias. Among the automatic thresholding algorithms available with ImageJ, only Otsu's thresholding algorithm (Otsu 1979) and the maximum entropy method performed well on most ROIs. Where possible, the binary masks of the vessels were obtained by thresholding according to the nonparametric approach described by Otsu (Otsu 1979), but a manual thresholding was sometimes necessary in the tumor ROIs because of the low contrast, variable background intensity and noise. After thresholding, the profiles were closed by dilatation followed by erosion and the vessel lumina were filled in. The binarized image and the original image were combined for verification of the binarization process, and the matched image was saved.

Particle Analysis was carried out using the "Analyse Particles" and the "Particles 8 Plus" plugins (cf. Appendix I: Plugin "Morphology"). These plugins derive a number of morphologic parameters such as surface, perimeter, center of mass, the Feret and the Breadth for each profile. The Feret diameter is defined as the longest distance between any two points along the structure boundary. The Breadth is the largest axis perpendicular to the Feret. Additionally, ellipses are fitted to each vessel profile, by equalizing the second order central moments of the ellipse to those of the pixel distribution. The resulting ellipse has also the same area as the irregular profile. The bounding box is the smallest rectangle that encloses the profile. The following parameters for each profile were saved to an Excel spreadsheet for further analysis: the surface, the diameter of the inscribed circle, the major and minor axes of the fitted ellipses, the height and width of the bounding box, the Feret and the Breadth. Additional parameters of interest

extracted from this analysis were the area of the ROI, the vessel density, the vascular area density, the sum of the ratios of the ellipse axes

$$\sum_{\text{vessel cross-sections}} a/b$$

and the length density L_v calculated according to. Eq. V-1.

The mean edge to edge vascular diameter including the lumen and the endothelial wall were approximated in four different ways, illustrated in Fig. V-3:

1. radius of the inscribed circle (IC)
2. minor axis of the ellipses (MAE)
3. small side of the bounding box (BB)
4. Breadth.

Fig. V-3: Scheme of an irregular vessel section (red) and the diameters measured. See text for abbreviations.

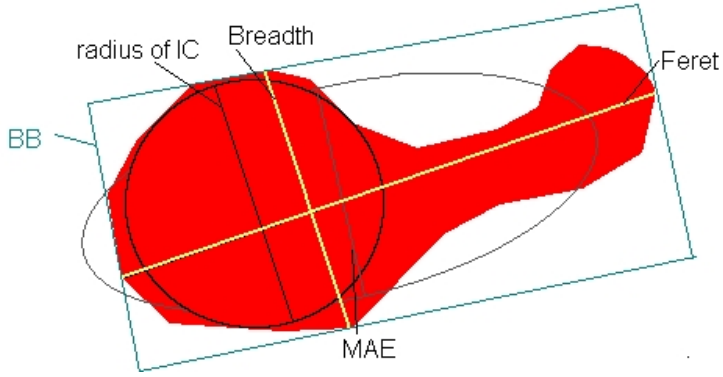

The diameters of all vessels in the ROI were averaged (without cut-off value to eliminate larger vessels), since the aim of this study was to compare the V_v with the CBVf obtained by the $RSST_1$ method, which is sensitive to all vessels sizes.

Such an Excel file was created for each brain section and for each ROI. Mean values were computed by averaging over all vessels in one ROI and over the corresponding ROIs on all available slices. The vascular volume was calculated according using the four different mean vessel diameters.

After image analysis of the anti-collagen IV stained images, the Hoechst fluorescence image carrying information about the functionality and the permeability of tumor vasculature was overlaid on the anti-collagen IV stained image in order to select the outline of the functional vessels by a Boolean AND operation. This assumes that the vessels in the two images are perfectly superimposed. Fortunately, the Hoechst dye diffuses around most tumor microvessels, such that the stained area is enlarged. Therefore, for the tumor tissue, the perfused vessels are correctly selected, even if a slight shift exists between the images. The analysis was then repeated for the selected vessels.

5.6. Results

5.6.1. Pilot study on a cylinder model

Before interpreting the results from brain vasculature, a pilot study was carried out to test the robustness of the algorithm. A three-dimensional numerical geometric model (Verant et al. 2007) composed of a number of straight cylinders with randomly varying diameters and orientations was created using a Turbo Pascal code written by J.C. Vial (Spectro Physics Laboratory, CNRS). The 512 $\times$ 512 $\times$ 512 cube was then decomposed into a stack of 512 images using ImageJ. The analysis was run on 18 images sampled at regular distances without defining a ROI. The obtained total cylinder volume was compared with the known total cylinder volume, to estimate the accuracy of the stereological algorithm. In addition, it was studied in which way the accuracy diminishes with a decreasing number of examined slices. The four methods for obtaining the diameter were also compared.

Four different numerical geometric models were generated by varying the number of cylinders and the cylinder diameters (Table V-1). The diameter range was created by $R := A + B \cdot \text{random}$, where R is the radius, A and B are scalars and “random” is a variable in the range of 0 to 1 with uniform probability density function.

Table V-1: geometrical parameters of the numerical cylinder models

stack	true volume fraction (%)	cylinder diameter (pixel)	number of cylinders
a	3.4	14 - 22	40
b	2.5	14 - 22	30
c	2.9	4 - 16	60
d	2	4 - 10	110

Diameter estimation

Table V-2 shows that the mean diameters computed in all four ways are within the range of true diameters. However the minor axis of the ellipse and the Breadth perform best, with respect to the true mean diameter, except for stacks c and d in which the mean cylinder diameter were systematically over- and underestimated, respecively. This might be caused by the small size of the structures in models c and d with respect to the pixel size. The mean capillary diameter is in the order of 7 µm which is 10 times larger than the pixel size in the images obtained from immunohistochemically stained sections. A misestimation due to this effect is therefore less likely when analyzing the histologic images.

Table V-2: comparison of mean diameters obtained from the numerical cylinder models by four different methods: diameter of inscribed circle (IC), minor axis of ellipse (MAE), small side of bounding box (BB) and Breadth

stack	mean cylinder diameter				
	true	**IC**	**MAE**	**BB**	**Breadth**
a	18	15.63	18.21	20.88	18.88
b	18	15.46	17.50	19.28	17.65
c	10	10.74	12.88	14.30	13.33
d	7	4.44	5.95	6.60	5.82

Volume estimation

For stack a, b and c, the total cylinder volume is slightly better estimated using the Breadth instead of the minor axis of the ellipse (cf Table V-3). For large diameters the precision is excellent when using the Breadth. For the range of diameters used in stack c the

underestimation is less than 10%. The mean diameter with respect to the image resolution (10 × pixel size) in stack c corresponds to the one in the histological images. The vascular area density also reflects the cylinder volume very well. All methods underestimate the total cylinder volume in stack d.

Table V-3: comparison of area and volume densities in the numerical cylinder model

stack	cylinder area density A_V [%]	cylinder volume density $V_v = pi/4\ \bar{d}^2\ L_v \cdot 100$ [%]			
		IC	MAE	BB	Breadth
a	3.39	2.32	3.14	4.13	3.38
b	2.44	1.94	2.48	3.01	2.52
c	2.74	1.70	2.45	3.02	2.62
d	1.63	0.72	1.29	1.59	1.24

Figure V-4 shows that from eight to ten sections upwards the length density and the mean diameters and therefore the volume density stabilize. For very few sections the error related to the sampling of non representative sections plays a role.

Fig. V-4: dependence of vessel diameter, vascular volume density (V_v) and length density (L_v) on the number of sampled sections in stack b

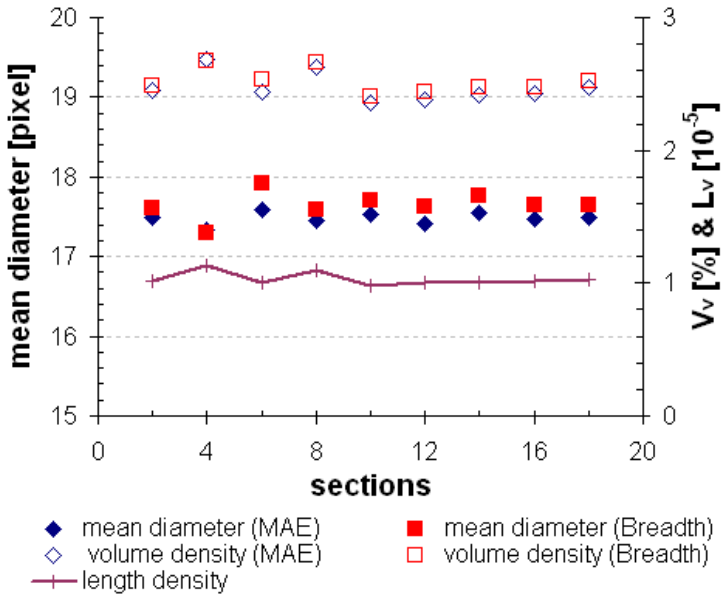

5.6.2. Vascular volume density and vessel diameters in healthy Wistar rats

It is interesting to compare the vascular parameters obtained from tumor tissue with those from healthy tissue. Unfortunately, the control rats from the MRI experiment were not enrolled in this histological study. To test whether the MRI results for normal brain tissue can be reproduced using the stereological technique, the analysis was carried out on images of immunohistochemically stained sections of three Wistar rat brains, which had undergone unilateral vessel occlusion in a previous cerebral ischemia experiment. Therefore, only structures in the normal appearing contralateral hemisphere were analyzed. Eight slices were available for each rat. The section thickness was 5 µm and the digitized image had a pixelsize of 1.379 µm. Cortical and subcortical gray matter (GM) ROIs and a white matter ROI (WM) in the corpus callosum were analyzed.

Table V-4: vascular parameters in three brain regions contralateral to the ischemic lesion
V_V = vascular volume density, A_V = vascular area density

ROI	MAE [µm^2]	Breadth [µm^2]	L_v [mm^{-2}]	V_v (MAE) [%]	V_v (Breadth) [%]	A_V [%]	vessel density [mm^{-2}]
cortical GM	4.9 ± 0.1	7.8 ± 0.1	12340 ± 72	2.38 ± 0.25	6.06 ± 0.46	4.60 ± 0.66	437.0 ± 34.2
WM	4.8 ± 0.2	7.3 ± 0.3	578 ± 111	1.00 ± 0.16	2.35 ± 0.41	1.93 ± 0.27	197.3 ± 23.6
subc. GM	4.9 ± 0.0	7.7 ± 0.2	898 ± 155	1.68 ± 0.27	4.07 ± 0.57	3.32 ± 0.47	319.5 ± 50.4

Vessel diameters

While the approximation of the vessel diameter by the minor axis of a fitted ellipse and by the Breadth yielded similar results for the elliptical profiles of cylinders (Table V-3), they differed by a factor of 1.6 for irregular shaped vessel profiles (Table V-4). However, both estimations yield diameters in the range of those reported in the literature, from 3 to 5 µm (Farrell et al. 1991; Schlageter et al. 1999) to 7 to 8 µm (Deane and Lantos 1981; Pathak et al. 2001). No significant regional differences in this parameter was found (nonparametric Wilcoxon signed rank test for paired comparisons) in accordance with literature (Schlageter et al. 1999; Weiss et al. 1982).

Vascular volume density

The V_v values resulting from the MAE and the Breadth differed by a factor > 2 (Table V-4). The V_v calculated using the average Breadth however is closer to the vascular area density, which has the advantage of being independent of any vessel diameter estimations. Schlageter et al found vascular area densities from 1.9 to 3.0 % for cortical gray matter (2.9% for the parietal cortex), 1.3% for white matter of the corpus callosum and 0.8 to 1.7% for subcortical gray matter (Schlageter et al. 1999). For the in vivo studies, the results obtained with the inscribed circle and the bounding box are omitted because these methods yield unphysiologically small and large vessel diameters, respectively.

The V_v ratios (Breadth) for cortical gray matter to white matter and for cortical gray matter to subcortical gray matter were 2.63 ± 0.51 and 1.51 ± 0.25, respectively. Calculating the same ratios for V_v obtained using the MAE yield 2.41 ± 0.45 for cortical gray matter to white matter and 1.44 ± 0.27 for cortical gray matter to subcortical gray matter. The corresponding vascular area density ratios were similar to the V_v ratios. The cortical to subcortical gray matter ratio is comparable to the CBVf ratios obtained by MRI (Table 0-4). The cortical gray matter to white matter ratio obtained with the stereological algorithm is greater than the one obtained by MRI (Schwarzbauer et al. 1997) and CT (Adam et al. 2003), but is not much higher than the vascular area density ratio found by Schlageter et al in normal rat brain (Schlageter et al. 1999).

5.6.3. Vascular volume density and vessel diameters in C6 tumor tissue

Vascular volume density

Figure V-5 shows two typical microscopic images of a tumor, on which the anti-collagen IV staining and the Hoechst staining were merged (Fig. V-5 a and b), reflecting the heterogeneous nature of the tumor. Figure V-5a is a ROI located in the periphery of the tumor in which deformed enlarged and permeable vessels coexist with vessels having a rather normal appearance. The ROI in Fig. V-5b covers a necrotic avascular part (left), an area with sparse massively enlarged vessels (middle), and an area with a slightly higher density of microvessels with irregular shape (right). It can be observed that only few of the vessels in this last area are perfused. The last two images show the anti-collagen IV stained microvasculature in the contralateral cortex (c) and in the contralateral corpus callosum (d) for comparison. The

microvessels are small and of regular shape and are better delineated, because the background noise (staining of the extravascular extracellular matrix) is reduced. The vessel density is homogeneous, and clearly higher in the gray matter than in the white matter.

For the tumor bearing rat brains only the V_v obtained from the Breadth is given in the figures and tables because it correlated better with the vascular area density. The histogram in Fig. V-6 shows the V_v in the tumor ROIs for each individual rat. Results are also reported for rats for which fewer than 20 histological sections were evaluated (I7 = 16, J0 = 8, J1 = 14 sections), since the stereological algorithm is supposed to work for any number of sampled sections and was shown to give reproducible results for eight and more sections. Averaged over all available rats the V_v in the tumor periphery and in the tumor center were 2.24 ± 0.96% and 1.10 ± 0.96%, respectively (n = 7), counting all vessels, and 1.26 ± 0.19% and 0.43 ± 0.29%, respectively (n = 4), counting the perfused vessels only. The V_v of perfused vessels was therefore by a factor of 0.6 and 0.4 smaller than the total V_v for the tumor periphery and the tumor center, respectively. The average vascular area densities in these two tumor ROIs were 1.97 ± 0.73% and 0.99 ± 0.76%, respectively, counting all vessels, and 1.04 ± 0.14% and 0.33 ± 0.21%, respectively, counting the perfused vessels only.

Normal appearing cortical regions were measured in six rats and white matter regions were measured in four rats, as the cortex and/or the corpus callosum could not be reliably differentiated from the tumor on the histological images of the other rats. The mean V_v in these ROIs were 4.98 ± 0.34% and 1.86 ± 0.36%, respectively. The mean vascular area densities were 4.53 ± 0.32% and 1.69 ± 0.36%, respectively. Only the anti-collagen IV stained images were analysed because it was supposed that all vessels were perfused in healthy brain tissue.

Fig. V-5:

a and b: Images showing the microvasculature in the periphery (a) and in the center of a C6 tumor (b). The anti-collagen IV and Hoechst staining are overlaid.

c and d: Anti-collagen IV staining of ROIs in the contralateral gray matter of the cortex (c) and in the white matter of the corpus callosum (d). Image size 1556 µm × 1176 µm.

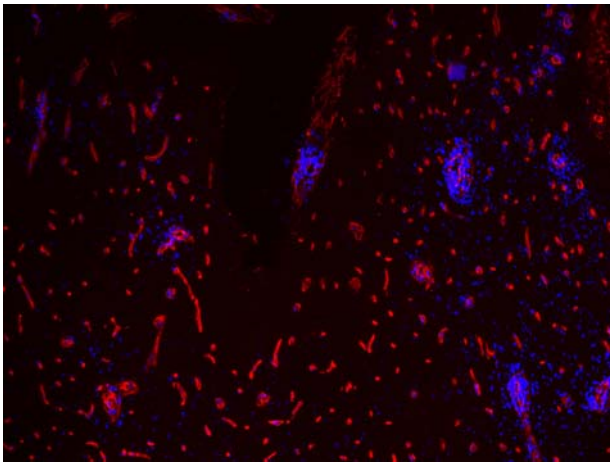

a

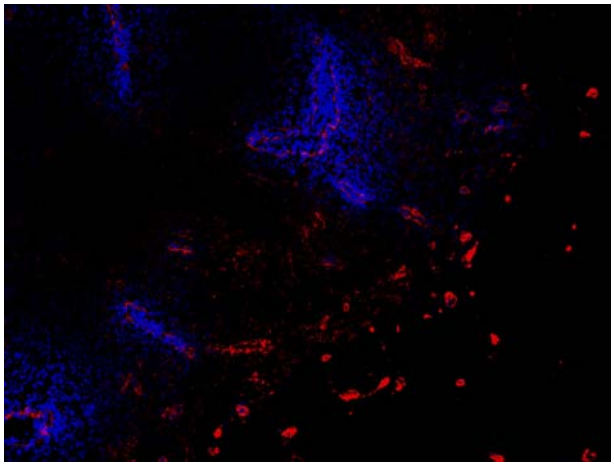

b

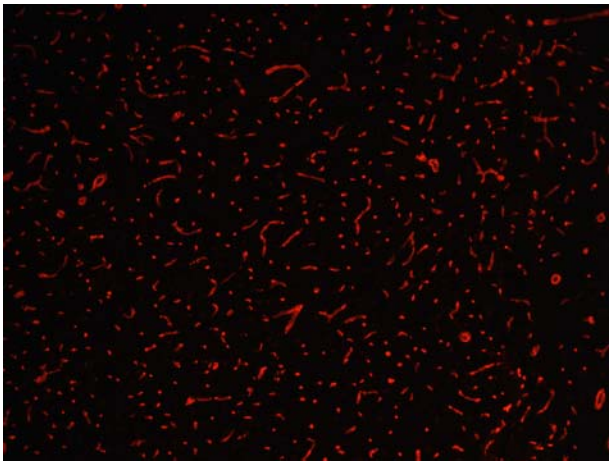

c

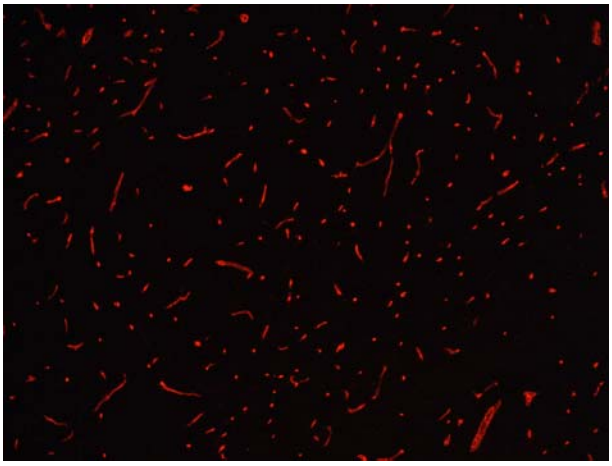

d

Fig. V-6: Vascular volume densities V_V of the total vascular bed (anti-collagen IV stain) and the perfused vascular bed (Hoechst stain) in the central and the peripheral part of C6 tumors. I7 to J5 are the designations of the rats involved in the MRI experiments and in the vascular morphometric analysis

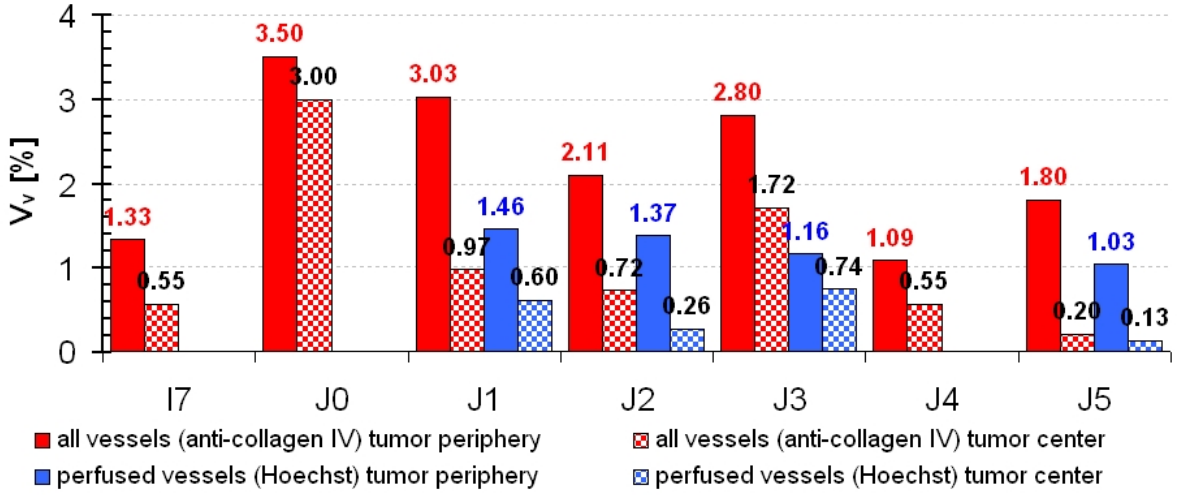

Using the V_v for perfused microvasculature derived from the Breadth, no correlation with the CBVf data obtained by MRI could be found using the Spearman nonparametric correlation (GraphPad Prism 5) for the four rats for which the perfused vascular bed was evaluated (Figure V-7). Using the V_v for perfused microvasculature derived from the MAE, the correlation coefficient r_S was 0.32, without being significant. Figure V-7 shows the blood volumes obtained by MRI and from histological data for the tumor peripheries. Either the V_v in one of these rat brains was overestimated, or the CBVf by MRI underestimated.

Fig. V-7: Correlation of the tumor blood volume fractions obtained by histology (perfused vessels only) and by MRI peripheral ROIs of the tumors

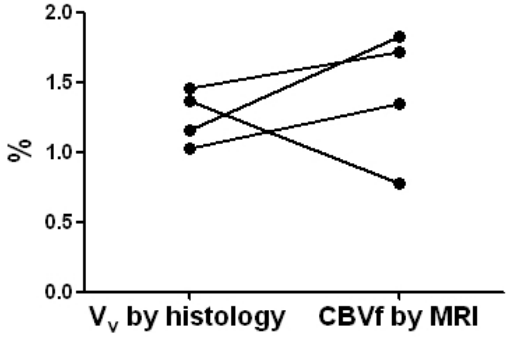

Vessel diameters

Although the mean diameters of perfused vessels were smaller in both tumor ROIs (Table V-5), the difference was not significant (nonparametric Wilcoxon signed rank test for paired comparisons) neither in the tumor periphery nor in the tumor center. Vessel collapse or compression is therefore unlikely as explanation for the reduced perfusion. Unperfused vessels are more likely to be occluded without major alteration of their sizes. There was no significant difference between the diameters of tumor vessels and of vessels in peritumoral gray matter and white matter, neither. The mean diameter obtained from the Breath of the vessel profiles were in accordance with published values for the healthy brain (Dennie et al. 1998; Pathak et al. 2001) and for the C6 tumor model (Farrell et al. 1991; Tropres et al. 2004). However, in the study published by Tropres et al (Tropres et al. 2004), the tumor vessels were enlarged (mean diameter in the tumor periphery 4.1 ± 2.1 μm and in the tumor center 5.8 ± 4.1 μm) with respect to the cortical microvessels in the contralateral hemisphere (mean diameter 3.1 ± 1.3 μm). Larger microvessels in a C6 tumor model (mean diameter 12.5 ± 6.8 μm) with respect to gray matter microvasculature (mean diameter 6.6 ± 2.1 μm) were also observed in the study carried out by Dennie et al (Dennie et al. 1998).

Table V-5: Mean vessel diameter (Breadth) for different cerebral ROIs

tumor periphery	**all vessels**	7.97 ± 1.31 μm
	perfused vessels	6.78 ± 0.77 μm
tumor center	**all vessels**	7.50 ± 1.46 μm
	perfused vessels	6.62 ± 0.31 μm
cortical GM	**all vessels**	8.67 ± 0.70 μm
WM	**all vessels**	8.95 ± 1.16 μm

5.7. Discussion

5.7.1. Vessel diameters

The large discrepancy between the calculations of the mean diameter, especially for the irregularly shaped vascular profiles is not surprising. What is the best way to define the diameter of a profile? For almost elliptical profiles, passing from the centre of mass, the centroid, rotating particle, inscribed circles, (max+min)/2, etc. will not considerably change the obtained diameter. However, the diameter of a convex object like the letter "O" must be quite different from a concave object, like the letter "C". In the cylinder model and in both histological experiments, the Breadth-based V_v-calculation was very similar to the vascular area density. Although the MAE-based estimation yielded smaller diameters and consequently smaller V_v, they were in accordance with published values. The true V_v probably lies between these estimations.

It is also rather difficult to compare vessel diameters measured by different investigators, since the method employed is rarely the same. In addition, some authors average the vessel diameters only over a particular range, defining for example microvasculature as vessels with diameters < 12 µm (Weiss et al. 1982). The stereological calculation of the V_v derived from the mean vessel diameter (factor d^2 !) is very sensitive to variations in this parameter. In this study, the V_v is always compared with the vascular area density, which, although more sensitive to the Holmes effect (projected size of the object $\geq$ real size (Hennig 1969)), is insensitive to miscalculation of the vascular diameter.

Since anti-collagen IV stains the basal lamina, the thickness of the vessel wall is included in the calculation of the vascular area and vascular volume fraction. Although with the studied MRI technique only the intravascular water should contribute to the signal, the water exchange probably extends the origin of the acquired signal to the vessel wall or beyond.

5.7.2. Method dependence

Apart from the fact that morphologic and quantitative functional parameters (e.g. the CBVf) describing the microvasculature in the gray matter and in particular in the cortex are very region specific (Bereczki et al. 1992; Cremer and Seville 1983; Schlageter et al. 1999), regional quantitative parameters vary even more between different techniques. For example, Cremer et

al and Bereczki et al (using radiolabeled erythrocytes and plasma) report CBVf values below 1.5% for most brain regions, while morphometric methods generally report CBVf or vascular area densities between 1 and 2% (Bar 1980; Dunn et al. 2004; Pathak et al. 2003; Pathak et al. 2001), although some authors found values up to 3% (Schlageter et al. 1999) or 5% (Weiss et al. 1982), depending on the stereological technique used. There also is evidence that not all vessels are perfused in healthy brain tissue (Shockley and LaManna 1988; Weiss et al. 1982).

However, the major methodological impact on CBVf measurement seems to originate from whether the CBVf is measured in vivo or post mortem. From Table 0-4 it can be seen that with few exceptions in vivo CBVf measurements yield values in the range from 2 to 4%. A comparison of in vivo CBVf measurements by a non invasive technique with post mortem CBVf evaluations has to be interpreted with caution.

5.7.3. Comparison between CBVf obtained by histology and MRI

Comparing in vivo MRI with an invasive method is technically challenging because the data (the brain sections) are not in the same format and have very different spatial resolutions. The main difficulty was to define similar ROIs on the MRI and histological slices. Each technique has additional limitations.

The blood water detected by the $RSST_1$-MRI technique for CBVf measurement, is the one contained in perfused vessels. The V_v of the two tumor regions obtained from Hoechst staining are very close to the corresponding CBVf obtained by MRI. However, only for four rats co-staining with Hoechst and anti-collagen IV was available for correlation analysis and as illustrated in Fig. V-5 no correlation could be found for tumor ROIs because of one rat for which the CBVf obtained by MRI was heavily underestimated or the V_v overestimated. If this rat was excluded, the Spearman correlation coefficient would be $r_S = 0.5$. This outsider had a tumor, which was too large to be included in one image. It is therefore possible that the ROI outlined on the histological image was less representative than the one on the MRI image.

It is generally easier to show correlation between two techniques when data from healthy brain is used, rather than data from heterogeneous tumor tissue (Pathak et al. 2001). Unfortunately, contralateral V_v for correlation with MRI data was not available in this experiment. While Pathak et al found a significant correlation between morphologic estimates and MRI-based CBVf in

healthy tissue, the correlation was as poor as in our study for the tumor microvasculature. Recent studies carried out in the laboratory (Valable et al. submitted 2007) compare the CBVf obtained in a C6 rat brain tumor model by the steady state ΔR_2^* method using SINEREM as CA with the vascular volume fraction computed by Pathak's stereological method for slice thickness correction. Six to nine microscopic fields (about 500 µm × 600 µm, slice thickness 20 µm) were scanned and analyzed. Although only anti-collagen IV staining was used for microvessel delineation in this study, the histological vascular volume fraction was only about one third of the CBVf measured by MRI but a significant correlation was observed between the histological and the MRI data.

Immunohistochemistry confirmed that tumor vascularity was not uniform, with blood volume highest in the tumor border and lowest in the tumor core. As for the CBVf obtained by MRI using the $RSST_1$ technique, in areas of necrosis, the CBVf was practically null.

The ratio of perfused V_v to total V_v was about 0.4 to 0.6 in this late stage glioma model. This is in accordance with observations by Bernsen et al who found that the perfused fraction of tumor vessels ranged from 0.20 to 0.85 in human glioma xenografts in mice (Bernsen et al. 1995). The authors have not found any morphological differences between the perfused and unperfused vascular bed, neither, so their values are likely to reflect the V_v ratio, too.

5.7.4. Technical considerations

A spatial shift between the anti-collagen IV stained and the Hoechst stained images was not observable, but can not be excluded. The precision of the motorized stage was reported to be as good as ± 1 µm, but apart visual inspection no criterion was available to test the correctness of the image alignment. A way to evaluate errors induced by misregistration, is to compare for example the vascular area density on non-tumor ROIs on anti-collagen IV and Hoechst stained images and on the combined image, since in healthy tissue Hoechst remains intravascular. Given the sharp outline of healthy vessels stained with anti-collagen IV and with Hoechst, the two images could be combined using appropriate image processing software, and visually inspected for a shift.

The impact of variations in threshold setting on the derived vascular parameters was studied by Rijken et al (Rijken et al. 1995). This, together with the way to calculate the vessel diameter, is probably the factor with the highest incertitude in this analysis.

5.8. Conclusion

There is no real gold-standard for quantifying the CBVf by histological vascular analysis. Here a technique for vascular volume density measurement is proposed, which requires the measurement of the vascular diameters. There is no gold standard for measuring the vascular diameters neither. We therefore calculate the vascular diameters in four different ways and we suggest the Breadth and the MAE as being an appropriate measure based on the criteria that the vascular volume density calculated with the mean diameter corresponding to the Breadth and the MAE correleate best with the vascular area density, which is a generally accepted histological surrogate for the CBVf measurement.

The vascular volume density evaluated in this study is only an estimation. Due to the multiple sources of inaccuracy detailed above, the impact of which is almost impossible to quantify, no incertitude interval can be given for the values.

6. Chapter VI: CBVf and CA leakage profiles in tumor tissue

6.1. Introduction

The signal behavior versus time in the $RSST_1$ condition provides only a static impression of signal enhancement, whereas it contains dynamic information as soon as the vasculature is permeable to the CA. The aim of this chapter is to demonstrate that, in the case of CA extravasation, apart of estimating the vascular volume fraction (CBVf in brain tissue), the $RSST_1$ method has an additional potential for the assessment of dynamic parameters associated with the microvascular permeability. CA and tissue specific enhancement rates, a parameter related to the vessel permeability, and leakage volume fractions can be derived as for other DCE-MRI methods without the measurement of the vascular CA concentration versus time (input function) during the $RSST_1$ interval. In this chapter, the leakage profiles of Gd-DOTA and P760 in muscle and in an RG2 tumor model in Fischer rats were analyzed.

French Introduction

Chapitre VI : VSC et profils d'extravasation des AC dans les tumeurs

L'évolution du signal acquis avec la méthode $RSST_1$ au cours du temps donne une information dynamique dans une région perméable à l'AC.
Le but de ce chapitre est de démontrer, que dans le cas de l'extravasation de l'AC, la méthode $RSST_1$ pourrait conduire à mesurer les paramètres dynamiques en relation avec la perméabilité du système vasculaire. La vitesse du rehaussement du signal et la fraction du volume de distribution extravasculaire peuvent être également obtenus comme dans le cas des méthodes dites "DCE –MRI", sans mesurer l'évolution du signal dans une région vasculaire (la fonction artérielle d'entrée).
Dans ce chapitre, les profils d'extravasation du Gd-DOTA et du P760 ont été analysés dans le muscle et dans le modèle de tumeur RG2 chez des rats Fischer pour estimer la fraction volumique sanguine, la perméabilité pour les AC et aussi le volume de distribution extravasculaire des AC.

6.1.1. The $RSST_1$ interval with blood pool CA

As described in the first chapter, the $RSST_1$ method using MR CA confined to the vascular compartment is designed to measure the vascular volume, during the time interval for which the conditions for a rapid steady state of the signal from the vascular compartment are fulfilled. This steady state signal amplitude is reached and maintained with an intravascular CA concentration C_{iv} above a critical value or, equivalently, a blood T_1 relaxation time below the critical value (T_1 < 1/5 T_{inv} of the sequence used). Under this condition the input function does not need to be known, although neither the blood CA concentration nor the T_1 relaxation time need to be constant during that interval. When the CA is confined to the vascular compartment, only the blood compartment has a short T_1 relaxation time allowing the acquisition of a tissue signal, which has a constant amplitude and corresponds to the equilibrium magnetization of the vascular compartment. In this case, the signal amplitude reflects the vascular volume fraction and the main advantage of a prolonged $RSST_1$ interval is to accumulate the signal for the improvement of the SNR.

6.1.2. The $RSST_1$ interval and CA leakage

If the CA is not confined to the vascular compartment, the tissue signal amplitude increases continuously because a signal contribution also arises from the extravascular space. Although the tissue signal amplitude is not constant, the $RSST_1$ conditions are fulfilled for the vascular signal! This can be verified by monitoring the signal amplitude in any large vessel, which is not permeable to the CA.

For typical small and intermediate molecular size Gd^{3+} based CA, which do not enter the intracellular space, the distribution volume beyond the vascular compartment is a particular part of the extravascular extracellular compartment, the size of which has to be determined. Here we call this particular space in which the CA diffuses the leakage compartment. Since typical signal versus time curves can be observed for various tissues and CAs, they are named tissue leakage profiles, and an attempt is made to derive parameters that describe these tissue and CA specific profiles, by estimating the leakage volume fraction and the enhancement rate, similar to DCE-MRI methods. It has previously been observed that CA uptake and washout curves could be used to determine some properties of tumor tissue (Gowland et al. 1992). Several studies using mathematical models adapted to measurements by CT (Yeung et al. 1992), PET (Iannotti et al.

1987; Ott et al. 1991) and MRI (Kenney et al. 1992; Krueck et al. 1994; Schmiedl et al. 1992) to characterize brain tumors have been published. The correlation between DCE-MRI derived parameters and WHO grade were studied in human brain tumors. Good correlation was found for both, CBV (Ludemann et al. 2000) and microvascular permeability (Roberts et al. 2000).

6.2. Theory

In the following analysis we propose to decompose the tissue signal into two components: a signal component originating from the intravascular compartment (iv) and a signal component originating from the extravascular compartment (ev).

$S = S_{iv} + S_{ev}$,

S, S_{iv} and S_{ev} symbolizing the signal intensities of the ROI, the intravascular and the extravascular compartment, respectively, because

$V_{total} = V_{iv} + V_{ev}$,

V_{total}, V_{iv} and V_{ev} symbolizing the volumes of the ROI, the intravascular and the extravascular compartment, respectively.

In contrast to the model of Kety (Kety 1951) and Tofts (Tofts 1997; Tofts et al. 1999; Tofts and Kermode 1991), we do take into account the contribution of the CA in the intravascular compartment.

Both compartments are composed of subcompartments, not all being accessible to the CA. The intravascular intracellular and the plasma compartment (p) compose the intravascular compartment. The CA does not attain the intracellular compartments, but the intravascular intracellular compartment (erythrocytes, ivi) contributes to the MR signal because its T_1 relaxation time is shortened by rapid transcytolemmal water exchange. Only a fraction of the extravascular compartment will be occupied by the CA, which is called leakage compartment (l). The leakage, the extravascular intracellular (evi) and the remaining extravascular extracellular (eve) compartment compose the extravascular compartment:

$V_{iv} = V_p + V_{ivi}$,

$V_{ev} = V_l + V_{evi} + V_{eve}$

V_p, V_{ivi} , V_l, V_{evi} and V_{eve} symbolizing the volumes of the plasma, intravascular intracellular, leakage, extravascular intracellular and the remaining extravascular extracellular compartment that is inaccessible to the CA, respectively.

6.2.1. Pharmacokinetic model

The CA is not regarded as freely diffusible across the BBB. The passive diffusive endothelial permeability to the CA is assumed to be small enough to dominate the leakage process. In the following we do consider only the plasma and leakage compartments accessible to the CA molecules, using a bidirectional two compartment kinetic model to describe the leakage process.

The transendothelial CA flow F_{pl} [mmol/s] between plasma and the leakage compartment is governed by the CA concentration gradient in plasma C_p and in the leakage compartment C_l (Tofts 1997; Tofts et al. 1999; Tofts and Kermode 1991):

$$F_{pl} = K^{trans}\left(C_p - C_l\right).$$

Here the plasma CA concentration is defined as:

$$C_p = \frac{C_{iv}}{1 - Hct}.$$

The proportionality constant K^{trans} (cm^3/s) is called the permeability coefficient and is the product of the diffusive permeability P (cm/s) of the endothelium for the CA and the total exchange surface S_v:

$$K^{trans} = P \cdot S_v.$$

We have assumed that the endothelial permeability is the same for the backflow of the CA from the leakage to the plasma compartment (Tofts and Kermode 1989; Tofts and Kermode 1991). If the blood flow F through the microvasculature is much larger than PS_v, than K^{trans} is also equal to the product of the blood flow F and the extraction fraction E:

$$K^{trans} = F \cdot E$$

where E is defined as (Crone 1963)

$$E = 1 - \exp\left(PS_v \middle/ F\right).$$

The change of the CA concentration in the leakage compartment dC_l/dt is proportional to the CA flow F_{pl} and inversely proportional to the leakage volume fraction v_l:

$$\frac{dC_l}{dt} = \frac{PS_v(C_p - C_l)}{v_l} = \frac{EF(C_p - C_l)}{v_l} \qquad \textbf{Eq. VI-1}$$

Eq. VI-1 is a first order linear differential equation in which C_p is regarded as constant during a short time interval after homogeneous distribution of the CA in the blood pool since the flowing blood replaces the small loss of CA from the plasma compartment due to the transendothelial leakage flow F_{pl}. With this approximation, the general solution to this differential equation is $C_l(t) = a(1 \pm \exp(-tb))$.

The initial condition is $C_l(t=0) = 0$, resulting in the following function for the CA concentration in the leakage compartment:

$$C_l(t) = C_p\left[1 - \exp\left(-t\frac{PS_v}{v_l}\right)\right]. \qquad \textbf{Eq. VI-2}$$

The CA is injected as a bolus of variable duration, but as described before in chapter I, the blood concentration of the CA after bolus passage and repeated recirculation reaches a value that remains above the critical concentration defining the conditions of the $RSST_1$. This results in a constant vascular signal for a certain time interval although the blood concentration of the CA might not be constant.

6.2.2. The phases of CA uptake in tissue

The signal enhancement is characterized by five phases. The diagram in Fig. VI-1 shows an idealized plot of the signal enhancement. The normalized signal S_{post}^{norm} defined by

$$S_{post}^{norm}(t) = \frac{S_{post}(t) - \langle S_{pre} \rangle}{\langle S_0 \rangle} \qquad \textbf{Eq. VI-3}$$

(equivalent to Eq. I-4 for a time varying signal) is plotted as a function of time. Unsuppressed signal components arising from tissue such as muscle tissue or white matter characterized by low T_1 are eliminated when using the S_{post}^{norm} signal. Therefore, before CA arrival in the vascular compartment of the tissue of interest (phase 0), the S_{post}^{norm} signal is null. Moreover, for the time interval for which the $RSST_1$ conditions are fulfilled, the S_{post}^{norm} signal amplitude corresponds to

the fractional distribution volume of the CA, which is v_{iv} if the CA is confined to the vasculature and v_d if it is not.

Fig. VI-1:
A model of the signal evolution during CA arrival and distribution in the tissue for two ROIs. The red plot represents the signal from a ROI, in which the CA is confined to the blood pool. The blue plot displays the idealized shape of a leakage profile. The five phases of CA uptake are explained in the main text. v_{iv} = intravascular volume fraction, v_l = volume fraction of the leakage compartment, v_d = distribution volume fraction

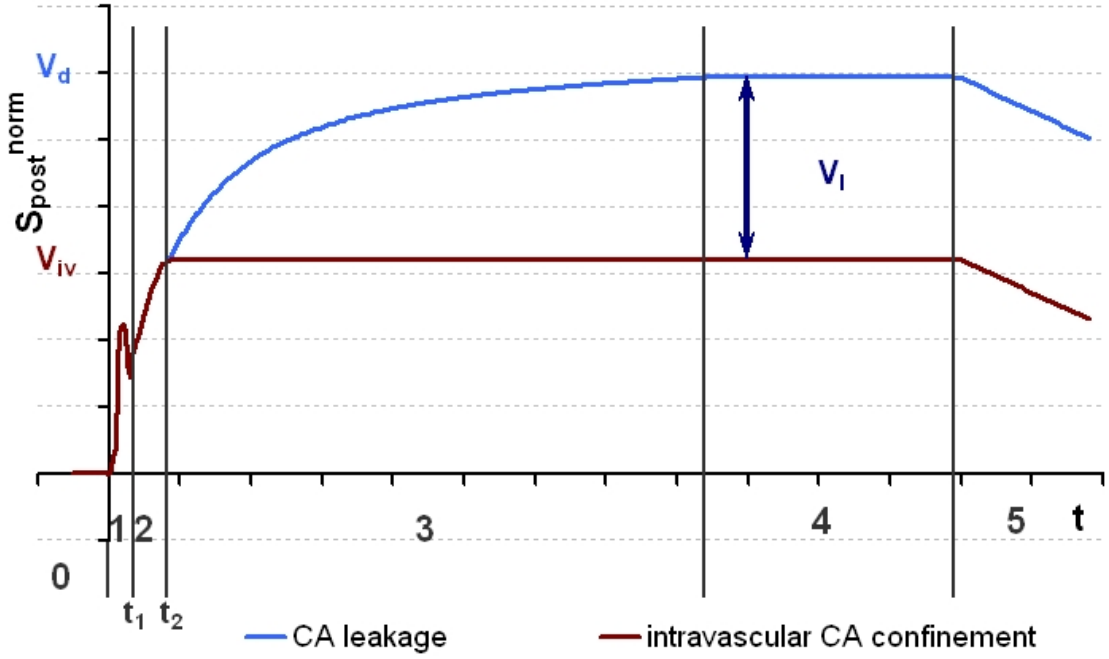

Bolus phase of the CA in the blood pool

The variable first part (phase 1) of the signal to time curve corresponding to the bolus passage is not analysed because of confounding T_2 and T_2* effects. Reliable analysis of this first part would require a standardized narrow bolus injection, a high temporal resolution and an accurate measurement of the local AIF. If the transverse relaxation effect at the high CA concentration during the bolus were negligible, the peak S^{norm}_{post} signal amplitude would reflect the CBVf.

Mixing phase of the CA in the blood pool

During the second part (phase 2, $t_1 < t < t_2$) of the signal to time curve, corresponding to the arrival and distribution of the CA in the intravascular compartment (mixing phase), the vascular signal increases due to stabilizing T_1 relaxation effects of the CA and decreasing T_2 relaxation effects. This part of the curve is dominated by a rapid signal enhancement of the vascular compartment approaching the maximum amplitude corresponding to the thermal equilibrium magnetization of the blood, which is attained at $t = t_2$ when the CA is homogeneously distributed in the blood pool resulting in a blood $T_1 < T_{inv}/5$.

CA leakage can become noticeable during this phase already. Therefore, a two compartment model is assumed for this phase and the tissue signal enhancement curves $S_{post}^{norm}(t)$ are described by a biexponential function of time:

$$S_{post}^{norm}(t) = S_{iv}\left[1-\exp(-t\kappa_{iv})\right] + S_{ev}\left[1-\exp(-t\kappa_{ev})\right], \text{ for } t_1 < t < t_2$$

κ_{iv} and κ_{ev} being the enhancement rates of the intravascular and the extravascular compartments, respectively. S_{iv} and S_{ev} symbolize the maximal intravascular and extravascular signal intensities, respectively, and correspond to the respective magnetization at thermal equilibrium.

Leakage phase of the CA into the extravascular compartment

During the following $RSST_1$ time interval (phase 3, $t > t_2$), the tissue signal is composed of a constant vascular signal component and a time dependent component which reflects the progressive leakage of CA into the leakage compartment. Owing to the constant vascular signal the tissue signal enhancement curve $S_{post}^{norm}(t)$ is described as follows:

$$S_{post}^{norm}(t) = S_{iv} + S_{ev}\left[1-\exp(-t\kappa_{ev})\right], \text{ for } t > t_2 \qquad \textbf{Eq. VI-4}$$

CA exchange equilibrium during the $RSST_1$ interval

If the $RSST_1$ interval is sufficiently long, the CA uptake curve can reach a constant value (phase 4) reflecting an equilibrium between CA leakage from the microvasculature into the extravascular leakage volume and backflow of CA from the leakage volume into the microvasculature. During this phase, the signal amplitude corresponds to the sum of the

fractional volumes of the intravascular and the extravascular leakage compartment, if the CA concentration in the leakage compartment is sufficiently high to result in a longitudinal relaxation time $T_1 < T_{inv}/5$ for this compartment.

Beyond this phase, the S_{post}^{norm} signal is not representing fractional distribution volumes any more (phase 5). This is the case when the CA concentration in the intravascular compartment decreases due to CA elimination from the blood pool. The CA concentration in the leakage compartment will decrease shortly afterwards due to backflow (washout) from the leakage compartment into the vascular compartment.

6.3. Material and Methods

6.3.1. Imaging protocol

The leakage profiles for P760 and Gd-DOTA of muscle and tumor ROIs were analysed in six male Fischer rats, three of them bearing unilateral intracerebral RG2 tumors 15 days after implantation. In the contralateral brain hemisphere and in three healthy Fischer rats, the CBVf was measured from the $RSST_1$ interval of the S_{post}^{norm} signal as described in chapter I.

MR imaging using IR-FLASH acquisitions under the $RSST_1$ conditions was performed. The sequence timing and image acquisition parameters were as usual: TR = 750 ms and T_{inv} = 325 ms for the S_{pre} and S_{post} acquisitions, TR = 10 s and T_{inv} = 8 s for the S_0 acquisition, TE = 3.2 ms, a single slice of 2 mm thickness, FOV 32 × 32, matrix 32 × 32, interpolated to 256 × 256. The equilibrium signal S_0 and the residual signal S_{pre} were acquired before CA administration. P760 at a dose of 0.05 mmol/kg was injected first, followed by an injection of 0.3 mmol/kg Gd-DOTA after a wash out time of at least one hour. All signals were acquired for 5 minutes.

6.3.2. Data analysis

The mean signal intensities $\langle S_{pre} \rangle$ and $\langle S_0 \rangle$ were computed from the acquisitions before CA administration (400 acquisitions for S_{pre} and 30 for S_0). Only the S_{post} signal is time dependent during and after CA administration.

The $S_{post}(t)$ signal was normalized according to Eq. VI-3 and plotted for ROIs in different tissues: temporal muscle and sinus cavernosus for all six rats, whole tumor, tumor border, tumor center and brain hemisphere contralateral to the tumor for the three tumor bearing rat brains, left hemisphere for the healthy rat brains. To demonstrate the different behavior of the signal in tissue ROIs with permeable and non permeable vasculature, a diagram showing the signal to time curves for ROIs in a tumor bearing brain is given in Fig. VI-2.

Fig. VI-2: $S_{post}^{norm}(t)$ was calculated using Eq. VI-3 for different ROIs in a RG2 tumor bearing rat brain obtained after injection of P760 and Gd-DOTA. In this rat, for both CAs, the RSST$_1$ condition is satisfied for 20 s < t < 90 s post injection, identified by a steady state signal from a ROI containing a major vessel. The red ordinate on the right is associated to the signal plot for the vascular ROI, the black ordinate on the left to all other signal plots. Since the normalized signal is plotted, the amplitude of a steady signal (sinus cavernosus, contralateral hemisphere) represents the vascular volume fraction. The signal obtained from the tumor ROI after Gd-DOTA injection shows a typical CA leakage profile.

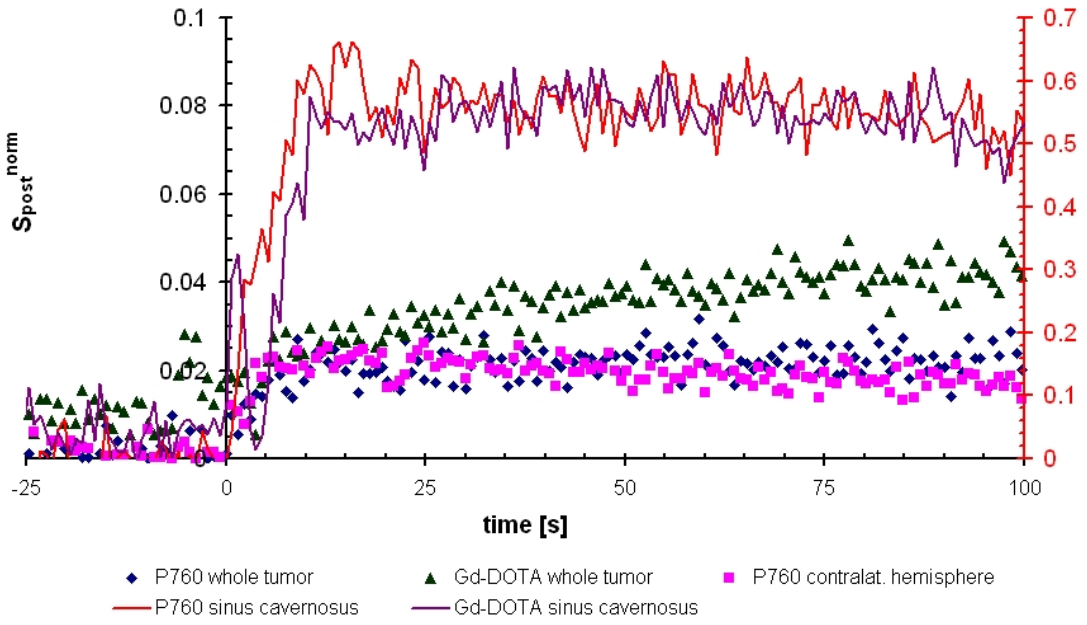

An ROI drawn on the sinus cavernosus was chosen because this was the largest vascular structure visible on the imaged slice, although not without partial volume effect. The vascular volume fraction in these ROIs was about 50 to 60%. No continuous signal increase indicative for a leakage profile was ever observed in a large vessel. The first signal enhancement in these vascular ROIs was interpreted as the arrival of CA, and defined as t = 0. The $RSST_1$ time interval for which the vascular signal is constant defines the signals from the CA leakage profiles that are fitted to Eq. VI-4. The fit is performed under Excel by adjusting the values of the variables in the model S_{iv}, S_{ev} and κ_{ev} to minimize the sum of the squares of the ordinate differences between the nonlinear model function and the experimental data points. In the nonlinear fit to the signal obtained by Gd-DOTA injection, the S_{iv} parameter had to be fixed to the value obtained by the fit from the P760 signal data, since the signal was not at its baseline value at the time of Gd-DOTA injection, due to incomplete washout of P760 (cf Fig. VI-2). The fit is performed for the following leakage profiles: muscle tissue (n = 6), tumor center (n = 3) and tumor border (n = 3). For all signal to time curves from ROIs displaying a constant signal amplitude during the $RSST_1$ interval, the average value over this time interval representing the vascular volume fraction is computed.

Figure VI-3 shows the tumor leakage profiles from the central part of a RG2 tumor of another rat after injection of P760 and Gd-DOTA along with the model functions obtained by nonlinear regression for the time interval shown by the continuous plots.

Fig. VI-3: Typical tumor leakage profiles $S_{post}^{norm}(t)$ from a RG2 tumor center (rat M5 in Table VI-2) after P760 and Gd-DOTA injection. The continuous colored lines represent the best fit to the exponential model and the time interval for which the $RSST_1$ condition was satisfied.

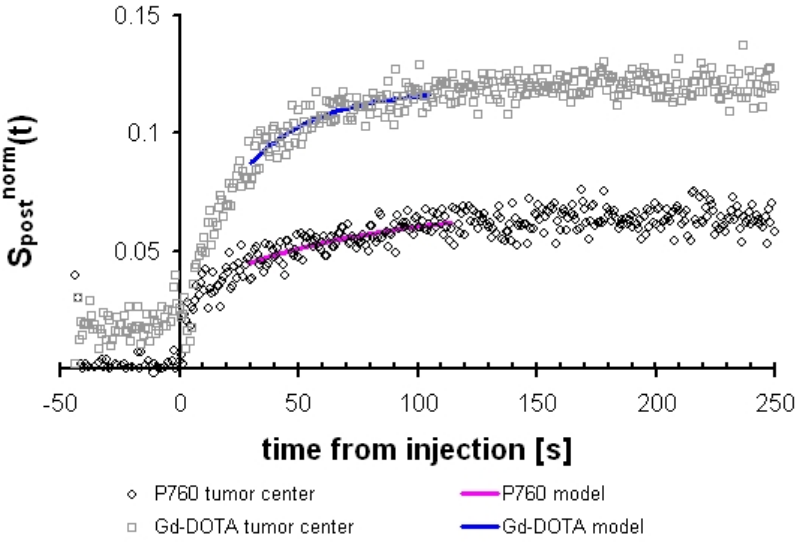

6.4. Results

6.4.1. The CBVf

Figure VI-4 summarizes the CBVf for brain ROIs that do not exhibit CA leakage. The CBVf contralateral to the tumor ranged from 1.22 to 1.68%, mean 1.52 ± 0.23%, while in healthy brain tissue the CBVf ranged from 2.18 to 2.80%, mean 2.39 ± 0.36% for P_aCO_2 values in the range of 36.7 to 43.4 mmHg. The signal amplitude from one out of three ROIs in the brain hemisphere contralateral to the tumor was not constant during the $RSST_1$ interval and was therefore excluded from this CBVf measurement.

Fig. VI-4: Histogram comparing CBVf (%) from healthy Fisher rat brain and brain tissue contralateral to RG2 tumors

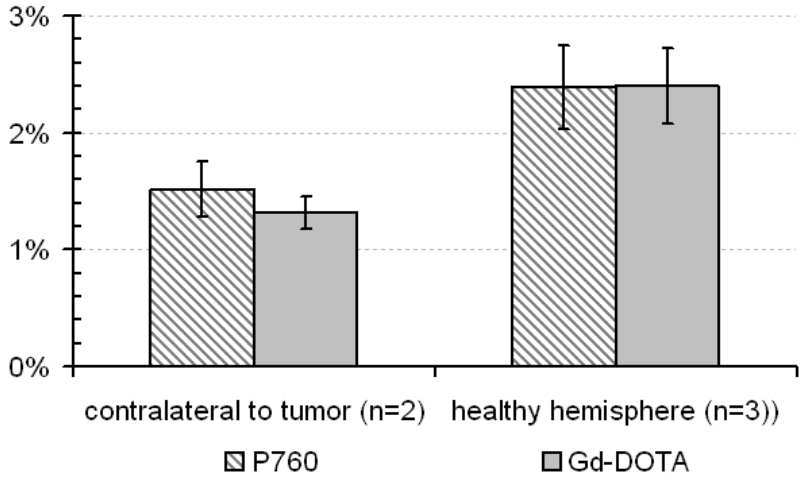

6.4.2. Leakage profiles in muscle and tumor ROIs

From leakage profiles such as shown in Fig. VI-1 and Fig. VI-2, it was observed that, for a given tissue ROI, the signal rise in function of time is always slower with P760 than with Gd-DOTA. When the $RSST_1$ interval is long enough, the signals after both CAs approach a constant value, which for all ROIs analyzed is higher after Gd-DOTA than after P760. These observations are the reason why we consider tissue and CA specific leakage profiles.

Table VI-1 shows the average (n = 6) adjusted parameters S_{iv}, S_{ev} and κ_{ev} for P760 and Gd-DOTA in muscle tissue.

Table VI-1: Mean vascular volume and leakage parameters for muscle tissue.

		mean	sd
P760	**S_{iv}**	0.028	0.013
P760	**S_{ev}**	0.044	0.024
P760	**κ_{ev}**	0.019	0.017
Gd-DOTA	**S_{iv}**	0.028	0.013
Gd-DOTA	**S_{ev}**	0.111	0.023
Gd-DOTA	**κ_{ev}**	0.080	0.034

Because of very variable leakage profile patterns for each tumor region, Table VI-2 shows the adjusted parameters for tumor ROIs for each rat individually and for both CA. The heterogeneity of tumor tissue and the small number of animals (n = 3) did not allow us to extract "typical" mean tumor parameters. The values marked with a cross correspond to data obtained from ROIs without typical leakage profile, and consequently the exponential model function does not fit the experimental data correctly.

Table VI-2: Individual vascular volume and leakage parameters for different RG2 tumors and tumor regions.

	rat	M4 tumor center	M5 tumor center	M6 tumor center	M4 tumor border	M5 tumor border	M6 tumor border
P760	S_{iv}	0.016 ×	0.032	0.013	0.019 ×	0.015 ×	0.013
P760	S_{ev}	0.408 ×	0.038	0.014	0.066 ×	0.055 ×	0.017
P760	κ_{ev}	0.000 ×	0.014	0.043	0.000 ×	0.000 ×	0.027
Gd-DOTA	S_{iv}	0.016	0.032	0.013	0.019 ×	0.015 ×	0.013
Gd-DOTA	S_{ev}	0.035	0.086	0.048	0.010 ×	0.002 ×	0.034
Gd-DOTA	κ_{ev}	0.030	0.034	0.020	0.027 ×	0.237 ×	0.019

6.5. Discussion

6.5.1. The CBVf

As shown in Fig. VI-4 brain tissue contralateral to tumor appears to have lower CBVf values, probably due to a compression effect from the tumor mass and associated edema. The difference is almost significant. Unfortunately, the low number of animals examined in this study, makes statistical analysis difficult (P = 0.059 using the Student t test) and does not justify definitive conclusions. But a similar result has been obtained for the contralateral hemisphere in a former experiment (cf. Chapter IV) using Gd-ACX in a C6 tumor model.

Only the CBVf contralateral to the RG2 tumor of two rats are summarized in the histogram because in the third rat the signal from this ROI after injection of Gd-DOTA exhibits an unusual behavior: the signal increases in a manner typical for a leakage profile. This is not observed with P760, where the signal remains perfectly constant during the $RSST_1$ time interval such as shown in Fig. VI-2.

The lower CBVf and the occasional pathologic signal enhancement pattern in brain tissue contralateral to a tumor indicate that this tissue should not be considered as healthy (Beaney et al. 1985; Ito et al. 1982). It is not without danger to use the contralateral CBVf for comparison with the tumor CBVf as is often done when reporting relative CBVf values (Cha et al. 2000a). It also shows the importance of studying truly healthy animals to derive "normal" CBVf values.

The global normocapnic CBVf obtained in this study using the IR-FLASH acquisition mode is in accordance with the CBVf = 2.07% found for the Fisher strain using the PR3D acquisition mode (chapter II) and not significantly different from the global CBVf for Wistar rats (chapter II and chapter IV).

6.5.2. Leakage profiles in muscle ROIs

The analysis of muscle ROIs shows that the microvasculature is permeable to both CA studied.

The vascular volume fraction

Depending on the speed of the intravenous CA injection, the equilibrium signal from the ROIs drawn in the sinus cavernosus is attained within 10 to 30 s after the first CA arrival marked by a signal enhancement. If we assume that during this time little CA has leaked out of the muscular microvasculature (Gowland et al. 1992), the value of the S_{iv} parameter is theoretically close to the vascular volume fraction (Roberts et al. 2000). For muscle we found a mean value of 2.8%, which is within the range of published values: 1.5 to 8% (Donahue et al. 1996), 11% (Kuwatsuru et al. 1993).

The leakage volume fraction

The signal from muscle tissue often approaches a constant value during the $RSST_1$ interval for large vessels, as if the intravascular-extravascular CA exchange has reached its equilibrium. The signal amplitude S_{post}^{norm} during this exchange equilibrium is only a few times larger than the vascular fraction, it could therefore be assumed that the extravascular CA concentration in the leakage compartment is sufficiently high (or equivalently the T_1 is sufficiently low) to satisfy the $RSST_1$ condition. In this case, the value of the S_{ev} parameter would be an estimate for the leakage volume fraction. Table VI-1 shows that the leakage volume for P760 in muscle tissue is only about twice the vascular volume fraction, while for Gd-DOTA it is in the order of 11%. This is in accordance with the leakage volume fraction of 10.4 ± 0.4% in muscle after Gd-DTPA injection reported by Parker et al (Parker et al. 1997).

The enhancement rate

Before the CA exchange equilibrium is attained, the IR-FLASH signal acquisitions monitor the speed of the CA leakage into the interstitium. The enhancement rate κ_{ev} could therefore be an estimate for the CA specific leakage rate. In muscle tissue, this enhancement rate is about 4 times higher for Gd-DOTA than for P760.

If, before attaining the CA exchange equilibrium, there is a linear relationship between the signal from the leakage compartment and the CA concentration C_l (Rosen et al. 1989) and if the plasmatic CA concentration were truly constant, then κ_{ev} would be equivalent to PS_v/v_l or EF/v_l (cf. Eq. VI-2) which is called rate constant $k_{ep} = K^{trans}/v_l$ (Tofts 1997; Tofts et al. 1999). This is a quantitative parameter that characterizes the microvascular leakage for a particular CA. If the extraction fraction E for a particular tissue and CA is known, the flow F can be deduced from this parameter (Larsson et al. 1994), and vice versa (Daldrup et al. 1998).

6.5.3. Leakage profiles in tumor ROIs

Although for all examined rats the leakage volume fraction and the enhancement rate were systematically smaller for P760 than for Gd-DOTA in muscle tissue, this observation could not be confirmed in the tumor ROIs. In two tumor ROIs the enhancement rate was greater for P760 than for Gd-DOTA. However, it was found that the leakage volume fraction for P760 is two to

three times smaller than the leakage volume fraction for Gd-DOTA, and for both CA smaller in the tumor ROIs than in the ROIs drawn in muscle tissue. The results listed in Table VI-2 show the large variability between the animals and the tumor regions.

Many studies have reported large intratumor heterogeneity in microvascular parameters such as CBVf and permeability for malignant tumors (Aronen et al. 1994; Donahue et al. 2000; Knopp et al. 1999; Sugahara et al. 1998). Since within a tumor the measured values can vary several fold (Cao et al. 2006), comparisons between studies and tumor types are even more difficult.

However the range of values obtained for the vascular volume fraction (1.3 to 3.2%) is in accordance with values reported by Ferrier (Ferrier et al. 2007) for a RG2 tumor model. In their study, the vascular volume fraction ranged from 1 to 5%, with a mean of 2.8 ± 1.3%. The leakage volume fraction ranged from 10 to 20% for Gd-DTPA, while in our study it ranges from 3.4 to 8.6% except for those ROIs for which the model could not be fitted to the experimental data. The enhancement rate κ_{ev} for Gd-DOTA in our study (0.019 to 0.034 s^{-1}) is by a factor of two to ten higher than the rate constants reported by them (0.003 to 0.011 s^{-1}) for Gd-DTPA. Although κ_{ev} derived from our model does not directly correspond to the rate constant k_{ep}, it is theoretically possible to derive quantitative parameters describing the leakage profiles, which have physiological meanings such as the vessel permeability surface product (PS_v) by monitoring the plasma concentration of the CA C_p.

Delay of CA arrival

The discrepancy of results is also due to uncertainties in estimations of t = 0. The arrival of the CA in the vascular ROI was already difficult to detect due to variable bolus transit duration along with large T_2 and T_2* effects. Since a draining vessel was chosen for the definition of t = 0, the arrival of the CA in brain tissue even happens slightly before t = 0. In addition, in different tumor parts, the CA arrival could have variable delay times (Gowland et al. 1992). The model chosen does not take this time parameter into account. By simple observation of the tumor leakage profiles, it can be noted that, in all regions, the signal S_{post}^{norm} after Gd-DOTA injection is larger for all t > 0 and therefore the κ_{ev} parameter for Gd-DOTA should have been constantly larger than for P760. However, the leakage volume fraction for Gd-DOTA in tumor and muscle tissue is systematically greater than the leakage volume fraction for P760. Such a behavior has also been demonstrated with Gd-DOTA and the intermediate molecular weight CA P792 in a rat

breast tumor model (Weidensteiner et al. 2006). There is evidence for a significantly enlarged extravascular leakage compartment in tissue lesions (Tofts and Kermode 1991) and particularly in tumors (Jain 1987) with respect to normal tissue.

Flow limited CA delivery

In two tumor ROIs a constant signal or even a slight signal decrease could be observed for both CAs during the $RSST_1$ interval. Such a case is shown in Fig. VI-2 for the ROI covering the whole tumor. For the same rat (M5), the signal increases in the ROI in the tumor center and decreases slightly in the tumor border. A possible explanation might be a flow limited CA delivery in this tumor region, such as occurs in beginning necrosis (Ludemann et al. 2000; Pivawer et al. 2007). In such cases, the model is not appropriate and can not correctly describe the leakage profile. In Table VI-2 the low κ_{ev} (P760 injection) or S_{ev} parameters (Gd-DOTA injection) for rat M4 and M5 in the tumor border are therefore not representative. A constant S_{post}^{norm} signal was also observed in a ROI in the tumor center of rat M4 after P760 injection, while a typical leakage profile was observed after Gd-DOTA injection one hour later.

6.5.4. Possible improvements

The derived enhancement rate κ_{ev} is linked to the microvascular volume via the surface area S_v and is in addition an intractable combination of microvascular permeability P, leakage volume, and in the flow limited case, also of blood flow. In addition, a truly constant plasma concentration of the CA is needed to derive physiologic parameters related to the microvascular permeability.

The complexity of tumor tissues and microvasculature might require a more sophisticated tissue model. In order to obtain more reliable results, improvements are possible at both levels: signal acquisition and mathematical model.

Without modifying any sequence timing parameters, efforts that can be made during signal acquisition include a more standardized and faster injection at a precise time point after the start of the acquisition, preferably using a mechanical power injector. CAs with pharmacokinetic profiles that allow a longer $RSST_1$ interval would be of advantage for the goodness of fit.

A model that takes in account the delay of CA arrival in tissue (Gowland et al. 1992), the existence of two or more extravascular leakage compartments with different enhancement rates and volumes (Ludemann et al. 2000), different bidirectional exchange rates of CA between compartments (Brix et al. 1991), flow limited CA delivery (Kety 1951) or even the water exchange effects at the vascular boundary might improve the fit to the experimental data. In order to link the derived parameters such as the enhancement rate κ_{ev} to physiological parameters other assumptions about the tissue compartments can be introduced such as the tissue homogeneity model (Johnson and Wilson 1966; Sawada et al. 1989), which assumes an instantaneous mixing of the CA within the entire compartment. We limited our study to a small number of parameters and assumptions because the experimental data was not sufficient to support a more complex model, and fitting a larger number of parameters would have reduced the reliability of the results. Although it might be a useful parameter to characterize tumor vasculature and blood flow, we have not attempted to derive κ_{iv} describing the rapid signal enhancement rate in the vascular compartment, because the time resolution in this study (750 ms) is rather modest for the rapid heart rate in rats (250 - 450/min). Theoretically it is also possible to study the washout phase of the CA from the leakage space using a similar model, if the signal evolution is monitored over a much longer time. In this case however, the plasma concentration of the CA needs to be measured for the whole washout phase (Gowland et al. 1992).

6.5.5. Conclusion

The advantages of the $RSST_1$-method in combination with the proposed compartment model is that the vascular signal can be considered as being constant during the $RSST_1$ interval and can thus be taken into account in the model. The second advantage is that, in contrast to other DCE MRI methods, it is not necessary to know the exact intravascular CA concentration C_{iv} during that time interval and whether or not there is a linearity between the intravascular CA concentration $C_{iv}(t)$ and the intravascular relaxation rates. Further advantages are not only the maximization of the signal change due to blood and tissue nulling before CA administration, but also a $RSST_1$ signal amplitude representing the thermal equilibrium magnetization in the compartment occupied by the CA, from which the compartment volume can be derived.

The purpose of this study was to show that the acquisition of leakage profiles by the IR-FLASH sequence with a time resolution of 750 ms allows distinguishing different CA and tissue properties by their leakage speed and pattern.

It has been shown how the $RSST_1$ method allows the estimation of the vascular volume in the presence of diffusion limited CA leakage. This method might therefore be of use for the characterization of different tumors not only by the vascular volume fraction, but also by the leakage volume fraction. Quantification of these parameters are a means of staging tumors and assessing early response to antiangiogenic therapy in clinical trials (Choyke et al. 2003; Jordan et al. 2005; Knopp et al. 2001).

General discussion

In this work, the emphasis lies on the methodological development of a MRI method for CBVf quantification. The aim is to establish a method that allows direct and reliable quantitative assessment of the angiogenesis occurring in malignant brain tumors, without a-priori assumptions regarding the microvascular architecture, without the need for blood sampling, and without complex post processing steps.

The $RSST_1$ method requires the injection of a blood pool CA. It was validated on the healthy rat brain and its sensitivity was evaluated by increasing the CBVf in a hypercapnia experiment.

Since the fragile vasculature in malignant tumor tissues is permeable to the CAs habitually employed in clinical routine, experimental CAs were evaluated for their vascular confinement. Such CAs could be used in biological research to study the fundamental mechanisms of tumor growth and spread related to the microvasculature, and in preclinical studies for the evaluation of therapeutic approaches, in particular antiangiogenic and antivascular approaches. However, the microvasculature in severely diseased tissue can become permeable to these CAs, too. For this reason, but also to allow of human studies with approved CAs such as Gd-DOTA, a method that allows CBVf quantification in the presence of CA leakage was evaluated in the last chapter of this work. This method is based on pharmacokinetic modelling similar to the one employed in dynamic contrast enhanced MRI, but makes use of the principle and conditions of the $RSST_1$ method. As a result, monitoring of the arterial CA concentration along with its technical difficulties can be avoided.

The number of animals involved in the final evaluation of the CBVf under different experimental conditions is small (mean of four to five animals), limiting the power of statistical analysis. The global and regional CBVf in healthy rats measured with the $RSST_1$ technique with four different CAs (2 to 3%) is in the range of CBVf reported in the literature (1.2 to 5.6%, cf. Table 0-3), and of CBVf obtained during the same experiments on the same rats using a steady state ΔR_2* MRI technique (1.5 to 2.5%) as well as in healthy rat brain using histological analysis combined with stereological correction (1 to 6%). For C6 tumor tissue, the CBVf obtained with Gd-ACX (range 0.8 to 1.8%) was confirmed by histology (range 1 to 1.5%). Despite the small number of animals, the standard deviations reflecting the CBVf variations between the measurements and between the individual rats (typically less than 0.7%) are also in the same range as those reported for

different techniques reviewed in Table 0-3. This is complicated by the fact that the CBVf is dependent on the chosen ROI and whether macrovascular structures are included or not. In addition, the CBVf is a physiologic parameter known to have a large distribution especially in malignant tumors (Aronen et al. 1994; Donahue et al. 2000). However, the aim of this work was not to study the CBVf itself, but rather to establish a method that can be used for angiogenesis assessment in larger studies.

Therefore, particular effort has been made to evaluate the reliability and precision of the CBVf measure. In addition to the possibility of CA leakage during the measurement, an error is inevitably induced by the T_2 weighting and by water exchange between compartments. We tried to estimate the measurement errors caused by these effects and we showed how the sequence parameters can be optimized to reduce them. However, the water exchange effect can not be completely avoided and has to be quantified with a different technique. The transverse relaxation effects can be reduced by using RF sequences with a short echo time.

1. Possible improvements of the $RSST_1$ method

1.1. R_2 weighting

For CBVf measurements with the $RSST_1$ method, any non-diffusible blood pool CA can be used, but CA with long plasma half lives, high r_1 relaxivity and low r_2 relaxivity are preferred. Owing to the independence of the MR signal from the intravascular T_1 once $T_1 < T_{inv}/5$, the method is not based on a linear relation between CA concentration and the blood relaxation, especially as this relation is not established for "high" doses of certain CA. The use of P760 and SINEREM, which both have r_2 relaxivities superior to the r_2 of Gd-DOTA, showed that the R_2-attenuation can be estimated and corrected for. If the R_2 decay is dominant, signal acquisitions with ultra-short TE have to be used.

The $RSST_1$ method is insensitive to transverse relaxation effects induced by a susceptibility difference between the intra- and the extravascular compartment, because the extravascular compartment does not contribute to the signal.

1.2. Water exchange effect

We have shown that by using the water exchange model of Moran and Prato (Moran and Prato 2004), there is an explicit accounting for the equilibrium exchange of water molecules between the intra and extravascular compartments and that the effect of water exchange on CBVf quantification can be estimated. The water exchange effect can be reduced by using shorter T_{inv} and TR, if the blood T_1 can be reduced to less than $T_{inv}/5$ by CAs with appropriate r_1 relaxivities. Owing to the water exchange across a healthy blood brain barrier, the CBVf is overestimated by less than 10% with the couple of T_{inv}/TR = 750ms/325 ms mainly employed in this work.

1.3. Inflow - outflow effects

In our study we have used a homogeneous RF coil for emission whose spatial sensitivity extends to the upper thorax of the rat. The inversion pulse used is spatially non selective inverting blood protons far away from the imaged slice. The inversion time T_{inv} = 325 ms was in the order of the mean arterial transit time in rats (0.3 s) (Thomas et al. 2006) therefore noninverted blood spins do not flow into the imaged brain slice before acquisition. Moreover, after excitation the signal is acquired with a TE of 3.2 ms which is short with respect to the blood velocity in capillaries. The method is therefore insensitive to blood inflow or outflow. If selective inversion pulses or RF coils with a smaller spatial sensitivity profile are used, inflow effects could occur.

In such a case, only the pre-contrast acquisition is affected by the blood flow, since noninverted water spins could enter the imaging slice resulting in an unsuppressed blood signal. After CA injection the magnetization of inflowing blood water is fully relaxed whether it has experienced the inversion pulse or not. Subtraction of the pre-contrast acquisition from the post-contrast acquisition might then result in a CBVf underestimation.

1.4. SNR

The main drawback of the technique is the low SNR, since only the water protons in the blood compartment (about 3%) contribute to the signal. By lengthening the steady state, the signal can be accumulated. It has been shown that a sufficient SNR (about 40) can be achieved with a steady state of about one minute.

The SNR could also be increased by improving the sensitivity of the RF coils, by parallel imaging with an array of local RF coils or by using higher field strengths. However, this requires blood pool CAs with a high r_1 relaxivity at high magnetic field strengths.

2. Possible applications of the $RSST_1$ method

2.1. Serial studies

The $RSST_1$ method allows quantification of the CBVf, is noninvasive and can be used repetitively. CBVf quantification with the $RSST_1$ method can also be performed at other field strengths by using appropriate timing parameters for signal suppression and by taking account of the CA relaxivity, Therefore, the measured parameter can be compared in a longitudinal study, or between subjects and centers. This is of particular interest for studying the progression of a pathologic process involving CBVf alterations, or for evaluating therapeutic effects. However, in order to apply the $RSST_1$ method to the intravital measurement of tumor angiogenesis and of the efficacy of antiangiogenic drugs, appropriate CAs that do not leak out of the tumor vasculature are needed.

2.2. Sensitivity to CBVf alterations

The sensitivity of the $RSST_1$ method was evaluated in a hypercapnia experiment. Per mmHg of $PaCO_2$, an increase of 1% of the CBVf (relative to its value at normocapnia) was observed, in accordance with reported values. The sensitivity of the $RSST_1$ method is therefore sufficient to be exploitable for example in functional MRI studies, in which CBVf (and CBF) increases by a factor of up to 1.5 are observed in activated brain areas (Belliveau et al. 1991).

Moreover, the method can be used for angiogenesis quantification to characterize the tumor stage. In certain cerebral tumors three- to eightfold CBVf increases with respect to the contralateral side have been reported (Aronen et al. 1994; Knopp et al. 1999). The $RSST_1$ method is expected to be applicable to other brain pathologies accompanied by vascular changes that among other hemodynamic parameters affect the CBVf. Such a disease is brain

infarction, for which CBVf decreases to one third with respect to normal perfused brain tissue are observed in severe cases (Hatazawa et al. 1999).

2.3. CBVf monitoring in dynamic studies

If desired, the $RSST_1$ interval can be lengthened by maintaining a sufficient CA concentration in blood via a continuous infusion or by using CAs with a long blood half life. Following an unique CA injection, a long vascular steady state signal, can not only be used for further signal averaging for increasing the SNR, for multiple slice acquisitions or for acquiring higher resolution images. If the evolution of the CBVf in a tissue of interest (cf. Eq. I-5) is monitored with rapid serial acquisitions such as with the IR-FLASH sequence (TR = 750 ms), the $RSST_1$ method can be used for various studies in which the CBVf is modulated, such as by varying the $PaCO_2$ or the core temperature, or during pharmacological tests.

2.4. Utility in fMRI

Moreover, given the good sensitivity of the method, a long $RSST_1$ interval could be easily exploited in functional MRI, when using fast $RSST_1$ acquisitions for real time monitoring of the CBVf during the steady state (cf. Eq. I-5). For the duration of cerebral activation, a CBVf increase would be detected in the corresponding brain area during continuous imaging. This is an advantage when opposed to first pass methods that necessitate two CA injections for CBVf measurement, one at baseline and a second in the activated state (Belliveau et al. 1991; Villringer et al. 1988). In functional MRI, measurement of the absolute CBVf and the BOLD signal under the same conditions could help separate and quantify the contributions of the different mechanisms to the complex BOLD signal.

3. Advantages of the $RSST_1$ method

The technique has a number of advantages over conventional MRI methods for CBVf mapping.

3.1. Few assumptions

The $RSST_1$-method is based on the longitudinal relaxation of tissue water and provides a direct measure of the blood water. The signal from each voxel is proportional to the number of water protons in the blood compartment, within which the CA is distributed. In contrast to the T_2* based methods for CBVf mapping, which are based on the signal of extravascular water protons, it does not rely on complex assumptions regarding the architecture of the microvasculature. For this reason, loss of intravascular CA compartmentalization will act synergistically on the $RSST_1$ signal intensity, which remains proportional to the distribution volume of the CA, as long as the $RSST_1$ conditions are satisfied.

Compared to other steady state methods, the $RSST_1$ method has the advantage of being independent of a linear relation between CA dose and blood relaxation rate. Blood sampling or high resolution imaging is not necessary to measure the signal or the T_1 of blood as long as the CA is known to reduce the blood T_1 to less than $T_{inv}/5$.

3.2. No AIF measure

The $RSST_1$ method does not suffer from any of the difficulties often encountered with first pass techniques such as necessity of high temporal resolution for accurate monitoring of the AIF, recirculation of the tracer, dependence on the deconvolution method or dependence on the injection mode. It is independent of the way the injection is carried out as long as a steady state signal can be observed.

Conclusion

In this work, an original method for CBVf quantification has been established. It is based on the nulling of the signals from blood and extravascular water in white and gray matter, which are characterized by a range of relatively long T_1 relaxation times. The tissue suppression is achieved with a fast inversion recovery sequence ($TR << T_1$). After intravenous injection of a blood pool CA, which shortens the blood relaxation times, the resulting signal is of intravascular origin. By using an appropriate CA dose, decreasing the blood T_1 to less than $T_{inv}/5$, this signal originates from fully relaxed water protons and is therefore proportional to the CBVf. For normalization, an acquisition of the proton density weighted signal of the intra- and extravascular compartment is used.

The experimental CAs P760, SINEREM and Gd-ACX as well as Gd-DOTA used in clinical practice have been studied, and the optimal dose for CBVf measurement has been determined.

The method has been validated using P760 and Gd-DOTA in healthy rat brain by inducing a CBVf increase in a hypercapnia experiment. The method correctly monitored the CBVf increase and the decrease after recovery to normocapnia. The sensitivity to CBVf changes is sufficient to be used in functional MRI studies.

The $RSST_1$ method has been applied to the CBVf measurement in C6 and RG2 rat brain tumor models to study CAs that preserve blood pool properties in tumor tissues. Such blood pool CAs result in a steady intravascular signal and allow direct CBVf measurements. The experimental paramagnetic CA Gd-ACX remains confined to the vasculature in the C6 glioma model. Identical CBVf values have been obtained with Gd-ACX and Gd-DOTA in the brain tissue contralateral to the tumor, and histological vascular morphometric analysis has been used on the same rats as studied by MRI to validate the CBVf measurements in tumor tissue.

SINEREM has been approved for clinical applications. In order to use this CA, which has a high transverse relaxivity, for the CBVf measurement with the $RSST_1$ method, a 3D projection reconstruction acquisition mode allowing short echo time has been implemented. The use of this CA for CBVf measurement was also motivated by the fact that its intravascular confinement in C6 tumor models has been reported. CBVf measurements in healthy rats using SINEREM with

the $RSST_1$ method have been validated with the steady state ΔR_2^* method for CBVf measurement following the same SINEREM injection.

Using SINEREM CBVf values up to 20% were measured in an advanced stage RG2 tumor model, suggesting that SINEREM is not a blood pool agent in this tumor. However, the $RSST_1$ method with a low temporal resolution, such as in this study (25 minutes for the 3D projection reconstruction acquisition), can not be used to reliably distinguish between high CBVf and overestimation due to extravasation. A CBVf measure independent of CA leakage is needed to verify this result.

Using the $RSST_1$ method with a fast acquisition mode, the CA extravasation can be monitored. We have shown how, using a pharmacokinetic two compartment model, the CBVf together with the extravascular distribution volume of the CA can be estimated from the leakage profile. In muscle tissue, the values derived from the leakage profiles for Gd-DOTA and P760 were in accordance with literature. In the RG2 tumor, in addition to a spatially heterogeneous CBVf distribution, this analysis revealed a spatially non uniform permeability of the microvasculature for these two CAs. The CBVf in this tumor was below 5%, proving that the CBVf measurement carried out with SINEREM in the same tumor model was overestimated due to leakage during the acquisition. Since the CBVf and the permeability of the blood brain barrier is spatially heterogeneous in a RG2 tumor model, the derived values have to be confirmed on a larger number of animals.

CBVf quantification using the $RSST_1$ method can be performed in a few minutes and does require neither blood sampling, nor monitoring of the AIF. The MRI signal is directly related to the CBVf, and the method does not rely on a linear relationship between signal change and CA concentration. Neither does it rely on complex assumptions and a geometrical model of the microvasculature. The CA can be administrated either as a bolus or as a continuous infusion. The imaging sequence can be applied on clinical MRI scanners. However, high gradient performance allowing ultra short echo times are of benefit to avoid CBVf underestimation due to transverse relaxation effects, when CAs with high transverse relaxivity are employed.

The method can be used repetitively in long-term time course studies due to its noninvasive and quantitative nature. In combination with blood pool CAs that do not leak through the BBB, the

method can now be used to evaluate the response to vascular targeted therapies. Gd-ACX could be a potential CA for the preclinical evaluation of antivascular or antiangiogenic drugs.

References

Aas AT, Brun A, Blennow C, Stromblad S, Salford LG. (1995) The RG2 rat glioma model. J Neurooncol 23:175-183

Abdulrauf SI, Edvardsen K, Ho KL, Yang XY, Rock JP, Rosenblum ML. (1998) Vascular endothelial growth factor expression and vascular density as prognostic markers of survival in patients with low-grade astrocytoma. J Neurosurg 88:513-520

Adair TH, Wells ML, Hang J, Montani JP. (1994) A stereological method for estimating length density of the arterial vascular system. Am J Physiol 266:H1434-1438

Adam G, Neuerburg J, Spuntrup E, Muhler A, Scherer K, Gunther RW. (1994) Dynamic contrast-enhanced MR imaging of the upper abdomen: enhancement properties of gadobutrol, gadolinium-DTPA-polylysine, and gadolinium-DTPA-cascade-polymer. Magn Reson Med 32:622-628

Adam JF, Elleaume H, Le Duc G, Corde S, Charvet AM, Tropres I, Le Bas JF, Esteve F. (2003) Absolute cerebral blood volume and blood flow measurements based on synchrotron radiation quantitative computed tomography. J Cereb Blood Flow Metab 23:499-512

Adam JF, Nemoz C, Bravin A, Fiedler S, Bayat S, Monfraix S, Berruyer G, Charvet AM, Le Bas JF, Elleaume H, Esteve F. (2005) High-resolution blood-brain barrier permeability and blood volume imaging using quantitative synchrotron radiation computed tomography: study on an F98 rat brain glioma. J Cereb Blood Flow Metab 25:145-153

Aime S, Botta M, Terreno E. (2005) Gd(III)-based contrast agents for MRI. Adv Inorg Chem 57:173-237

Aksoy FG, Lev MH. (2000) Dynamic contrast-enhanced brain perfusion imaging: technique and clinical applications. Semin Ultrasound CT MR 21:462-477

American-Cancer-Society. (2007) Cancer Facts and Figures 2007, Atlanta: American Cancer Society

Andrasko J. (1976) Water diffusion permeability of human erythrocytes studied by a pulsed gradient NMR technique. Biochim Biophys Acta 428:304-311

Archer DP, Labrecque P, Tyler JL, Meyer E, Trop D. (1987) Cerebral blood volume is increased in dogs during administration of nitrous oxide or isoflurane. Anesthesiology 67:642-648

Aronen HJ, Gazit IE, Louis DN, Buchbinder BR, Pardo FS, Weisskoff RM, Harsh GR, Cosgrove GR, Halpern EF, Hochberg FH, et al. (1994) Cerebral blood volume maps of gliomas: comparison with tumor grade and histologic findings. Radiology 191:41-51

Artru AA. (1984) Relationship between cerebral blood volume and CSF pressure during anesthesia with isoflurane or fentanyl in dogs. Anesthesiology 60:575-579

Assimakopoulou M, Sotiropoulou-Bonikou G, Maraziotis T, Papadakis N, Varakis I. (1997) Microvessel density in brain tumors. Anticancer Res 17:4747-4753

Axel L. (1980) Cerebral blood flow determination by rapid-sequence computed tomography: theoretical analysis. Radiology 137:679-686

Bar T. (1980) The vascular system of the cerebral cortex. Adv Anat Embryol Cell Biol 59:I-VI,1-62

Barbier EL, Silva AC, Kim SG, Koretsky AP. (2001) Perfusion imaging using dynamic arterial spin labeling (DASL). Magn Reson Med 45:1021-1029

Barbier EL, St Lawrence KS, Grillon E, Koretsky AP, Decorps M. (2002) A model of blood-brain barrier permeability to water: accounting for blood inflow and longitudinal relaxation effects. Magn Reson Med 47:1100-1109

Barth RF. (1998) Rat brain tumor models in experimental neuro-oncology: the 9L, C6, T9, F98, RG2 (D74), RT-2 and CNS-1 gliomas. J Neurooncol 36:91-102

Beaney RP, Brooks DJ, Leenders KL, Thomas DG, Jones T, Halnan KE. (1985) Blood flow and oxygen utilisation in the contralateral cerebral cortex of patients with untreated intracranial tumours as studied by positron emission tomography, with observations on the effect of decompressive surgery. J Neurol Neurosurg Psychiatry 48:310-319

Belliveau JW, Kennedy DN, Jr., McKinstry RC, Buchbinder BR, Weisskoff RM, Cohen MS, Vevea JM, Brady TJ, Rosen BR. (1991) Functional mapping of the human visual cortex by magnetic resonance imaging. Science 254:716-719

Belliveau JW, Rosen BR, Kantor HL, Rzedzian RR, Kennedy DN, McKinstry RC, Vevea JM, Cohen MS, Pykett IL, Brady TJ. (1990) Functional cerebral imaging by susceptibility-contrast NMR. Magn Reson Med 14:538-546

Benda P, Lightbody J, Sato G, Levine L, Sweet W. (1968) Differentiated rat glial cell strain in tissue culture. Science 161:370-371

Benda P, Someda K, Messer J, Sweet WH. (1971) Morphological and immunochemical studies of rat glial tumors and clonal strains propagated in culture. J Neurosurg 34:310-323

Bereczki D, Wei L, Acuff V, Gruber K, Tajima A, Patlak C, Fenstermacher J. (1992) Technique-dependent variations in cerebral microvessel blood volumes and hematocrits in the rat. J Appl Physiol 73:918-924

Bereczki D, Wei L, Otsuka T, Acuff V, Pettigrew K, Patlak C, Fenstermacher J. (1993a) Hypoxia increases velocity of blood flow through parenchymal microvascular systems in rat brain. J Cereb Blood Flow Metab 13:475-486

Bereczki D, Wei L, Otsuka T, Hans FJ, Acuff V, Patlak C, Fenstermacher J. (1993b) Hypercapnia slightly raises blood volume and sizably elevates flow velocity in brain microvessels. Am J Physiol 264:H1360-1369

Bernsen HJ, Rijken PF, Oostendorp T, van der Kogel AJ. (1995) Vascularity and perfusion of human gliomas xenografted in the athymic nude mouse. Br J Cancer 71:721-726

Betz AL, Goldstein GW. (1978) Polarity of the blood-brain barrier: neutral amino acid transport into isolated brain capillaries. Science 202:225-227

Bonnet C, Gadelle A, Pecaut J, Fries PH, Delangle P. (2005) Inclusion complexes of trivalent lutetium cations with an acidic derivative of per(3,6-anhydro)-alpha-cyclodextrin. Chem Commun (Camb):625-627

Boxerman JL, Hamberg LM, Rosen BR, Weisskoff RM. (1995) MR contrast due to intravascular magnetic susceptibility perturbations. Magn Reson Med 34:555-566

Brady TJ, Gebhardt MC, Pykett IL, Buonanno FS, Newhouse JH, Burt CT, Smith RJ, Mankin HJ, Kistler JP, Goldman MR, Hinshaw WS, Pohost GM. (1982) NMR imaging of forearms in healthy volunteers and patients with giant-cell tumor of bone. Radiology 144:549-552

Brasch RC, Weinmann HJ, Wesbey GE. (1984) Contrast-enhanced NMR imaging: animal studies using gadolinium-DTPA complex. AJR Am J Roentgenol 142:625-630

Brem H, Folkman J. (1975) Inhibition of tumor angiogenesis mediated by cartilage. J Exp Med 141:427-439

Brem S, Cotran R, Folkman J. (1972) Tumor angiogenesis: a quantitative method for histologic grading. J Natl Cancer Inst 48:347-356

Brix G, Semmler W, Port R, Schad LR, Layer G, Lorenz WJ. (1991) Pharmacokinetic parameters in CNS Gd-DTPA enhanced MR imaging. J Comput Assist Tomogr 15:621-628

Brookes MJ, Morris PG, Gowland PA, Francis ST. (2007) Noninvasive measurement of arterial cerebral blood volume using Look-Locker EPI and arterial spin labeling. Magn Reson Med 58:41-54

Broom KA, Anthony DC, Blamire AM, Waters S, Styles P, Perry VH, Sibson NR. (2005) MRI reveals that early changes in cerebral blood volume precede blood-brain barrier breakdown and overt pathology in MS-like lesions in rat brain. J Cereb Blood Flow Metab 25:204-216

Brownson EA, Abbruscato TJ, Gillespie TJ, Hruby VJ, Davis TP. (1994) Effect of peptidases at the blood brain barrier on the permeability of enkephalin. J Pharmacol Exp Ther 270:675-680

Bullitt E, Zeng D, Gerig G, Aylward S, Joshi S, Smith JK, Lin W, Ewend MG. (2005) Vessel tortuosity and brain tumor malignancy: a blinded study. Acad Radiol 12:1232-1240

Calamante F, Gadian DG, Connelly A. (2000) Delay and dispersion effects in dynamic susceptibility contrast MRI: simulations using singular value decomposition. Magn Reson Med 44:466-473

Calamante F, Gadian DG, Connelly A. (2002) Quantification of perfusion using bolus tracking magnetic resonance imaging in stroke: assumptions, limitations, and potential implications for clinical use. Stroke 33:1146-1151

Calamante F, Thomas DL, Pell GS, Wiersma J, Turner R. (1999) Measuring cerebral blood flow using magnetic resonance imaging techniques. J Cereb Blood Flow Metab 19:701-735

Cameron J. (1999) Physics of the Body. Madison, WI: Medical Physics Publishing

Cao Y, Sundgren PC, Tsien CI, Chenevert TT, Junck L. (2006) Physiologic and metabolic magnetic resonance imaging in gliomas. J Clin Oncol 24:1228-1235

Caravan P, Cloutier NJ, Greenfield MT, McDermid SA, Dunham SU, Bulte JW, Amedio JC, Jr., Looby RJ, Supkowski RM, Horrocks WD, Jr., McMurry TJ, Lauffer RB. (2002) The interaction of MS-325 with human serum albumin and its effect on proton relaxation rates. J Am Chem Soc 124:3152-3162

Caravan P, Ellison JJ, McMurry TJ, Lauffer RB. (1999) Gadolinium(III) Chelates as MRI Contrast Agents: Structure, Dynamics, and Applications. Chem Rev 99:2293-2352

Carmeliet P, Jain RK. (2000) Angiogenesis in cancer and other diseases. Nature 407:249-257

Carr DH, Brown J, Bydder GM, Weinmann HJ, Speck U, Thomas DJ, Young IR. (1984) Intravenous chelated gadolinium as a contrast agent in NMR imaging of cerebral tumours. Lancet 1:484-486

Cenic A, Craen RA, Howard-Lech VL, Lee TY, Gelb AW. (2000) Cerebral blood volume and blood flow at varying arterial carbon dioxide tension levels in rabbits during propofol anesthesia. Anesth Analg 90:1376-1383

Cenic A, Craen RA, Lee TY, Gelb AW. (2002) Cerebral blood volume and blood flow responses to hyperventilation in brain tumors during isoflurane or propofol anesthesia. Anesth Analg 94:661-666

Cha S, Knopp EA, Johnson G, Litt A, Glass J, Gruber ML, Lu S, Zagzag D. (2000a) Dynamic contrast-enhanced T2-weighted MR imaging of recurrent malignant gliomas treated with thalidomide and carboplatin. AJNR Am J Neuroradiol 21:881-890

Cha S, Lu S, Johnson G, Knopp EA. (2000b) Dynamic susceptibility contrast MR imaging: correlation of signal intensity changes with cerebral blood volume measurements. J Magn Reson Imaging 11:114-119

Chambon C, Clement O, Le Blanche A, Schouman-Claeys E, Frija G. (1993) Superparamagnetic iron oxides as positive MR contrast agents: in vitro and in vivo evidence. Magn Reson Imaging 11:509-519

Chang BL, Yamakawa T, Nuccio J, Pace R, Bing RJ. (1982) Microcirculation of left atrial muscle, cerebral cortex and mesentery of the cat. A comparative analysis. Circ Res 50:240-249

Chieze L. (2005) Quantification du volume sanguin cérébral par RMN en présence de rupture de la barrière hémato-encéphalique. In: Functional and Metabolic Neuroimaging Department U594, Grenoble: Joseph Fourier University

Choyke PL, Dwyer AJ, Knopp MV. (2003) Functional tumor imaging with dynamic contrast-enhanced magnetic resonance imaging. J Magn Reson Imaging 17:509-520

Cockerill GW, Gamble JR, Vadas MA. (1995) Angiogenesis: models and modulators. Int Rev Cytol 159:113-160

Cooley J, Tukey J. (1965) An algorithm for the machine computation of complex Fourier series. Math. Comput. 19:297-301

Coomber BL, Stewart PA. (1985) Morphometric analysis of CNS microvascular endothelium. Microvasc Res 30:99-115

Copeland DD, Vogel FS, Bigner DD. (1975) The induction of intractranial neoplasms by the inoculation of avian sarcoma virus in perinatal and adult rats. J Neuropathol Exp Neurol 34:340-358

Corot C, Port M, Raynal I, Dencausse A, Schaefer M, Rousseaux O, Simonot C, Devoldere L, Lin J, Foulon M, Bourrinet P, Bonnemain B, Meyer D. (2000a) Physical, chemical, and biological evaluations of P760: a new gadolinium complex characterized by a low rate of interstitial diffusion. J Magn Reson Imaging 11:182-191

Corot C, Violas X, Robert P, Port M. (2000b) Pharmacokinetics of three gadolinium chelates with different molecular sizes shortly after intravenous injection in rabbits: relevance to MR angiography. Invest Radiol 35:213-218

Corot CA, Violas X, Robert P, Port M. (2002) Arterial concentration profiles of two blood pool agents and Gd-DOTA after intravenous injection in rabbits. Acad Radiol 9 Suppl 1:S137-139

Cremer JE, Seville MP. (1983) Regional brain blood flow, blood volume, and haematocrit values in the adult rat. J Cereb Blood Flow Metab 3:254-256

Crone C. (1963) The Permeability of Capillaries in Various Organs as Determined by Use of the 'Indicator Diffusion' Method. Acta Physiol Scand 58:292-305

Cuenod CA, Fournier L, Balvay D, Guinebretiere JM. (2006) Tumor angiogenesis: pathophysiology and implications for contrast-enhanced MRI and CT assessment. Abdom Imaging 31:188-193

Daldrup HE, Shames DM, Husseini W, Wendland MF, Okuhata Y, Brasch RC. (1998) Quantification of the extraction fraction for gadopentetate across breast cancer capillaries. Magn Reson Med 40:537-543

Damadian R. (1971) Tumor detection by nuclear magnetic resonance. Science 171:1151-1153

de Haen C, Morisetti A, Bertani F, Tirone P. (1994) The factor time in acute intravenous toxicity studies of contrast media. Invest Radiol 29 Suppl 2:S108-110

Dean BL, Lee C, Kirsch JE, Runge VM, Dempsey RM, Pettigrew LC. (1992) Cerebral hemodynamics and cerebral blood volume: MR assessment using gadolinium contrast agents and T1-weighted Turbo-FLASH imaging. AJNR Am J Neuroradiol 13:39-48

Deane BR, Lantos PL. (1981) The vasculature of experimental brain tumours. Part 2. A quantitative assessment of morphological abnormalities. J Neurol Sci 49:67-77

Debouzy J, Tymen H, Le Gall B, Fauvelle F, Martel B, Gadelle A. (2002) First evaluation of per(3,6-anhydro, 2-O-carboxymethyl)-alpha-cyclodextrin for biological decontamination of cobalt. STP Pharma Sciences 12:397-402

Debouzy JC, Fauvelle F, Gadelle A, Baudin C, Richard M, Perly B, Chouteau F, Joets J, Tazz JJ, Daveloose D. (1998) Interaction of per 3,6-anhydro-alpha cyclodextrins (alpha 36CD) and lead-alpha 36CD complex with biological systems. Boll Chim Farm 137:144-151

Delesse A. (1848) Procede mecanique pour determiner la composition des roches. Ann. Mines 13:379-388

Dennie J, Mandeville JB, Boxerman JL, Packard SD, Rosen BR, Weisskoff RM. (1998) NMR imaging of changes in vascular morphology due to tumor angiogenesis. Magn Reson Med 40:793-799

Dewhirst MW, Tso CY, Oliver R, Gustafson CS, Secomb TW, Gross JF. (1989) Morphologic and hemodynamic comparison of tumor and healing normal tissue microvasculature. Int J Radiat Oncol Biol Phys 17:91-99

Djedaïni F, Perly B. (1991) New Trends in Cyclodextrins and Derivatives. In: Edition de la Santé (Duchêne D, ed), Paris, France, pp 217–246

Dockery P, Fraher J. (2007) The quantification of vascular beds: a stereological approach. Exp Mol Pathol 82:110-120

Donahue KM, Burstein D, Manning WJ, Gray ML. (1994) Studies of Gd-DTPA relaxivity and proton exchange rates in tissue. Magn Reson Med 32:66-76

Donahue KM, Krouwer HG, Rand SD, Pathak AP, Marszalkowski CS, Censky SC, Prost RW. (2000) Utility of simultaneously acquired gradient-echo and spin-echo cerebral blood volume and morphology maps in brain tumor patients. Magn Reson Med 43:845-853

Donahue KM, Weisskoff RM, Burstein D. (1997) Water diffusion and exchange as they influence contrast enhancement. J Magn Reson Imaging 7:102-110

Donahue KM, Weisskoff RM, Chesler DA, Kwong KK, Bogdanov AA, Jr., Mandeville JB, Rosen BR. (1996) Improving MR quantification of regional blood volume with intravascular T1 contrast agents: accuracy, precision, and water exchange. Magn Reson Med 36:858-867

Dunn JF, Roche MA, Springett R, Abajian M, Merlis J, Daghlian CP, Lu SY, Makki M. (2004) Monitoring angiogenesis in brain using steady-state quantification of DeltaR2 with MION infusion. Magn Reson Med 51:55-61

Duvernoy H, Delon S, Vannson JL. (1983) The vascularization of the human cerebellar cortex. Brain Res Bull 11:419-480

Edelman RR, Warach S. (1993a) Magnetic resonance imaging (1). N Engl J Med 328:708-716

Edelman RR, Warach S. (1993b) Magnetic resonance imaging (2). N Engl J Med 328:785-791

Eichling JO, Raichle ME, Grubb RL, Jr., Ter-Pogossian MM. (1974) Evidence of the limitations of water as a freely diffusible tracer in brain of the rhesus monkey. Circ Res 35:358-364

El-Sayed IH, Huang X, El-Sayed MA. (2006) Selective laser photo-thermal therapy of epithelial carcinoma using anti-EGFR antibody conjugated gold nanoparticles. Cancer Lett 239:129-135

Enochs WS, Harsh G, Hochberg F, Weissleder R. (1999) Improved delineation of human brain tumors on MR images using a long-circulating, superparamagnetic iron oxide agent. J Magn Reson Imaging 9:228-232

Ernst TM, Chang L, Witt MD, Aronow HA, Cornford ME, Walot I, Goldberg MA. (1998) Cerebral toxoplasmosis and lymphoma in AIDS: perfusion MR imaging experience in 13 patients. Radiology 208:663-669

Ewend MG, Brem S, Gilbert M, Goodkin R, Penar PL, Varia M, Cush S, Carey LA. (2007) Treatment of single brain metastasis with resection, intracavity carmustine polymer wafers, and radiation therapy is safe and provides excellent local control. Clin Cancer Res 13:3637-3641

Ewing JR, Knight RA, Nagaraja TN, Yee JS, Nagesh V, Whitton PA, Li L, Fenstermacher JD. (2003) Patlak plots of Gd-DTPA MRI data yield blood-brain transfer constants concordant with those of 14C-sucrose in areas of blood-brain opening. Magn Reson Med 50:283-292

Farrell CL, Farrell CR, Stewart PA, Del Maestro RF, Ellis CG. (1991) The functional microcirculation in a glioma model. Int J Radiat Biol 60:131-137

Farrell CL, Pardridge WM. (1991) Blood-brain barrier glucose transporter is asymmetrically distributed on brain capillary endothelial lumenal and ablumenal membranes: an electron microscopic immunogold study. Proc Natl Acad Sci U S A 88:5779-5783

Fauvelle F. (1999) Decontamination biologique des cations toxiques: la voie des cyclodextrines, Grenoble: University Joseph Fourier, p 274

Fauvelle F, Gadelle A, Pailler Y, Aous S, Debouzy JC. (2002) Acidic Derivative of Per(3,6-anhydro)-alpha-cyclodextrin: Preparation and a First Evaluation of Its Affinity for Lanthanides by ^{1}H NMR. Journal of Inclusion Phenomena and Macrocyclic Chemistry 42:203-207(205)

Favre JB, Ravussin P, Chiolero R, Bissonnette B. (1996) [Hypertonic solutions and intracranial pressure]. Schweiz Med Wochenschr 126:1635-1643

Ferrier MC, Sarin H, Fung SH, Schatlo B, Pluta RM, Gupta SN, Choyke PL, Oldfield EH, Thomasson D, Butman JA. (2007) Validation of dynamic contrast-enhanced magnetic resonance imaging-derived vascular permeability measurements using quantitative autoradiography in the RG2 rat brain tumor model. Neoplasia 9:546-555

Flickinger FW, Allison JD, Sherry RM, Wright JC. (1993) Differentiation of benign from malignant breast masses by time-intensity evaluation of contrast enhanced MRI. Magn Reson Imaging 11:617-620

Folberg R, Hendrix MJ, Maniotis AJ. (2000) Vasculogenic mimicry and tumor angiogenesis. Am J Pathol 156:361-381

Folkman J. (1971) Tumor angiogenesis: therapeutic implications. N Engl J Med 285:1182-1186

Folkman J. (1992) The role of angiogenesis in tumor growth. Semin Cancer Biol 3:65-71

Folkman J. (1996) New perspectives in clinical oncology from angiogenesis research. Eur J Cancer 32A:2534-2539

Folkman J, Ingber D. (1992) Inhibition of angiogenesis. Semin Cancer Biol 3:89-96

Fonchy E, Lahrech H, Francois-Joubert A, Dupeyre R, Benderbous S, Corot C, Farion R, Rubin C, Decorps M, Remy C. (2001) A new gadolinium-based contrast agent for magnetic resonance imaging of brain tumors: kinetic study on a C6 rat glioma model. J Magn Reson Imaging 14:97-105

Frahm J, Haase A, Matthaei D. (1986) Rapid NMR imaging of dynamic processes using the FLASH technique. Magn Reson Med 3:321-327

Frahm J, Merboldt KD, Bruhn H, Gyngell ML, Hanicke W, Chien D. (1990) 0.3-second FLASH MRI of the human heart. Magn Reson Med 13:150-157

Gadelle A, Defaye J. (1991) Selective halogenation of primary positions of cyclomaltosaccharides and synthesis of per-(3,6-anhydro) cyclomalto-oligosacccharides. Angew. Chem. Int. Ed. Engl 30:78-80

Galle P. (1997) Toxiques nucléaires. Paris, France: Masson

Garnett MR, Blamire AM, Corkill RG, Rajagopalan B, Young JD, Cadoux-Hudson TA, Styles P. (2001) Abnormal cerebral blood volume in regions of contused and normal appearing brain following traumatic brain injury using perfusion magnetic resonance imaging. J Neurotrauma 18:585-593

Gillis P, Peto S, Moiny F, Mispelter J, Cuenod CA. (1995) Proton transverse nuclear magnetic relaxation in oxidized blood: a numerical approach. Magn Reson Med 33:93-100

Ginsberg MD, Busto R, Harik SI. (1985) Regional blood-brain barrier permeability to water and cerebral blood flow during status epilepticus: insensitivity to norepinephrine depletion. Brain Res 337:59-71

Glover GH, Pauly JM. (1992) Projection reconstruction techniques for reduction of motion effects in MRI. Magn Reson Med 28:275-289

Goldman MR, Brady TJ, Pykett IL, Burt CT, Buonanno FS, Kistler JP, Newhouse JH, Hinshaw WS, Pohost GM. (1982) Quantification of experimental myocardial infarction using nuclear magnetic resonance imaging and paramagnetic ion contrast enhancement in excised canine hearts. Circulation 66:1012-1016

Gowland P, Mansfield P, Bullock P, Stehling M, Worthington B, Firth J. (1992) Dynamic studies of gadolinium uptake in brain tumors using inversion-recovery echo-planar imaging. Magn Reson Med 26:241-258

Grist TM, Korosec FR, Peters DC, Witte S, Walovitch RC, Dolan RP, Bridson WE, Yucel EK, Mistretta CA. (1998) Steady-state and dynamic MR angiography with MS-325: initial experience in humans. Radiology 207:539-544

Guccione S, Li KC, Bednarski MD. (2004) Molecular imaging and therapy directed at the neovasculature in pathologies. How imaging can be incorporated into vascular-targeted delivery systems to generate active therapeutic agents. IEEE Eng Med Biol Mag 23:50-56

Gur D, Yonas H, Good WF. (1989) Local cerebral blood flow by xenon-enhanced CT: current status, potential improvements, and future directions. Cerebrovasc Brain Metab Rev 1:68-86

Guyton A, Hall J. (1997) Human Physiology and Mechanisms of Disease. Philadelphia PA: W.B. Saunders Company

Haase A. (1990) Snapshot FLASH MRI. Applications to T1, T2, and chemical-shift imaging. Magn Reson Med 13:77-89

Hacklander T, Hofer M, Reichenbach JR, Rascher K, Furst G, Modder U. (1996) Cerebral blood volume maps with dynamic contrast-enhanced T1-weighted FLASH imaging: normal values and preliminary clinical results. J Comput Assist Tomogr 20:532-539

Hakumaki JM, Brindle KM. (2003) Techniques: Visualizing apoptosis using nuclear magnetic resonance. Trends Pharmacol Sci 24:146-149

Hamberg LM, Boccalini P, Stranjalis G, Hunter GJ, Huang Z, Halpern E, Weisskoff RM, Moskowitz MA, Rosen BR. (1996) Continuous assessment of relative cerebral blood volume in transient ischemia using steady state susceptibility-contrast MRI. Magn Reson Med 35:168-173

Harkness JE, Wagner JE. (1989) The Biology and Medicine of Rabbits and Rodents. Philadelphia, PA: Lea & Febiger

Harris GJ, Lewis RF, Satlin A, English CD, Scott TM, Yurgelun-Todd DA, Renshaw PF. (1996) Dynamic susceptibility contrast MRI of regional cerebral blood volume in Alzheimer's disease. Am J Psychiatry 153:721-724

Harris GJ, Lewis RF, Satlin A, English CD, Scott TM, Yurgelun-Todd DA, Renshaw PF. (1998) Dynamic susceptibility contrast MR imaging of regional cerebral blood volume in Alzheimer disease: a promising alternative to nuclear medicine. AJNR Am J Neuroradiol 19:1727-1732

Hatazawa J, Shimosegawa E, Toyoshima H, Ardekani BA, Suzuki A, Okudera T, Miura Y. (1999) Cerebral blood volume in acute brain infarction: A combined study with dynamic susceptibility contrast MRI and 99mTc-HMPAO-SPECT. Stroke 30:800-806

Hawighorst H, Weikel W, Knapstein PG, Knopp MV, Zuna I, Schonberg SO, Vaupel P, van Kaick G. (1998) Angiogenic activity of cervical carcinoma: assessment by functional magnetic resonance imaging-based parameters and a histomorphological approach in correlation with disease outcome. Clin Cancer Res 4:2305-2312

Hennig A. (1969) [ERRORS IN VOLUME DETERMINATION FROM AREA RELATION of thick secTIONS (Holmes effect)]. Mikroskopie 25:154-174

Herbst MD, Goldstein JH. (1989) A review of water diffusion measurement by NMR in human red blood cells. Am J Physiol 256:C1097-1104

Herscovitch P, Markham J, Raichle ME. (1983) Brain blood flow measured with intravenous H2(15)O. I. Theory and error analysis. J Nucl Med 24:782-789

Herscovitch P, Raichle ME. (1985) What is the correct value for the brain--blood partition coefficient for water? J Cereb Blood Flow Metab 5:65-69

Herscovitch P, Raichle ME, Kilbourn MR, Welch MJ. (1987) Positron emission tomographic measurement of cerebral blood flow and permeability-surface area product of water using [15O]water and [11C]butanol. J Cereb Blood Flow Metab 7:527-542

Hormigo A, Gutin PH, Rafii S. (2007) Tracking normalization of brain tumor vasculature by magnetic imaging and proangiogenic biomarkers. Cancer Cell 11:6-8

Huber JD, Egleton RD, Davis TP. (2001) Molecular physiology and pathophysiology of tight junctions in the blood-brain barrier. Trends Neurosci 24:719-725

Hutter A, Schwetye KE, Bierhals AJ, McKinstry RC. (2003) Brain neoplasms: epidemiology, diagnosis, and prospects for cost-effective imaging. Neuroimaging Clin N Am 13:237-250, x-xi

Iannotti F, Fieschi C, Alfano B, Picozzi P, Mansi L, Pozzilli C, Punzo A, Del Vecchio G, Lenzi GL, Salvatore M, et al. (1987) Simplified, noninvasive PET measurement of blood-brain barrier permeability. J Comput Assist Tomogr 11:390-397

Ito M, Lammertsma AA, Wise RJ, Bernardi S, Frackowiak RS, Heather JD, McKenzie CG, Thomas DG, Jones T. (1982) Measurement of regional cerebral blood flow and oxygen utilisation in patients with cerebral tumours using 15O and positron emission tomography: analytical techniques and preliminary results. Neuroradiology 23:63-74

Jain RK. (1987) Transport of molecules in the tumor interstitium: a review. Cancer Res 47:3039-3051

Jivan A, Horsfield MA, Moody AR, Cherryman GR. (1997) Dynamic T1 measurement using snapshot-FLASH MRI. J Magn Reson 127:65-72

Johanson K. (1994) Metal in urban and rural areas- cycling and critical loads. In: SNV (Tryck L, ed, Stockholm: Swedish Environmental Agency SNV, pp 1-32

Johnson DW, Stringer WA, Marks MP, Yonas H, Good WF, Gur D. (1991) Stable xenon CT cerebral blood flow imaging: rationale for and role in clinical decision making. AJNR Am J Neuroradiol 12:201-213

Johnson JA, Wilson TA. (1966) A model for capillary exchange. Am J Physiol 210:1299-1303

Jordan BF, Runquist M, Raghunand N, Baker A, Williams R, Kirkpatrick L, Powis G, Gillies RJ. (2005) Dynamic contrast-enhanced and diffusion MRI show rapid and dramatic changes in tumor microenvironment in response to inhibition of HIF-1alpha using PX-478. Neoplasia 7:475-485

Julien-Dolbec C, Tropres I, Montigon O, Reutenauer H, Ziegler A, Decorps M, Payen JF. (2002) Regional response of cerebral blood volume to graded hypoxic hypoxia in rat brain. Br J Anaesth 89:287-293

Julien C, Payen JF, Tropres I, Farion R, Grillon E, Montigon O, Remy C. (2004) Assessment of vascular reactivity in rat brain glioma by measuring regional blood volume during graded hypoxic hypoxia. Br J Cancer 91:374-380

Kahle W. (1991) Taschenatlas der Anatomie: für Studium und Praxis. Stuttgart: Georg Thieme Verlag

Kamena A, Streitparth F, Grieser C, Lehmkuhl L, Jamil B, Wojtal K, Ricke J, Pech M. (2007) Dynamic perfusion CT: Optimizing the temporal resolution for the calculation of perfusion CT parameters in stroke patients. Eur J Radiol

Kenney J, Schmiedl U, Maravilla K, Starr F, Graham M, Spence A, Nelson J. (1992) Measurement of blood-brain barrier permeability in a tumor model using magnetic resonance imaging with gadolinium-DTPA. Magn Reson Med 27:68-75

Kety SS. (1951) The theory and applications of the exchange of inert gas at the lungs and tissues. Pharmacol Rev 3:1-41

Keyeux A, Ochrymowicz-Bemelmans D, Charlier AA. (1995) Induced response to hypercapnia in the two-compartment total cerebral blood volume: influence on brain vascular reserve and flow efficiency. J Cereb Blood Flow Metab 15:1121-1131

Kim DH, Adalsteinsson E, Spielman DM. (2003) Simple analytic variable density spiral design. Magn Reson Med 50:214-219

Kim T, Kim SG. (2005) Quantification of cerebral arterial blood volume and cerebral blood flow using MRI with modulation of tissue and vessel (MOTIVE) signals. Magn Reson Med 54:333-342

Kim T, Kim SG. (2006) Quantification of cerebral arterial blood volume using arterial spin labeling with intravoxel incoherent motion-sensitive gradients. Magn Reson Med 55:1047-1057

Kim YR, Rebro KJ, Schmainda KM. (2002) Water exchange and inflow affect the accuracy of T1-GRE blood volume measurements: implications for the evaluation of tumor angiogenesis. Magn Reson Med 47:1110-1120

Kirsch M, Santarius T, Black PM, Schackert G. (2001) Therapeutic anti-angiogenesis for malignant brain tumors. Onkologie 24:423-430

Kiselev VG. (2001) On the theoretical basis of perfusion measurements by dynamic susceptibility contrast MRI. Magn Reson Med 46:1113-1122

Kleihues P, Burger PC, Scheithauer BW. (1993) The new WHO classification of brain tumours. Brain Pathol 3:255-268

Knopp EA, Cha S, Johnson G, Mazumdar A, Golfinos JG, Zagzag D, Miller DC, Kelly PJ, Kricheff, II. (1999) Glial neoplasms: dynamic contrast-enhanced T2*-weighted MR imaging. Radiology 211:791-798

Knopp MV, Giesel FL, Marcos H, von Tengg-Kobligk H, Choyke P. (2001) Dynamic contrast-enhanced magnetic resonance imaging in oncology. Top Magn Reson Imaging 12:301-308

Ko L, Koestner A, Wechsler W. (1980) Morphological characterization of nitrosourea-induced glioma cell lines and clones. Acta Neuropathol (Berl) 51:23-31

Kobayashi H, Brechbiel MW. (2003) Dendrimer-based macromolecular MRI contrast agents: characteristics and application. Mol Imaging 2:1-10

Kobayashi N, Allen N, Clendenon NR, Ko LW. (1980) An improved rat brain-tumor model. J Neurosurg 53:808-815

Koenig SH, Spiller M, Brown RD, 3rd, Wolf GL. (1986) Relaxation of water protons in the intra- and extracellular regions of blood containing Gd(DTPA). Magn Reson Med 3:791-795

Kooi ME, Cappendijk VC, Cleutjens KB, Kessels AG, Kitslaar PJ, Borgers M, Frederik PM, Daemen MJ, van Engelshoven JM. (2003) Accumulation of ultrasmall superparamagnetic particles of iron oxide in human atherosclerotic plaques can be detected by in vivo magnetic resonance imaging. Circulation 107:2453-2458

Krueck WG, Schmiedl UP, Maravilla KR, Spence AM, Starr FL, Kenney J. (1994) MR assessment of radiation-induced blood-brain barrier permeability changes in rat glioma model. AJNR Am J Neuroradiol 15:625-632

Kukowska-Latallo JF, Candido KA, Cao Z, Nigavekar SS, Majoros IJ, Thomas TP, Balogh LP, Khan MK, Baker JR, Jr. (2005) Nanoparticle targeting of anticancer drug improves therapeutic response in animal model of human epithelial cancer. Cancer Res 65:5317-5324

Kuppusamy K, Lin W, Cizek GR, Haacke EM. (1996) In vivo regional cerebral blood volume: quantitative assessment with 3D T1-weighted pre- and postcontrast MR imaging. Radiology 201:106-112

Kuwatsuru R, Shames DM, Muhler A, Mintorovitch J, Vexler V, Mann JS, Cohn F, Price D, Huberty J, Brasch RC. (1993) Quantification of tissue plasma volume in the rat by contrast-enhanced magnetic resonance imaging. Magn Reson Med 30:76-81

Labadie C, Lee JH, Vetek G, Springer CS, Jr. (1994) Relaxographic imaging. J Magn Reson B 105:99-112

Ladd DL, Hollister R, Peng X, Wei D, Wu G, Delecki D, Snow RA, Toner JL, Kellar K, Eck J, Desai VC, Raymond G, Kinter LB, Desser TS, Rubin DL. (1999) Polymeric gadolinium chelate magnetic resonance imaging contrast agents: design, synthesis, and properties. Bioconjug Chem 10:361-370

Landis CS, Li X, Telang FW, Molina PE, Palyka I, Vetek G, Springer CS, Jr. (1999) Equilibrium transcytolemmal water-exchange kinetics in skeletal muscle in vivo. Magn Reson Med 42:467-478

Larsson HB, Rosenbaum S, Fritz-Hansen T. (2001) Quantification of the effect of water exchange in dynamic contrast MRI perfusion measurements in the brain and heart. Magn Reson Med 46:272-281

Larsson HB, Stubgaard M, Frederiksen JL, Jensen M, Henriksen O, Paulson OB. (1990) Quantitation of blood-brain barrier defect by magnetic resonance imaging and gadolinium-DTPA in patients with multiple sclerosis and brain tumors. Magn Reson Med 16:117-131

Larsson HB, Stubgaard M, Sondergaard L, Henriksen O. (1994) In vivo quantification of the unidirectional influx constant for Gd-DTPA diffusion across the myocardial capillaries with MR imaging. J Magn Reson Imaging 4:433-440

Lauffer RB. (1987) Paramagnetic metal complexes as water proton relaxation agents for NMR imaging: theory and design. Chem. Rev. 87:901-927

Lauffer RB, Parmelee DJ, Dunham SU, Ouellet HS, Dolan RP, Witte S, McMurry TJ, Walovitch RC. (1998) MS-325: albumin-targeted contrast agent for MR angiography. Radiology 207:529-538

Lauterbur P. (1973) Image Formation by Induced Local Interactions: Examples Employing Nuclear Magnetic Resonance. Nature 242:190-191

Le Duc G, Peoc'h M, Remy C, Charpy O, Muller RN, Le Bas JF, Decorps M. (1999) Use of T(2)-weighted susceptibility contrast MRI for mapping the blood volume in the glioma-bearing rat brain. Magn Reson Med 42:754-761

Lee HB, Blaufox MD. (1985) Blood volume in the rat. J Nucl Med 26:72-76

Leggett DA, Miles KA, Kelley BB. (1999) Blood-brain barrier and blood volume imaging of cerebral glioma using functional CT: a pictorial review. Eur J Radiol 30:185-190

Leon SP, Folkerth RD, Black PM. (1996) Microvessel density is a prognostic indicator for patients with astroglial brain tumors. Cancer 77:362-372

Levin V, Leibel S, Gutin P. (2001) Neoplasms of the central nervous system. In: Cancer: Principles and Practice of Oncology. (DeVita VJ, Hellman S, Rosenberg S, eds), Philadelphia: Lippincott Williams & Wilkins, pp 2100-2160

Li X, Rooney WD, Springer CS, Jr. (2005) A unified magnetic resonance imaging pharmacokinetic theory: intravascular and extracellular contrast reagents. Magn Reson Med 54:1351-1359

Lin W, Celik A, Paczynski RP, Hsu CY, Powers WJ. (1999) Quantitative magnetic resonance imaging in experimental hypercapnia: improvement in the relation between changes in brain R2 and the oxygen saturation of venous blood after correction for changes in cerebral blood volume. J Cereb Blood Flow Metab 19:853-862

Lin W, Paczynski RP, Kuppusamy K, Hsu CY, Haacke EM. (1997) Quantitative measurements of regional cerebral blood volume using MRI in rats: effects of arterial carbon dioxide tension and mannitol. Magn Reson Med 38:420-428

Livramento J, Sour A, Borel A, Merbach A, Tóth É. (2006a) Six Gd3+ ions densely packed within a starburst-shaped heterometallic compound Chem Eur J 12:989-1003

Livramento J, Weidensteiner C, Prata M, Allegrini P, Geraldes C, Helm L, Kneuer R, Merbach A, Santos A, Schmidt P, Tóth É. (2006b) First in vivo MRI assessment of a self-assembled metallostar compound endowed with a ramarkable high field relaxivity Contrast Med Mol Imaging 1:30-39

Lorenz IH, Kolbitsch C, Hormann C, Luger TJ, Schocke M, Felber S, Zschiegner F, Hinteregger M, Kremser C, Benzer A. (2001) Influence of equianaesthetic concentrations of nitrous oxide and isoflurane on regional cerebral blood flow, regional cerebral blood volume, and regional mean transit time in human volunteers. Br J Anaesth 87:691-698

Lu H, Golay X, Pekar JJ, Van Zijl PC. (2003) Functional magnetic resonance imaging based on changes in vascular space occupancy. Magn Reson Med 50:263-274

Lu H, Law M, Johnson G, Ge Y, van Zijl PC, Helpern JA. (2005) Novel approach to the measurement of absolute cerebral blood volume using vascular-space-occupancy magnetic resonance imaging. Magn Reson Med 54:1403-1411

Lu H, van Zijl PC. (2005) Experimental measurement of extravascular parenchymal BOLD effects and tissue oxygen extraction fractions using multi-echo VASO fMRI at 1.5 and 3.0 T. Magn Reson Med 53:808-816

Ludemann L, Hamm B, Zimmer C. (2000) Pharmacokinetic analysis of glioma compartments with dynamic Gd-DTPA-enhanced magnetic resonance imaging. Magn Reson Imaging 18:1201-1214

Lyle S, Rahman M. (1963) Complexometric titration of yttrium and the lanthanons – I A comparison of direct methods. Talanta 10:1177-1182

Maas LC, Harris GJ, Satlin A, English CD, Lewis RF, Renshaw PF. (1997) Regional cerebral blood volume measured by dynamic susceptibility contrast MR imaging in Alzheimer's disease: a principal components analysis. J Magn Reson Imaging 7:215-219

Maeda M, Maley JE, Crosby DL, Quets JP, Zhu MW, Lee GJ, Lawler GJ, Ueda T, Bendixen BH, Yuh WT. (1997) Application of contrast agents in the evaluation of stroke: conventional MR and echo-planar MR imaging. J Magn Reson Imaging 7:23-28

Mathai JC, Mori S, Smith BL, Preston GM, Mohandas N, Collins M, van Zijl PC, Zeidel ML, Agre P. (1996) Functional analysis of aquaporin-1 deficient red cells. The Colton-null phenotype. J Biol Chem 271:1309-1313

Mazurchuk R, Zhou R, Straubinger RM, Chau RI, Grossman Z. (1999) Functional magnetic resonance (fMR) imaging of a rat brain tumor model: implications for evaluation of tumor microvasculature and therapeutic response. Magn Reson Imaging 17:537-548

Meier P, Zierler KL. (1954) On the theory of the indicator-dilution method for measurement of blood flow and volume. J Appl Physiol 6:731-744

Minn A, Ghersi-Egea JF, Perrin R, Leininger B, Siest G. (1991) Drug metabolizing enzymes in the brain and cerebral microvessels. Brain Res Brain Res Rev 16:65-82

Moran GR, Prato FS. (2004) Modeling (1H) exchange: an estimate of the error introduced in MRI by assuming the fast exchange limit in bolus tracking. Magn Reson Med 51:816-827

Mulder WJ, Strijkers GJ, van Tilborg GA, Griffioen AW, Nicolay K. (2006) Lipid-based nanoparticles for contrast-enhanced MRI and molecular imaging. NMR Biomed 19:142-164

Negendank WG, Sauter R, Brown TR, Evelhoch JL, Falini A, Gotsis ED, Heerschap A, Kamada K, Lee BC, Mengeot MM, Moser E, Padavic-Shaller KA, Sanders JA, Spraggins TA, Stillman AE, Terwey B, Vogl TJ, Wicklow K, Zimmerman RA. (1996) Proton magnetic resonance spectroscopy in patients with glial tumors: a multicenter study. J Neurosurg 84:449-458

Noll DC, Pauly JM, Meyer CH, Nishimura DG, Macovski A. (1992) Deblurring for non-2D Fourier transform magnetic resonance imaging. Magn Reson Med 25:319-333

O'Reilly MS, Holmgren L, Shing Y, Chen C, Rosenthal RA, Moses M, Lane WS, Cao Y, Sage EH, Folkman J. (1994) Angiostatin: a novel angiogenesis inhibitor that mediates the suppression of metastases by a Lewis lung carcinoma. Cell 79:315-328

Ocak I, Baluk P, Barrett T, McDonald DM, Choyke P. (2007) The biologic basis of in vivo angiogenesis imaging. Front Biosci 12:3601-3616

Ogawa S, Menon RS, Tank DW, Kim SG, Merkle H, Ellermann JM, Ugurbil K. (1993) Functional brain mapping by blood oxygenation level-dependent contrast magnetic resonance imaging. A comparison of signal characteristics with a biophysical model. Biophys J 64:803-812

Orrison W, Lewine J, Sanders J, Hartshorne M. (1995) Functional magnetic resonance imaging. St. Louis: Mosby

Ostergaard L, Hochberg FH, Rabinov JD, Sorensen AG, Lev M, Kim L, Weisskoff RM, Gonzalez RG, Gyldensted C, Rosen BR. (1999) Early changes measured by magnetic resonance imaging in cerebral blood flow, blood volume, and blood-brain barrier permeability following dexamethasone treatment in patients with brain tumors. J Neurosurg 90:300-305

Ostergaard L, Weisskoff RM, Chesler DA, Gyldensted C, Rosen BR. (1996) High resolution measurement of cerebral blood flow using intravascular tracer bolus passages. Part I: Mathematical approach and statistical analysis. Magn Reson Med 36:715-725

Otsu N. (1979) A threshold selection method from gray scale histogram. IEEE Trans. on Syst. Man and Cyber 1:62-66

Ott RJ, Brada M, Flower MA, Babich JW, Cherry SR, Deehan BJ. (1991) Measurements of blood-brain barrier permeability in patients undergoing radiotherapy and chemotherapy for primary cerebral lymphoma. Eur J Cancer 27:1356-1361

Oudkerk M, Sijens PE, Van Beek EJ, Kuijpers TJ. (1995) Safety and efficacy of dotarem (Gd-DOTA) versus magnevist (Gd-DTPA) in magnetic resonance imaging of the central nervous system. Invest Radiol 30:75-78

Packard SD, Mandeville JB, Ichikawa T, Ikeda K, Terada K, Niloff S, Chiocca EA, Rosen BR, Marota JJ. (2003) Functional response of tumor vasculature to PaCO2: determination of total and microvascular blood volume by MRI. Neoplasia 5:330-338

Padhani AR. (2003) MRI for assessing antivascular cancer treatments. Br J Radiol 76 Spec No 1:S60-80

Pardridge WM, Triguero D, Yang J, Cancilla PA. (1990) Comparison of in vitro and in vivo models of drug transcytosis through the blood-brain barrier. J Pharmacol Exp Ther 253:884-891

Parker GJ, Suckling J, Tanner SF, Padhani AR, Revell PB, Husband JE, Leach MO. (1997) Probing tumor microvascularity by measurement, analysis and display of contrast agent uptake kinetics. J Magn Reson Imaging 7:564-574

Parkes LM, Tofts PS. (2002) Improved accuracy of human cerebral blood perfusion measurements using arterial spin labeling: accounting for capillary water permeability. Magn Reson Med 48:27-41

Parkin DM, Bray F, Ferlay J, Pisani P. (2001) Estimating the world cancer burden: Globocan 2000. Int J Cancer 94:153-156

Patchell RA. (2003) The management of brain metastases. Cancer Treat Rev 29:533-540

Pathak AP, Rand SD, Schmainda KM. (2003) The effect of brain tumor angiogenesis on the in vivo relationship between the gradient-echo relaxation rate change (DeltaR2*) and contrast agent (MION) dose. J Magn Reson Imaging 18:397-403

Pathak AP, Schmainda KM, Ward BD, Linderman JR, Rebro KJ, Greene AS. (2001) MR-derived cerebral blood volume maps: issues regarding histological validation and assessment of tumor angiogenesis. Magn Reson Med 46:735-747

Patlak CS, Blasberg RG. (1985) Graphical evaluation of blood-to-brain transfer constants from multiple-time uptake data. Generalizations. J Cereb Blood Flow Metab 5:584-590

Patlak CS, Blasberg RG, Fenstermacher JD. (1983) Graphical evaluation of blood-to-brain transfer constants from multiple-time uptake data. J Cereb Blood Flow Metab 3:1-7

Pauling L, Coryell CD. (1936) The Magnetic Properties and Structure of Hemoglobin, Oxyhemoglobin and Carbonmonoxyhemoglobin. Proc Natl Acad Sci U S A 22:210-216

Paulson OB, Hertz MM, Bolwig TG, Lassen NA. (1977) Filtration and diffusion of water across the blood-brain barrier in man. Microvasc Res 13:113-124

Payen JF, Briot E, Tropres I, Julien-Dolbec C, Montigon O, Decorps M. (2000) Regional cerebral blood volume response to hypocapnia using susceptibility contrast MRI. NMR Biomed 13:384-391

Payen JF, Vath A, Koenigsberg B, Bourlier V, Decorps M. (1998) Regional cerebral plasma volume response to carbon dioxide using magnetic resonance imaging. Anesthesiology 88:984-992

Perles-Barbacaru AT, Lahrech H. (2007) A new Magnetic Resonance Imaging method for mapping the cerebral blood volume fraction: the rapid steady-state T1 method. J Cereb Blood Flow Metab 27:618-631

Perthen JE, Calamante F, Gadian DG, Connelly A. (2002) Is quantification of bolus tracking MRI reliable without deconvolution? Magn Reson Med 47:61-67

Peterson HI, Appelgren L, Alpsten M, Karlsson L, Kullberg AB, Mattsson J, Selander D. (1984) Intratumor distribution of capillary permeability surface area product (PS) correlated to tumor vascular space and blood flow. Microcirc Endothelium Lymphatics 1:491-507

Pfeiffer S, Herschman H, Lightbody J, Sato G. (1969) Synthesis by a clonal line of rat glial cells of a protein to the nervous system. J Cell Physiol 75:329-340

Pivawer G, Law M, Zagzag D. (2007) Perfusion MR imaging and proton MR spectroscopic imaging in differentiating necrotizing cerebritis from glioblastoma multiforme. Magn Reson Imaging 25:238-243

Port M, Meyer D, Bonnemain B, Corot C, Schaefer M, Rousseaux O, Simonot C, Bourrinet P, Benderbous S, Dencausse A, Devoldere L. (1999) P760 and P775: MRI contrast agents characterized by new pharmacokinetic properties. Magma 8:172-176

Powell D, Dhubhghaill O, Pubanz D, Helm L, Lebedev Y, Schlaepfer W, Merbach A. (1996) Structural and Dynamic Parameters obtained from 17O NMR, EPR, and NMRD studies of monomeric and dimeric Gd3+ complexes of interest in magnetic resonance imaging: an integrated and theoretically self – consistent approach. J Am Chem Soc 118:9333-9346

Preul MC, Caramanos Z, Collins DL, Villemure JG, Leblanc R, Olivier A, Pokrupa R, Arnold DL. (1996) Accurate, noninvasive diagnosis of human brain tumors by using proton magnetic resonance spectroscopy. Nat Med 2:323-325

Purves W, Sadava D, Heller H, Orians G. (1995) Life: The Science of Biology, Eighth Edition. Sunderland: Co-published by Sinauer Associates, Inc., and W. H. Freeman and Company.

Pykett IL, Rzedzian RR. (1987) Instant images of the body by magnetic resonance. Magn Reson Med 5:563-571

Quirk JD, Bretthorst GL, Duong TQ, Snyder AZ, Springer CS, Jr., Ackerman JJ, Neil JJ. (2003) Equilibrium water exchange between the intra- and extracellular spaces of mammalian brain. Magn Reson Med 50:493-499

Raichle ME, Martin WR, Herscovitch P, Mintun MA, Markham J. (1983) Brain blood flow measured with intravenous H2(15)O. II. Implementation and validation. J Nucl Med 24:790-798

Reid AC, Teasdale GM, McCulloch J. (1983) The effects of dexamethasone administration and withdrawal on water permeability across the blood-brain barrier. Ann Neurol 13:28-31

Rijken PF, Bernsen HJ, van der Kogel AJ. (1995) Application of an image analysis system to the quantitation of tumor perfusion and vascularity in human glioma xenografts. Microvasc Res 50:141-153

Roberts DA, Rizi R, Lenkinski RE, Leigh JS, Jr. (1996) Magnetic resonance imaging of the brain: blood partition coefficient for water: application to spin-tagging measurement of perfusion. J Magn Reson Imaging 6:363-366

Roberts HC, Roberts TP, Brasch RC, Dillon WP. (2000) Quantitative measurement of microvascular permeability in human brain tumors achieved using dynamic contrast-enhanced MR imaging: correlation with histologic grade. AJNR Am J Neuroradiol 21:891-899

Robinson S. (2005) Blood oxygenation level dependent (BOLD) imaging of tumours. In: New Techniques in Oncologic Imaging (Padhani A, Choyke P, eds), Boca Raton: Taylor & Francis, pp 257-272

Robinson S. (2006) Imaging of Tumors. In: New technologies in oncologic imaging (Padhani AR, Choyke P, eds), London: Taylor & Francis Group, pp 258-260

Rosen BR. (1992) MR studies of perfusion in the brain. Current Practice in Radiology. Philadelphia, PA: Mosby Yearbook

Rosen BR, Belliveau JW, Chien D. (1989) Perfusion imaging by nuclear magnetic resonance. Magn Reson Q 5:263-281

Rosen BR, Belliveau JW, Vevea JM, Brady TJ. (1990) Perfusion imaging with NMR contrast agents. Magn Reson Med 14:249-265

Ross J. (1991) Section 2: Cardiovascular System. In: Best and Taylor's Physiological Basis of Medical Practice), Baltimore MD: Williams & Wilkins

Rother J, Guckel F, Neff W, Schwartz A, Hennerici M. (1996) Assessment of regional cerebral blood volume in acute human stroke by use of single-slice dynamic susceptibility contrast-enhanced magnetic resonance imaging. Stroke 27:1088-1093

Rudin M, Sauter A. (1991) Noninvasive determination of regional cerebral blood flow in rats using dynamic imaging with Gd(DTPA). Magn Reson Med 22:32-46

Russell D, Rubinstein L. (1989) Tumours of central neuroepithelial origin. In: Pathology of tumours of the central nervous system (Rubinstein L, ed), Baltimore: Williams & Wilkins, pp 83 - 350

Sawada Y, Patlak CS, Blasberg RG. (1989) Kinetic analysis of cerebrovascular transport based on indicator diffusion technique. Am J Physiol 256:H794-812

Scheffler K, Seifritz E, Haselhorst R, Bilecen D. (1999) Titration of the BOLD effect: separation and quantitation of blood volume and oxygenation changes in the human cerebral cortex during neuronal activation and ferumoxide infusion. Magn Reson Med 42:829-836

Schlageter KE, Molnar P, Lapin GD, Groothuis DR. (1999) Microvessel organization and structure in experimental brain tumors: microvessel populations with distinctive structural and functional properties. Microvasc Res 58:312-328

Schmidek HH, Nielsen SL, Schiller AL, Messer J. (1971) Morphological studies of rat brain tumors induced by N-nitrosomethylurea. J Neurosurg 34:335-340

Schmiedl U, Ogan M, Paajanen H, Marotti M, Crooks LE, Brito AC, Brasch RC. (1987) Albumin labeled with Gd-DTPA as an intravascular, blood pool-enhancing agent for MR imaging: biodistribution and imaging studies. Radiology 162:205-210

Schmiedl UP, Kenney J, Maravilla KR. (1992) Dyke Award Paper. Kinetics of pathologic blood-brain-barrier permeability in an astrocytic glioma using contrast-enhanced MR. AJNR Am J Neuroradiol 13:5-14

Schwarzbauer C, Morrissey SP, Deichmann R, Hillenbrand C, Syha J, Adolf H, Noth U, Haase A. (1997) Quantitative magnetic resonance imaging of capillary water permeability and regional blood volume with an intravascular MR contrast agent. Magn Reson Med 37:769-777

Schwarzbauer C, Syha J, Haase A. (1993) Quantification of regional blood volumes by rapid T1 mapping. Magn Reson Med 29:709-712

Seitz RJ, Deckert M, Wechsler W. (1988) Vascularization of syngenic intracerebral RG2 and F98 rat transplantation tumors. A histochemical and morphometric study by use of ricinus communis agglutinin I. Acta Neuropathol (Berl) 76:599-605

Shin W, Cashen TA, Horowitz SW, Sawlani R, Carroll TJ. (2006) Quantitative CBV measurement from static T1 changes in tissue and correction for intravascular water exchange. Magn Reson Med 56:138-145

Shockley RP, LaManna JC. (1988) Determination of rat cerebral cortical blood volume changes by capillary mean transit time analysis during hypoxia, hypercapnia and hyperventilation. Brain Res 454:170-178

Shortt AJ, Howell K, O'Brien C, McLoughlin P. (2004) Chronic systemic hypoxia causes intra-retinal angiogenesis. J Anat 205:349-356

Sibson NR, Blamire AM, Perry VH, Gauldie J, Styles P, Anthony DC. (2002) TNF-alpha reduces cerebral blood volume and disrupts tissue homeostasis via an endothelin- and TNFR2-dependent pathway. Brain 125:2446-2459

Simonsen CZ, Ostergaard L, Vestergaard-Poulsen P, Rohl L, Bjornerud A, Gyldensted C. (1999) CBF and CBV measurements by USPIO bolus tracking: reproducibility and comparison with Gd-based values. J Magn Reson Imaging 9:342-347

Sobol WT, Jackels SC, Cothran RL, Hinson WH. (1991) NMR spin-lattice relaxation in tissues with high concentration of paramagnetic contrast media: evaluation of water exchange rates in intact rat muscle. Med Phys 18:243-250

Spencer AJ, Wilson SA, Batchelor J, Reid A, Rees J, Harpur E. (1997) Gadolinium chloride toxicity in the rat. Toxicol Pathol 25:245-255

Sugahara T, Korogi Y, Kochi M, Ikushima I, Hirai T, Okuda T, Shigematsu Y, Liang L, Ge Y, Ushio Y, Takahashi M. (1998) Correlation of MR imaging-determined cerebral blood volume maps with histologic and angiographic determination of vascularity of gliomas. AJR Am J Roentgenol 171:1479-1486

Sugahara T, Korogi Y, Tomiguchi S, Shigematsu Y, Ikushima I, Kira T, Liang L, Ushio Y, Takahashi M. (2000) Posttherapeutic intraaxial brain tumor: the value of perfusion-sensitive contrast-enhanced MR imaging for differentiating tumor recurrence from nonneoplastic contrast-enhancing tissue. AJNR Am J Neuroradiol 21:901-909

Sunaert S. (2006) Presurgical planning for tumor resectioning. J Magn Reson Imaging 23:887-905

Svoboda K, Yasuda R. (2006) Principles of two-photon excitation microscopy and its applications to neuroscience. Neuron 50:823-839

Swenberg JA, Koestner A, Wechsler W, Denlinger RH. (1972) Quantitative aspects of transplacental tumor induction with ethylnitrosourea in rats. Cancer Res 32:2656-2660

Tamargo RJ, Epstein JI, Brem H. (1988) Heterotransplantation of malignant human gliomas in neonatal rats. J Neurosurg 69:928-933

Tanner JE. (1983) Intracellular diffusion of water. Arch Biochem Biophys 224:416-428

Tatum JL, Kelloff GJ, Gillies RJ, Arbeit JM, Brown JM, Chao KS, Chapman JD, Eckelman WC, Fyles AW, Giaccia AJ, Hill RP, Koch CJ, Krishna MC, Krohn KA, Lewis JS, Mason RP, Melillo G, Padhani AR, Powis G, Rajendran JG, Reba R, Robinson SP, Semenza GL, Swartz HM, Vaupel P, Yang D, Croft B, Hoffman J, Liu G, Stone H, Sullivan D. (2006) Hypoxia: importance in tumor biology, noninvasive measurement by imaging, and value of its measurement in the management of cancer therapy. Int J Radiat Biol 82:699-757

Taylor JS, Reddick WE. (2000) Evolution from empirical dynamic contrast-enhanced magnetic resonance imaging to pharmacokinetic MRI. Adv Drug Deliv Rev 41:91-110

Thomas DL, Lythgoe MF, Calamante F, Gadian DG, Ordidge RJ. (2001) Simultaneous noninvasive measurement of CBF and CBV using double-echo FAIR (DEFAIR). Magn Reson Med 45:853-863

Thomas DL, Lythgoe MF, van der Weerd L, Ordidge RJ, Gadian DG. (2006) Regional variation of cerebral blood flow and arterial transit time in the normal and hypoperfused rat brain measured using continuous arterial spin labeling MRI. J Cereb Blood Flow Metab 26:274-282

Thompson HK, Jr., Starmer CF, Whalen RE, McIntosh HD. (1964) Indicator Transit Time Considered as a Gamma Variate. Circ Res 14:502-515

Todd MM, Weeks J. (1996) Comparative effects of propofol, pentobarbital, and isoflurane on cerebral blood flow and blood volume. J Neurosurg Anesthesiol 8:296-303

Todd MM, Weeks JB, Warner DS. (1992) Cerebral blood flow, blood volume, and brain tissue hematocrit during isovolemic hemodilution with hetastarch in rats. Am J Physiol 263:H75-82

Todd MM, Weeks JB, Warner DS. (1993) The influence of intravascular volume expansion on cerebral blood flow and blood volume in normal rats. Anesthesiology 78:945-953

Tofts PS. (1997) Modeling tracer kinetics in dynamic Gd-DTPA MR imaging. J Magn Reson Imaging 7:91-101

Tofts PS, Brix G, Buckley DL, Evelhoch JL, Henderson E, Knopp MV, Larsson HB, Lee TY, Mayr NA, Parker GJ, Port RE, Taylor J, Weisskoff RM. (1999) Estimating kinetic parameters from dynamic contrast-enhanced T(1)-weighted MRI of a diffusable tracer: standardized quantities and symbols. J Magn Reson Imaging 10:223-232

Tofts PS, Kermode AG. (1989) Blood brain barrier permeability in multiple sclerosis using labelled DTPA with PET, CT and MRI. J Neurol Neurosurg Psychiatry 52:1019-1020

Tofts PS, Kermode AG. (1991) Measurement of the blood-brain barrier permeability and leakage space using dynamic MR imaging. 1. Fundamental concepts. Magn Reson Med 17:357-367

Tozer GM, Lewis S, Michalowski A, Aber V. (1990) The relationship between regional variations in blood flow and histology in a transplanted rat fibrosarcoma. Br J Cancer 61:250-257

Tracey I, Hamberg LM, Guimaraes AR, Hunter G, Chang I, Navia BA, Gonzalez RG. (1998) Increased cerebral blood volume in HIV-positive patients detected by functional MRI. Neurology 50:1821-1826

Tropres I, Grimault S, Vaeth A, Grillon E, Julien C, Payen JF, Lamalle L, Decorps M. (2001) Vessel size imaging. Magn Reson Med 45:397-408

Tropres I, Lamalle L, Peoc'h M, Farion R, Usson Y, Decorps M, Remy C. (2004) In vivo assessment of tumoral angiogenesis. Magn Reson Med 51:533-541

Turetschek K, Floyd E, Helbich T, Roberts TP, Shames DM, Wendland MF, Carter WO, Brasch RC. (2001) MRI assessment of microvascular characteristics in experimental breast tumors using a new blood pool contrast agent (MS-325) with correlations to histopathology. J Magn Reson Imaging 14:237-242

Vaeth A. (1998) Imagerie du volume sanguin cérébral - applications -. In: INSERM U 438 - Résonance magnétique nucléaire bioclinique -, Grenoble: Joseph Fourier University, p 137

Valable S, Lemasson B, Rarion R, Beaumont M, Segebarth C, Remy C, Barbier EL. (submitted 2007) Longitudinal assessment of Blood Volume, Vessel Size and angiogenic factors in two rat glioma models. NMR Biomed

Valable S, Segebarth C, Remy C, Barbier EL. (2006) Does repeated injections of an iron-based contrast agent lead to an accumulation of iron in the brain parenchyma? In: ISMRM 14th. Scientific Meeting and Exhibition, Seattle, Washington, USA

van Vaals JJ, Brummer ME, Dixon WT, Tuithof HH, Engels H, Nelson RC, Gerety BM, Chezmar JL, den Boer JA. (1993) "Keyhole" method for accelerating imaging of contrast agent uptake. J Magn Reson Imaging 3:671-675

Vander Elst L, Port M, Raynal I, Simonot C, Muller R. (2003) Physicochemical characterization of P760, a new macromolecular contrast agent with high relaxivity. Eur J Inorg Chem:2495-2501

Vander Elst L, Raynal I, Port M, Tisnes P, Muller R. (2005) In vitro Relaxometric and Luminescence Characterization of P792 (Gadomelitol, Vistarem), an Efficient and Rapid Clearance Blood Pool MRI Contrast Agent. Eur. J. Inorg. Chem.:1142-1148

Verant P, Serduc R, Van Der Sanden B, Remy C, Vial JC. (2007) A direct method for measuring mouse capillary cortical blood volume using multiphoton laser scanning microscopy. J Cereb Blood Flow Metab 27:1072-1081

Villringer A, Rosen BR, Belliveau JW, Ackerman JL, Lauffer RB, Buxton RB, Chao YS, Wedeen VJ, Brady TJ. (1988) Dynamic imaging with lanthanide chelates in normal brain: contrast due to magnetic susceptibility effects. Magn Reson Med 6:164-174

Wald LL, Nelson SJ, Day MR, Noworolski SE, Henry RG, Huhn SL, Chang S, Prados MD, Sneed PK, Larson DA, Wara WM, McDermott M, Dillon WP, Gutin PH, Vigneron DB. (1997) Serial proton magnetic resonance spectroscopy imaging of glioblastoma multiforme after brachytherapy. J Neurosurg 87:525-534

Weibel E. (1980) Stereological Methods, Vol. 2. Theoretical Foundations. London: Academic Press

Weidensteiner C, Rausch M, McSheehy PM, Allegrini PR. (2006) Quantitative dynamic contrast-enhanced MRI in tumor-bearing rats and mice with inversion recovery TrueFISP and two contrast agents at 4.7 T. J Magn Reson Imaging 24:646-656

Weidner N, Semple JP, Welch WR, Folkman J. (1991) Tumor angiogenesis and metastasis--correlation in invasive breast carcinoma. N Engl J Med 324:1-8

Weil C. (1952) Tables for convenient calculation of median-effective dose (LD50 or ED50) and instructions in their use. Biometrics 8:249-263

Weinmann HJ, Brasch RC, Press WR, Wesbey GE. (1984) Characteristics of gadolinium-DTPA complex: a potential NMR contrast agent. AJR Am J Roentgenol 142:619-624

Weiss HR, Buchweitz E, Murtha TJ, Auletta M. (1982) Quantitative regional determination of morphometric indices of the total and perfused capillary network in the rat brain. Circ Res 51:494-503

Weissleder R, Elizondo G, Wittenberg J, Lee AS, Josephson L, Brady TJ. (1990a) Ultrasmall superparamagnetic iron oxide: an intravenous contrast agent for assessing lymph nodes with MR imaging. Radiology 175:494-498

Weissleder R, Elizondo G, Wittenberg J, Rabito CA, Bengele HH, Josephson L. (1990b) Ultrasmall superparamagnetic iron oxide: characterization of a new class of contrast agents for MR imaging. Radiology 175:489-493

Weissleder R, Mahmood U. (2001) Molecular imaging. Radiology 219:316-333

Weissleder R, Moore A, Mahmood U, Bhorade R, Benveniste H, Chiocca EA, Basilion JP. (2000) In vivo magnetic resonance imaging of transgene expression. Nat Med 6:351-355

Winter PM, Caruthers SD, Wickline SA, Lanza GM. (2006) Molecular imaging by MRI. Curr Cardiol Rep 8:65-69

Yablonskiy DA, Haacke EM. (1994) Theory of NMR signal behavior in magnetically inhomogeneous tissues: the static dephasing regime. Magn Reson Med 32:749-763

Yankeelov TE, Rooney WD, Li X, Springer CS, Jr. (2003) Variation of the relaxographic "shutter-speed" for transcytolemmal water exchange affects the CR bolus-tracking curve shape. Magn Reson Med 50:1151-1169

Yeung WT, Lee TY, Del Maestro RF, Kozak R, Brown T. (1992) In vivo CT measurement of blood-brain transfer constant of iopamidol in human brain tumors. J Neurooncol 14:177-187

Zama A, Tamura M, Inoue HK. (1991) Three-dimensional observations on microvascular growth in rat glioma using a vascular casting method. J Cancer Res Clin Oncol 117:396-402

Zhou J, Wilson DA, Ulatowski JA, Traystman RJ, van Zijl PC. (2001) Two-compartment exchange model for perfusion quantification using arterial spin tagging. J Cereb Blood Flow Metab 21:440-455

Zimmer C, Weissleder R, Poss K, Bogdanova A, Wright SC, Jr., Enochs WS. (1995) MR imaging of phagocytosis in experimental gliomas. Radiology 197:533-538

List of publications

Peer-Reviewed Articles

- Perles-Barbacaru AT, Lahrech H (Mar 2007). A New MRI Method for Mapping the Cerebral Blood Volume Fraction : the Rapid Stady State T_1 Method. J Cereb Blood Flow Metab 27(3):618-631
- Lahrech H, Perles-Barbacaru AT, Gadelle A, Aous S, Farion R, Le Bas JF, Debouzy JC, Fries HP. Cerebral blood volume quantification in a C6 tumor model using Gadolinium Per (3,6) Anhydro Alpha Cyclodextrin as a new MRI preclinical contrast agent (J Cereb Blood Flow Metab, in press)

Oral conference communications

- Perles-Barbacaru AT, Chiese L, Van der Sanden B, Farion R, Segebarth C, Lahrech H (Sep 2006). Cerebral blood volume fraction mapping in a C6 brain tumor model using $RSST_1$-MRI with an intravascular contrast agent: Gd-ACX. 23rd Annual Scientific Meeting of the European Society for Magnetic Resonance in Medicine and Biology, Magn Reson Mater Phy Suppl 7 Sep 2006, S66. Warsaw (Poland).
- Lahrech H, Perles-Barbacaru AT, Gadelle A, Aous S, Farion R, Le Bas JF, Debouzy JC, Fries HP (May 2006). Characterization and potential of Gd-ACX, a new contrast agent for Magnetic Resonance Neuroimaging. International Society for Magnetic Resonance in Medicine, p.24, Seattle (USA)
- Lahrech H, Perles-Barbacaru AT, Aous S, Farion R, Debouzy JC, Gadelle A, Fries PH (Sep 2005). Potential of a new contrast agent: gadolinium per (3,6) anhydro alpha cyclodextrin for magnetic resonance neuroimaging. 22nd Annual Scientific Meeting of the European Society for Magnetic Resonance in Medicine and Biology, Magn Reson Mater Phy Suppl 7 Sep 2005, S96-97. Basle (Switzerland).
- Perles-Barbacaru AT (May 2005). Imagerie par resonance magnétique du volume sanguin pour la caractérisation de la néovascularisation des tumeurs cérébrales expérimentales et chez l'Homme: méthode T_1 stationnaire rapide. 5ème Journée de l'Ecole Doctorale Ingénierie pour la Santé, la Cognition et l'Environnement, Grenoble (France)

- Perles-Barbacaru AT, Lahrech H (Mar 2005). Cartographie du volume sanguin cérébral absolu : utilisation d'une méthode T_1 rapide stationnaire. 11th congress of the GRAMM (Groupe de Recherche sur les Applications du Magnétisme en Médecine, Research Group for Applications of Magnetism in Medicine), p. GRAMM7. Nancy (France)
- Lahrech H, Perles-Barbacaru AT, Fries HP, Debouzy JC, and Gadelle A (Mar 2005). Vascularization of the brain of a sound rat. European Molecular Imaging Laboratories, Cyclope Conferences "Combattre le cancer" ("Fight Cancer"). Atomic Energy Commission (CEA), Saclay (France)
- Lahrech H, Barbacaru AT, Fries HP, Aous S, Farion R, Le Bas JF, Debouzy JC, Gadelle A (Nov 2004). Potentiel des Cyclodextrines pour la caractérisation de la microvascularisation dans un modèle de tumeur intracérébrale. "Microimaging Day" organized by CGRM (Center for Magnetic Resonance Grenoble), Grenoble (France)
- Lahrech H, Barbacaru AT (Sep 2004). Absolute Cerebral Blood Volume mapping using high contrast agent relaxivity: rapid steady state T_1 method. 21st Annual Scientific Meeting of the European Society for Magnetic Resonance in Medicine and Biology, Magn Reson Mater Phy Suppl 1 Sep 2004 S63-65. Copenhagen (Denmark)
- Barbacaru AT, Lahrech H (Mar 2004). Absolute Cerebral Blood Volume mapping using high contrast agent relaxivity: rapid steady state T_1 method. International Society for Magnetic Resonance in Medicine, Workshop on Quantitative Cerebral Perfusion Imaging Using MRI: A Technical Perspective, p.16. Venise (Italy)
- Lahrech H, Barbacaru AT (Dec 2003). Cartographie du volume sanguin cérébral absolu par IRM: méthode T_1. 2nd NMR & MRI Meeting of GERRIMN (Groupe d'Etude et de Recherche en Resonance Magnétique Nucléaire et en Imagerie par Resonanace Magnétique, Study and Research Group of Nuclear Magnetic Resonance and Magnetic Resonance Imaging). Mohammedia (Maroc)
- Barbacaru AT, Farion R, Segebarth C, Lahrech H (Jun 2003). IRM du volume sanguin cérébral: méthode T_1. Journées Scientifiques de l'IFR « RMN Biomédicale : de la cellule à l'homme », Col de Porte (France)

Poster communications

- Perles-Barbacaru AT, Chiese L, Van der Sanden B, Farion R, Segebarth C, Lahrech H (May 2007) Cerebral blood volume fraction mapping in a C6 brain tumor model using $RSST_1$-MRI with an intravascular contrast agent: Gd-ACX. Joint Meeting International Society for

Magnetic Resonance in Medicine/ European Society for Magnetic Resonance in Medicine and Biology Berlin (Germany)

- Perles-Barbacaru AT, Chieze L, Van der Sanden B, Farion R, Segebarth C, Lahrech H (Apr 2007) Cerebral blood volume fraction mapping in a C6 brain tumor model using $RSST_1$-MRI with an intravascular contrast agent: Gd-ACX. Journées de la Recherche Médicale, Grenoble (France)
- Perles-Barbacaru AT, Segebarth C, Lahrech H (Mar 2007). Cerebral blood volume quantification aimed at the longitudinal assessment of angiogenesis in brain tumors. Cancéropôle Lyon Auvergne Rhône-Alpes. Grenoble (France)
- Lahrech H, Perles-Barbacaru AT, Aous S, Farion R, Debouzy JC, Gadelle A, Fries PH (Oct 2006). Potential of a new contrast agent: gadolinium per (3,6) anhydro alpha cyclodextrin for magnetic resonance neuroimaging. European BioAlpine Convention, Grenoble (France)
- Perles-Barbacaru AT, Chieze L, Van der Sanden B, Farion R, Segebarth C, Lahrech H (Oct 2006) Cerebral blood volume fraction mapping in a C6 brain tumor model using $RSST_1$-MRI with an intravascular contrast agent: Gd-ACX. MR of Cancer Study Group Workshop: Frontiers in Metabolic, Molecular and Clinical Imaging. Pocono Manor, Pennsylvania (USA)
- Perles-Barbacaru AT, Chiese L, Van der Sanden B, Farion R, Segebarth C, Lahrech H (Oct 2006). Cerebral blood volume fraction mapping in a C6 brain tumor model using $RSST_1$-MRI with an intravascular contrast agent: Gd-ACX. 9th NMR Meeting Rhône-Alpes, p.13. Lyon (France)
- Lahrech H, Perles-Barbacaru AT, Aous S, Farion R, Debouzy JC, Gadelle A, Fries PH (Oct 2006). Potential of a new contrast agent: gadolinium per (3,6) anhydro alpha cyclodextrin for magnetic resonance neuroimaging. 9th NMR Meeting Rhône-Alpes, p.12. Lyon (France)
- Perles-Barbacaru AT, Lahrech H. (May 2006). Rapid steady state T_1 method for cerebral blood volume fraction mapping: sensitivity determination under hypercapnia. International Society for Magnetic Resonance in Medicine, p.217, Seattle (USA)
- Perles-Barbacaru AT, Segebarth C, Lahrech H (Apr 2006). Nouvelle méthode IRM pour la quantification du Volume Sanguin Cérébral: Méthode T_1 stationnaire rapide. Journées de la Recherche Médicale, Grenoble (France)
- Lahrech H, Perles-Barbacaru AT, Aous S, Farion R, Debouzy JC, Gadelle A, Fries PH (Apr 2006). Potentiel d'un nouveau agent de contraste: gadolinium per (3,6) anhydro alpha cyclodextrine pour la neuroimagerie par resonance magnétique. Journées de la Recherche Médicale, Grenoble (France)

- Perles-Barbacaru AT, Lahrech H (Oct 2005). Nouvelle méthode pour la quantification du Volume Sanguin Cérébral: Méthode T_1 stationnaire rapide. 8th NMR Meeting Rhône-Alpes, p.15. Grenoble (France)

Invited seminars

- Perles-Barbacaru AT, Lahrech H (Mar 2005). Nouvel outil IRM pour la quantification de l'angiogénèse tumorale. Cancéropôle. Grenoble (France)
- Perles-Barbacaru AT, Lahrech H (Jun 2005) Effet de la relaxation longitudinale des agents de contraste paramagnétiques pour la quantification du volume sanguin cérébral chez le rat. Seminar at Guerbet Laboratories. Aulnay-sous-Bois (France)

Other

- Perles-Barbacaru AT (Feb 2007) Imagerie du volume sanguine cérébral. MoZaicA, on-line journal http://journalmozaica.free.fr
- Perles-Barbacaru AT (Jan 2007) Imagerie du volume sanguine cérébral. Le Gluon, journal of scientific vulgarization of the Joseph Fourier University, http://www.ujf-grenoble.fr/76056968/0
- Barbacaru AT, Master thesis "Models and Instruments for Medicine and Biology" (Sep 2003). Absolute cerebral blood volume in rats using the T_1 effect of paramagnetic contrast agents. Joseph Fourier University Grenoble (France)
- Barbacaru AT, Physics Diploma (Sep 2003). Cerebral blood volume quantification: new method using paramagnetic contrast agents and fast Magnetic Resonance Imaging. Hamburg University (Germany)

Awards

- Perles-Barbacaru AT, Chieze L, Van der Sanden B, Farion R, Segebarth C, Lahrech H (Oct 2006) Cerebral blood volume fraction mapping in a C6 brain tumor model using $RSST_1$-MRI with an intravascular contrast agent: Gd-ACX. Poster Prize "Neuro Imaging" category, European BioAlpine Convention, Grenoble (France)

- Barbacaru AT (Oct 2004) Absolute Cerebral Blood Volume using high Contrast Agent relaxivity: rapid steady state T_1 method. Prize “Alexandre Joël” Master category, Association for Research against Cancer (ARC), Paris (France)
- Educational Stipends

- Joint Meeting ISMRM-ESMRMB 2007, Berlin, Germany
- 14th Scientific Meeting 2006, Seattle, WA, USA

Fellowships

- PhD graduate research fellowship granted by the French Association for Research against Cancer (ARC), 2004 – 2007

one year research fellowship granted by the French National Academy of Medicine, 2006 (declined)

- one year research fellowship granted by the German Academic Exchange Service (DAAD), 2004 (declined)

Curriculum vitae

Adriana-Teodora PERLES-BARBACARU

Date of birth: October 29, 1973 **place of birth:** Bucharest, Romania **Nationality:** German, naturalized in 1983

DEGREES

Oct. 2003	German postgraduate Degree in in Fundamental Physics with Astronomy and Astrophysics as minor subject qualifying for doctorate studies, grade 1, Hamburg University, Germany
Sep. 2003	"Diplôme d'Etudes Approfondies", French postgraduate Degree granted 5 years after Baccalaureate qualifying for doctorate studies, Grade 3, Grenoble, France
Oct. 1998	Graduation from Medical University with "Final State Examination", Grade: 2, Hamburg University, Germany

EDUCATION AND TRAINING

starting Jan. 2008	Postdoctoral position, Beckman Institute, Biological Imaging Center, Pasadena, CA, US
May 2004 to Dec. 2007	PhD project: Magnetic resonance imaging of the cerebral blood volume for the characterization of experimental brain tumor neovascularization, INSERM (French National Institute for Health and Medical Research), Laboratory for Functional and Metabolic Neuroimaging, Grenoble, France
Oct. 2002 – Sep. 2003	training at INSERM as part of the "Diplôme d'Etudes Approfondies"- program, specializing in "Models and Instruments in Medicine and Biology", University Joseph Fourier, Grenoble, France
Jun. - Aug. 2001	training period at the Institute of Protontherapy, Biophysics, Orsay, France
Sep. 2000 - Jul. 2002	graduate studies in Fundamental Physics and Astrophysics, Orsay, France
Oct. 1998 - Jul. 2000	two-year undergraduate course in Physics and Astrophysics at Hamburg University
Oct. 1997 - Sep. 1998	three clinical internships each of four month duration in Medical Colleges and general hospitals in India, Israel and Switzerland (elective in Neurosurgery and Radiotherapy)
Oct. 1992 – Sep. 1997	medical studies, University Hospital Hamburg-Eppendorf, including different clerkships (26 weeks) requested by the Medical Faculty, and additional courses in Nuclear Medicine, Image Processing and Radiotherapy, Hamburg Germany

WORK RECORD

1992 - 2003	all living and university expenses financed by various vacation jobs and part-time jobs including nursing and private lessons in Hamburg, Paris and Grenoble
Nov. 2003 – Apr. 2004	resident in psychiatry, University Hospital Grenoble (CHU), France
Feb. 1999 – Jul. 2000	assistant in orthopedic surgery, Endoklinik, Hamburg, Germany
Dec. 1998 – Jul. 2000	teacher for natural sciences and mathematics at a private school, Studienkreis Norderstedt, Germany
Feb. 1995 – Sep. 1997	assistant for a dental surgeon, Doctor Ergun Orcun, Hamburg, Germany
Oct. – Feb. 1994/95, 1995/96, 1996/97	academic advisor and assistant for anatomical dissections for students in medicine and dentistry, Hamburg University, Germany
Jan. 1993 – Sep. 1997	translator at the foreigners registration authority, Hamburg, Germany

LANGUAGES

Romanian, German:	native languages
English, French:	fluent
informatics:	PASCAL, FORTRAN, IDL/MATLAB, ImageJ, Office Pack, EndNote, AnalySIS

PUBLICATIONS

AT Perles-Barbacaru, H Lahrech. A new Magnetic Resonance Imaging method for mapping the cerebral blood volume fraction: the rapid steady-state T_1 method.	J Cereb Blood Flow Metab 27(3):618-631(2007)
H Lahrech, AT Barbacaru, S Aous, JF Le Bas, JC Debouzy, A Gadelle, PH Fries. Cerebral blood volume quantification in a C6 tumor model using Gadolinium Per (3,6) Anhydro Alpha Cyclodextrin as a new MRI preclinical contrast agent	J Cereb Blood Flow Metab in press

Appendix

- **Appendix I: ImageJ (version 1.38a) macro for vascular morphometric analysis**

- **Appendix II: A New MRI Method for Mapping the Cerebral Blood Volume Fraction: the Rapid Steady State T_1 Method**

Perles-Barbacaru AT, Lahrech H

Mar 2007

J Cereb Blood Flow Metab 27(3):618-631

p 1 - 14

- **Appendix III: Cerebral blood volume quantification in a C6 tumor model using Gadolinium Per (3,6) Anhydro Alpha Cyclodextrin as a new MRI preclinical contrast agent**

Lahrech H, Perles-Barbacaru AT, Gadelle A, Aous S, Farion R, Le Bas JF, Debouzy JC, Fries HP

submitted to: J Cereb Blood Flow Metab

p 1 - 36

- **Appendix IV: Imagerie du volume sanguine cérébral**

Perles-Barbacaru AT

Jan 2007

Le Gluon

p 1 - 4

Appendix I: ImageJ (version 1.38a) macro for vascular morphometric analysis

To use this macro for vascular morphometric analysis you need to download:

1°) ImageJ :

http://rsb.info.nih.gov/ij/download.html

2) To update to a newer version of ImageJ :

http://rsb.info.nih.gov/ij/upgrade/ij.jar

3) Plugin "otsu thresholding":

http://rsb.info.nih.gov/ij/plugins/otsu-thresholding.html

4) Plugin "Morphology"

http://www.dentistry.bham.ac.uk/landinig/software/software.html

Download the full set as a single zip file from here

```
// Goal: calculate vascular morphologic parameters from anti-Collagen IV
immunofluorescence images using stereological methods:
// -  number of blood vessels in a ROI
// -  the blood vessel density (nb/mm)
// -  the "2D-blood volume" = the vascular surface fraction (%)
// -  the vessel diameters (by 4 different methods)
// -  the length density of the vessels Lv (mm/mm3) = Sum[a/b]/At for each
slice/image
// -  the sum of Lv for each slice is needed to compute the blood volume
per unit volume
//    Vv (mm3/mm3) = pi/4 d² Sum[Lv] assuming blood vessels are perfect
cylindical tubes

// some procedures are taken from the macro analyse_vaisseaux - Marion
Gandit (06/09/2005)
// modifications by Adriana T. Perles-Barbacaru - October 12, 2006
// modifications by BvdS, October 23, 2006
// modifications by Adriana T. Perles-Barbacaru - April 3, 2007
// with magnification factor 10, the size of one pixel is 1.533 µm for
acquired gray scale acquisitions and 0.767 µm for color acquisitions
// or gray scale images converted from color acquisitions
// 1.518 µm in Marion's macro!!! 1.379 µm for the brain acquisitions from
BvdS (Uetrecht)

// Declaration of global variables:
var title  = "a title";
var title2 = "a title";
var title3 = "a title";
var title4 = "a title";
var overestimation = "a title"
```

```
var underestimation = "a title"
//var pixelsize = 1.379;
var pixelsize = 0.76667;
var slice = "a slice or image number"
var ImageDirectory = "the directory of the image";
var flagROI = 0;
var ROIareamillim = 0;
var ROIarea = 0;
var imagebin = 0;

//
°°°°°°°°°°°°°°°°°°°°°°°°°°°°°°°°°°°°°°°°°°°°°°°°°°°°°°°°°°°°°°°°°°°°°°°°°°°
°°°
macro "Define an ROI [F4]"
{
// asks to open the image, if not a grayscale image the color channel is
extracted
{
{open();}}
title=getTitle;
slice=substring(title,2,4);
ImageDirectory=getDirectory("image");
bit=bitDepth();
if (bit==8){
    pixelsize = 0.76667;
    }
// if not a grayscale image, selection of the red color channel
if (bit!=8){
    pixelsize = 0.76667;
    //showMessage("pixelsize in µm", pixelsize);
    run("RGB Split");
    selectWindow(title+" (blue)");
    close();
    selectWindow(title+" (green)");
    close();
    selectWindow(title+" (red)");
    rename(title);
    }
// Define the ROI
flagROI = 0;
ROI=getBoolean("Do you want to open a saved ROI? Cancel selects the whole
image but you need to press F5 to continue.");
if (ROI==1){
    showMessage("ROI","Open the ROI, then press F5 to continue");
    open();
    flagROI=1;
    selectWindow(title);
    }
else if (ROI==0){
    showMessage("ROI","Draw the ROI, then press F5 to continue");
    flagROI=2;
    selectWindow(title);
    setTool(3);
    }
exit;
}
//
°°°°°°°°°°°°°°°°°°°°°°°°°°°°°°°°°°°°°°°°°°°°°°°°°°°°°°°°°°°°°°°°°°°°°°°°°°°
°°°°°°
macro "image processing [F5]"
// {
```

```
// saves the ROI, measures the ROI parameters
{
if (flagROI!=0){
    if (flagROI==2){
        saveAs("Selection");}
    run("Crop");
    run("Select None");
    run("Duplicate...", "title="+title+"_roi");
    run("Duplicate...", "title="+title+"_copyroi");
    run("Restore Selection");
    run("Set Measurements...", "area limit redirect=None decimal=6");
    run("Measure");
    setForegroundColor(0, 0, 0);
    run("Fill");
    ROIarea=getResult("Area", 0);
    // conversion to µm² and mm²
    ROIareamicrom=ROIarea*pixelsize*pixelsize;
    ROIareamillim=ROIarea*pixelsize*pixelsize/1000000;
    print(ImageDirectory);
    print("slice: "+title);
    print("ROI surface(mm²) : "+ROIareamillim);
    run("Image Calculator...", "image1="+title+"_copyroi operation=XOR
image2="+title+"_roi create");
    rename("OriginalSelection"+title);
    }
else if (flagROI==0){
    run("Duplicate...", "title="+title+"_roi");
    H=getHeight();
    W=getWidth();
    ROIarea = W*H;
    ROIareamillim = W*H*pixelsize*pixelsize/1000000;
    print("slice: "+ImageDirectory +title);
    print("ROI surface (mm²) : "+ROIareamillim);
    run("Duplicate...", "title="+title+"_roi");
    run("Duplicate...", "title="+title+"_copyroi");
    makeRectangle(3, 3, W, H);
    setForegroundColor(0, 0, 0);
    run("Fill");
    run("Image Calculator...", "image1="+title+"_copyroi operation=XOR
image2="+title+"_roi create");
    rename("OriginalSelection"+title);
    }
title2=getTitle;
run("Duplicate...", "title=BeforeImageProcessing");
selectWindow(title+"_roi");
close();
selectWindow(title+"_copyroi");
close();
selectWindow(title);
close();
selectWindow("BeforeImageProcessing");
run("Background Correction ", "number=2 radius=4 auto-contrast");
title3=getTitle;
decision=getBoolean("Do you want to apply the Rolling Ball Background
Subtraction?");
if (decision==1){
    rayon=getNumber("radius",15);
    run("Subtract Background...","rolling="+rayon);
    }
run("Despeckle");
```

```
showMessage("press F2 for Otsu thresholding or F3 for manual
thresholding");
exit;
}
//
°°°°°°°°°°°°°°°°°°°°°°°°°°°°°°°°°°°°°°°°°°°°°°°°°°°°°°°°°°°°°°°°°°°°°°°°°°°°
°°°°°°°°
macro "manual Thresholding [F3]"
{
showMessage("adjust the Threshold manually and press the apply button");
selectWindow(title3);
run("Duplicate...");
rename("Threshold");
setAutoThreshold();
updateDisplay();
run("Threshold...");
showMessage("when finished, close threshold interface and press F7 to
continue segmentation");
exit;
}
//
°°°°°°°°°°°°°°°°°°°°°°°°°°°°°°°°°°°°°°°°°°°°°°°°°°°°°°°°°°°°°°°°°°°°°°°°°°°°
°°°°°°
macro "Otsu Thresholding [F2]"
{
selectWindow(title3);
run("Otsu Thresholding");
run("Invert");
run("Make Binary");
selectWindow(title2);
close();
selectWindow("Threshold");
//erosions=getNumber("Erosions", 0);
//run("BinaryFilterReconstruct ", "erosion="+erosions+" ");
run("Options...", "iterations=5 count=8");
run("Close-");
// The function "Binary Fill" does not seem to work correctly, replaced by
the function "Fill Holes".
// But "Fill Holes" does not fill the holes located on the border of ROI.
run("Fill Holes");
selectWindow(title3);
run("Magenta Hot");
run("Image Calculator...", "image1="+title3+" operation=XOR
image2=Threshold create");
//this image shows the over- and underestimation in color
rename("OverUnder");
title4=getTitle;
run("Image Calculator...", "image1="+title3+" operation=OR image2=Threshold
create");
//this image shows the overestimation in color
rename("Overestimation");
overestimation=getTitle;
run("Image Calculator...", "image1="+title4+" operation=Difference
image2="+overestimation+" create");
//this image shows the underestimation in color
rename("Underestimation");
underestimation=getTitle;
run("Tile");
selectWindow("Threshold");
run("Duplicate...", "title=Binary"+title2+"");
imagebin=getTitle;
```

```
selectWindow("Threshold");
close();
selectWindow(title4);
close();
selectWindow(overestimation);
saveAs("Jpeg");
close();
selectWindow(underestimation);
saveAs("Jpeg");
close();
// select vessel parameters
selectWindow(imagebin);
run("Set Measurements...", "area centroid perimeter bounding fit
circularity feret's limit redirect=None decimal=6");
run("Analyze Particles...", "size=25-Infinity circularity=0.00-1.00
show=Ellipses display clear record");
rename("Ellipses.tif");
run("Image Calculator...", "image1="+title3+" operation=Difference
image2=Ellipses.tif create");
rename("MergedEllipses");
for (i=0; i<nResults; i++)
    {Major = newArray(nResults);
    Minor = newArray(nResults);
    MajorDivMinor = newArray(nResults);
    Major[i]=getResult('Major',i);
    Minor[i]=getResult('Minor',i);
    MajorDivMinor[i] = Major[i]/Minor[i];
    setResult("a/b",i,MajorDivMinor[i]);
    HeightBounding = newArray(nResults);
    WidthBounding = newArray(nResults);
    MinDistBounding = newArray(nResults);
    MinDistBounding2 = newArray(nResults);
    HeightBounding[i]=getResult('Height',i);
    WidthBounding[i]=getResult('Width',i);
    MinDistBounding[i]=minOf(HeightBounding[i],WidthBounding[i]);
    MinDistBounding2[i]=MinDistBounding[i]*pixelsize;
    setResult("MinDistBoundingBox(µm)",i,MinDistBounding2[i]);
    }
updateResults();
//compute vessel parameters
area=0;
SumMajorDivMinor=0;
for (i=0; i<nResults; i++)
    {area+=getResult("Area", i);
    SumMajorDivMinor+=getResult("a/b",i);
    SumMinor+=getResult("Minor",i);
    SumMinDistBoundingBox+=getResult("MinDistBoundingBox(µm)",i);
    }
// compute other mean vessel diameters
selectWindow(imagebin);
run("Particles8 Plus", " exclude label show=Particles filter minimum=25
maximum=999999 display overwrite");
feretmin = newArray(nResults);
feretmin1 = newArray(nResults);
feretminmm = newArray(nResults);
for (i=0; i<nResults; i++) {
    feretmin1[i] = getResult('MinR',i);
    feretmin[i]  =  2*feretmin1[i] * pixelsize;
    feretminmm[i] = 2*feretmin1[i] * pixelsize/1000;
    Breadth = newArray(nResults);
    Breadthmm = newArray(nResults);
```

```
    Breadth[i] = getResult('Breadth',i);
    Breadthmm[i] = Breadth[i]*pixelsize/1000;
    setResult("diameterBreadth(mm)", i, Breadthmm[i]);
    }
run("Select None");
for (i=0; i<nResults; i++) {
    setResult("diameterFeretMin(µm)", i, feretmin[i]);
    setResult("diameterFeretMin(mm)", i, feretminmm[i]);
    }
updateResults();
feret=0;
for (i=0; i<nResults; i++){
    feret+=getResult("diameterFeretMin(µm)",i);
    breadth+=getResult("diameterBreadth(mm)",i);
    }
vesselarea=area*pixelsize*pixelsize;
Lv = SumMajorDivMinor/ROIareamillim
// print results to a text file
print ("number of detected vessels: "+nResults);
print ("total vessel surface (µm²): "+vesselarea);
print ("mean vessel surface (µm²): "+vesselarea/nResults);
print ("vascular volume 2D-method (en %): "+area*100/ROIarea);
print ("vessel density (nb /mm²): "+nResults/ROIareamillim);
print ("mean vessel diameter from minor ellipse diameter (mm):
"+SumMinor/nResults/1000);
print ("mean vessel diameter from inscribed circle (mm):
"+feret/nResults/1000);
print ("mean vessel diameter from bounding box (mm):
"+SumMinDistBoundingBox/nResults/1000);
print ("mean vessel diameter from breadth perpendicular to feret (mm):
"+breadth/nResults);
print ("sum of a/b over all detected vessels: "+SumMajorDivMinor);
print ("mean vascular length density Lv for this slice in mm-² is: "+Lv);
print ("slice number "+slice);
// enter additional results into the excel file
setResult("MeanVesselDiameterIC",0,feret/nResults/1000);
setResult("MeanVesselDiameterMAE",0,SumMinor/nResults/1000);
setResult("MeanVesselDiameterBB",0,SumMinDistBoundingBox/nResults/1000);
setResult("MeanVesselDiameterBreadth",0,breadth/nResults);
setResult("LengthDensity(Lv,mm-²)",0,Lv);
setResult ("ROIarea(mm²)",0,ROIareamillim);
setResult ("VascVol(2D)",0,area*100/ROIarea);
setResult ("Sum_a/b",0,SumMajorDivMinor);
setResult ("VesselDensity(nb/mm²)",0,nResults/ROIareamillim);
updateResults();
// Save binary image and measures
selectWindow("MergedEllipses");
rename("MergedEllipses"+title);
saveAs("Jpeg");
close();
selectWindow("BeforeImageProcessing");
close();
selectWindow(imagebin);
rename("Binary"+title);
saveAs("Jpeg");
close();
selectWindow("Results");
saveAs("text");
selectWindow("Log");
saveAs("text");
selectWindow(title3);
```

```
close();
selectWindow("Ellipses.tif");
close();
exit;
}
//
∘∘∘∘∘∘∘∘∘∘∘∘∘∘∘∘∘∘∘∘∘∘∘∘∘∘∘∘∘∘∘∘∘∘∘∘∘∘∘∘∘∘∘∘∘∘∘∘∘∘∘∘∘∘∘∘∘∘∘∘∘∘∘∘∘∘∘∘∘∘∘∘∘∘∘
∘∘∘∘∘∘
macro "Segmentation [F7]"
{
run("Make Binary");
selectWindow(title2);
close();
selectWindow("Threshold");
//erosions=getNumber("Erosions", 0);
//run("BinaryFilterReconstruct ", "erosion="+erosions+" ");
run("Options...", "iterations=5 count=8");
run("Close-");
run("Fill Holes");
selectWindow(title3);
run("Magenta Hot");
run("Image Calculator...", "image1="+title3+" operation=XOR
image2=Threshold create");
rename("OverUnder");
title4=getTitle;
run("Image Calculator...", "image1="+title3+" operation=OR image2=Threshold
create");
rename("Overestimation");
overestimation=getTitle;
run("Image Calculator...", "image1="+title4+" operation=Difference
image2="+overestimation+" create");
rename("Underestimation");
underestimation=getTitle;
run("Tile");
selectWindow("Threshold");
run("Otsu Thresholding");
run("Invert");
imagebin=getTitle;
selectWindow("Threshold");
close();
selectWindow(title4);
close();
selectWindow(overestimation);
saveAs("Jpeg");
close();
selectWindow(underestimation);
saveAs("Jpeg");
close();
showMessage("press F6 for the measurement of the segmented structures");
exit;
}
//
∘∘∘∘∘∘∘∘∘∘∘∘∘∘∘∘∘∘∘∘∘∘∘∘∘∘∘∘∘∘∘∘∘∘∘∘∘∘∘∘∘∘∘∘∘∘∘∘∘∘∘∘∘∘∘∘∘∘∘∘∘∘∘∘∘∘∘∘∘∘∘∘∘∘∘
∘∘∘∘∘∘∘∘
macro "measurements [F6]"
{
// select vessel parameters
selectWindow(imagebin);
run("Set Measurements...", "area centroid perimeter bounding fit
circularity feret's limit redirect=None decimal=6");
```

```
run("Analyze Particles...", "size=25-Infinity circularity=0.00-1.00
show=Ellipses display clear record");
rename("Ellipses.tif");
run("Image Calculator...", "image1="+title3+" operation=Difference
image2=Ellipses.tif create");
rename("MergedEllipses");
for (i=0; i<nResults; i++)
    {Major = newArray(nResults);
    Minor = newArray(nResults);
    MajorDivMinor = newArray(nResults);
    Major[i]=getResult('Major',i);
    Minor[i]=getResult('Minor',i);
    MajorDivMinor[i] = Major[i]/Minor[i];
    setResult("a/b",i,MajorDivMinor[i]);
    HeightBounding = newArray(nResults);
    WidthBounding = newArray(nResults);
    MinDistBounding = newArray(nResults);
    MinDistBounding2 = newArray(nResults);
    HeightBounding[i]=getResult('Height',i);
    WidthBounding[i]=getResult('Width',i);
    MinDistBounding[i]=minOf(HeightBounding[i],WidthBounding[i]);
    MinDistBounding2[i]=MinDistBounding[i]*pixelsize;
    setResult("MinDistBoundingBox(µm)",i,MinDistBounding2[i]);
    }
updateResults();
//compute vessel parameters
area=0;
SumMajorDivMinor=0;
for (i=0; i<nResults; i++)
    {area+=getResult("Area", i);
    SumMajorDivMinor+=getResult("a/b",i);
    SumMinor+=getResult("Minor",i);
    SumMinDistBoundingBox+=getResult("MinDistBoundingBox(µm)",i);
    }
// compute other mean vessel diameters
selectWindow(imagebin);
run("Particles8 Plus", " exclude label show=Particles filter minimum=25
maximum=999999 display overwrite");
feretmin = newArray(nResults);
feretmin1 = newArray(nResults);
feretminmm = newArray(nResults);
for (i=0; i<nResults; i++) {
    feretmin1[i] = getResult('MinR',i);
    feretmin[i]  =  2*feretmin1[i] * pixelsize;
    feretminmm[i] = 2*feretmin1[i] * pixelsize/1000;
    Breadth = newArray(nResults);
    Breadthmm = newArray(nResults);
    Breadth[i] = getResult('Breadth',i);
    Breadthmm[i] = Breadth[i]*pixelsize/1000;
    setResult("diameterBreadth(mm)", i, Breadthmm[i]);
    }
run("Select None");
for (i=0; i<nResults; i++) {
    setResult("diameterFeretMin(µm)", i, feretmin[i]);
    setResult("diameterFeretMin(mm)", i, feretminmm[i]);
    }
updateResults();
feret=0;
for (i=0; i<nResults; i++){
    feret+=getResult("diameterFeretMin(µm)",i);
    breadth+=getResult("diameterBreadth(mm)",i);
```

```
    }
vesselarea=area*pixelsize*pixelsize;
Lv = SumMajorDivMinor/ROIareamillim
// print results to a text file
print ("number of detected vessels: "+nResults);
print ("total vessel surface (µm²): "+vesselarea);
print ("mean vessel surface (µm²): "+vesselarea/nResults);
print ("vascular volume 2D-method (en %): "+area*100/ROIarea);
print ("vessel density (nb /mm²): "+nResults/ROIareamillim);
print ("mean vessel diameter from minor ellipse diameter (mm):
"+SumMinor/nResults/1000);
print ("mean vessel diameter from inscribed circle (mm):
"+feret/nResults/1000);
print ("mean vessel diameter from bounding box (mm):
"+SumMinDistBoundingBox/nResults/1000);
print ("mean vessel diameter from breadth perpendicular to feret (mm):
"+breadth/nResults);
print ("sum of a/b over all detected vessels: "+SumMajorDivMinor);
print ("mean vascular length density Lv for this slice in mm-² is: "+Lv);
print ("slice number "+slice);
// enter additional results into the excel file
setResult("MeanVesselDiameterIC",0,feret/nResults/1000);
setResult("MeanVesselDiameterMAE",0,SumMinor/nResults/1000);
setResult("MeanVesselDiameterBB",0,SumMinDistBoundingBox/nResults/1000);
setResult("MeanVesselDiameterBreadth",0,breadth/nResults);
setResult("LengthDensity(Lv,mm-²)",0,Lv);
setResult ("ROIarea(mm²)",0,ROIareamillim);
setResult ("VascVol(2D)",0,area*100/ROIarea);
setResult ("Sum_a/b",0,SumMajorDivMinor);
setResult ("VesselDensity(nb/mm²)",0,nResults/ROIareamillim);
updateResults();
// Save binary image and measures
selectWindow("MergedEllipses");
rename("MergedEllipses"+title);
saveAs("Jpeg");
close();
selectWindow("BeforeImageProcessing");
close();
selectWindow(imagebin);
rename("Binary"+title);
saveAs("Jpeg");
close();
selectWindow("Results");
saveAs("text");
selectWindow("Log");
saveAs("text");
// Close images
selectWindow(title3);
close();
selectWindow("Ellipses.tif");
close();
}
}}
```

Appendix II: A new Magnetic Resonance Imaging method for mapping the cerebral blood volume fraction: the rapid steady-state T_1 method

Perles-Barbacaru AT, Lahrech H

Mar 2007

J Cereb Blood Flow Metab 27(3):618-631

Appendix III: Cerebral blood volume quantification in a C6 tumor model using Gadolinium Per (3,6) Anhydro Alpha Cyclodextrin as a new MRI preclinical contrast agent

Lahrech H, Perles-Barbacaru AT, Gadelle A, Aous S, Farion R, Le Bas JF, Debouzy JC, Fries HP

in press

J Cereb Blood Flow Metab

Appendix IV: Imagerie du volume sanguin cérébral

Perles-Barbacaru AT

Jan 2007

Le Gluon, journal of scientific vulgarization of the Joseph Fourier University,

http://www.ujf-grenoble.fr/76056968/0

Imagerie du volume sanguin cérébral

Ingénierie / Santé

Savez-vous de combien d'eau est constitué votre cerveau ? D'environ 95% ! Et de sang ? L'Imagerie par Résonance Magnétique (IRM) peut donner la réponse, car elle détecte un signal émis par des molécules d'eau, leur quantité et leur localisation spatiale. Depuis l'invention de son principe en 1973 par Paul Lauterbour (Prix Nobel de médecine 1993), l'IRM ne cesse d'évoluer grâce au développement de l'informatique et à des applications de plus en plus nombreuses.

Le volume sanguin cérébral

L'irrigation du cerveau, dite perfusion sanguine, est une donnée très importante dans un cadre clinique car elle permet de caractériser différents types de lésions cérébrales (cancer, accidents vasculaires, maladie d'Alzheimer, etc.). Les variations de la perfusion se produisent principalement à l'échelle des vaisseaux microscopiques. Actuellement le volume sanguin cérébral – c'est-à-dire le volume occupé par le sang dans les micro-vaisseaux par unité de volume du tissu – n'est mesurable que par biopsie de tissu cérébral (cf. glossaire), opération délicate, quand elle est possible, et qu'on ne pratique qu'en dernier recours. Les techniques d'imagerie médicale (IRM, scanner X et autres) présentent une alternative moins invasive (cf. glossaire) permettant de quantifier certains paramètres de la perfusion, dont le volume sanguin cérébral. Cependant, ces techniques présentent des contraintes majeures, comme l'injection d'un produit radioactif ou une faible résolution spatiale. De plus, elles ne procurent souvent que des valeurs relatives du volume sanguin cérébral qui ne permettent pas d'interpréter une variation de ce paramètre dans l'évolution d'une maladie ou au cours d'une thérapie. Par exemple, chez les mammifères le volume sanguin cérébral est en moyenne de 2 à 5%, mais c'est la connaissance de la valeur exacte pour chaque espèce et chaque structure cérébrale saine qui permettrait d'asseoir les interprétations.

Ils existent des techniques IRM qui fournissent des valeurs absolues mais elles sont souvent basées sur des hypothèses complexes, difficiles à mettre en œuvre en pratique hospitalière ou nécessitant des mesures supplémentaires sur des prélèvements de sang du patient.

Une nouvelle méthodologie IRM simple, rapide, fiable et peu invasive, donnant accès à des valeurs absolues, a été élaborée par une équipe de l'INSERM à Grenoble qui mesure directement le volume sanguin cérébral après injection d'un produit de contraste qui

LE GLUON

Source : Zlokovic, Apuzo, Neurosurgery 43(4) : 877-878, 1998, Lippincot Williams & Wilkins.

Figure 1. L'architecture vasculaire du cerveau humain. Les « micro-vaisseaux » dont on cherche à mesurer le volume en IRM, sont de trop faible taille pour être rendus visible par la présente méthode de fixation.

assigne des propriétés détectables au sang.

La technique IRM

En IRM le contraste dépend de quelques paramètres physico-chimiques propres au tissu, mais l'astuce de cette technique est de les pondérer différemment par des paramètres machine, afin d'arriver à exploiter les propriétés du tissu auxquelles on s'intéresse dans un cas particulier. L'objectif de la recherche méthodologique est de développer des techniques fiables, rapides et peu invasives et sans effet nocif pour les patients, mais aussi simples à mettre en œuvre dans la routine clinique.

La méthode RSST1

La méthode développée, appelée RSST1 (cf. glossaire), exploite une technique d'imagerie permettant d'annuler le signal provenant des molécules d'eau de tous les tissus cérébraux qui ne sont pas en contact avec le produit injecté, tandis que les molécules d'eau du sang émettent un signal détectable et proportionnel à leur densité. Pour normaliser ce signal on utilise une autre acquisition plus lente qui permet à toutes les molécules d'eau du cerveau d'émettre un signal proportionnel à leur densité. Le rapport entre ces deux acquisitions est le volume sanguin cérébral absolu, car la densité de l'eau est la même dans le tissu et le sang.

La méthode a été appliquée sur le cerveau de rat sain et la sensibilité a été démontrée en augmentant d'une façon contrôlée le volume sanguin cérébral par inhalation de CO_2 de seulement quelques pour cent de la valeur initiale. Les valeurs obtenues dans différentes structures cérébrales sont compatibles avec les données de la littérature obtenues par d'autres méthodes.

Grâce à des produits de contraste qui ne quittent pas les vaisseaux fragilisés, des mesures du volume sanguin cérébral absolu ont été obtenues dans un type de tumeur cérébrale de rat. Cette méthode permettra alors de suivre les variations du volume sanguin cérébral au cours du développement de la tumeur ainsi que de tester l'efficacité des nouvelles thérapies anti-tumorales chez l'animal. Cette méthode pourra être transférée en clinique, dès que des agents de contraste ayant cette propriété et qui sont actuellement en cours d'étude pharmaco-clinique, auront été autorisés chez l'Homme.

T.-A. Barbacaru

GLOSSAIRE

Biopsie :
Prélèvement, in vivo, d'un fragment de tissu pour établir un diagnostic.

Invasif :
Acte médical qui implique un passage à travers la peau.

RSST1 :
Acronyme anglais : Rapid Steady State T1 .

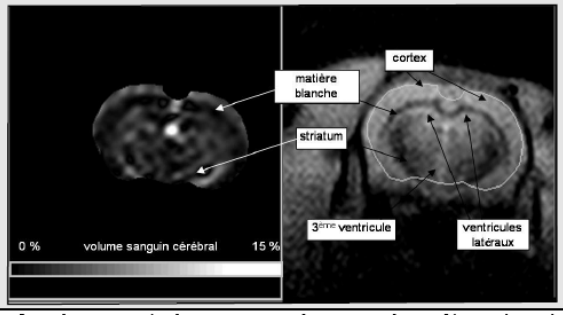

Figure 2. Le volume sanguin dans une coupe du cerveau de rat. L'image de gauche montre une cartographie du volume sanguin cérébral d'une coupe de 2 mm d'épaisseur dans un cerveau de rat sain avec la méthode RSST1. Les structures cérébrales (mieux visualisées dans l'image IRM conventionnelle de droite), se distinguent par des volumes sanguins régionaux différents.

CONSEILS DE LECTURE

Perles-Barbacaru AT, Lahrech H. *A new Magnetic Resonance Imaging method for mapping the cerebral blood volume fraction: the rapid steady-state T1 method.* J Cereb Blood Flow Metab (accepted 2006 Jul 19).

Barbier E. *IRM de la microvascularisaton cérébrale.* Le Gluon Janvier 2005

L'AUTEUR

Originaire de la Roumanie, j'ai étudié la médecine à l'Université de Hambourg-Eppendorf en Allemagne, avec des stages cliniques de spécialisation en Radiothérapie et Neurochirurgie en Inde, en Israël et en Suisse. Ayant aussi une passion pour les « maths », et non seulement pour la « bio », j'ai enchainé avec des études de physique fondamentale et astrophysique en partie à Hambourg et en partie à Paris-Orsay. Intéressée tout de même par les applications médicales des méthodes physiques j'ai effectué un stage de maîtrise à l'Institut de Protonthérapie à Orsay et le stage de DEA dans l'unité mixte UJF/INSERM U594 de Neuroimagerie Fonctionnelle et Métabolique à Grenoble où j'ai déjà travaillé sur la mise en place de la méthode IRM décrite dans cet article. Mon projet de thèse au sein de l'équipe de micro-vascularisation de cette unité est de développer cette méthode et d'étudier des agents de contraste associés pour qu'elle soit utilisable pour l'étude des tumeurs cérébrales dans des modèles animales et chez l'Homme.

Adriana T. Perles-Barbacaru
INSERM — Neuroimagerie Fonctionnelle et Métabolique
Teodora-Adriana.Barbacaru@ujf-grenoble.fr

LE GLUON

Comité de rédaction
Nicolas Arnaud, Laurence Bolling, Emilie Demarsy, Alexandre Donzé, Gaël Le Bec, Céline Lopez-Velasco, Julie Regaud-Six.
Directeur du CIES
Didier Retour
Chargée culture scientifique UJF
Isabelle Joncour
Directeur de la publication
Patrice Gadelle
Contact
Nicolas.Arnaud@imag.fr
Impression
Imprimerie des Ecureuils
Nombre d'exemplaires
2000
ISSN (demande en cours)
Publication mensuelle réalisée par un groupe de doctorants et de moniteurs (atelier de 3ème année du CIES)